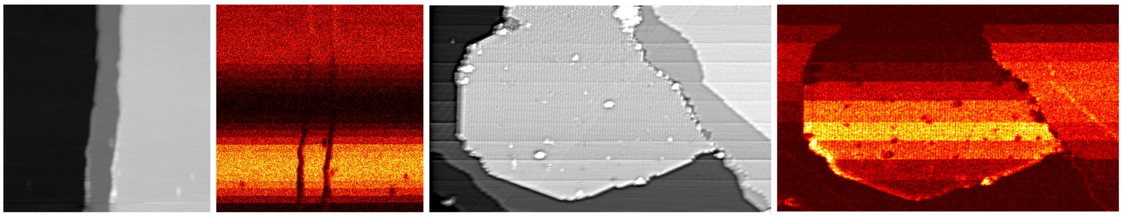

LIGHT EMISSION INDUCED BY TUNNELING ELECTRONS

DISSERTATION

vorgelegt der
Fakultät für Physik
der
UNIVERSITÄT DUISBURG-ESSEN

zur Erlangung des akademischen Grades
Doktor der Naturwissenschaften

Dr. rer. nat

von

MAREN CHRISTINA COTTIN

geboren am 1. Juli 1986 in Duisburg

EINGEREICHT AM	1. Oktober 2015
1. GUTACHTER	Prof. Dr. Rolf Möller
2. GUTACHTER	Prof. Dr. José Ignacio Pascual
DATUM DER DISPUTATION	17. November 2015

ABSTRACT

This thesis presents the analysis of light emitted from the tip-sample junction of a scanning tunneling microscope (STM) which is induced by the tunneling current flowing between the tip and the sample. In the course of this thesis, an experiment that combines STM with highly sensitive photon detection was set up. This technique is also referred to as STM-induced light emission (STM-LE). Different modes of measurement reveal the lateral distribution of the induced emission yield as well as the dependency of the emission intensity on the applied bias voltage and the spectral distribution of the emitted light in STM-LE spectra. Different sample systems are applied to study the effect of various factors that may influence the emission intensity. This gives access to energy transfer processes with atomic scale precision.

The careful analysis of the light emission induced on pristine and adsorbate covered Ag(111)-surfaces reveals that mainly the local density of states (LDOS) of the sample governs the lateral variation of the emission intensity.

A special focus of this thesis lies on the analysis of the effect of organic adlayers on the induced light emission. For molecules adsorbed on Ag(111), the induced light emission intensity is reduced as compared to the bare Ag-surface. In contrast, the light emission induced on monolayers of archetype organic molecules adsorbed on various ultrathin layered Bi-structures on Cu(111) is enhanced as compared to the substrate.

Spectroscopic measurements on C_{60} and 3,4,9,10-perylene-tetracarboxylic-dianhydride (PTCDA) adsorbed on the initial monolayer of bismuth (Bi) on Cu(111) show that the LDOS provided by the organic molecules significantly manipulates the dependency of the emission intensity on the applied bias voltage. However, the enhancement of the emission yield may additionally be associated to a rather low interaction between the ultrathin Bi-structures and the organic overlayers.

A careful analysis of the spectral distribution of the light emitted from the tip-sample junction provides the identification of the pathways of excitation as well as the particular involved energetic transitions. For the organic layers on Bi/Cu(111), the enhancement of the induced light emission intensity does not involve radiative transitions between molecular states. Like in the case of the pristine surfaces, inelastically tunneling electrons drive collective electronic excitations localized to the tip-sample junction, so called tip induced plasmons (TIPs), which subsequently decay radiatively. The electronic states of the adsorbed molecules are directly involved in the inelastic tunneling processes and actively modify the coupling to the TIP modes.

KURZFASSUNG

Die vorliegende Arbeit befasst sich mit der Analyse von Licht, das angeregt durch den fließenden Tunnelstrom vom Spitze-Probe-Kontakt eines Rastertunnelmikroskops (STM, vom Englischen: scanning tunneling microscope) emittiert wird. Im Zuge der Arbeit wurde ein entsprechendes Experiment aufgebaut, in dem ein Rastertunnelmikroskop mit einem hochempfindlichen Aufbau zur Lichtdetektion kombiniert wurde. Die zugehörige experimentelle Technik wird auch als STM-induzierte Lichtemission (STM-LE) bezeichnet.

Der experimentelle Aufbau erlaubt es, sowohl die laterale Verteilung als auch den Verlauf der induzierten Lichtintensität mit der angelegten Tunnelspannung aufzuzeichnen. Zudem ist eine spektrale Analyse des emittierten Lichts möglich. Verschiedene Modellsysteme werden im Hinblick auf den Einfluss unterschiedlicher Faktoren auf die Emissionsintensität untersucht. Dies erlaubt einen Einblick in Energietransferprozesse auf atomarer Skala.

Die Analyse der Lichtemission von reinen und adsorbatbedeckten Ag(111)-Oberflächen zeigt, dass für die laterale Verteilung der Emissionsintensität hauptsächlich die lokale Zustandsdichte (LDOS, vom Englischen: local density of states) der Probe verantwortlich ist.

Ein besonderer Schwerpunkt der hier gezeigten Experimente liegt auf der Untersuchung des Einflusses organischer Molekülschichten auf die induzierte Lichtemission. Für adsorbierte Molekülschichten auf Ag(111) beobachtet man eine Abnahme der induzierten Emissionsintensität im Vergleich zur Anregung auf der reinen Substratoberfläche. Im Gegensatz hierzu ist die Intensität der Lichtemission im Vergleich zum Substrat stärker, wenn sie auf organischen Monolagen auf verschieden dicken Bismut-Filmen auf Cu(111) induziert wird.

Spektroskopische Untersuchungen an den beiden Modellmolekülen C_{60} und 3,4,9,10-Perylen-Tetracarbonsäure-Dianhydrid (PTCDA) adsorbiert auf einer Monolage Bismut auf Cu(111) zeigen, dass die LDOS der Moleküle den Verlauf der Emissionsintensität als Funktion der angelegten Tunnelspannung bestimmt. Die beobachtete Erhöhung der Lichtausbeute für die Molekülschichten wird zudem mit einer schwachen Wechselwirkung der Moleküle mit dem Substrat verbunden.

Die eingehende Analyse der spektralen Verteilung des emittierten Lichts erlaubt es, die zugrundeliegenden energetischen Übergänge zu identifizieren. Im Falle von Molekülen auf Bismut auf Cu(111) sind bei der Anregung der Lichtemission keine strahlenden Übergänge innerhalb der Moleküle involviert. Wie im Fall der reinen Silber- und Bismut-Kupfer-Oberflächen beruht die Anregung der Lichtemission rein auf inelastischen Tunnelprozessen zwischen der Spitze und der Probe. Diese koppeln an kollektive elektronische Anregungen des Spitze-Probe-Kontakts, sogenannte spitzeninduzierte Plasmonen (TIPs, vom Englischen: tip induced plasmons), die strahlend zerfallen. Die adsorbierten Moleküle stellen Zustände für die inelastischen Tunnelprozesse zur Verfügung und beeinflussen aktiv die Kopplungsstärke zu den TIP-Moden.

‘The only way you can know -
you give it all you have.’

One Republic, I lived

CONTENTS

Part I

INTRODUCTION AND MOTIVATION

1

INTRODUCTION

Electronic devices have become an essential part of our everyday life. Computers, cell phones and other mobile devices accompany us in our daily routines and are the base of today's worldwide network of communication and data processing. These devices sustainably influence our work and lifestyle.

Today's smartphones may easily outperform five year old computers. With growing storage capacities also the number of e.g. digital pictures, videos or music files on our devices constantly grows. The rapid development of the capacities and working speeds of these devices already seems natural to us. Cell phone plans provide us with the newest cell phones every one or two years. While up to a few years ago TV-sets lasted in our living rooms for ten or more years, nowadays, we replace them after a few years with new state-of-the-art technology.

When thinking about the development of future electronic devices, people tend to think of clean-rooms, computer-aided design, and prototypes presented on fairs. Big vacuum-chambers equipped with scanning probe techniques or electron spectroscopy units will only rarely cross people's mind. However, though it does not always provide ready-to-use devices or prototypes right away, basic research holds a big share in bringing our technological development forward. It aims for providing a basic understanding of the underlying physical phenomena and therefore provides the key prerequisites for successful future engineering.

A steady goal of research is to increase the efficiency and cost of electronic devices and their components. This is oftentimes connected to a miniaturization of the utilized building blocks. One way to address this challenge is the so called "top down" approach. Based on state of the art-devices, components are downscaled to yield improved properties such as larger storage densities and lower energy consumption. Basic research oftentimes addresses the challenge of downscaling with another approach, the so called "bottom up" approach. Here, the smallest possible building blocks, i.e. single molecules and atoms, are characterized. This provides a construction kit to build miniaturized electronic components on the smallest possible scale.

The performance of electronic devices is governed by the efficiency of the energy transfer within the components. Energy may be transported e.g. by the flow of an electric current, however, also the transformation from one energy form into another plays a crucial role in electronic components. A very straightforward example for such energy conversion is a light bulb where electric energy is converted into light. However, in this approach a lot of energy is lost through heat. Light emitting diodes (LEDs) are a more effective way to convert electric energy to light. Their functioning principle is based on semiconductor physics. Light is emitted when electrons and holes recombine. Due to their high efficiency as compared to conventional light sources, they have become widely used energy-saving alternatives in lighting and are commonly used for the illumination of displays.

Classically, semiconductor devices such as LEDs are fabricated from inorganic materials such as silicon, germanium, or gallium arsenide. However, semiconducting organic molecules are great low cost and easy to process alternatives to conventional inorganic semiconductors. Samsung's Galaxy line for smartphones is only one example for organic LED technology that is already established on the market [1]. Semiconducting organic molecules may be printed on flexible substrates [2], allowing a variety of applications in electronic devices that may e.g. also find use in medicine and biology [1], [3]. A thorough characterization of such molecules and their coupling to prototype substrates paves the way for the development and improvement of future devices.

Scanning tunneling microscopy (STM) is capable of analyzing the properties of materials on the nanoscale. It can give insight into different properties such as the ordering and electronic structure of molecules adsorbed on surfaces and may reveal molecule-molecule and molecule-substrate interactions. A unique property of the STM is that it is also capable of manipulating structures on the nanoscale. This e.g. allows an *in situ* nano-scale "prototyping" of archetype structures which can subsequently be characterized within the same experimental run. This allows a direct study of the influence of microscopic changes on the properties of the structures.

Our research presented in this thesis especially focuses on organic molecules with a prospect use in opto-electronic devices, e.g. LEDs, photodetectors or photovoltaics. So called optical antennas can be used to couple a local electric field to a propagating field and may make such devices more efficient [4–7]. In their basic functioning principle they may in many ways be viewed in analogy to radio antennas which convert electric signals into propagating radio waves and vice versa.

In the case of optical antennas, energy may be converted back and forth between collective electronic excitations, so called plasmons, and propagating electromagnetic waves, in this case light. In particular, antennas may localize energy collected from electromagnetic waves to a small volume, conversely they may efficiently extract radiation from a subwavelength source, e.g. single molecules or atoms [8]. Also, the plasmonic excitation of an optical antenna may be driven very locally, on the scale of a few nm, by coupling to an electric current.

Typical optical antennas have sizes in the regime of the wavelength of the transmitted or received propagating radiation [6]. Nonoscaled receiver or transmitter structures, e.g. organic dye molecules with a size of a few nm, are usually too small to act as efficient antennas for electromagnetic radiation in the visible range themselves [8]. Coupling such nanostructures to an optical antenna may greatly enhance the interaction area between the the emission rate, i.e. the efficiency of the energy transfer between localized excitations and propagating radiation and thus bare the potential to make light emitting devices, photodetectors, etc. more efficient [6–9].

The tunneling current flowing between the tip and the sample in an STM may excite plasmons localized to the tip-sample junction, so called tip-induced plasmons (TIPs). Further, the tunneling current may excite molecules that are additionally introduced to the junction. A possible relaxation channel for these excitations is a radiative decay. In fact, the tip of the STM may be viewed as an optical antenna in this case.

The corresponding experimental technique is referred to as STM-induced light emission (STM-LE) [10]. It combines a regular STM-experiment with highly sensitive photon detection.

STM-LE allows us to study the characteristic coupling between an electric current, a local plasmonic excitation, and light. The spectral distribution of the light emitted from the tip-sample junction bears information about the junction geometry [11], but may also reveal different channels of excitation, i.e. energy transfer processes in the tip-sample junction. These may e.g. be inelastic transitions from tip states to sample states [12, 13] and vice versa [14] or radiative transitions inside organic molecules [15–19]. Additionally, channels for non-radiative energy transfer may be revealed [20].

The possible energetic transitions that drive the light emission depend on the local electronic structure of the sample. Organic molecules adsorbed on metal surfaces may selectively provide a certain electronic structure [13] and therefore significantly impact the efficiency of the induced light emission [14, 21]. Further, the efficiency of the energy conversion from tunneling electrons to emitted light mediated by organic molecules crucially depends on the coupling of the molecules to their local environment, e.g. the substrate. The driving current for the excitation is the tunneling current which is injected with atomic scale precision. This allows a highly spatially resolved excitation mapping, also referred to as photon mapping, down to the single molecule level and even submolecular resolution [14, 16]. Additionally, spectra of the emission intensity versus the bias voltage may reveal important information about the involved transitions.

In the experiments presented in this thesis, we studied the STM-induced light emission from pristine and molecule covered surfaces. Our investigations aimed to further understand the fundamental physical processes that drive the light emission from such nanoscaled junctions.

In particular, this thesis will address the following questions:

- How does the specific nanoscale junction influence the induced light emission? What are the specific roles of the tip and the sample, e.g. their particular geometries and material for the induced light emission?
- What are the governing factors for the induced emission intensity? What factors may be involved in the lateral variations of the emission intensity? Which factors govern the excitation efficiency versus the applied bias voltage?
- Can we tune the emission intensity by selectively applying organic layers to a substrate? How does the local density of electronic states (LDOS) provided by the electronic states of adsorbed molecules affect the excitation efficiency? How does the coupling between adsorbed organic molecules and the substrate control the emission intensity?

As part of this thesis, a light detection unit was implemented to an existing STM setup. The adaption of the setup to the new experimental requirements also included the customization of the STM itself, i.e. a new scanning unit was built and the heat shielding was modified to allow an efficient collection and guiding of light from the STM junction out of the chamber with minimum possible heat intake.

The newly established experimental setup allowed us to conduct state of the art STM-LE experiments. As a first sample system we chose pristine Ag(111). We use our data on this well studied prototype system to discuss the role of the tip geometry for the emission characteristics. Further, we elucidate general contrast mechanisms in photon mapping as well as the emission intensity versus the bias voltage.

We present photon maps for different archetype organic molecules that were applied to a Ag(111) surface. This serves as a starting point for the discussion of the role of such molecules in the light emission from the STM junction.

Then we pass on to a more complex sample system: Bi on Cu(111). After the characterization of the pristine substrate, we deposited two different archetype organic species, PTCDA and C_{60} onto the initial monolayer of Bi on Cu(111). In particular, we investigate the correlation between the electronic structure provided by the molecules and the intensity of the light emission. Further, we discuss the role of the Bi/Cu(111)-substrate for the emission intensity.

The fundamental understanding gained from such experiments paves the way for further improving the efficiency of opto-electronic devices by selectively tuning their properties on the nanoscale.

Part II

FUNDAMENTALS

2

FUNDAMENTALS

This chapter is meant to give a short introduction into scanning tunneling microscopy (STM) and STM-induced light emission (STM-LE). The latter is an extension of the regular STM-technique where the experimental setup is extended with a setup to collect and detect the light generated by inelastically tunneling electrons. This allows us to study excitations that lead to the emission of photons with atomic scale lateral precision.

2.1 SCIENTIFIC CONTEXT

2.1.1 *Scanning Tunneling Microscopy (STM)*

First STM topographic data were published by Binnig et al. in the early 1980's [22]. Until this point, surface science mainly relied on diffraction techniques to determine the atomic structure of samples. However, these techniques are usually limited to the dominating surface structures and periodicity in reciprocal space. Field emission and field ion microscopy (FEM and FIM) were the only techniques able to resolve structures with atomic resolution in real space. However, they were limited to the few frontmost atoms of sharp metal tips.

In contrast, STM was the first technique to directly image real space on the atomic scale. As compared to FEM and FIM, relatively large surface areas up to several μm may be analyzed with STM. Especially, nonperiodic surface structures and local surface defects may be studied. STM can be used to image and spectroscopically analyze the electronic structure of both, occupied and unoccupied states. However, the capabilities of the STM go far beyond the pure characterization of surfaces: The STM tip can be used to actively manipulate the surface, e.g. to build artificial structures. This way, archetype structures can be created and studied in the same experimental run, making STM one of the most popular techniques in basic research e.g. for the miniaturization and advancement of future electronic devices. Its invention was a widely appreciated breakthrough in surface analysis for which Binnig and Rohrer were awarded the nobel prize in physics in 1986 jointly with Ruska for the conception of the electron microscope [23].

2.1.2 *STM-Incuced Light Emission(STM-LE)*

The first STM-LE experiments were published by Gimzewski et al. in 1988 [10]. STM-LE experiments combine optical spectroscopic information with the ultimate lateral resolution of an STM. The light emission is triggered very locally by the tunnling current, allowing for an excitation mapping that reaches down to the submolcular [16, 18] or even the atomic scale [24, 25] level. At the same time, the electronic, e.g.

molecular, states involved in the light emission process may be indentified down to the vibronic level [16, 18].

STM-LE is an emerging tool in basic research to characterize light emission on the nanoscale to complement scanning nearfield optical microscopy (SNOM) and Raman spectropy. It particular, it has so far been used to study metals [12, 25–27] semiconductors [28, 29], and especially organic molecules [15, 16, 30–34] on the route to specifically tailor optical properties of future electronic applications, e.g. light emitting diodes (LEDs) or solar cells.

2.2 SCANNING TUNNELING MICROSCOPY (STM)

STM is based on the quantum mechanical effect of electron tunneling: A particle, e.g. an electron, can pass a barrier, even though its energy would classically not suffice to surmount the latter. On a basic level, the effect can be understood in terms of Heisenberg's uncertainty principle, where the position and the momentum of a particle cannot be known with infinite precision at the same time. Thus, if a particle of a given momentum is close enough to a non infinite barrier, it may be found on either side of the barrier with a non-zero probability.

To be able to quantify the tunneling between the tip and the sample of an STM, we need to gather further general understanding of the tunneling effect.

2.2.1 *The Concept of Tunneling*

Within the wave particle duality, a particle is fully described by its wave function Ψ. The probability to find a particle at a certain position x is given by the square of the absolute value of its wave function $|\Psi(x)|^2$. The wavefunction has to fulfill Schrödinger's equation. Looking at the stationary case, the time-independent version of the equation may be applied

$$\left[-\frac{\hbar^2}{2m}\frac{d^2}{dx^2}+V(x)\right]\Psi(x)=E\Psi(x), \tag{1}$$

where $\hbar$ is the reduced Planck constant, m and E are the mass and the energy of the particle, and $V(x)$ is the potential at the position x.

An archetype example for the quantitative treatment of the tunneling probability is the one dimensional rectangular potential barrier. The problem may be devided into three regions, left of the barrier, inside the barrier, and right of the barrier. With a general ansatz for Ψ and assuming continuity of $\Psi(x)$ and its derivative $\Psi'(x)$ at the edges of the potential barrier, one can derive the expression for the wavefunction in all three regions and therefore the transmission probability through the barrier. As the problem is extensively treated in textbooks, e.g. [35], [36], here, we will directly refer to the results of the calculation.

The wavefunction decays approximately exponentially into the barrier. The exponential decay is overlain with a very small exponential exponential rise due to the reflextion of the wavefunction at the inside of the barrier. The latter part, however, can usually be neglected so that one can derive an approximate transmission probability $T(E)$

$$T(E) \cong \frac{16(\kappa k)^2}{(\kappa^2 + k^2)^2} e^{-2\kappa d}, \tag{2}$$

with

$$k = \sqrt{\frac{2mE}{\hbar^2}} \quad \text{and} \quad \kappa = \sqrt{\frac{2m(V_0 - E)}{\hbar^2}}.$$

Here, E and m are the energy and the mass of the particle. V_0 and d are the height and width of the potential barrier. In an STM experiment, the term $(V_0 - E)$ would correspond to the work funtion ϕ of the tip or the sample.

Table 1: Values for the work function Φ and the inverse decay length κ for typical metals used in STM-experiments. E.g. the low-index surfaces of the noble metals silver (Ag), copper (Cu), and gold (Au) are popular archetype samples. Polycrystalline tungsten (W) wires are widely used to fabricate STM-tips. Values for Φ from [37]. A realistic general error estimate for the work functions Φ is ±0.3eV [37].

	Ag		**Cu**		**Au**		**W**	
surface orientation	Φ (eV)	κ ($Å^{-1}$)	Φ (eV)	κ ($Å^{-1}$)	Φ (eV)	κ ($Å^{-1}$)	Φ (eV)	κ ($Å^{-1}$)
(111)	4.74	1.12	4.94	1.14	5.31	1.18	4.47	1.08
(100)	4.64	1.10	4.59	1.10	5.47	1.20	4.63	1.10
(110)	4.52	1.09	4.48	1.08	5.37	1.19	5.52	1.20
polycrystalline	4.26	1.06	4.65	1.10	5.10	1.16	4.60	1.10

To obtain the simple exponential dependency in eq. (2), $\sinh(\kappa d)$ was approximated to $1/2e^{\kappa d}$. Such an approximation is most accurate for large κd. Typical values for ϕ and κ for common metals used in STM experiments are displayed in table 1. The width of the potential barrier d (the tunneling distance) is usually in the order of 5Å. With these values, the approximation as an exponential decay of the transmission probability within the vacuum barrier of an STM is well justified.

What is even more important for the operating principle of the STM than the exponential decay itself, is the order of magnitude for the inverse decay length κ. For typical metals used in STM experiments, κ is in the order of $1Å^{-1}$. According to (2), this means that the tunneling current changes by around one order of magnitude (e^{-2}) per Å. Thus, we can already get an idea of how sensitive the STM is in surface normal direction.

2.2.2 *Estimation of the Lateral Resolution of the STM*

We can also use the expression for the transmission probability in (2) to approximate the lateral resolution of an STM [38]. STM tips are either electrochemically etched or, if the material is soft enough, they are directly cut. In both cases, the radius of curvature

R near the tip-end can be assumed to be much larger than the tunneling distance d. Near the tip end, the tunneling current will flow in good approximation perpendicular to the sample surface. For $R >> d$, the increase of the tip-surface distance Δz at a lateral distance Δx from the very front of the tip apex can be approximated with a simple geometric estimation using the Pythagorean theorem (see Fig. 1)

$$\Delta z \approx \frac{\Delta x^2}{2R}. \tag{3}$$

Following (2), the tunneling current flowing at distance Δx from the tip apex would be

$$I(\Delta z) \approx I(0)e^{-2\kappa\frac{\Delta x^2}{2R}}, \tag{4}$$

where $I(0)$ is the tunneling current flowing at the tip apex.

According to (4), for typical values of $\kappa = 1\text{Å}^{-1}$ and $R = 10\text{Å}$ the current drops by around one order of magnitude for $\Delta x \approx 4.5\text{Å}$. This would mean a lateral resoltion in the order of 9Å.

While this already gives a taste of the high spacial resution of an STM, even smaller structures, e.g. single atoms within densly packed hexagonally ordered (111)-surfaces, may readily be resolved. The atomic distances of these structures lie in the order of $3-5\text{Å}$. More elaborate models of the tip-sample geometry, that are able to explain this resolution will be shortly discussed in section 2.4.1.

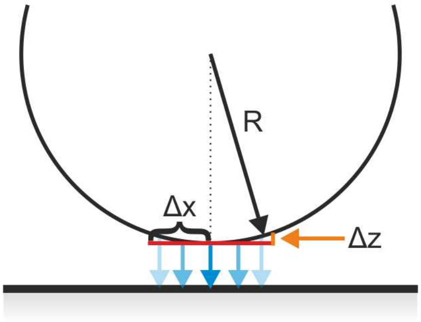

Figure 1: Illustration of a simple geometric estimation to approximate the lateral resolution of the STM. The radius of curvature R of the tip is usually much larger than the tunneling distance d. The change in the tunneling distance Δz at a lateral distance Δx from the very front of the tip apex can then be easily approximated using the Pythagorean theorem. The change of tunneling distance yields the tunneling current at Δx. With this, using typical values for the tip apex radius and the inverse decay length κ, the lateral resoltion of the STM can be approximated (see text).

2.3 STM: PRINCIPLE OF MEASUREMENT AND TECHNICAL REALIZATION

Section 2.2.1 allows a first understanding of the measurement principle of the STM: A sample surface and a probe tip are brought into close proximity in the order of a few Å so that their wave functions overlap. This allows electrons to tunnel from the tip to the sample and vice versa. Both electrodes, the tip and the sample do not physically touch. Thus, STM has the advantage of usually being a non-destructive technique.

Initially, the probabilities for electrons to tunnel in either direction are equally large. No net tunneling current can be measured. By applying a bias voltage in the order of a few mV to a few V between the tip or the sample, the Fermi energies of the tip and the sample are shifted with respect to each other. This way, within the energy range $E_F + eV$ the occupied states of one electrode oppose the unoccupied states of the other electrode within this energy window. Thus, the tunneling electrons are imprinted a predominant direction and can be measured as a net tunneling current. Usual tunneling currents lie in the order of a few pA to several nA.

To obtain a laterally resolved image of the surface structure, the tip is scanned across the surface line by line in x,y-direction, while the tunneling current is monitored (see Fig. 2). The mostly applied mode of STM operation is the so called *constant current mode*, where the tip follows the z-contour of the surface. A feedback loop constantly compares the obtained tunneling current value to a given set point. Deviations are reacted to by regulating the tip-sample distance. The corresponding electric signal to this movement is recorded as the topography signal. Usually, along with the topography signal also other signal channels, such as the tunneling current itself as an error signal, or the derivative of the tunneling current with respect to the bias voltage (dI/dV-signal, see section 2.5) are recorded.

Before it is fed into the feedback loop, the tunneling current signal passes a current-to-voltage-converter (IVC). A typical factor for the conversion is $10^9 V/A$. This yields voltage signals in the order of $10 mV$ to a few Volts, which are significantly easier to handle in the further signal processing than the original tunneling current signal.

As the tunneling current depends exponentially on the tip-sample distance, for easier signal processing, the feedback loop works with the logarithm of the tunneling current which is directly proportional to the tip-sample distance.

The high sensitivity of the tunneling current to changes in the tunneling distance can only be used if high mechanical stability of the experiment is granted. Thus, the damping against mechanical vibrations was one of the key points for the development of the STM [22, 39]. Binnig and Rohrer achieved this by a soft suspension of a compact tunneling unit [39]. For further mechanical decoupling of the STM from the environment, e.g viton stacks or pneumatic feet on which the experimental setup rests may be applied.

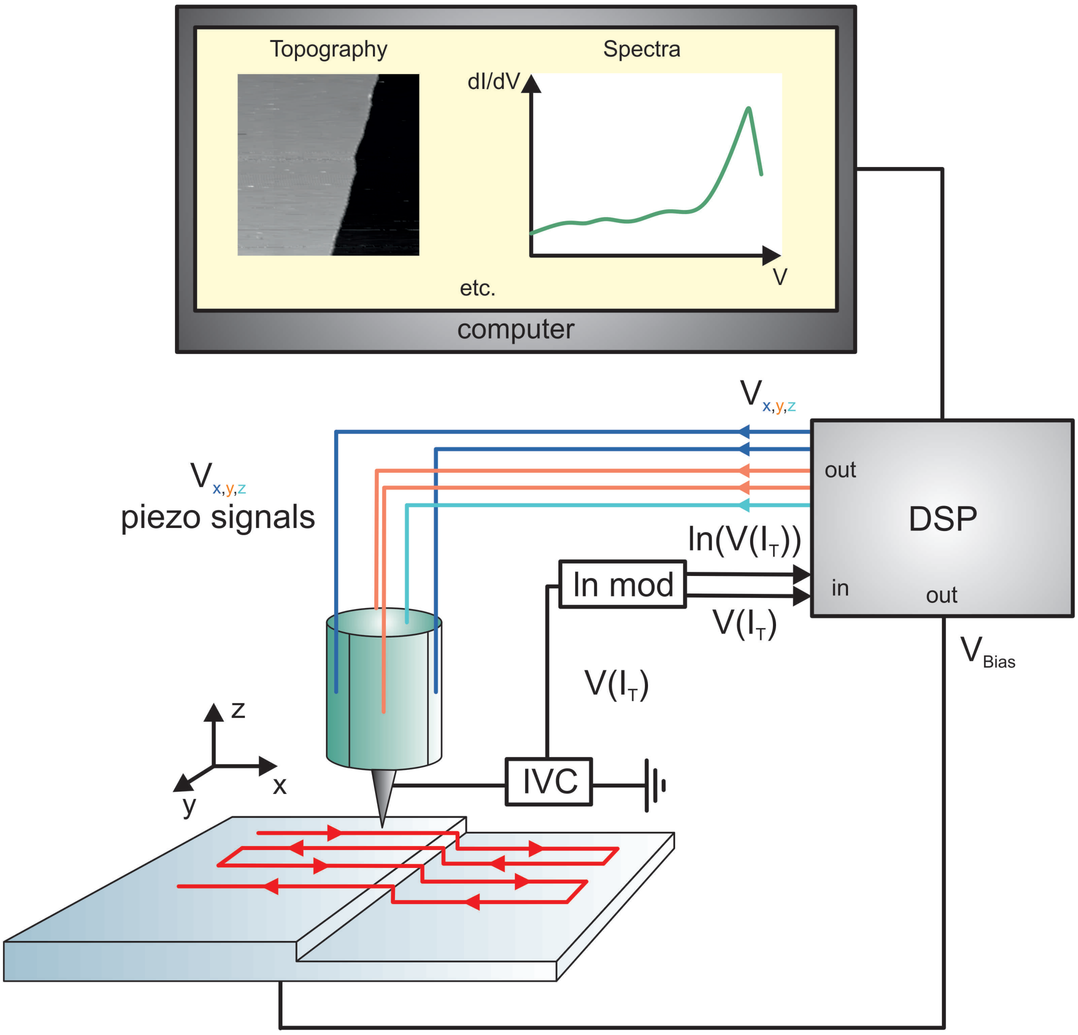

Figure 2: Scheme of an STM setup. The tip scans the surface while the tunneling current I_T is recorded. The tunneling current signal is transformed into a voltage signal $V(I_T)$ by a current-to-voltage converter (IVC). In the following, the signal is logarithmized in the ln-module (ln-mod) and fed into the digital signal processing (DSP) unit. Here, the value for the tunneling current is compared to a given set point and the tip sample distance is regulated accordingly in order to keep the tunneling current constant. The z-movement of the tip is recorded as the topography signal. Simultaneously, other signal channels, e.g. the tunneling current as an error signal for the feedback loop, the dI/dV-signal, etc. may be acquired. Point spectroscpy STS measurements are obtained by keeping the tip at a fixed lateral position above the sample and varying the bias voltage while recording the dI/dV-signal (see section 2.5).

2.3.1 *The Piezoelectric Effect*

The piezoelectric effect is the occurance of an electric field, i.e. a voltage drop, upon deformation of a solid material. Conversely, the inverse piezoelectric effect generates the deformation of a piezoelectric crystal when a voltage is applied (see Fig. 3). The piezoelectric effect is used, e.g. to create the spark to ignite electric lighters. Piezoelectric components that use the inverse piezoelectric effect are e.g. applied in loudspeakers. As the deformation of modern piezoelectric ceramics can be tuned very precisely, piezoelectric tubes or stacks are used to position the tips or samples in STM experiments with atomic precision.

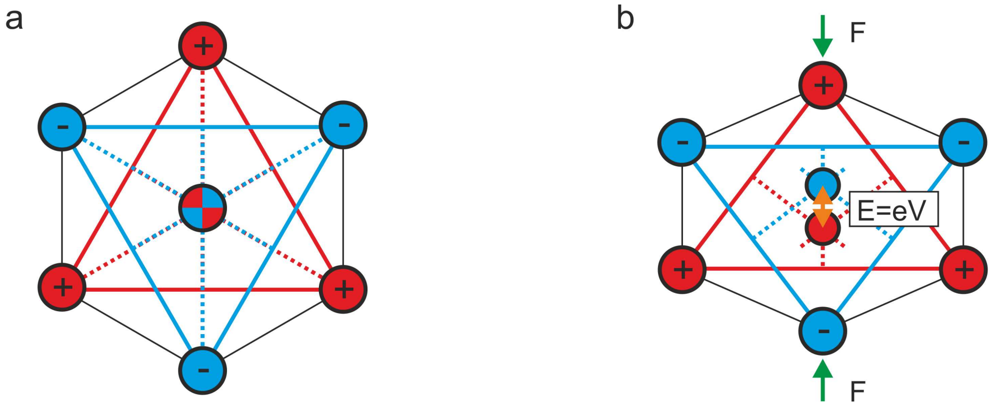

Figure 3: Scheme of the piezoelectric effect. a) Exemplary atomic structure of a piezoelectric material. When the crystal is in a relaxed shape and no voltage is applied, the centers of charge for positive and negative charge coincide. b) When a force is applied and deforms the piezoelectric crystal lattice, the centers of charge are separated which results in a voltage drop. Conversely, when a voltage is applied to the relaxed piezo crystal, the separation of the centers of mass forces they crystal to deform.

Piezoelectric materials are nonconducting and exhibit at least one polar axis but no symmetry (inversion) center in their crystal lattice. An exemplary scheme of the atomic structure of a piezoelectric material is shown in Fig. 3. In its original, relaxed position, the centers of charge for positive and negative charge lie on top of each other. Upon deformation, the centers of charge are separated, resulting in an electric field, i.e. a voltage drop. Conversely, an applied voltage will act on the charges of different sign, resulting in a deformation of the crystal and a separation of the centers of charge.

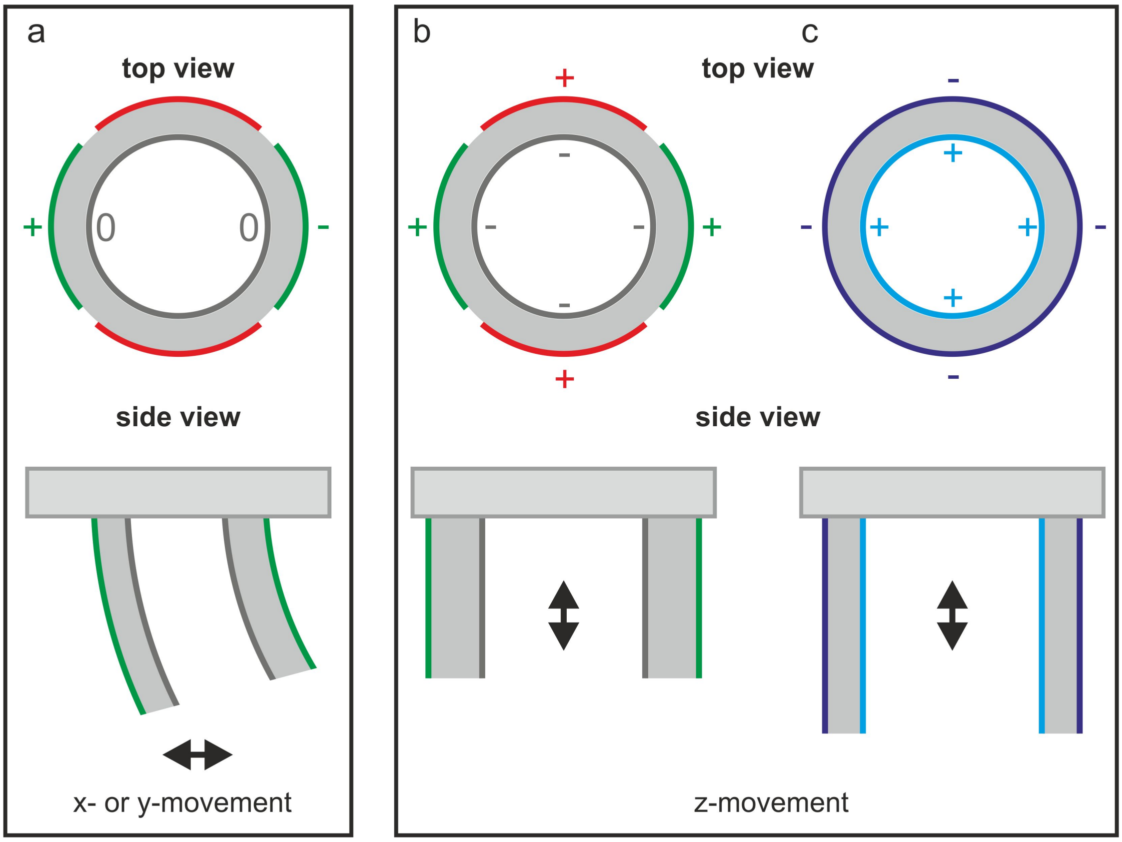

Figure 4: Scheme of a piezotube actuator. a) A movement in x- and y-direction is realized by segmented piezo tubes. Here, a voltage is applied between two opposing outer electrodes. b) and c) A deformation of the piezo tube in z-direction is realized by applying a voltage between the inner and outer electrodes. This is true for segmented (b) and non-segmented piezo tubes (c).

In the STM setup used here, piezoelectric actuator tubes are used to position the STM tip. Fig. 4 shows a schematic representation of the movement of such piezotubes when a voltage is applied either between the opposing outer electrodes of a segmented piezo tube (Fig. 4 a, x,y-movement) or the inner and outer electrodes of a segmented or non-segmented piezo tube (Fig. 4 b and c, z-movement).

2.4 THEORETICAL TREATMENT OF THE TUNNELING IN AN STM

Section 2.2.1 gave a short introduction to the tunneling effect. The realistic treatment of the tunneling in an STM is of course far more complex and requires a three-dimensional approach. An overview of the advancements in theoretical description of the tunneling in an STM experiment up to the 1990s is given by F. Besenbacher in [40]. A further nice introduction into the theory of STM is given in the lecture notes by S. Lounis [38]. Both were used as a guideline for the following section.

The first quantitative STM theory was presented by Tersoff and Hamann shortly after the publication of the first STM results [41, 42]. The aim of the authors was to be able to have a theoretical comparison to data acquired with the newly developed STM technique.

The expression for the tunneling current that the authors use as a starting point, is based on a many particle, first-order perturbation theory approach which has already been applied by Bardeen for planar tunneling junctions well before the invention of the STM in 1961 [43]. Here, Bardeen calculated the tunneling current between two metal electrodes separated by an oxide barrier. The expression for the tunneling current within this formalism is

$$I = \frac{2\pi e}{\hbar} \sum_{\mu\nu} f(E_\mu)\,[1 - f(E_\nu + eV)]\,|M_{\mu\nu}|^2 \delta(E_\mu - E_\nu), \tag{5}$$

where $f(E)$ is the Fermi function, V is the applied bias voltage, $M_{\mu\nu}$ is the tunneling matrix element between the states Ψ_μ of the tip and Ψ_ν of the sample, and E_μ E_ν are the energies of the states Ψ_μ and Ψ_ν in the absence of tunneling.

Basically, (5) describes the tunneling from the filled states of the tip, indexed μ, into the empty states of the sample, indexed ν. The Fermi functions describe the respective occupation of the states of tip and sample. Through the delta function $\delta(E_\mu - E_\nu)$ only elastic tunneling processes are taken into account, i.e. the energy of the tunneling electrons is conserved during the tunneling process.

The work by Bardeen [43] yielded the tunneling matrix element $M_{\mu\nu}$ as the overlap of the wave functions Ψ_μ of the tip and Ψ_ν of the surface which exponentially decay into the tunneling barrier [41, 42]

$$M_{\mu\nu} = \frac{\hbar^2}{2m} \int (\Psi^*_\mu \nabla \psi_\nu - \Psi_\nu \nabla \psi^*_\mu) d\vec{S}. \tag{6}$$

The integration may happen over any arbitrary surface that lies entirely within the tunneling barrier.

The experiments modeled by Tersoff and Hamann used bias voltages in the regime of a few meV. In the limit of small bias voltage V, the transition probability in the range of E_F to $E_F + eV$ can be assumed to be constant. The sum over all energies within this energy range can then be accounted for simply by multiplying by the width of the energy window in which the electrons tunnel. This is simply eV, where e is the elementary charge and V is the applied bias voltage.

Further Tersoff and Hamann worked in the limit of low temperatures, where the Fermi distribution can be approximated by a sharp distribution where all states below the Fermi energy are filled and all states above the Fermi energy are empty. Reverse tunneling can be neglected. The Fermi functions then vanish from the sum and the task of calculating the tunneling current can be narrowed down to evaluating the tunneling matrix element $M_{\mu\nu}$ as (5) simplifies to

$$I = \frac{2\pi e^2 V}{\hbar} \sum_{\mu\nu} |M_{\mu\nu}|^2 \delta(E_\mu - E_F)\delta(E_\nu - E_F). \tag{7}$$

The challenge for Tersoff and Hamann was now to find a model accurate enough to describe the tip sample junction in sufficient detail to model a realistic STM experiment but still simple enough to be able calculate $M_{\mu\nu}$. In their model, they expressed the surface in an "exact" description by Bloch wave functions. In contrast, the tip in the proximity of the sample was modeled as a simple spherical s-wave tip wavefunction. Applying this model, the evaluation of (7) finally yielded

$$I = \frac{32\pi^3 e\phi^2 R^2}{\hbar\kappa^4} e^{2\kappa R} D_t(E_F) eV \times \underbrace{\sum_\nu |\Psi_\nu(\vec{r_0})|^2 \delta(E_\nu - E_F)}_{\mathrm{LDOS}_{sample}\text{ at }E_F}, \tag{8}$$

where V is the bias voltage, ϕ is the workfunction which in this case was assumed to be equal for the tip and the sample, R is the radius of curvature of the tip, D_t is the density of states per unit volume of the tip which was considered to be constant, κ is the inverse decay length for the wave functions into the vacuum. $\Psi_\nu(\vec{r_0})$ is the value of the surface wave function at $\vec{r_0}$, i.e. the position of the central atom of the spherical tip.

The expression in (8) first appears rather complicated. However, it allows a quite straightforward interpretation of STM images, when dividing the term on the right into its central parts: The first term in (8) includes natural constants as well intrinsic geometric and material dependent properties of the tip and the sample. eV represents the energy range in which electrons can tunnel, see (**??**). The last term in (8) corresponds to the local density of states (LDOS) of the sample at the Fermi energy at the center of the spherical tip.

Thus, STM topographic images obtained as constant current can be interpreted as contour maps of constant surface LDOS. This means, that adsorbates on the surface might appear as indentations, even when geometrically speaking they would protrude out of the surface, because they lead to a local reduction of the surface LDOS. This is e.g. the case for CO-molecules on Cu(111) at certain tunneling energies.

2.4.1 *Estimation of the Lateral Resolution*

The exponential dependence of the tunneling current on the tunneling distance is intrinsically included in the Tersoff-Hamann model, since the assumed wavefunctions for the tip and the sample exponentially decay into the vacuum so that $|\Psi_\nu(\vec{r_0})|^2 \propto e^{-2\kappa(R+d)}$ [42]. More importantly, with their model of the tip-sample junction, in particular by modeling the tip as a simple sphere, Tersoff and Hamann were able to give an elaborate estimation of the lateral resolution on an STM.

With the suppression of higher Fourier components in the expressions for the wave functions for the tip and the sample, they approximate the resolution to roughly $[2\kappa^{-1}(R+d)]^{1/2}$. But a small factor, this agrees well to the value estimated for the lateral resolution of the STM estimated from the very simple geometric consideration presented earlier (see section 2.2.2).

For a tip with a radius of curvature of $R = 9$Å and a tunneling distance of 6Å this would yield a resolution of 5Å. This nicely corresponds to the experimental data of Binnig et al. who were able to resolve the (2×1)-reconstruction of Au(110) that possesses rows with a width of 8Å.

However, the STM is capable to resolve much smaller structures, e.g. single atoms of Cu, Ag or Au(111) hexagonally packed structures where the atomic distances are in the order of only $3-5$Å. This was resolved by later considerations by Chen et al., who modeled the tip by p_z- and d_{z^2}-orbitals that have a more localized charge density than the s-orbital considered by Tersoff and Hamann [44]. With this assumption for the tip geometry, Chen et al. were able to explain the resolution achieved in these later STM-experiments.

However, the exact tip-geometry in STM is usually not known and the precise modeling of STM-data is still an ongoing challenge. For the precise treatment of the tunneling probability, the exact knowledge of the microtip that supports the tunneling current would be needed. As mentioned above, FIM is a technique that can be used to characterize tunneling tips on the atomic scale. However, usually, the characterization of the tips by FIM and the STM experiments are carried out separately. Thus, the probability of microscopic tip changes in between both experiments is relatively high. A combined FIM/STM setup to overcome this problem is currently developed in the Möller group [45]. Here, the FIM is directly integrated in the STM-setup so that the FIM characterization may capture the actual tip that is used during the experiment.

The Tersoff-Hamann model is still the most used one in the theoretical treatment of STM-images for realistic systems [38]. Constant current STM images can be simulated by looking for $\mathrm{LDOS}_{sample}(\vec{r_0}, E_{F,sample}) = const.$, while simulated spectroscopic dI/dV-maps are obtained by calculating the samples DOS in vacuum, i.e. $\mathrm{LDOS}_{sample}(\vec{r_0}, E_{F,sample} + eV)$. Where $\vec{r_0}$ is the position of the tip.

2.5 SCANNING TUNNELING SPECTROSCOPY

Apart from using the STM to obtain images of the surface topography, a regularly applied mode of STM operation is scanning tunneling spectroscopy (STS). Point spectroscopy STS probes the energetic distribution of the LDOS of the sample within a certain energy range at a certain lateral position. For this purpose, the tip is held at a fixed lateral position over the surface, while the tunneling voltage is ramped from one set value to another and the tunneling current is being recorded. There are two ways to perform point spectroscopy STS: constant distance and constant current mode. In constant distance STS, the tip is held at a fixed z-position above the sample during the taking of the spectra. In constant current STS, the feedback loop regulates the tip sample distance while the bias voltage is being ramped (see section 2.5.1).

The equation for the tunneling current derived in (8) included an approximation for small bias voltages, so that the summation over the energy range eV was replaced by the multiplication by eV. In STS, usually energy ranges of up to a few eV are examined. To quantitatively treat this case, we go back to finding an appropriate expression for the tunneling current, where the summation, i.e. the integration, over the corresponding energy range has not yet been carried out.

$$I \propto \int_{E_F}^{E_F+eV} \mathrm{LDOS}_{tip}(E-eV)\mathrm{LDOS}_{sample}(E)T(E,eV)dE, \tag{9}$$

where E_F is the Fermi energy of the tip, $\mathrm{LDOS}_{tip(sample)}(E)$ is the local density of states of the tip (sample) at the energy E and $T(E,V)$ is the transmission probability for an electron through the tunneling barrier.

We can subsume, that the tunneling current is generally proportional to the integrated local densities of states of both, the tip *and* the sample integrated over the energy range defined given by the bias voltage. Usually however, the goal of STS measurements is to examine the LDOS of the sample. For this purpose, rather blunt, disordered, metallic tips may be used that have a rather featureless LDOS, so that the LDOS of the sample dominates the spectrum [40]. The tips used for STS are usually characterized prior to the experiments. If the tips exhibit an approximately linear and featureless I/V-curve on a metallic surface, their density of states may in good approximation be assumed to be constant.

In this case (9) simplifies to

$$I \propto \int_{E_F}^{E_F+eV} \mathrm{LDOS}_{sample}(E)T(E,eV)dE. \tag{10}$$

Naturally, the derivative of the tunneling current with respect to the bias voltage (dI/dV) is far more sensitive to changes in the LDOS than the tunneling current itself. Thus, in a more sophisticated approach, spectroscopy is performed by recording the dI/dV-signal versus the bias voltage. The dI/dV-signal is obtained analog using a lock-in technique. Thereby, the bias voltage is modulated with an amplitude of a few meV to then obtain the derivative by the reaction of the tunneling current signal.

Taking the derivative of (10), we obtain [46]

$$\begin{aligned} dI/dV \propto & \quad e\mathrm{LDOS}_{sample}(E_F+eV)T(E_F+eV,eV) \\ & +e\int_{E_F}^{E_F+eV} \mathrm{LDOS}_{sample}(E)\frac{d}{d(E_F+eV)}T(E,eV)dE. \end{aligned} \tag{11}$$

The dI/dV-signal diverges exponentially with the tunneling distance and with the bias voltage. To account for this effect, Feenstra et al. proposed a normalization of the dI/dV-signal, i.e. the differential conductance with the total conductivity I/V, as

$(\mathrm{d}I/\mathrm{d}V)/(I/V) = \mathrm{d}(\ln I)/\mathrm{d}(\ln V)$ [46]. Carrying out this normalization and reorganizing the respective terms yields

$$\frac{\mathrm{d}I/\mathrm{d}V}{I/V} \propto \frac{\mathrm{LDOS}_{\mathrm{sample}}(E_F + eV) + \int\limits_{E_F}^{E_F+eV} \frac{\mathrm{LDOS}_{\mathrm{sample}}(E)}{T(E_F+eV,eV)} \frac{\mathrm{d}}{\mathrm{d}(E_F+eV)} T(E, eV)\,\mathrm{d}E}{\frac{1}{eV} \int\limits_{E_F}^{E_F+eV} \mathrm{LDOS}_{\mathrm{sample}}(E) \frac{T(E,eV)}{T(E_F+eV,eV)}\,\mathrm{d}E}. \quad (12)$$

From this term, Feenstra et al. drew some important conclusions for the evaluation of STS data [46]. The transmission coefficients $T(E, eV)$ and $T(E_F + eV, V)$ only appear as ratios in (12). Their exponential dependencies on the tunneling distance and the bias voltage tend to cancel. The second term in the numerator is a "background" term resulting from the changes in the electric field in the tunnel junctions when the bias voltage is ramped.

For both tunneling directions, the transmission probability is strongly peaked around the Fermi energy of the negatively biased electrode [46]. For a positively biased sample, i.e. tunneling from the tip to the sample, this means the transmission probability $T(E, V)$ is smaller than the transmission probability at $E_F + eV$. Thus, the majority of the electrons tunnels at energies close to $E = E_F + eV$, which is the shifted Fermi energy of the tip. For this bias polarity, each term in (12) is in the same order of magnitude. The normalized $\mathrm{d}I/\mathrm{d}V$-signal then gives a measure of the normalized sample LDOS along with an almost constant "background".

For a negatively biased sample, i.e. tunneling from the sample to the tip, the transmission probability $T(E, V)$ is larger than the transmission probability at $E_F + eV$. The majority of the electrons then tunnels at energies close to $E = E_F$, which is the Fermi energy of the sample. At this bias polarity, the background term in the numerator of the expression in (12) and the normalization term in the denominator are in the same order of magnitude. However, both are larger than the contribution of the normalized sample LDOS. Here, the energetically low-lying features are suppressed, as the majority of the electrons tunnels at higher energies. Therefore, it is more difficult to gain access to low-lying occupied states of the sample, while unoccupied states may be accessed quite conveniently by STS. A schematic representation of the situation is shown in Fig. 5.

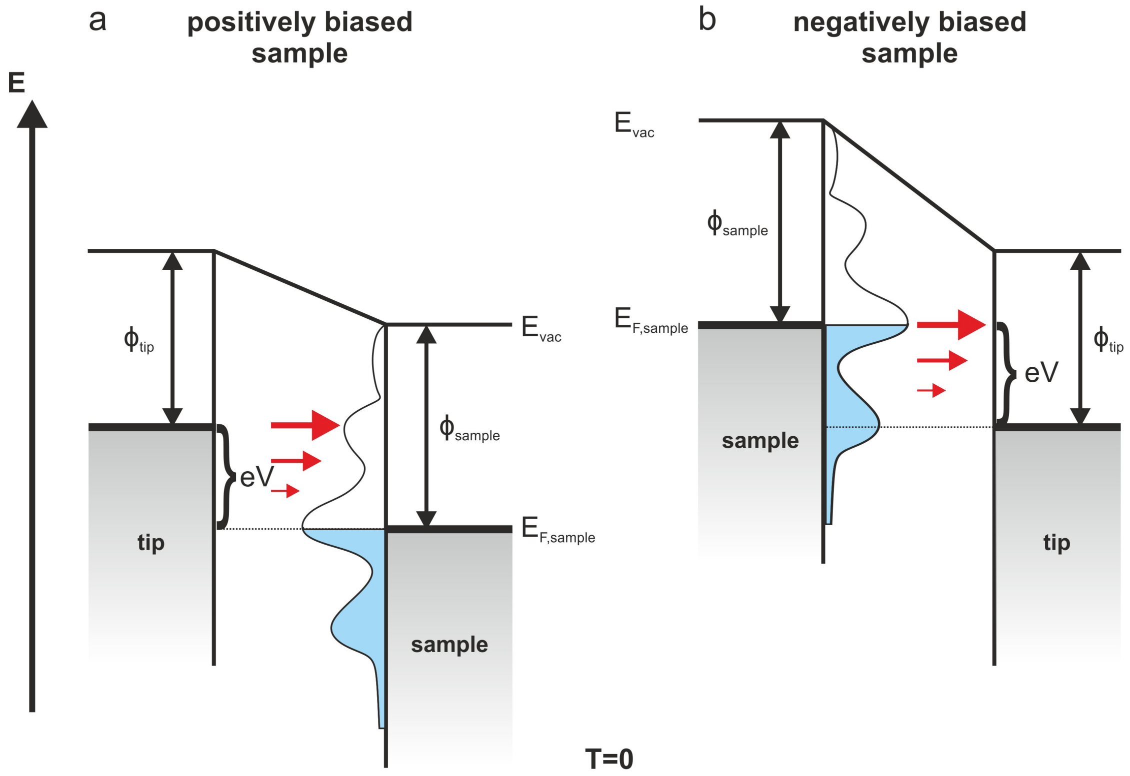

Figure 5: Energy scheme for the tunneling junction in an STM when the sample biased negatively (a) or positively (b) at $T = 0$ (Fermi functions are assumed as step functions). The tunneling probability for the electrons is highest close to the respective Fermi level of the negatively biases electrode. This makes it hard to access low lying occupied states of the sample by STS.

2.5.1 *STS at Constant Distance vs. STS at Constant Current*

Usually, STS is performed at constant distance. The feedback loop is switched off. Therefore, continuous measurements from positive to negative bias voltage are possible without the danger of a tip-sample crash at zero bias voltage. Also, the measurements can usually be performed faster than constant current STS, as there are no necessary integration times for the feedback loop.

In this mode, the tunneling current varies during the measurement, i.e. it usually rises with rising the bias voltage[1]. In the later data processing, this can be accounted for by normalizing the dI/dV-signal with I/V as proposed above.

In constant current spectroscopy, the feedback loop stays on during the measurement. The latter constantly regulates the tip-sample distance, so that a small energy window around the Fermi energy has to be exempt in order to prevent tip-sample collisions. For spectra over a wide energetic range, this way of performing spectroscopy especially increases the sensitivity for electronic states with a small LDOS near the Fermi energy. At small bias voltage, the tip-sample distance is decreased so that the overlap between tip and sample wavefunctions becomes larger.

For the purposes of STM-LE, a rise of the tunneling current during the spectroscopic measurements at constant distance can obscure the photon emission data, since the number of incident electrons has a direct impact on the excitation yield of the tip-sample junction. Thus, spectra of the overall photon yield are often gathered at constant tunneling current. In the latter case, however, the change in the tunneling distance influences the electric field in the tunneling junction, which may in turn also impact the photon yield. Thus, the best mode for STM-LE spectroscopy is still a highly discussed topic [14].

For the data presented in this thesis, spectroscopy was performed at constant tunneling current. The dI/dV-data were subsequently normalized by multiplying by the bias voltage V to account for the roughly linear increase of the tunneling current with V that would be given in constant distance spectroscopy. Further normalization with I/V as described above was omitted, since this would have obscured states with a comparably low density of states close to the Fermi energy that may still play an important role for the inelastic transitions analyzed in the experiments presented here. The focus in this case lies on the energetic positions of the states instead of quantitative considerations.

---

[1] Even though this seems counter-intuitive first, cases of negative differential conductance, e.g. for C_{60} on Ag(111) have been reported ([14] supplementary material and [47]).

2.5.2 *dI/dV-maps*

In addition to point spectroscopy, the dI/dV-signal may also be recorded as an additional signal channel during STM imaging. Here, the $dI/dV - signal$, i.e. the LDOS, is probed at a fixed tunneling voltage. Thus, laterally resolved maps of the LDOS at the respective tunneling energy may be obtained. These may give access to e.g. the lateral extend of molecular orbitals or the distribution of the LDOS near local surface defects, e.g. step edges.

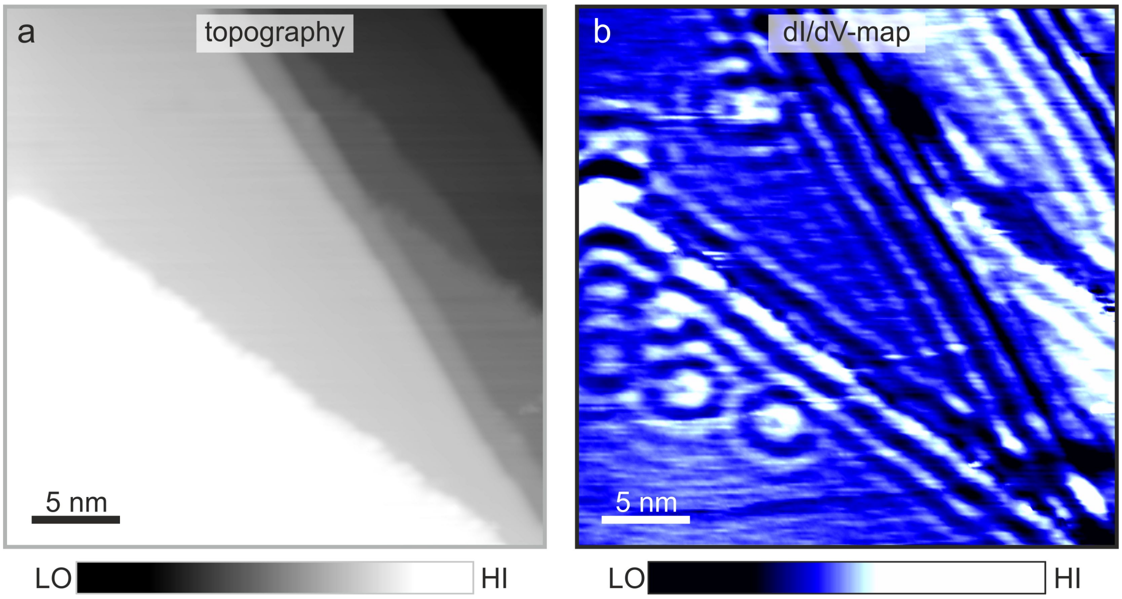

Figure 6: Exemplary topography (a) and dI/dV-map (b) of a Ag(111) surface. The dI/dV-maps reveals standing wave patterns in the LDOS that result from the scattering of surface state electrons at step edges and other surface defects. $V_{sample} = 0.1V$, $I = 100pA$, $T = 80K$.

2.6 STM-INDUCED LIGHT EMISSION

STM induced light emission (STM-LE) is an experimental technique that directly evolved from regular scanning tunneling microscopy [10]. The focus of standard STM experiments usually lies in the analysis of elastically tunneling electrons, i.e. electrons that do not loose energy during the tunneling process. Inelastically tunneling electrons are intrinsically inherent to any tunneling experiment. The fraction of inelastically tunneling electrons, however, is usually very small so that the general statements about the tunneling current made above remain unaffected.

The analysis of inelastic processes from the tunneling current is a challenging task. One technique to do so is inelastic electron tunneling spectroscopy (IETS) [48, 49]. By detecting the second derivative d^2I/dV^2 of the tunneling current, IETS may be used to study e.g. vibrations of adsorbed molecules [50] or spin excitations of adatoms [51]. In IETS, like in STS, the tunneling voltage is ramped and the tunneling current is monitored. When the tunneling energy of the electrons becomes large enough to induce sample excitations, an additional (inelastic) tunneling channel opens. This leads to an increase of the overall tunneling current, i.e. a kink in the I/V-curve. This kink is usually very small and hard to detect. Stronger manifestations of the sample excitations can be found in the derivatives of the tunneling current. At the according positions of the opening of the inelastic channels, the dI/dV-signal exhibits steps and the d^2I/dV^2-signal exhibits peaks. The energetic peak positions in the d^2I/dV^2 then directly yield the energies of the excitation modes.

In contrast, STM-LE experiments detect photons which are emitted during the relaxation of excitations evoked by tunneling electrons. The analysis of the intensity and spectral distribution of the emitted light can give insight into the involved optical transitions, while laterally resolved "photon maps" allow an excitation mapping with atomic scale lateral precision.

The light emission happens on a fs to ns time scale. This is much faster than the usual integration times in STM-imaging or spectroscopy which lie in the order of ms. Also the photon detection works much faster than the scanning or voltage ramping of the STM (see section 2.6.3.1). This is the key to how the lateral resolution in STM-LE is obtained. Here, the technique solely relies on the position of the STM tip at the moment in which the light is detected. For laterally resolved STM-LE imaging, the photon intensity is measured at each pixel of an STM image. Here, it is important to note, that these so called "photon maps" do not provide information about where the photon is emitted as no spatially resolved photon detection is applied. Instead the photon maps provide laterally resolved information of the excitation efficiency with the ultimate spatial resolution of an STM. Further, spectroscopic measurements of the photon intensity and the energetic distribution of the emitted light may reveal important information about the underlying physical processes.

A nice overview of important works in the field of STM-LE, especially concening the light emission induced on molecularly covered surfaces is e.g. given in a review paper by Rossel et al. [30]. A further review that especially focuses on the instrumental developments in STM-LE has recently been published by Zhang et al. [52].

2.6.1 *Basic Setup*

A general STM-LE setup consists of a standard STM with an additional light detection unit. The latter involves an *in situ* light collection close to the tip sample junction and an *ex situ* highly sensitive photon detection.

Both, the tip-sample junction and the light detection unit are well shielded from any external light source. Thus, all detected photons may be ascribed to processes within the tip sample region without any further spacial resolution within the light detection. To rule out effects of remaining stray light, dark spectra/count rates may be subtracted from the recorded data.

2.6.1.1 *In Situ Light Collection*

To collect the light *in situ* from the tip-sample junction, three different methods are established. The light is either collected by an optical fiber, a (parabolic) mirror or a lens [30, 52] (see Fig. 7). All possibilities exhibit different advantages and experimental difficulties, so that the respective method has to be chosen considering the geometry of the experimental setup and other specific experimental requirements.

The STM-LE experiment that was set up in the course of the work for the present thesis uses a lens close to the tip-sample junction to collect the light. For a wide acceptance angle, the lens is usually placed as close as possible to the tip-sample junction. For low temperature STM experiments, the closest possible proximity to the latter may be limited by the heat shielding. The lens is aligned so that the tip-sample junction is in the focal point of the lens. Thus, the light leaves the lens as a parallel beam. It then usually leaves the vacuum recipient for an *ex situ* light detection.

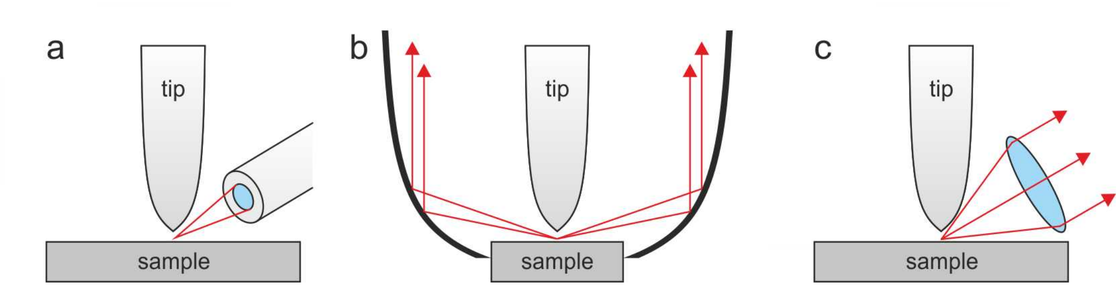

Figure 7: Different concepts for the *in situ* light collection in STM-LE experiments. a) An optical fiber. b) A mirror. c) A lens. In the experiments presented here, the light was collected with a lens. (Adapted from [30]).

2.6.1.2 *Ex Situ Light Detection*

In STM-LE, there are mainly two different quantities of interest: the overall photon yield and the spectral distribution of the emitted light. Further, also the polarization of the emitted light can be analyzed [52, 53] and time-correlated measurements can be performed[2] [52, 54].

Spectroscopic information is usually gathered using a spectrograph equipped with a highly sensitive CCD camera (see 2.6.3.2). The emission spectra give insight into

---

[2] The STM-LE setup in our group is currently extended with a setup to perform such experiments.

the energy of the emitted photons and the respective intensities (see Fig. 8 a). With an integration over the entire spectrum, the overall photon yield can be derived. For a sufficient signal to noise ratio, integration times of several hundred seconds are usually needed.

For a faster measure of the overall photon yield, avalanche photodiodes (APDs) (see 2.6.3.1) or photomultiplier tubes (PMTs) may be used. These devices usually need a lot shorter integration times, in the order of a few ms. Thus, they may conveniently be used to detect the overall photon yield simultaneously to regular STM imaging and spectroscopy (see Fig. 8 b). This way, photon maps may be gathered simultaneously to the topography. Additionally, spectra of the overall light intensity versus the bias voltage or the tunneling distance may be obtained. In contrast to a spectrograph, APDs and PMTs do not provide a measure of the spectral distribution of the emitted photons. However, some information may be gathered with the help of filters. For comprehensive data sets, usually complementary spectroscopic measurements are performed.

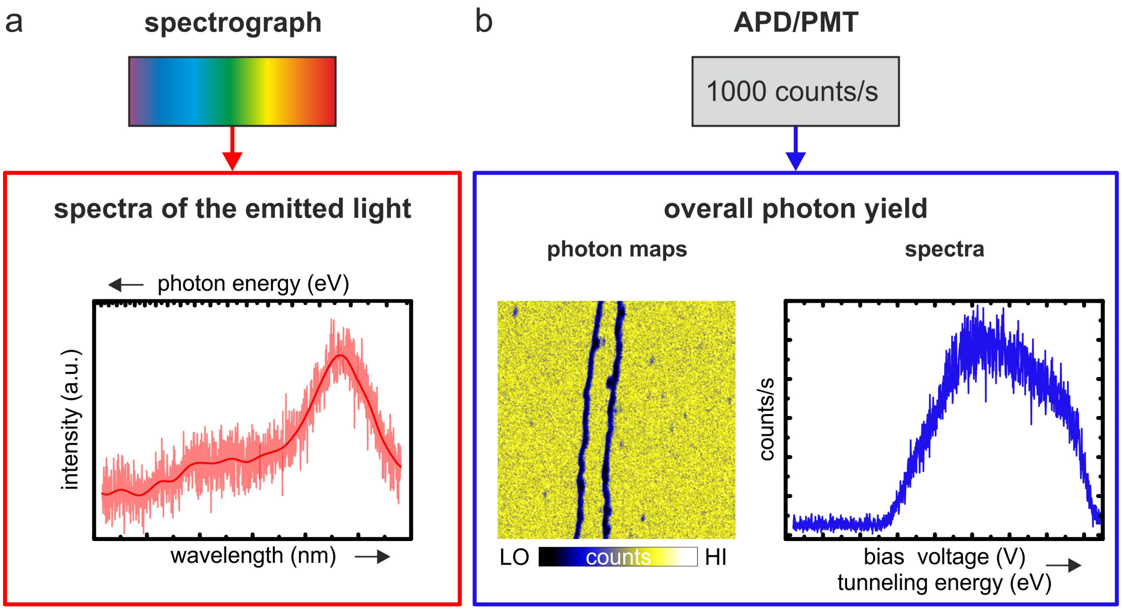

Figure 8: Complementary ways of light detection in STM experiments. a) A spectrograph yields the spectroscopically resolved intensity distribution of the emitted photons. The integration over the recorded spectra yields the overall photon yield within a certain energy range. b) Avalanche photodiodes (APDs) or photomultiplier tubes (PMTs) may be used to detect the overall photon yield. The latter provide the advantage that the usual integration times for the light collection are much smaller. This way, photon maps and spectra of the overall photon yield may be recorded as additional signal channels simultaneously to STM imaging and spectroscopy.

The light emitted from the tip-sample junction is detected simultaneously to other signal channels, such as the topography, the tunneling current, or the dI/dV-signal, while the tip is scanned across the surface or spectroscopic measurements are performed. This way, comprehensive data sets are gathered that allow a detailed analysis of correlations between different quantities and disentangle the contributions of different effects in the data evaluation.

2.6.2 *The Origin of the Emitted Light*

The light emitted in an STM-LE experiment results from the relaxation of excitations in the tip-sample junction. The specific excitation channels may vary depending on the properties of the studied system. However, generally, the junction acts as a radiating antenna for the emitted photons, i.e. plamonic modes localized in the tip-sample junction (see 2.6.2.1) may resonantly enhance the emission from different excitation channels. The particular paths of energy transfer that finally lead to the emission of light are still a highly discussed topic and stay in the focus of current research. Especially for systems that contain adlayers, e.g. organic molecules, the number of energy dissipation channels is enhanced. One of the challenges in STM-LE is to reveal and disentangle the contributions of these different channels.

In the following, a quick overview of different excitation mechanisms will be given.

2.6.2.1 *STM-induced Light Emission from Metallic Systems*

The STM-induced light emission from metallic surfaces stems from the radiative decay of collective electronic excitations that are localized at the tip-sample junction. In literature, these plasmonic modes are referred to as tip induced plasmons (TIPs), localized surface plasmons (LSPs), nanocavity plasmons (NCPs) or gap plasmons.

TIPs differ from "classic" plasmonic excitations of the bulk or surface in several important ways. They are an excitation of the tip-sample junction as a whole. In contrast to surface plasmon polaritons (SPPs) which may propagate along a surface, TIPs are localized to the tip-sample junction. The dispersion relation for SPPs has no intersection with the light line. Thus, without any geometric feature providing the necessary k-vectors, e.g. a surface defect such as a step edge, they cannot decay radiatively. For TIPs, the k-vectors for a radiative decay are intrinsically provided by the tip geometry.

The TIP modes experience a field enhancement through the electric field in the tip-sample junction. The electric field strength is dominated by the junction geometry and particularly depends on the specific tip used.

The excitation of the TIPs is driven by the inelastic fraction of the tunneling current. The spectrum of TIP modes for a particular tip-sample junction depends on the respective materials present in the junction and on the microscopic junction geometry [11, 55, 56]. Thus, experiments conducted on the same macroscopic system may yield completely different emission spectra after the occurrence of a microscopic tip change. This matter will be discussed in further detail in chapter 8.3.

2.6.2.2 *STM-induced Light Emission from Molecules*

When molecules are adsorbed on a (metallic) surface, the may provide additional excitation/emission channels (see Fig. 9). When electrons tunnel elastically into a molecular orbital, this injection of a hot electron puts the molecule into an excited state. The relaxation may happen via the inelastic transition into an energetically lower state, e.g. a lower molecular orbital.

When the molecules are adsorbed directly on a metallic surface, the strong coupling between the two usually provides a great number non-radiative decay channels. In this case, the excited molecular state is depopulated is too fast, i.e. the residence time of

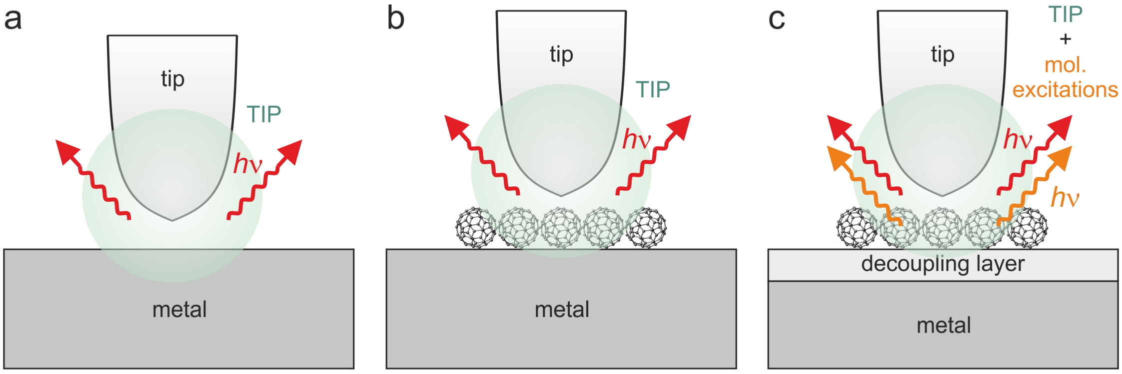

Figure 9: Schematic representation of different excitations that may be involved in STM induced light emission. a) STM-LE on metallic surfaces originates from the radiative decay of tip induced plasmons (TIPs). b) Molecules adsorbed directly a metal surface may significantly modify particularly the intensity of the plasmonic light emission. However, the emission spectra usually do not contain direct molecular features. c) When the molecules are sufficiently decoupled from the metallic substrate, electronic excitations of the molecule may directly contribute to the emission spectrum.

the electrons within the molecular orbitals is too short, for a radiative transition inside the molecule [57]. However, even in the absence of direct molecular fluorescence, light emission from the radiative decay of TIP modes may be detected [13, 14, 58, 59]. The molecules placed in the tip-sample junction may considerably affect the plasmonic light emission. They influence the interaction between the tip and the underlying substrate and can have a significant effect on the induced photon yield. One of the key points of the thesis is to gain further insight into the exact role of the molecules in this case.

Further decoupling from the substrate enhances the residence time of the electrons within the molecular states. This may happen either by introducing a thin insulating layer, e.g. an oxide [16, 18], salt [15], or several layers of organic molecules [60]. Also, molecules have been synthesized that exhibited an intrinsic geometric decoupling by standing up on functional groups [34]. Besides the plasmonic background, the corresponding emission spectra may then contain emission features that directly reflect electronic transitions within the molecules. This emission channel is enhanced by the tip induced plasmons. This may reach down to resolving single vibronic progressions in the emission spectra [16, 18, 60].

2.6.2.3 *STM-induced Light Emission from Semiconducting Surfaces*

The main channel of excitations induced on semiconductor surfaces is due to the recombination of electron-hole pairs. Luminescence through the relaxation of such excitons may be induced in both tunneling directions. When tunneling from the sample to the tip, holes may be injected directly into the valance band of the semiconductor, i.e. electrons tunnel from the valance band into the tip and leave a hole. The subsequent recombination with an electron from the conduction band may then lead to the emission of a photon. When tunneling from the tip to the sample, hot electrons injected by the tip may create an electron-hole pair by impact ionization which may decay radiatively [28, 29].

The energy of the emitted photons in both cases reflects the band gap of the semiconductor. When tunneling on low-conductivity semiconductors, a tip induced band-bending may play a significant role such that the apparent gap position may vary [28]. Also, the tunneling barrier may extend into the semiconductor so that also subsurface and bulk properties may be probed [28, 29].

2.6.3 *High Efficiency Photon Detection*

Due to the small fraction of inelastically tunneling electrons in the overall tunneling current, the excitation efficiency in STM-LE experiments is typically very low (in the order of 10^{-5} to 10^{-2} photons/electron [52]). The collection efficiency of our experimental setup lies in the order of 10^{-4}. When the photon yield is mapped simultaneously to the topography, the integration times for the overall photon yield are typically rather low in the order of a few $\mathrm{ms/pixel}$.

These low amounts of light require sensitive and yet fast photon counting devices. This is achieved by detecting the overall photon yield using photomultipliers or avalanche photodiodes. The spectral distribution of the light is analysed using grating spectrometers equipped with highly sensitive, cooled CCD cameras. For this analysis step, higher integration times of several minutes are required.

2.6.3.1 *Avalanche Photodiodes*

Avalanche photodiodes (APDs) are highly sensitive semiconductor photodiodes. Along with their very high sensitivity down to a single photon level, they can be operated at high speeds[3].

APDs are typical semiconductor devices. They may be fabricated e.g. from combinations of III-VI-semiconductors e.g. GaAs or from silicon or germanium. For the experiments presented in this thesis, a Perkin Elmer SPCM-AQR-14 silicon APD was used.

In semiconductor photodiodes, incident photons create electron-hole pairs by the inner photoelectric effect. This happens in the so called adsorption region. In regular p-i-n photodiodes, one incoming photon can only create one electron that contributes to the photocurrrent. Light amounts measured with this kind of photodiode have to be large enough so that the sum of created electrons yields a measureable photocurrent.

APDs are especially designed to detect small amounts of light. Besides an adsorption region, that functions analog to that of a regular p-i-n photodiode, APDs additionally possess a so called multiplication region, in which the charge carriers created in the adsorption region may be manyfolded. In consequence a single incoming photon may lead to the creation of a plurality of charge carriers, so that APDs under certain conditions may even be used as single photon counting devices.

Fig. 10 a and b schematically show the doping profile and the the electric field distribution within an APD. A typically used APD doping profile is of the form p^+ipn^+. The slightly p-doped intrinsic (i) region forms the adsorption region. The electric field within this region separates the created charge carriers that drift to the respective majority sides. The holes drift to the p^+-region, while the electrons drift towards the pn^+ space-charge region (multiplication region). The field strength in the adsorption region is not yet high enough to lead to an impact ionization of charge carriers.

This changes in the multiplication region. Through the pn^+ doping profile and an applied reverse bias voltage, very high field strengths occur in the multiplication region. Once the electrons reach this region, they are accelerated until they have a high enough energy to create a new electron-hole pair by impact ionization. The created secondary

---

[3] e.g. $50-60\mathrm{ns}$ dead time [61] and 300ps rise and fall time [62]

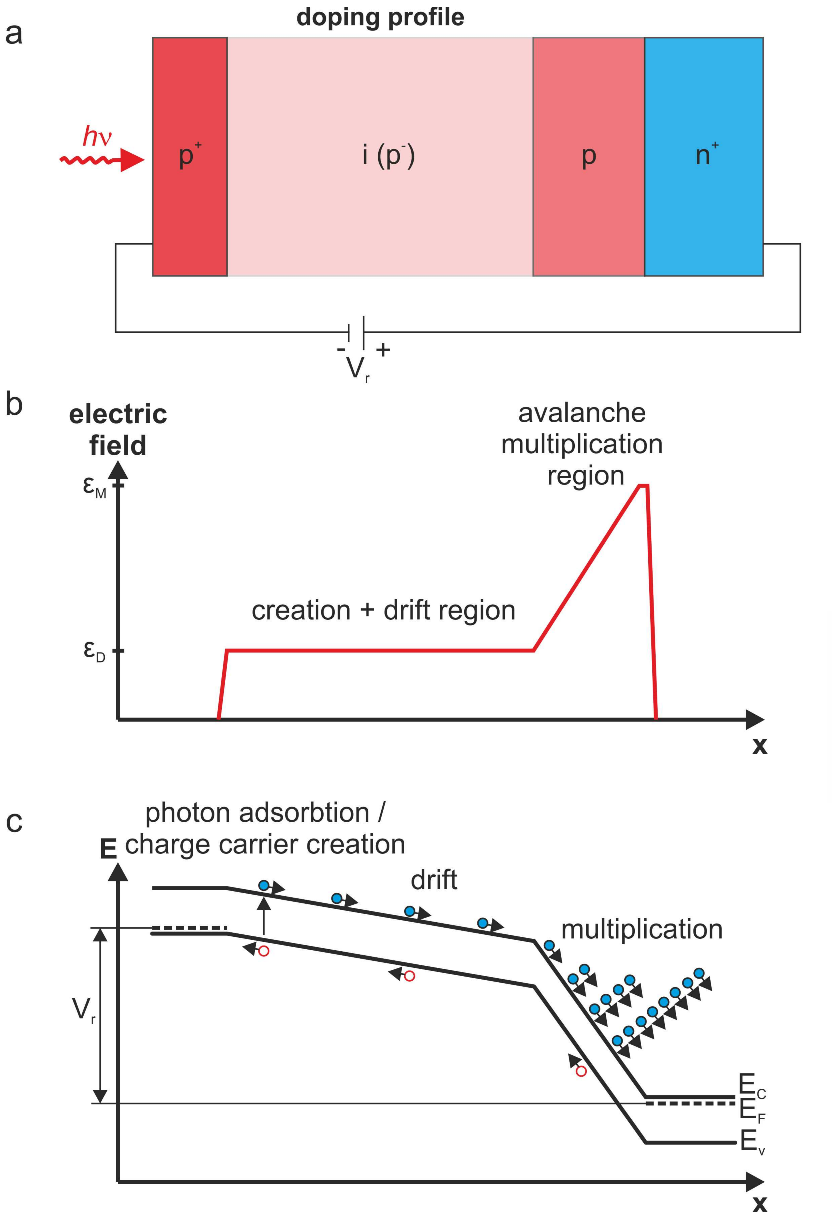

Figure 10: Scheme of an avalanche photodiode. a) Exemplary doping profile. b) Corresponding plot of the electric field. ϵ_D is the electric field strength in the adsorption region which leads to the drift of the carge carriers to the respective majority sides. ϵ_M is the maximum electric field strength in the multiplication region. Those high field stregth accelerate the electrons so much, that they are multiplied by impact ionization. c) Corresponding energy-band diagram.

charge carriers are then also accelerated until they can create a further electron-hole pair themselves an so on. This leads to an "avalanche"-like multiplication of charge carriers inside the APD. This way hundreds up to millions[4] of electrons can be created per incident photon [63].

In our case, we use the APD as a single photon counting module. This mode of operation is also referred to as Geiger-mode. In this mode, the APD is reversely biased above its breakdown voltage. Due to the high electric field in the adsorption region, even a single incident photon may evoke a self-sustaining avalanche, i.e. a sharp increase of the current. Rise times for the current are in the order of ns or below [64]. The current flows until the bias voltage is lowered below the breakdown voltage.

There are two main ways to realize the lowering of the bias voltage and the associated quenching of the avalanche [64]: A so called passive quenching of the avalanche current can be achieved with a high impedance load (e.g. $100\mathrm{k}\Omega$ [64]). With the voltage drop that the avalanche current causes at the impedance, it quenches itself. The bias voltage then recovers back to its original value. The output pulse for photon counting can be derived with a resistor on the ground lead of the circuit.

In contrast, so called active quenching uses a feedback loop that controls the bias voltage. A fast comparator senses the avalanche current. The output of the comparator first switches the bias voltage below the breakdown voltage and then switches it back on after a defined hold-off time. At the same time the output signal of the comparator may be used for photon counting. This way of quenching usually yields a comparably fast and defined reset of the bias voltage and a short resulting deadtime in which no photons can be detected.

For further technical specifications, several APD manufactures offer user guides [62, 63, 65]. Further information about the semiconductor physics of APDs is e.g. given in standard textbooks such as [66] or [67]. A nice overview of APDs in single photon counting mode is given in Ref. [64].

---

[4] In Geiger-mode, i.e. when the APD is biased above its breakdown voltage.

2.6.3.2 *Charge Coupled Devices*

Charge Coupled Devices (CCD) have initially been invented as shift registers for data processing. As arrays of light sensitive devices, i.e. single photodiodes, CCD-sensors are nowadays widely used e.g. in digital cameras. For the invention of the CCD-sensor Willard S. Boyle and George E. Smith were awarded the nobel prize in physics 2009 [23].

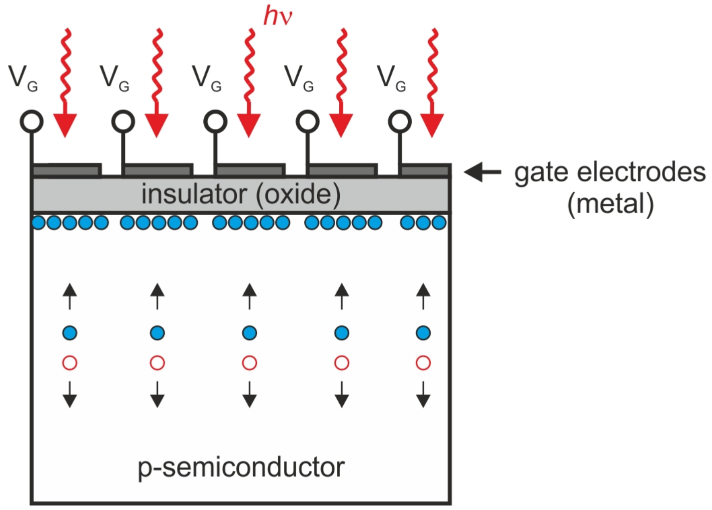

Figure 11: Structure of a common surface channel CCD. The single photodetectors are formed by metal-insulator(oxide)-semiconductor(MOS)-structures. The charge carriers are generated in the depleted p-semiconductor. During integration, the charge is stored underneath the gates. Later the charge packets are transferred and detected. (Based on [66].)

A CCD image sensor consists of a certain number of single MOS[5]-capacitors acting as photodiodes (see Fig. 11). These form the pixels of a CCD-chip. A CCD consists of one or two-dimensional arrays of pixels. Most common, e.g. in photography are two-dimensional arrays, so that 2d-images may be detected.

When light is shone onto the CCD sensor, electron-hole pairs are created in the respective photodiodes (see 2.6.3.1). The resulting charge, which is proportional to the number of incoming photons, is stored in potential wells for each pixel. After a certain integration time, the array is read out by applying certain voltages to the pixel gates. Hereby, the charge is shifted between the respective potential wells to the neighboring pixel. Following a given scheme, the charge packets are gradually transferred in parallel (left or right) or serial (top or bottom) direction until they reach the measurement electronics where the voltage signal evoked by the charge is then further processed. Two different schemes for CCD readout are presented in Fig. 12.

A vivid introduction into the functioning principle of CCDs including animated schemes is e.g. given on the website of Scientific Instruments [68]. Further details on CCD-devices are also given in [66].

In STM-LE experiments, CCD-cameras are used to detect the spectra of the emitted light provided by the grating spectrometer. The incoming light from the tip sample junction is deflected by a grating onto the CCD chip. After calibration with a known

---

[5] Metal-Oxide-Semiconductor

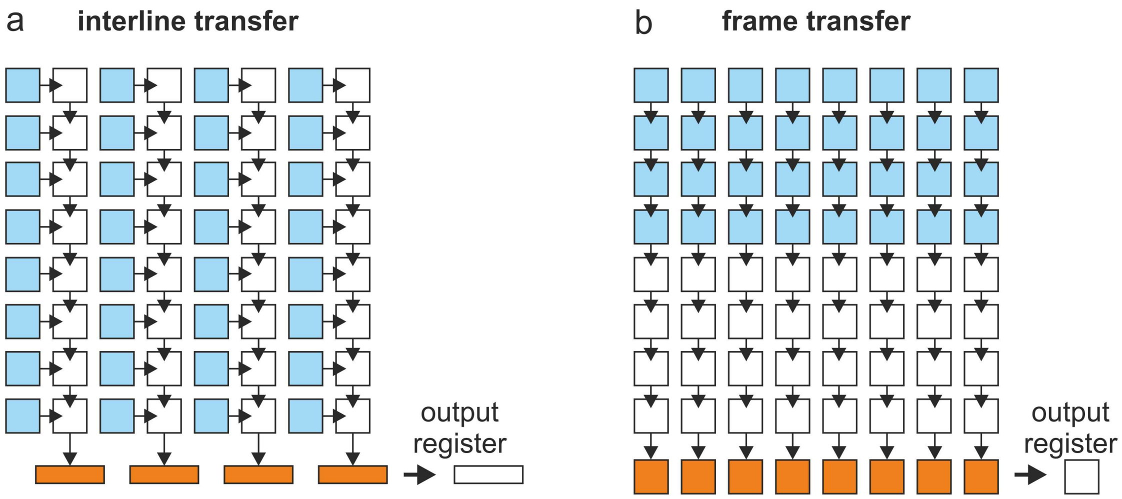

Figure 12: Two different schemes for CCD readout. a) Interline transfer. b) Frame transfer. The charge is first integrated underneath the sensor pixels, then transported to the storage pixels and from there transported to the output register where it is finally detected. (Based on [66].)

spectrum, e.g. from a Hg-lamp, the position of incidence on the CCD-chip can be correlated with the specific energy of each photon. The readout of the CCD-chip then provides a spectrum with the light intensity, for each specific photon energy (wavelength) without the need to use color filters.

Note, that the CCD-cameras (and APDs) in an STM-LE experiment are not used to provide any laterally resolved information about the position where the light is emitted. The lateral resolution in STM-LE experiments is solely given by the position of the STM-tip above the sample and the light is detected without any further lateral resolution.

3

SYSTEMS

3.1 SILVER AS A SAMPLE SYSTEM AND TIP MATERIAL

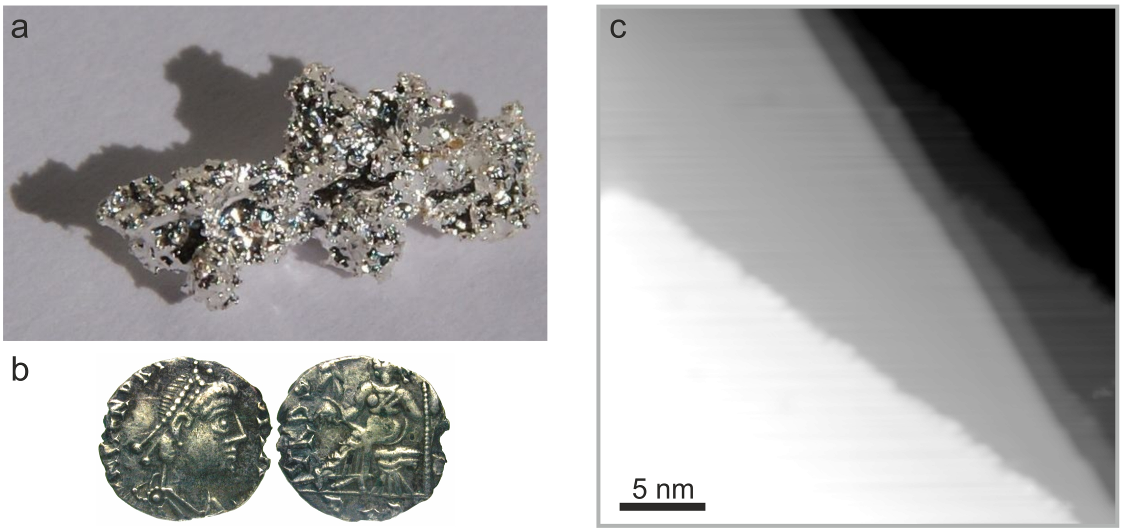

Figure 13: Silver. a) A natural silver nugget [69]. b) Anchient silver coins [70]. c) STM image of an atomically flat Ag(111)-surface exhibiting several surface steps $V = 0.1V$, $V = 100pA$, $T = 80K$. Silver has a lot of applications in daily life. Also in basic research it is a popular sample system. In STM-LE it is valued for its low internal damping.

Silver (Ag) is a group 11 transition metal. As a noble metal it possesses a high chemical inertness. It is very ductile and has been a favored material for e.g. jewelery, mirrors, and as a coinage metal.

Since antiquity, it has been used as an antimicrobial in daily life and medicine. However, its mechanisms of action are still a topic of recent medical research [71].

Ag possesses fully occupied d-orbitals and only one electron in its s-shell [72]. Is exhibits a high electric and thermal conductivity [72]. In technological applications, it is e.g. used in printed circuits or for high quality radio frequency applications.

Ag crystallizes in face centered cubic Bravais lattices. Hence, its (111)-surface exhibit a hexagonal structure. In basic research, noble metals, such as Ag, are popular archetype systems in a variety of fields.

For example, pristine Ag(111) surfaces have been extensively studied by various surface science techniques. Well prepared Ag(111) surfaces show up to several hundred nm wide terraces in STM experiments. Monoatomic Ag-steps exhibit a height of 2.36Å (Ag) [73]. It exhibits a Shockley-type surface state around $65meV$ below the Fermi energy that is well characterized by e.g. angle resolved photoelectron spectroscopy (ARPES) [74–78] or STS [76, 79–81].

In STM, Ag(111) is commonly used as a substrate when studying e.g. the self assembly [82–86] or the electronic structure [84, 87, 88] of organic molecules adsorbed on surfaces.

3.1.1 *Ag as a Tip Material in STM-LE Experiments*

Ag is oftentimes used as a tip material in STM-LE experiments [12, 16, 89]. Due to the small imaginary component of its dielectric constant, it exhibits low internal damping for the tip induced plasmons (TIPs) which are crucial for the light emission in STM-LE (see 2.6.2.1) [52, 57, 90]. Thus, Ag-tips may yield significantly higher count rates than e.g. tungsten tips. They may be entirely fabricated from Ag by electrochemical etching [12, 16] or tips fabricated from other materials may be covered by Ag by e.g. indenting the tips into an Ag-surface [13] or evaporating Ag onto the tips [14].

For all STM-LE experiments presented in this thesis, Ag-covered Pt/Ir-tips were used. The coating of the tip apex with silver usually increased the photon yield significantly and thus yielded better signal-to-noise ratios.

3.1.2 *Ag as a Sample Surface in STM-LE Experiments*

Ag thin films and surfaces, in particular Ag(111), have been used as archetype systems in some of the first STM-LE studies [90–92]. They were also popular candidates in model calculations complementing STM-LE experiments by theory [11, 55, 56, 93].

Quite recently, Chen et al. tailored silver chains of different length by manipulation with the STM tip [12]. The photon maps gathered in the subsequent STM-LE experiments on these artificial structures exhibit characteristic nodes. The nodes are assigned to a modulation in the density of states according to particle in a box states of the Ag chain. Thereby, the system served as a visualization of Fermi's golden rule.

Besides studies on the pristine surface [25], e.g. Ag(111) has also been applied as a template for e.g. organic molecules in a variety of STM-LE studies [94].

In this thesis, STM-LE experiments on pristine and adsorbate covered Ag(111) serve as a starting point for the discussion of contrast mechanisms in photon mapping and the role of organic adlayers on STM-induced plasmonic light emission.

3.2 ULTRATHIN BISMUTH FILMS

Bismuth (Bi) is a group 14 semimetal. With an atomic mass of 209 amu, Bi is the heaviest (almost) stable element[1].

It crystallizes in a rhombohedral Bravais lattice [96] (see Fig. 14). It has a low carrier density, but high carrier mobility [97].

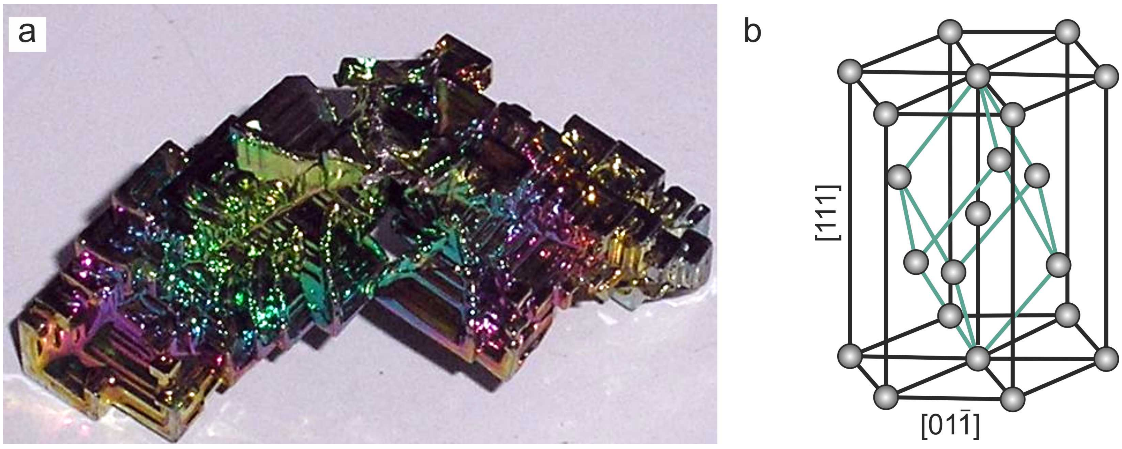

Figure 14: Bismuth. a) A nugget of crystalline bismuth [98]. b) Bulk Bi exhibits a rhombohedral structure. Consequently, its (111)-surface is hexagonally ordered while its (110)-surface exhibits a quasicubic structure.

When downscaling devices, ratio of the surface area to the bulk volume increases and the electronic properties are mainly governed by the surface, while the influence of the bulk loses importance. Bi thin films are archetype systems for such a case. The exploration of their electronic properties thus paves the way for future nanoscaled technological applications. In particular, the symmetry that is usually given in bulk is broken at the surface, leading to the emerge of physical properties, that may be totally different from those of the bulk.

Such phenomena include e.g. the occurrence of surface states. Although bulk bismuth is semimetallic, several of its surfaces, e.g. the (111)-, (100) or (110)-surface exhibit metallic surface states [99–101]. As a further result of the broken symmetry at the surface, these states are subject to a Rashba-type spin-orbit splitting, which is rather large due to the large atomic mass of Bi [102]. This makes Bi not only an interesting candidate for spintronic applications, but also a great model system for basic research to study transport phenomena under the influence of large spin orbit splitting [103, 104].

The electronic transport in the Bi surface states is influenced by the availability of possible electronic scattering channels [105, 106]. Due to the peculiar spin structure of the surface states, certain scattering processes may be suppressed [107–109]. For the surface state bands of eg. Bi(110) and Bi(111), opposing parts of the constant energy contours have opposing spin configurations. Thus, classical backscattering from $\vec{k}$ to $-\vec{k}$ is suppressed. However, other scattering channels are still open. For Bi(111), we analyzed the oscillations of the LDOS evoked by the scattering of surface state electrons

---

[1] For a long time, Bi was assumed to be entirely stable. However, in 2003 it was shown that it decays with a very low probability. The emitted alpha-particles have very low energy and are hence very difficult to detect. The measured half-life was approx. 2×10^{19} years [95].

in the vicinity of surface defects [108, 109]. By a Fourier transform analysis of the scattering patterns, we could show that the spin structure considerably restricts the scattering processes. By tuning the energy of the surface state electrons, the scattering mechanism, e.g. at step edges, may be selected [109].

The restricted amount of scattering channels are a similar characteristic to that of topological insulators, which have recently attracted a lot of attention due to their peculiar transport properties [110]. For this class of materials, the electronic transport is not influenced by nonmagnetic impurities, as scattering is forbidden by their spin structure. In fact, single Bi(111)-bilayers have been demonstrated to exhibit edge-states that are two dimensional topological insulators [111, 112].

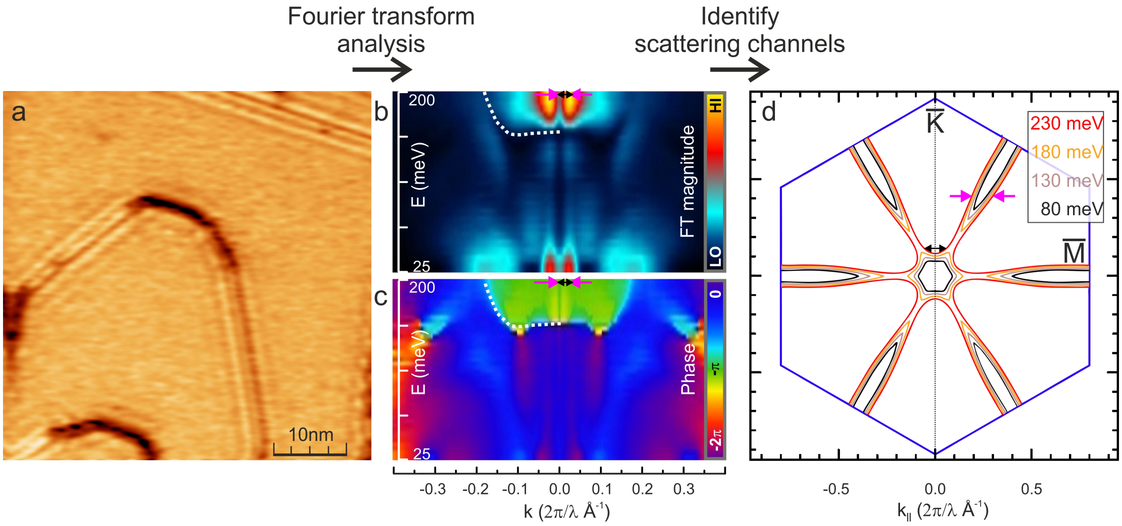

Figure 15: Analysis of electronic scattering in Bi(111) surface states by Fourier transform STS. The spin structure of the surface states restricts possible scattering channels. By analyzing the oscillations of the LDOS in the vicinity of surface defects by STS (dI/dV-mapping), we could show that depending on the energy of the surface state electrons, the dominating scattering mechanism may vary from mainly forward scattering to mainly backward scattering. a) Exemplary dI/dV-map of a Bi(111)-surface area exhibiting several step edges. $V = 175meV$. b) Plots of the amplitude (top) and phase (bottom) of the Fourier transforms of the scattering patterns at a step edge for different energies in between $25meV$ and $200meV$. c) Calculated constant energy contours for different exemplary energies. Two different scattering processes are indicated by pink (forward scattering) and black (backward scattering) arrows. For further details see [109]. (Figure similarly published in [109, 113]).

3.2.1 *Ultrathin Bi-overlayers on Cu(111) and Ag(111)*

Even though immiscible in bulk, Bi forms $\sqrt{3} \times \sqrt{3}$-ordered surface alloys with e.g. Cu or Ag (see Fig. 16). These are fully developed at a Bi-coverage of $1/3ML$ on Cu(111) and Ag(111)[2]. Recently, these surface alloys have been highly discussed because of their spin-split surface states [114–116]. The spin-splitting is even larger than for the pure Bi-surfaces discussed above. In the latter case, the Rashba-type spin splitting is caused

---

[2] Here, the coverage is given with respect to the (111)-ordered substrate, i.e. every third Cu(Ag)-atom in the (111)-ordered surface layer is replaced by a Bi-atom.

by a potential gradient in surface normal direction due to the broken symmetry at the surface. For the surface alloys, upon incorporation, the larger Bi-atoms are displaced out of the Ag-surface plane. The resulting additional in-plane surface gradient causes the so called "giant" Rashba-splitting of the surface bands [114, 117].

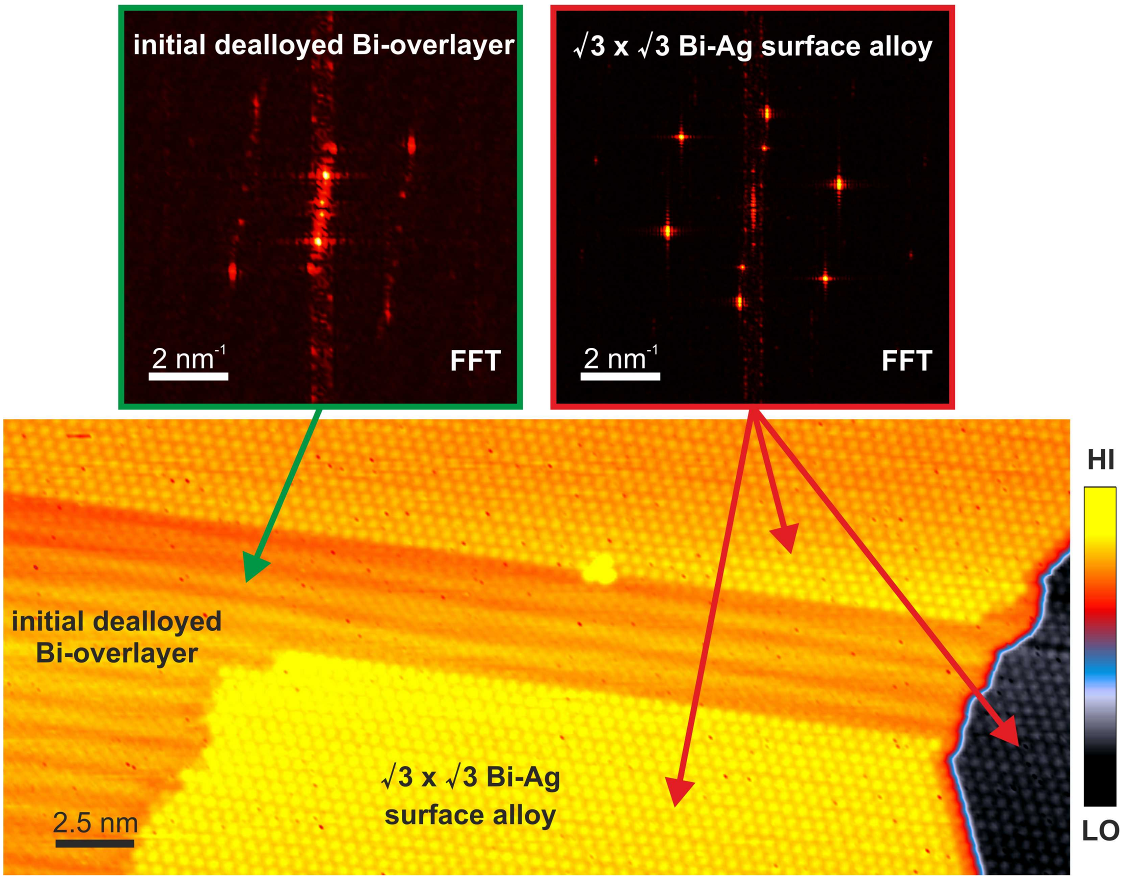

Figure 16: The Bi/Ag surface alloy and initial dealloyed overlayer phase. a) Atomically resolved STM-topography of an Ag(111)-single crystal covered with the $\sqrt{3} \times \sqrt{3}$ Bi-Ag surface alloy, $V = 0.1V$, $V = 55pA$, $T = 80K$. Due to a slight overcoverage of Bi, a gradual dealloying has already set in. The dealloyed areas exhibit a striped appearance in the topography. b) and c) Fourier Transforms of the $\sqrt{3} \times \sqrt{3}$ Bi-Ag surface alloy and the initial dealloyed layer, respectively.

In a collaboration with the group of Prof. Enrique Ortega, we could recently show that the surface state of the $\sqrt{3} \times \sqrt{3}$-Bi/Ag(111) surface alloy is rather robust against different organic overlayers, i.e. the ARPES-signal vanished due to the thickness of the overlayers without any observable change of the surface state band structure [118]. This will be discussed in further detail in the appendix chapter A.

When the Bi-coverage is increased above the ideal coverage for the Bi/Cu(Ag)(111)-surface alloy, a gradual dealloying of the surface layer takes place (see Fig. 16). In this low-Bi-coverage regime, different Bi-overlayer structures occur, which crucially depend on the amount of Bi-deposited on the surface.

Just recently, also the appeal of the peculiar electronic structure of the initial dealloyed Bi-overlayer has been further stressed in literature. This overlayer is fully developed at a Bi-coverage of about 0.5ML. For Bi on Cu(111), quantum well states form within the layer which exhibit a spin-orbit splitting similarly large as that of the Bi/Cu(Ag)-surface alloys [119, 120].

If the Bi coverage is further increased for Bi on Ag(111), the Bi-growth has been reported to take place in bilayers [121]. In our experiments, we find a similar growth mode for Bi on Cu(111).

Further details on the initial growth and electronic structure of Bi on Cu(111) will be given in chapter 11.

In this thesis, a special focus lies on the STM-induced light emission on the initial Bi-monolayer on Cu(111). Especially, the latter is used as a substrate for archetype organic layers. The comparison to data acquired for the same molecules adsorbed on noble metals hints towards a quite peculiarly low interaction between the organic layers and the Bi/Cu(111)-substrate.

3.3 THE FULLERENE C60

Fullerenes are molecules consisting entirely of carbon. For their role in the discovery of fullerenes, Robert F. Curl Jr., Sir Harold W. Kroto and Richard E. Smalley were awarded the Noble prize in chemistry 1996 [23].

C_{60} is a commonly used fullerene in industry and basic research. Its 60 carbon atoms are assembled into a sphere of 20 hexagons and 12 pentagons, very similar to the structure of a soccerball. Other well known fullerenes are e.g. C_{70} or carbon nanotubes.

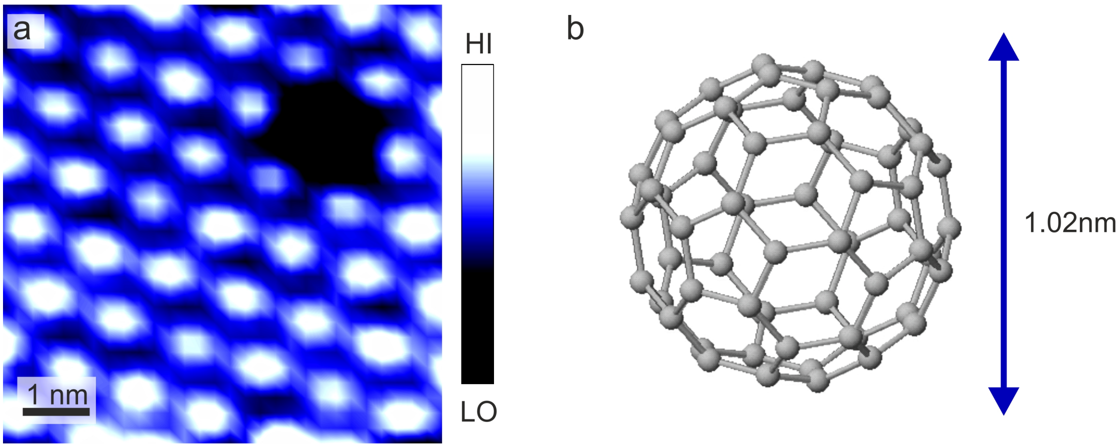

Figure 17: The Fullerene C_{60}. a) STM image of a hexagonally ordered C_{60}-domain on Ag(111). In the upper right quadrant of the image, there is a defect in the C_{60}-layer. V = 2.7V, V = 250pA, T = 80K. b) Structural model of C_{60} [122]. The van der Waals radius is 1.02nm [123].

C_{60} occurs naturally e.g. in candle soot and can be synthesized by evaporating graphite in a helium atmosphere [124]. As an organic semiconductor, C_{60} is used in photovoltaic cells [125], e.g. as an n-type semiconductor in heterojunctions with pentacene or phthalocyanines [126] or as a dopand in the transport layers of organic light emitting diodes [127].

3.3.1 *C_{60} in Basic Research*

In basic research C_{60} is oftentimes used as an archetype organic molecule and has been subject to a wealth of STM studies on a variety of substrates [128–133] (and many more).

On noble metal substrates such as Cu(111) or Ag(111), upon deposition at room temperature, the C_{60}-molecules decorate the step edges first, before they form densely packed molecular domains nucleating from these structures at higher coverages [129, 134] (see Fig. 17 a). Within the molecular domains, the molecules assume a hexagonal order with an intermolecular distance close to that in fcc ordered C_{60} crystals, of about 10Å [129, 135].

C_{60} is a strong electron acceptor and can be easily doped e.g. with alkaline atoms. A doping with these atoms has been shown to induce a superconducting state at 18K [136].

For the use in organic photovoltaic devices, combinations of several molecular species in binary molecular structures, e.g. of copper-phthalocyanine (CuPc) and C_{60} is of mayor interest. For a subsequent deposition of the latter on Au(111), Stöhr et al. found a coexistance of well-ordered domains of each molecular species but no highly ordered intermixed phase or a heteroepitactic structure of both [137]. However, individual CuPc molecules adsorbed on the densely packed C_{60} islands were found to perform a thermally driven, hindered eccentric rotation [138, 139].

In later studies, Huang et al. observed a heteroepitactic growth of CuPc on a closed monolayer of C_{60} [125]. In these experiments, both, monolayer and multilayer films of CuPc adopted a standing-up configuration on the C_{60}. The molecular orientation within the overlayers affects the photon absorption and charge transport within the CuPc:C_{60} based solar cells.

3.3.2 *C_{60} in STM-LE Experiments*

Already in early STM-LE experiments, Berndt et al. studied C_{60} layers on Au(110) as an archetype system [140]. For their possible use in organic light emitting devices, they are still subject of quite recent STM-LE studies. One highly discussed topic is e.g. the origin of the molecular resolution in photon maps of C_{60}-monolayers on Au(111) [58] or Ag(111) [14] which will also be discussed in this thesis.

Other recent experiments focused on the light emission from the single molecular contact of a C_{60} molecule in between a Cu-covered tungsten tip and a Cu(111) substrate [141]. The C_{60} was shown to have drastic influence on the light emission from the quantum contact.

Besides STM-LE experiments that aim on gathering information about the role of C_{60} itself, single or double layers of C_{60} have been used as buffer layers, to electronically decouple other organic complexes placed on top, e.g. from a Ag(111) substrate [14, 21].

3.4 3,4,9,10-PERYLENE-TETRADICARBOXYLIC-DIANHYDRIDE (PTCDA)

3,4,9,10-perylene tetracarboxylic dianhydride (PTCDA) is a perylene based organic molecule. It is industrially used in dyes [142] or as a material for organic semiconductor components, e.g. organic field effect transistors [143], organic light emitting devices [144] or solar cells [145]. In basic research, it is a popular archetype system to study e.g. molecular self assembly [146–148], thin film growth [149] or electronic transport [132].

PTCDA has the elemental formula $C_{24}H_8O_6$. It is a planar molecule with a size of $0.92nm \times 1.42nm$ and a mass of $392amu$[3]. It consists of a perylene core and hydrogen atoms on the "long edges" and oxygen atoms on the "short" edges. The structural formula of PTCDA is shown in Fig. 18 a.

It exhibits a conjugated π-system, where the electrons are delocalized over the entire molecule. The oxygen atoms are electronegative, while the hydrogen atoms are electropositive. Thus, PTCDA is a polar molecule (see Fig. 18) which leads to a very strong intermolecular electrostatic interaction. Therefore, upon deposition at room temperature the molecules form ordered islands on most substrates. On a lot of substrates, including Ag(111), Au(111), Cu(111) [146, 150], Bi(111) [132] or $BiAg_2$ PTCDA assembles into the so called Herringbone structure (see Fig. 18 c and d).

PTCDA has a strong tendency to form highly ordered crystalline structures, even on amorphous structures such as e.g. glass [149]. Such "quasi-epitactic"-growth has been assigned to strong interplanar van der Waals forces between the stacks.

When a submonolayer coverage of PTCDA is evaporated at low temperature, i.e. below $150K$, Killian et al. find an additional phase of PTCDA on Ag(111) [151]. In this configuration, the molecules arrange in irregularly shaped and sized dendritic clusters, in which the molecules assume a tail-to-edge configuration, which still points to the strong intermolecular interaction. Upon annealing, the layer gradually converts into the well known herringbone structure found at room temperature. Here, a fragile interplay between intermolecular interactions and adsorption state is held responsible for the ordering of the molecules at the respective temperature.

PTCDA is an organic semiconductor, for which p-type semiconductivity has been reported. However also n-type semiconductivity as a result of impurity doping or both types of semiconductivity depending on the orientation of molecular planes with respect to the measurement direction have been proposed [152] (and references within).

As part of binary molecular structures, PTCDA has been subject of studies on highly ordered mixed molecular phases, e.g. together with CuPc [153, 154]. Here, the ordering of the molecules depends crucially on the preparation sequence and annealing of the sample. Also, heteroepitactic structures of CuPc on PTCDA could be grown, where the structure of the CuPc layer is dominated by charge transfer processes to the underlying PTCDA layer [155].

---

[3] Carbon has two stable isotopes. About 98.9% of the carbon atoms on earth are ^{12}C, while about 1.1% are ^{13}C. $392amu$ is the mass of a PTCDA molecule that entirely contains ^{12}C. Due to the different carbon isotopes, only about 77% of all PTCDA molecules possess this mass. Around 20% of the PTCDA molecules have a mass of $393amu$. The rest has a mass of $394amu$ or higher.

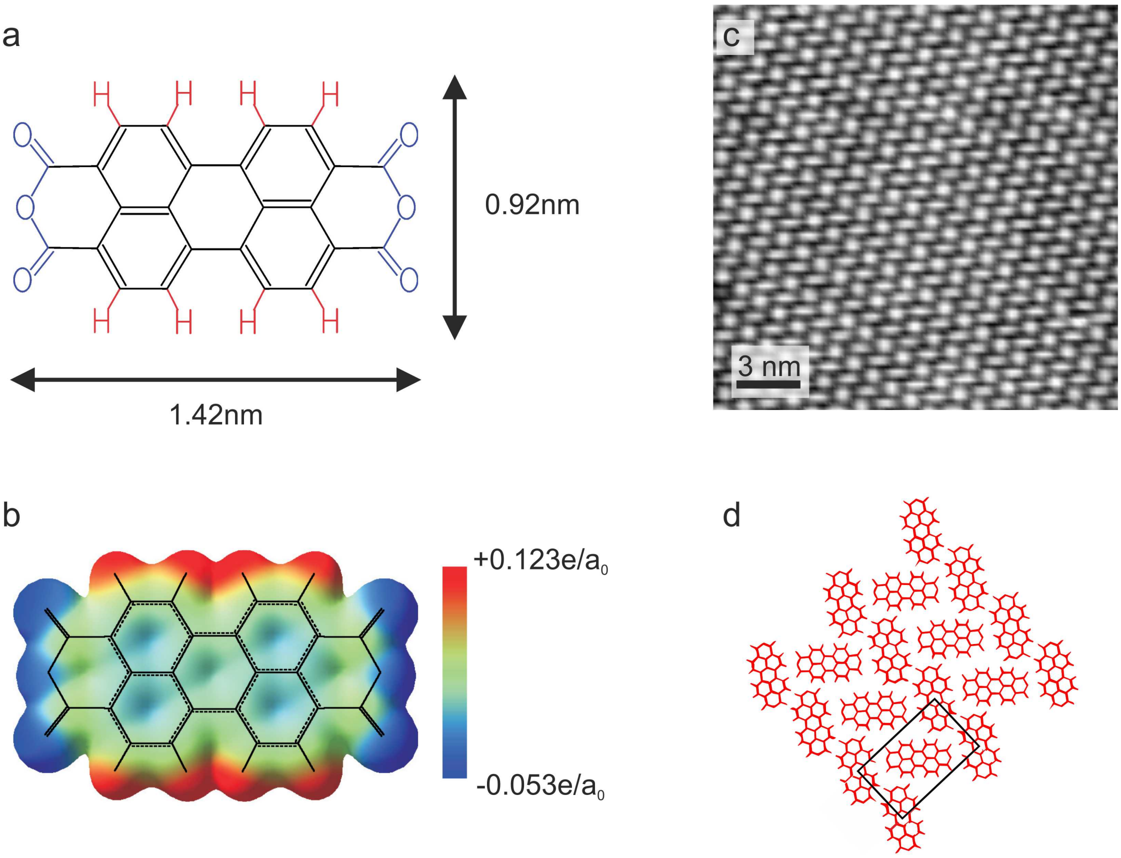

Figure 18: PTCDA. a) Chemical structure of PTCDA. b) Electrochemical potential calculated with Hyperchem. e is the elementary charge and a_0 is the Bohr radius (a and b from [156, 157]). c) PTCDA on Ag(111), $V = 2V$, $V = 30pA$, $T = 80K$. The molecules order in the so called Herringbone structure, where the molecules assume a braid-like order. A structural model of this configuration is shown in d) (d from [158]).

3.4.1 *PTCDA in STM-LE Experiments*

STM-LE measurements have been performed on PTCDA layers on Ag(111) and Au(111) in the group of M. Kawai [94, 159]. STM-induced fluorescence has been proposed for higher layers of PTCDA that have been electronically decoupled by the PTCDA layers beneath them.

In the experiments presented in this thesis, PTCDA served as a second archetype molecule besides C_{60} to demonstrate the effect of the LDOS provided by the molecules as well as to demonstrate the peculiar inertness of the Bi/Cu(111) substrate against molecular overlayers.

3.5 COPPER-PHTHALOCYANINE

Copper-phthalocyanine (CuPc) is a blue dye molecule. It is one of the many representatives of the molecular family of phthalocyanines. All phthalocyanines share the phthalocyanine structural basis consisting of four inner pyrrole rings and four outer benzene rings. The Me^{2+} central ion, e.g. Cu^{2+}, Sn^{2+}, Zn^{2+}, Fe^{2+}, etc., governs the physical properties of each molecular species.

CuPc is a planar molecule. Its elemental formula is $C_{32}N_8H_{16}Cu$. Its structural formula is shown in Fig. 19 a. It has a size of $1.68\mathrm{nm} \times 1.68\mathrm{nm}$. Depending on the Cu-isotope that provides the central ion, it has a mass of $575\mathrm{amu}$ or $577\mathrm{amu}$[4]. Like PTCDA it exhibits a conjugated π-system, that is spread out over the entire phthalocyanine basis. The calculated electrochemical potential is shown in Fig. 19 b.

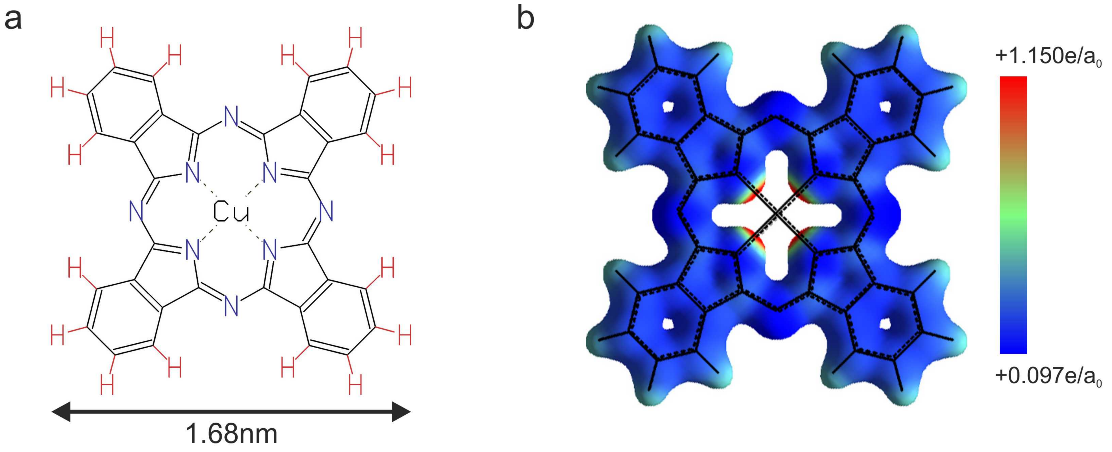

Figure 19: Copper-Phthalocyanine (CuPc). a) Chemical structure of CuPc. b) Electrochemical potential calculated with Hyperchem. e is the elementary charge and a_0 is the Bohr radius [156, 157].

CuPc is used industrially in dyes and as an organic semiconductor in e.g. solar cells [145, 160], transistors [143] or LEDs [161, 162]. Here, it is e.g. used as a p-type semiconductor in heterojunctions with C_{60} [126].

In basic research is used as a model system, e.g. for molecular self assembly on different substrates [129] or as a component for molecular donor-acceptor heterostructures e.g. in laterally mixed or layered structures with PTCDA [153–155, 163].

At low coverage and low temperature, CuPc adsorbs individually on metallic surfaces, e.g. Cu(111) [164] or Ag(111) [165]. This behavior may be assigned to a competition of the molecules for charge-transfer with the substrate, which drives them to assume a maximum average distance from each other [166]. At room temperature, individual CuPc molecules are mobile on flat metallic surfaces [164]. At higher coverage ($\approx 0.75 - 0.9\mathrm{ML}$ depending on the specific substrate the temperature) it forms ordered layers [165, 167].

---

[4] Also carbon has two stable isotopes. About 98.9% of the carbon atoms on earth are ^{12}C, while about 1.1% are ^{13}C. $575\mathrm{amu}$ and $577\mathrm{amu}$ are the masses of CuPc molecules that entirely contain ^{12}C. Due to the different carbon isotopes, only about 70% of all CuPc molecules possess these masses. Around 25% of the CuPc molecules have masses of $576\mathrm{amu}$ or $578\mathrm{amu}$. The rest have masses of $577\mathrm{amu}$ and $579\mathrm{amu}$ or higher.

On Cu(111), individually adsorbed CuPc has been shown to perform a tunneling current driven frustrated rotation (libration) [168], which makes it also an interesting candidate to study dynamics at surfaces as well as inelastic processes.

Part III

EXPERIMENTAL DETAILS

4

EXPERIMENTAL SETUP

The experimental setup used for the experiments presented in this thesis consists of three interconnected vacuum chambers and an *ex-situ* light detection unit. Samples were prepared in the preparation chamber and pre-checked for sample quality in the photoelectron spectroscopy/LEED-chamber. The STM-experiments were conducted in the LT-STM-chamber. Valves between the chambers allow independent activities in every experimental unit.

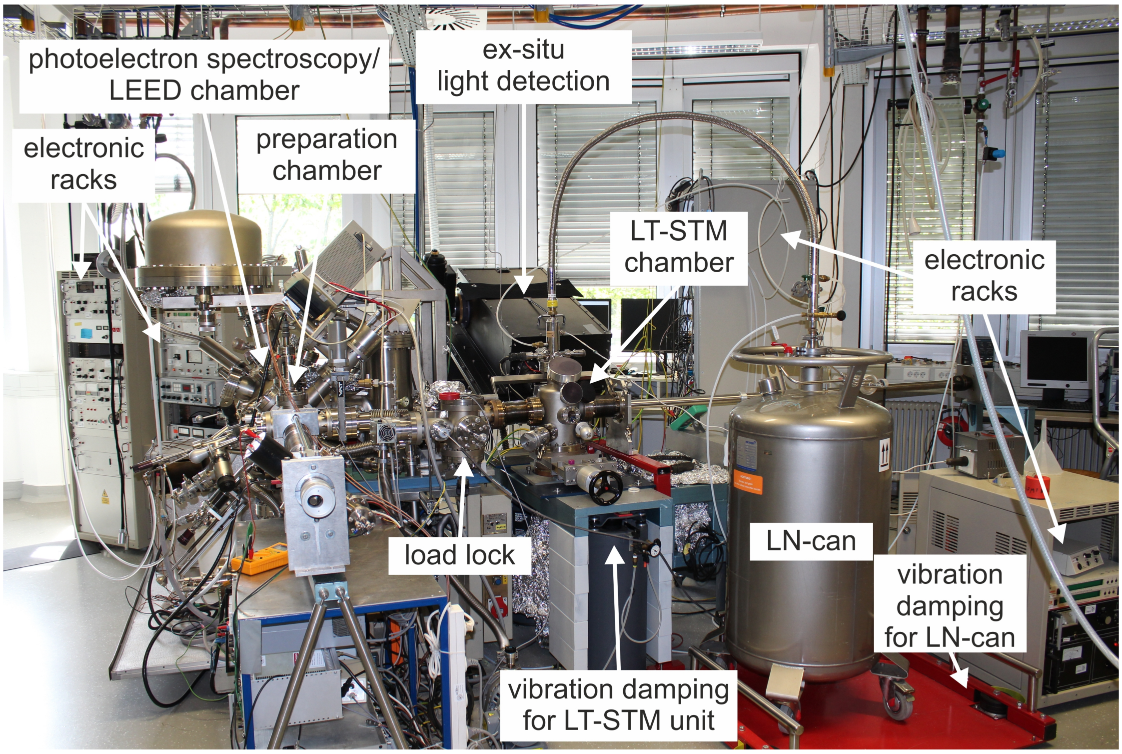

Figure 20: Photograph of the entire experimental setup including all three vacuum chambers and the *ex-situ* light detection unit.

4.1 VACUUM CONDITIONS

The base pressure for all chambers is normally in the range of $1-5\times10^{-10}\mathrm{mbar}$. After bakeout, the pressure is maintained by ion getter pumps and titanium sublimation pumps. As opposed to turbomolecular pumps, these pumps do not cause vibrations which would cause unwanted noise in STM experiments. However, the ion pumps cannot be used to maintain the vacuum during sample preparation by sputtering. The noble gases that are used as sputtering gases, in this case Argon, are not gettered by the ion pumps. Instead of being pumped, the Argon in the chamber would be ionized inside the pump and sputter the gettering surfaces. This would lead to a release of particles inside the chamber which would counteract a clean sample preparation. To avoid this problem, the ion pump in the preparation chamber is turned off and an oil diffusion pump is used to maintain the vacuum during ion sputtering.

4.2 THE LT-STM UNIT

A new LT-STM was built in the course of the experimental work conducted for this thesis. The original, very compact STM design was continuously advanced through generations of STMs in the Möller group and adjusted to the respective requirements of the desired experiments. The fundamental design used here was also applied for other STM and AFM setups in the Möller group [169]. This bares the advantage, that spare parts and know-how can be exchanged in between the experiments. This aids the consecutive advance of the setup and helps to keep repair times as short as possible.

Here, the design of the previous LT-STM was adapted to the requirements of STM-LE experiments. Also, we eliminated weaknesses found in the design of previous versions to further enhance the experimental performance. The main changes from earlier versions consisted in adaptions of the heat shielding to allow for the out-coupling of photons, minor changes in the base unit design and an adaption of the sample holding inside the base unit.

The entire LT-STM design, including the most recent changes, will be presented in the following.

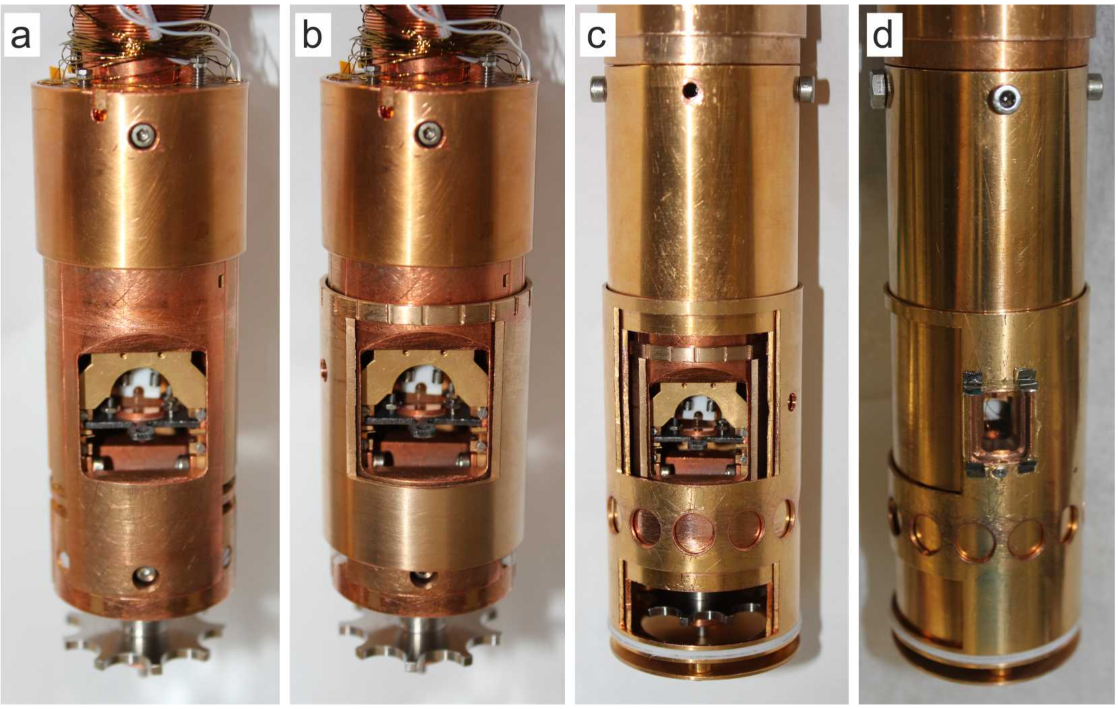

Figure 21: STM including heat shielding. a)-c) STM front view. a) STM when just the inner static shield has been mounted. b) STM with inner static and inner movable shield. c) STM with all shields attached and movable shields opened. d) STM back view. The movable shields are closed. Light from the tip-sample junction can still be coupled out through an ITO-covered glass window.

4.2.1 *Base Unit*

To minimize the cryogenic consumption, the LT-STM design is kept very compact. The base unit has dimensions of only $21\mathrm{mm} \times 24\mathrm{mm} \times 16\mathrm{mm}$ (width×height×depth).

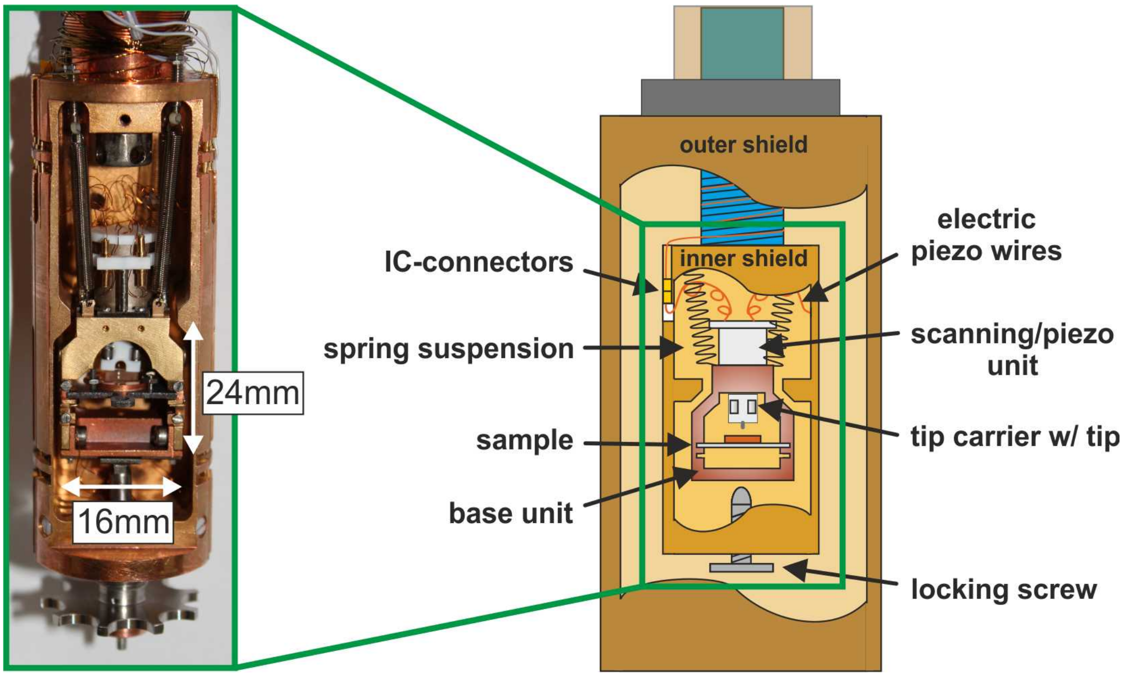

Figure 22: Schematic of the homebuilt LT-STM. Left hand side: Photograph of the STM with shields removed. Right hand side: Schematic outlining the most important parts of the STM. (STM schematic adapted from [170]).

The entire base unit was milled from a single piece of copper to assure maximum thermal conductance for efficient cooling and thermal equilibrium during the measurements. It holds the scanning unit and provides two slots for samples of different height. Within these slots, the sample holder rests on three stainless steel balls onto which it is pushed down by copper-beryllium springs. This yields very defined three-point bearing and prevents wiggling of the samples inside the slots which might cause excess noise in the tunneling current signal.

The base unit is surrounded by several layers of gold-coated copper heat shielding to prevent heat intake through thermal radiation (see Fig. 21). The shielding consists of overall four different layers. Two of the shields are static. They have openings in the front and in the back. These allow for an easy exchange of tips and samples from the front and an unhindered view of the tunneling junction from the back of the STM. Two additional movable shields close these openings while not in use. Even when otherwise entirely closed, the shielding still bares an opening to collect the emitted photons from the back of the STM. To minimize heat intake, the respective cutout in the outermost movable shield is covered by an ITO[1]-covered glass window in the back. ITO blocks infrared heat radiation while at the same time it is transmissive for visible light.

For cool down, the base unit is pressed against the inner heat shielding which is directly connected to the cold finger of the cryostat. This is done by tightening a locking

---

[1] indium-tin-oxide

screw that can be turned with the wobble stick. The locking screw can be turned even if the inner shield is closed. This prevents excess heat intake and contamination of the sample when the locking screw is loosened after cooldown. The cooldown of a freshly prepared sample in the cooled down STM usually takes a few minutes.

4.2.2 *Insulation against Mechanical Vibrations*

After cooldown, the base unit is suspended on springs for vibrational decoupling from the environment. Cobalt samarium magnets embedded in the side walls of the base unit provide an effective eddy current damping when the base unit swings inside the copper shielding.

For damping of external mechanical vibrations, the STM chamber rests on pneumatic feet. These are effective also for low frequencies (in the order of a few Hz), e.g. vibrations of the building.

4.2.3 *Scanning Unit*

The scanning unit consists of two piezo crystal tubes. The outer piezo is directly mounted onto the base unit. It is not segmented and exclusively performs movements in z-direction (surface normal direction). The inner piezo is four-fold segmented to additionally allow tip positioning and scanning in x- and y-direction (surface lateral directions). It is nested into the outer piezo with a marcor piece connecting the two.

Here, the inner piezo is usually used to perform the z-movement during scanning. The outer piezo is used for the automated approach of the tip to the sample and to readjust the idle position of the inner piezo. However, the roles of the piezos in the z-movement of the tip may be variably exchanged.

The scanning unit design with two nested piezo tubes bares several advantages, e.g. an enhanced flexibility and a possible adjustment of the idle position of the scanning piezo. Still, all basic functions of the scanning unit, including the automated approach mechanism described below might also be performed with only the inner piezo crystal. (However, this would require for the additional mixing of two electronic signals during approach.)

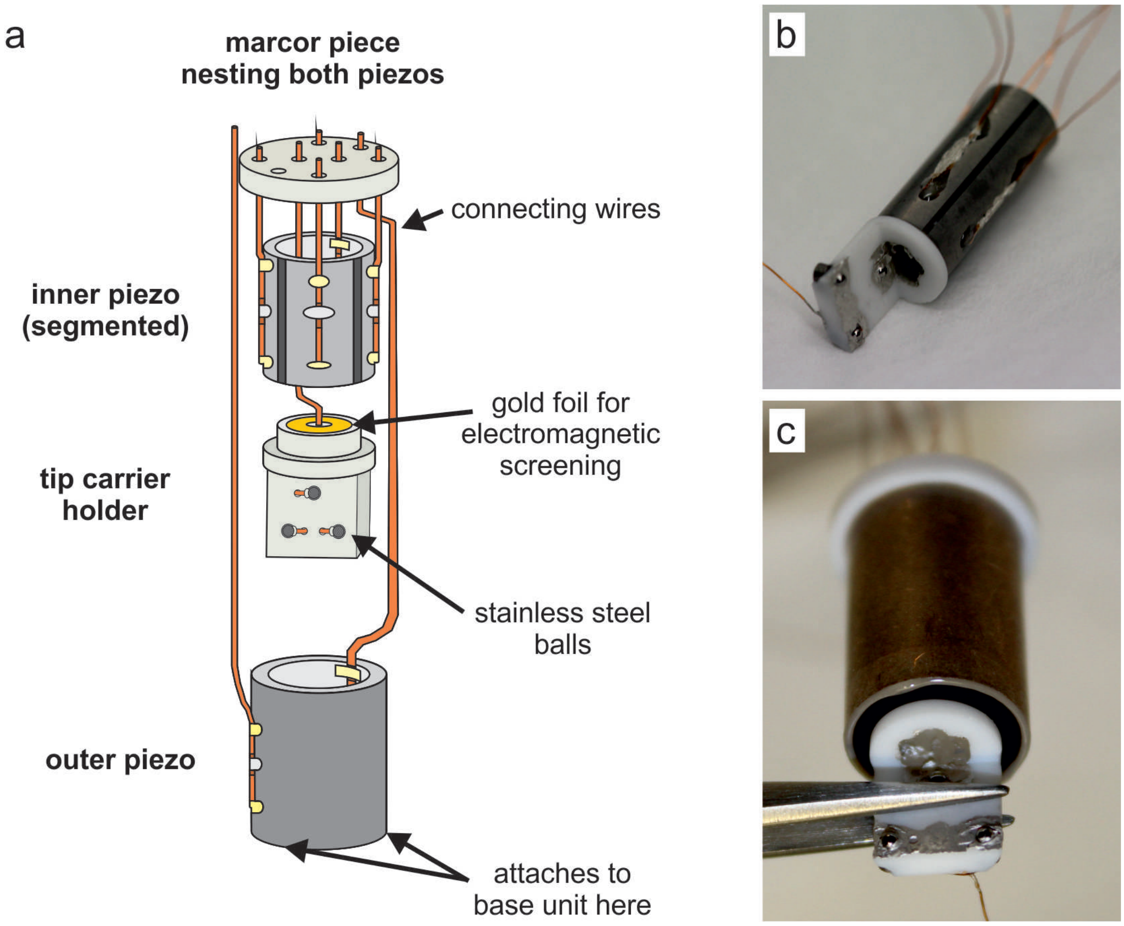

Figure 23: The STM scanning unit. a) Explosion drawing of the scanning unit (from [170], [171]). b) and c) Photographs. b) The inner, segmented piezo tube with the tip carrier holder attached to it. c) Inner and outer piezo tube assembled into the scanning unit in which the piezos are nested inside of each other.

4.2.4 *Tip carriers*

The STM-tips are attached to a tip carrier. This way, the tips may be transferred and exchanged *in situ* more easily.

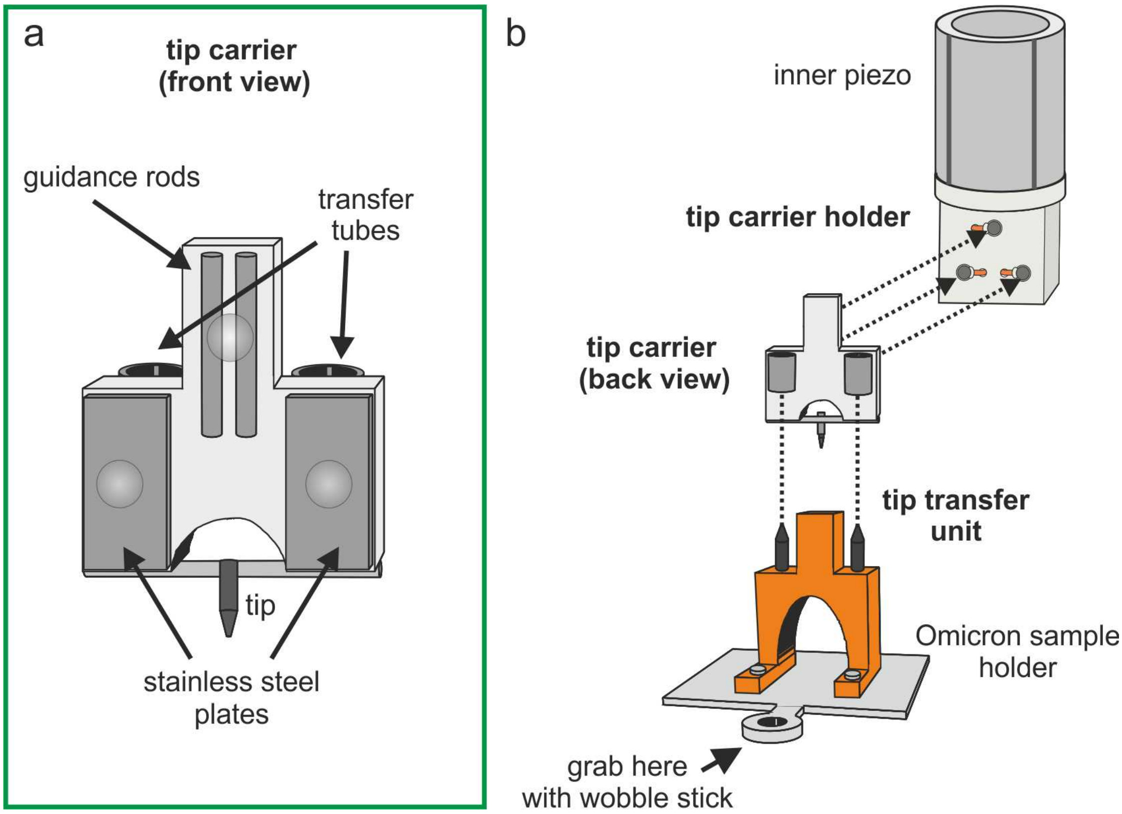

Figure 24: Schematic of the tip carriers. a) Front view of a tip carrier. The stainless steel balls of the tip carrier holder on which the tip carrier rests inside the STM are indicated. b) The tip carriers may be slit onto a tip transfer unit which is mounted on an Omicron-style sample holder. This way the tips can be easily transferred and can be exchanged in the cooled STM within minutes. Inside the STM, the tip carrier is held magnetically on three stainless steel balls on a marcor piece attached to the bottom of the inner piezo. (Based on drawings previously used in [172] and originally created by Dennis van Vörden, as well as parts of drawings by Manfred Lange [171], [170].)

The tip carriers are made from a very thin marcor piece to which two stainless steel plates and two stainless steel rods are glued (see Fig. 24 a). The tip carriers attach magnetically to the marcor piece at the bottom of the inner piezo tube. The latter building block will be further referred to as the tip carrier holder (see Fig. 24 b). It provides a three-point bearing of stainless steel balls (1 mm diameter) on which the stainless steel parts of the tip carrier can slide. Behind each ball, a cobalt samarium magnet is mounted. The magnetic force is large enough to keep the tip carrier from falling but still allows for a directed motion through piezo movements by a stick-slip-mechanism (as described in 4.2.5).

The magnetic mounting of the tip carriers allows for a fast and easy exchange of STM tips. Even during an experiment, while the STM is cooled down, the tip can be exchanged in about one to five minutes. During tip exchange, the temperature of the base unit is hardly affected when cooled down to liquid nitrogen temperature. However, as the sample has to be removed for a tip change, a heating of the sample up to an undefined temperature cannot be avoided.

The tips are spot welded onto a cross connection between the two stainless steel plates (see Fig. 24 a). The stainless steel plates electrically connect the tip through the stainless steel balls to the wiring of the STM. The upper stainless steel ball connects to the upper stainless steel rods. This provides an additional electric contact, which can be used to extend the functionality of the STM through modifications of the tip holder.

While not in the STM, the tip carriers are stored on transfer units (see 24 b). These are mounted on Omicron[2]-design sample holders and can thus easily be grabbed with a wobblestick and transferred. Usually, around $3-4$ tips are kept ready for use in the vacuum chamber, to be able to quickly exchange the tip when needed.

4.2.5 *Automated Approach Mechanism*

The automated approach mechanism applied in our experimental setup uses an interplay of both piezos (see Fig. 25).

One of the piezos is provided with a sawtooth-like voltage signal ($V_{\text{piezo 1}}$). Thereby, in the first step of the approach mechanism the piezo is expanded and the tip is moved towards the sample at a constant speed. If no tunneling current is detected until reaching the maximum expansion of the piezo crystal, it is quickly contracted back to its original length.

Then, the other piezo comes into play. While the first piezo is held at a constant length, a cyclic voltage function is applied to the second piezo ($V_{\text{piezo 2}}$). During the expansion of the piezo, the tip carrier sticks on the tip carrier holder due to static friction. Close to the peaks of the cyclic function, the slope is very steep. At the peak of the cyclic function, when the motion is reversed, the acceleration of the tip carrier holder is very large and overcomes static friction. The entire tip carrier keeps moving forward (slips) and slides towards the sample on the stainless steel balls of the tip carrier holder, while the piezo is contracted. This mechanism is also called stick-slip mechanism.

The cyclic function applied to the second piezo is adjusted so that the described stick-slip forward movement is about one third smaller than the maximum expansion of the first piezo due to the sawtooth. This assures that the stick-slip mechanism only moves the tip within a "safe range". From this new starting point, the procedure is repeated until a tunneling current corresponding to the desired set value is detected.

Once the tunneling distance is reached, prior to the measurement, an interplay of both piezos adjusts the idle position of the piezo that drives the z-moment during scanning. The latter is relaxed into its neutral position while the distance to sample is kept constant by the simultaneous movement of the piezo. This allows for a maximum traveling distance of the z-scanning piezo in both, positive and negative z-direction, to react to sample roughness during scanning.

---

[2] Omicron NanoTechnology GmbH, now: Scienta Omicron GmbH, Limburger Straße 75, D-65232Taunusstein

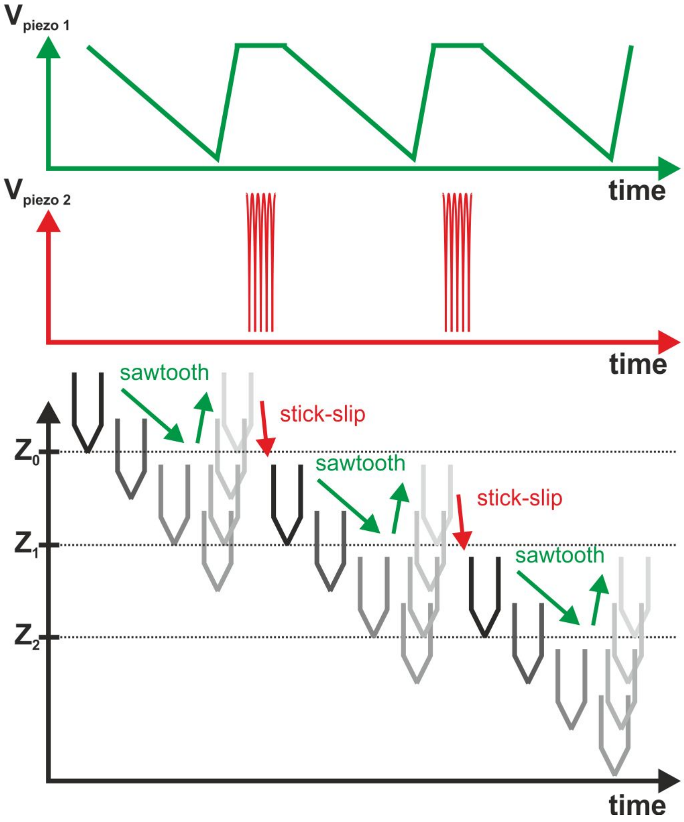

Figure 25: Scheme of the automated mechanism used to approach the tip to the sample.

4.2.6 *Wiring*

The wiring of the STM is realized in different sections. The wires are fixated and electrically connected using IC plug-in connectors. This way, mass contacts or cable breaks can be localized easily by analyzing the cables section wise. It also permits an easy and minimally invasive repair in case of a cable break, as only a short section of the wire has to be exchanged.

There are two types of capton insulated wires used as cables for the STM: All cables that have a direct connection to room temperature parts, i.e. the cables that lead to the plugs connecting the STM to the *ex-situ* electronics, are made of a special stainless steel alloy[3] with a rather low heat conductivity. Additionally, these cables are wrapped around the cryostate several times for cooling. This way, the heat intake is minimized.

The further *in-situ* wiring is realized by $0.12\mathrm{mm}$ diameter capton insulated copper wire. These cables are rather well heat conductors. Once the STM base unit is cooled down suspended on the springs, the cooling is entirely maintained through these cables and the stainless steel springs. This way, the base unit including tip and sample can be kept at a constant temperature of around $79\mathrm{K}$ for cooling with liquid nitrogen and $7\mathrm{K}$ for cooling with liquid helium, respectively.

Considering the light weight of the base unit (approx. $40\mathrm{g}$ including the piezo scanners, tip and sample), the wires e.g. connecting the piezo act as springs and may influence the swinging of the base unit as the result of outside vibrations. During the

---

[3] MDC Caburn KAP 4K-014

assembly of the STM, particular attention has to be paid when arranging the wires to allow for an unhindered swinging of the base unit in order to prevent excess noise in the tunneling current signal.

4.2.7 *Ex situ cooling system*

The LT-STM is cooled using an ACS Helitran LT-3B continuous flow cryostat. For the experiments presented in this thesis, the cryostat was operated with liquid nitrogen as a cryogenic. If desired, the system can be also operated with liquid helium. However, due to the lower heat capacity of liquid helium, the consumption of cryogenic liquid in the latter case is significantly higher. Additionally, helium is very expensive and recent developments on the world helium market lead to increasing supply shortages. For the sample systems studied here, the stability at liquid nitrogen temperature was adequate, making the use of liquid helium redundant.

The cryogenic liquid is provided from storage dewars that usually hold $100 - 150\mathrm{l}$. An excess pressure of around $0.4\mathrm{mbar}$ (during cool down from room temperature) or $0.15\mathrm{mbar}$ (during regular cooling) inside the dewar presses the cryogenic liquid through a transfer line into the reservoir of the cryostat. The excess pressure is either built up internally through the vapor pressure of the croygenic liquid or may be applied externally. It is controlled through pressure relief valves.

The shielding of the transfer line is evacuated to about $10^{-3}\mathrm{mbar}$ for thermal insulation. It holds two capillaries through which the coolant flows. The first capillary (cryostat line) directly carries the cryogenic liquid from the storage dewar into the reservoir of the cryostat (solid dark blue arrows in Fig. 26). There, it cools down the STM including the shields and the wiring. Thereby, the coolant is heated up and evaporates. The gas phase coolant then leaves the reservoir through an exhaust. When cooling with liquid helium, this exhaust is connected to a helium-recycling line.

The second capillary (cooling line) encloses the first capillary. For an efficient cooling of the first capillary, it runs from the dewar, where the liquid coolant is pressed into the capillary, all the way down to where the first capillary ends into the reservoir, and back to the other side of the transfer line where the coolant leaves the line as a gas (see red arrows in Fig. 26).

The respective flow through each capillary is monitored by flow meters and may be controlled by adjustable valves. Additionally the coolant flow into the reservoir of the cryostat can be controlled by an additional needle valve (see Fig. 26). This ensures a smooth and continuous laminar flow of the coolant to keep the mechanical noise produced by the cryostat on a minimum level.

Using liquid nitrogen, the cryogenic consumption of the cryostat is about $10\mathrm{l}$ per day. The liquid helium consumption lies roughly around $18 - 20\mathrm{l}$ per day.

To prevent a freezing of the outside part of the cryostat associated with a risk of causing possible vacuum leaks through extensive thermal expansion, counter heating holds the outside part of the cryostat slightly below room temperature. Additionally, the cryostat is equipped with wires for counter heating close to the cold finger. This enables experiments at variable temperatures above the minimum temperature reached with the respective cryogenic liquid.

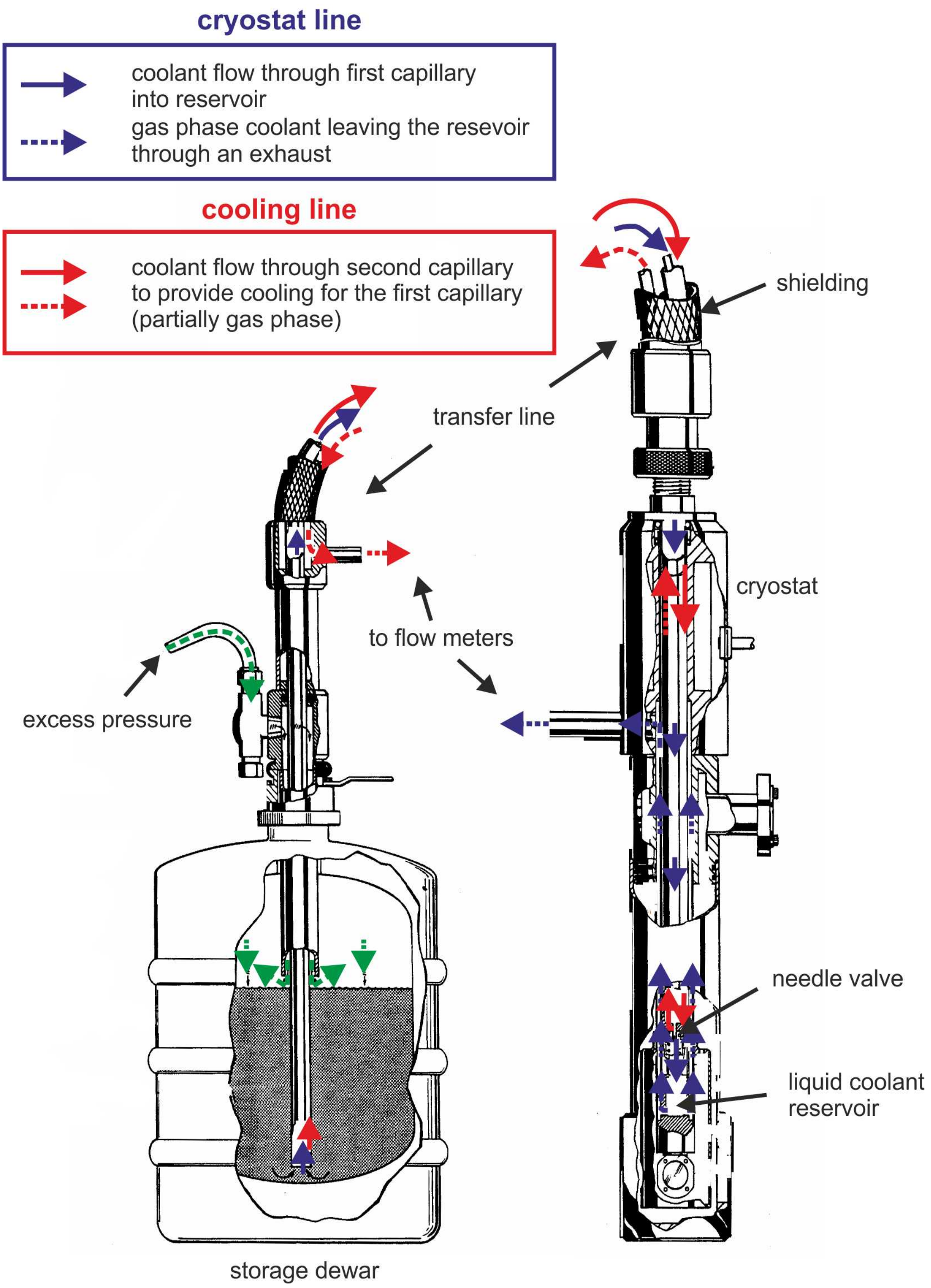

Figure 26: Schematic of the cooling system. The coolant flow is indicated by colored arrows. Inside the transfer line, liquid coolant flows from the storage dewar to the reservoir of the cryostat through a coolant capillary which is cooled by a second cooling capillary. The flow through both capillaries can be controlled by adjustable valves at the gas exhaust of the reservoir and the cooling capillary as well as a needle valve which controls the flow from the coolant capillary into the reservoir. (Adapted from [170], base drawing originally from [173].)

4.2.8 *Additional Features of the LT-STM Chamber*

Additionally to the LT-STM itself, the LT-STM chamber offers a carbon monoxide doser and a stage for transferable molecular evaporators. A carousel below the STM can store up to 10 tips, samples, transferable molecular evaporators and other tools. This way, these devices can be kept ready for use under UHV conditions and e.g. tips may be exchanged quickly during the experiment.

4.2.8.1 *Carbon Monoxide Doser*

Carbon Monoxide (CO) has been shown to successfully functionalize STM tips to achieve intramolecular resolution [174], [175]. The CO is usually brought to the tip by picking up a CO molecule from a surface, e.g. by applying voltage pulses to the tip placed above a CO-molecule [176], [177] (and supporting material). The CO on the surface results from the adsorption of residual gas from the chamber. Although CO is a very common residual gas particle in every vacuum chamber, the CO concentration within the residual gas can be purposefully enhanced by letting gas into the chamber through an inlet.

The LT-STM-chamber possesses a leak valve that points directly onto the sample within the STM. This allows the directed dosing of CO onto the cooled sample. At low temperature, the sticking coefficient of the CO is significantly larger than at room temperature. This way, experiments with on CO covered surfaces become possible, e.g. CO on Cu(111), which has recently been shown to be a rather interesting candidate for STM field-induced switching by STM [178].

4.2.8.2 *Transferable Molecular Evaporators*

The assembly of organic molecules on a sample surface crucially depends on the preparation parameters. One important factor is e.g. the sample temperature. At room temperature, many organic species tend to form (ordered) molecular domains due to intermolecular interactions.

To be able to discriminate the properties of a single molecule from effects due to intermolecular interaction, studies on singly adsorbed molecules are of special interest. For a lot of organic molecules, this requires for deposition at low temperatures were surface diffusion is widely suppressed. Thus, if the coverage is low enough, even molecules with the tendency to form domains at e.g. room temperature, may adsorb individually. However, a subsequent annealing to higher temperatures, even to room temperature or below, during the transfer of the sample, would again lead to the formation of molecular islands.

To be able to evaporate molecules directly onto the cooled sample within the STM, transferable molecular evaporators were constructed in the Möller group [179], [180]. The freshly prepared samples may subsequently be analyzed without ever exposing the sample to higher temperatures, i.e. annealing the sample.

The evaporators consist of an L-shaped crucible embedded into a filament mounted on top of an Omicron sample holder. Thus, they may be easily brought into the vacuum chamber through the load lock without the need for a bakeout. The transferable evaporators are slit into a stage in front of the STM and are thereby electrically con-

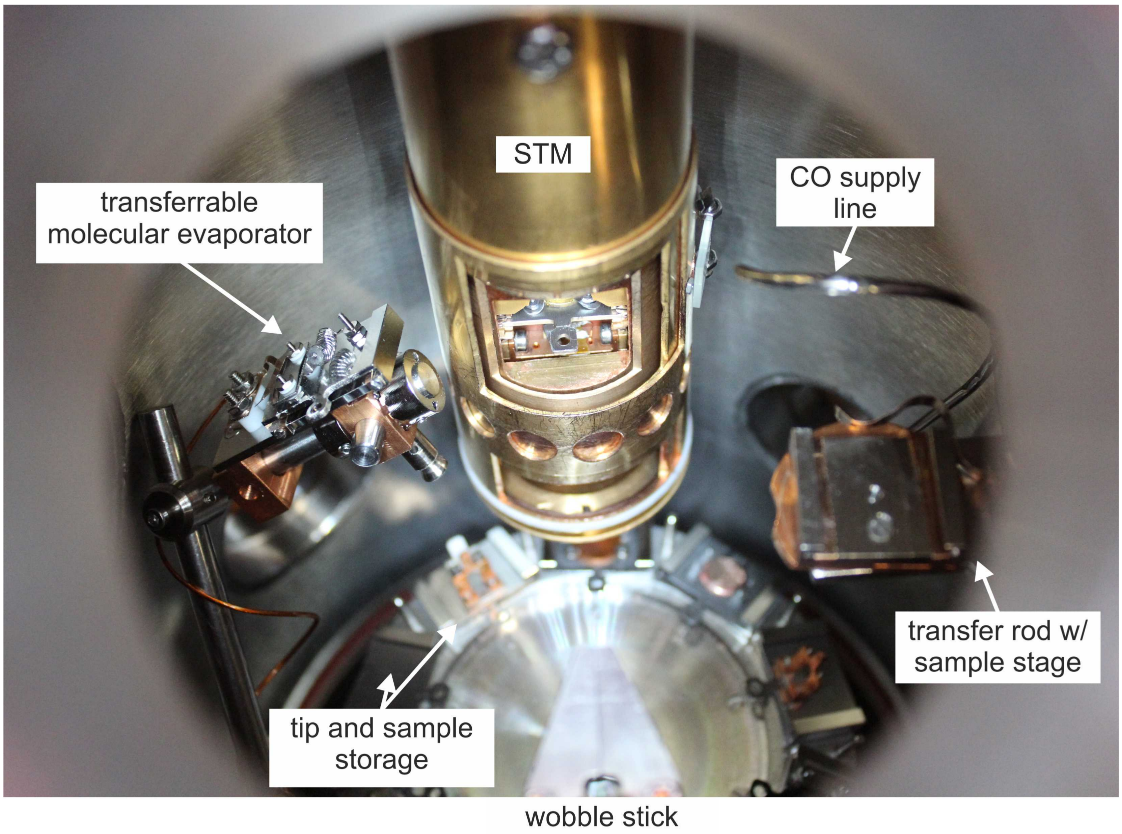

Figure 27: View into the STM chamber through one of the flange windows. The image shows: The stage to electrically connect transferable molecular evaporators. The LT-STM with shields open. The CO-supply line pointing towards the opening in the shielding of the STM. The transfer rod for transfer into the load lock or the preparation chamber. A carousel to store up to ten tips, samples, transferable evaporators etc..

nected, so that a current can be passed through the filament. The evaporation angle may be adjusted with the wobble stick. When not in use, the stage is turned out of the way as seen in Fig. 27.

4.3 LIGHT DETECTION

The special focus of the work presented here lies in the detection of photons emitted from the tunneling junction of an STM experiment. One of the tasks was the design and implementation of a light detection unit to the experimental setup.

4.3.1 *In Situ Light Detection*

The light emitted from the tunneling junction is collected *in situ* with a plano-convex collective lens ($27.1\mathrm{mm}$ diameter, $38\mathrm{mm}$ focal length). The lens is placed such that the tip-sample junction lies in its focus, directing the emitted light into a parallel beam.

The lens is held in a stainless steel tube (lens holder). Its position inside the vacuum can be adjusted by an x-y-gimbal and an additional custom designed z-manipulator. Focusing in the direction normal to the beam of light is usually performed before each experimental run. This optimizes the photon yield since different samples exhibit different heights and the position of the tip slightly varies with every coarse approach of the tip. The focusing may be monitored either using a webcam image of the tip-sample junction and directing the image onto a predefined spot or optimizing the count rate of the avalanche photodiode (APD) (see below). For robust sample systems that are not effected by the procedure, this may optionally happen during field emission which yields significantly higher count rates than regular tunneling experiments. This enhances the accuracy of the focusing.

The parallel light beam exits the vacuum chamber through a boron silicate window. The material of the window was especially chosen for its high and constant transmittance in the visible and near infrared range. Further, the window was manufactured and mounted especially planar to not distort the outcoming light beam.

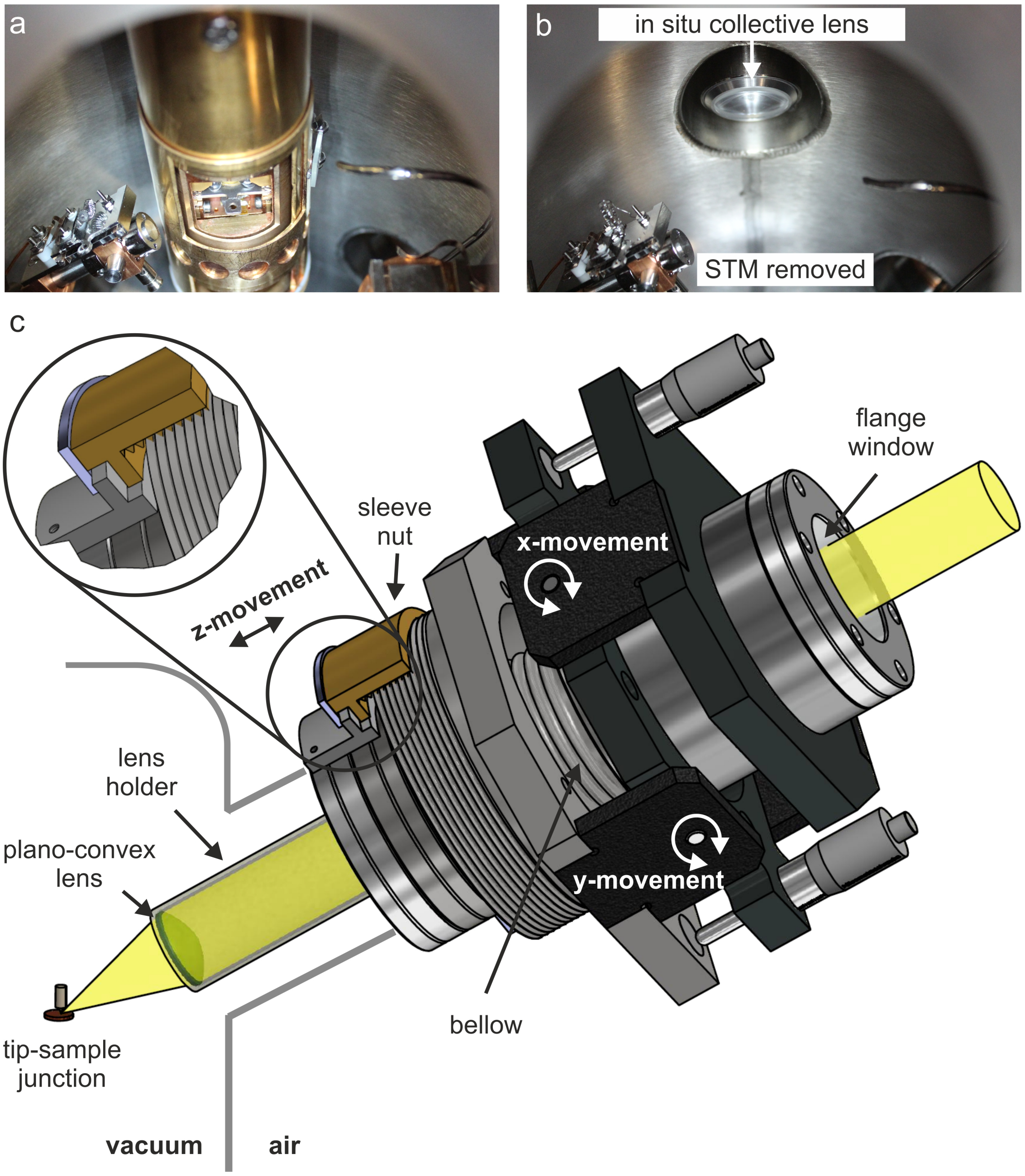

Figure 28: *In situ* light detection. The light is *in situ* collected with a lens inside the vacuum around 4cm away from the tip sample junction which lies in the focal point of the lens. The parallel beam leaves the vacuum through a boron silicate flange window. a) View into the LT-STM chamber. b) When the STM is removed from the recipient, the lens which focuses onto the tip-sample junction from the backside is revealed. c) Schematic representation of the *in-situ* light detection unit. The lens position may be adjusted in x,y,- and z-direction to refocus for different sample heights and lateral positions of the tip on the sample. Drawing of the x,y,z-positioning unit courtesy of Tobias Roos.

4.3.2 *Ex Situ Light Detection*

Due to the design of the existing LT-STM vacuum chamber and the position of the existing flanges, the lens holder approaches the tip-sample junction from an angle of about 20° from the horizontal plane (see Fig. 28). Consequently, also the lens exhibits this angle from the sample plane. Deflection mirrors in the beam path always lead to a loss of detected photons. In order to minimize losses, the optical table on which the *ex situ* light detection system is placed, was set up at the same 20°-angle from the horizontal plane.

The light may be optionally directed onto a webcam, an avalanche photodiode (APD) or spectrograph equipped with a liquid nitrogen cooled CCD[4] camera (see Fig. 29). For this purpose especially mounted deflection mirrors are used which can be removed and subsequently brought back into the light path at very reproducible positions.

An additional collective lens in front of each device focuses the light on the respective detectors. The length of the optical paths to all devices is about equal. This way, a small misalignment of the optics in the beam lateral direction causes similar beam deflections on each detector which are then easier to identify and correct.

4.3.2.1 *Webcam*

With a first deflection mirror, the light can be directed onto a webcam. The webcam is used to monitor the coarse approach of the tip towards the sample. Furthermore, it is used to monitor the focusing of the *in situ* lens and the adjustment of the entire optical table after bakeout.

4.3.2.2 *Avalanche Photodiode*

Removing the first deflection mirror and placing a second one directs the light onto the APD. The APD gives a fast measure of the overall photon yield (usual integration times of a few ms), however, without any energy resolved information. Here, the APD used was a Perkin Elmer SPCM-AQR-14. This specific APD model is sensitive to photons in the wavelength range of $400\mathrm{nm}$ to $1060\mathrm{nm}$ and has a specified dark count rate of about 100 counts/s [61]. The overall photon yield is measured as an additional signal channel to e.g. the z-displacement of the tip or the dI/dV-signal. This way photon maps reflecting the spatially resolved excitability of the tip-sample junction can be obtained simultaneously to the topography. Also, spectra of the overall photon yield with respect to the applied bias voltage, i.e. the energy of the injected electrons, can be recorded simultaneously to STS spectra.

4.3.2.3 *Grating Spectrometer*

Removing all deflective mirrors from the optical paths, the light is directed straight onto a Princeton Instruments Acton SP 2300 spectrometer [181]. The spectrometer is equipped with three different gratings ($600\mathrm{l/mm}$, $300\mathrm{l/mm}$, $150\mathrm{l/mm}$). This way, different resolutions can be chosen for the analysis of the energetic distribution of the

---

[4] charge coupled device

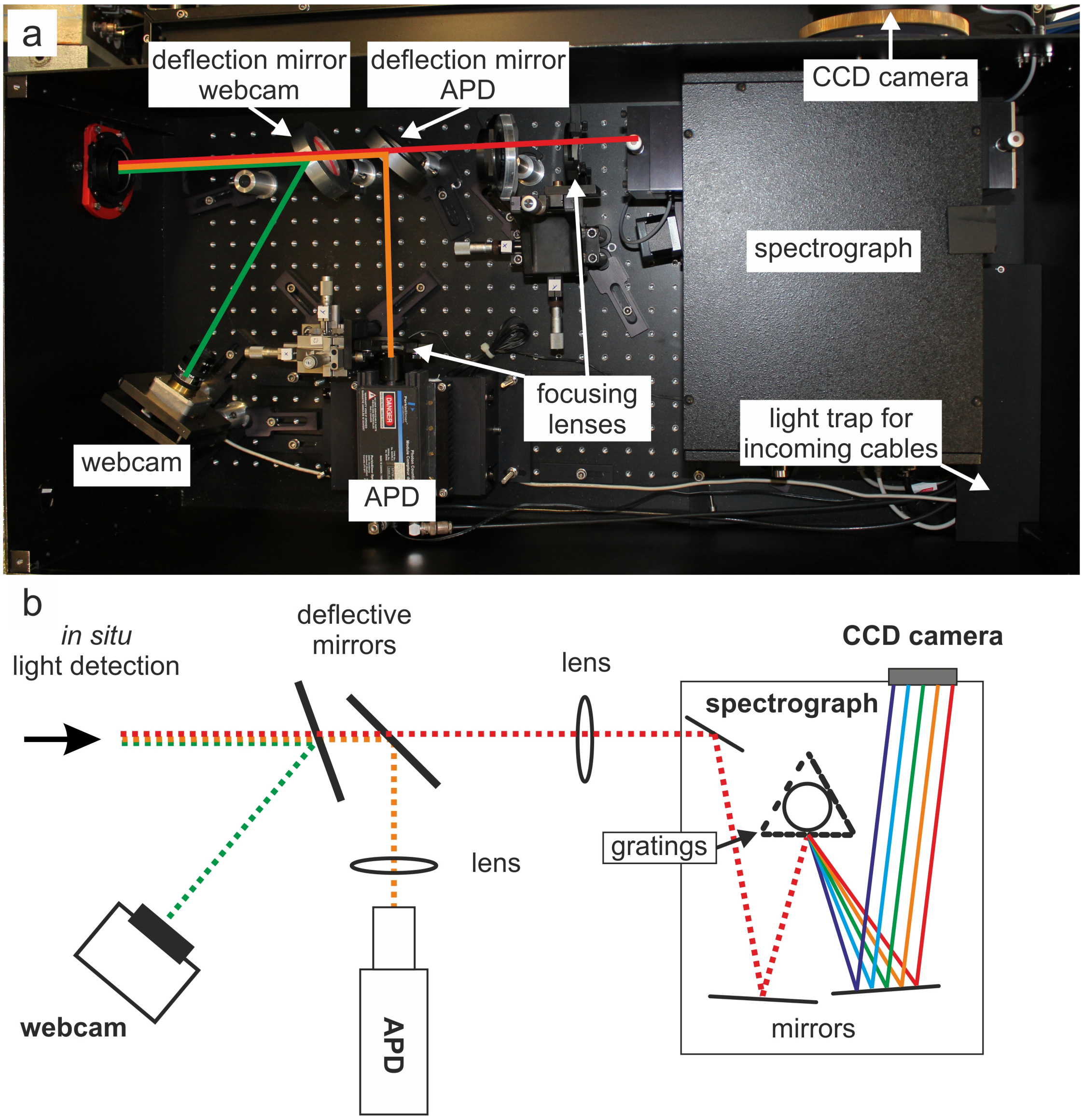

Figure 29: *Ex situ* light detection. a) Photograph of the optical table with the entire *ex situ* light detection unit. The different light paths are indicated: to the webcam (green), the APD (orange), and to the spectrograph (red). The light is optionally directed onto one of these paths by placing or removing mirrors. b) Schematic of the *ex-situ* light detection setup. This representation additionally shows a scheme of the setup inside the spectrograph. The light is directed onto one of three gratings by mirrors and subsequently directed onto the LN-cooled CCD-camera. The gratings are mounted on a rotatable stage. The used grating as well as the center wavelength may be adjusted through the rotation of this stage.

emitted photons. The respective wavelength range which is detected is chosen by rotating the grating while the deflection mirrors inside the spectrograph are held stationary. A CCD camera[5] is directly attached to the spectrograph. The $1340\text{pixel} \times 100\text{pixel}$ detector is cooled with liquid nitrogen to minimize image noise. Here, the integration times for acceptable signal to noise ratios usually lie in the order of $5 - 10\mathrm{min}$ per spectrum.

4.3.2.4 *Shielding from Stray Light*

The entire experimental setup is sealed off ambient light by flange caps covering all window flanges. The optical table holding all *ex situ* light detection is completely shielded from ambient stray light by a surrounding black box. The flange through which the light is coupled out of the vacuum chamber is connected to the opening of the black box by a vulcanized black rubber bellow. Cables going to the devices inside the black box are lead through a light trap. Shielded against light in this way, experiments can be mostly performed under ambient light conditions in the lab without an influence on the zero count rate of the APD.

---

[5] The pixel size of the CCD are $20\mu\mathrm{m}$. The CCD resolution is $0.14\mathrm{nm}$, at $438.5\mathrm{nm}$ measured with a $1200\mathrm{l/mm}$ grating at an entry slit width of $20\mu\mathrm{m}$ [181]. Here, the entry slit size was a significantly larger and the wavelength of interest were located at higher wavelengths, so that the resolution somewhat smaller for the data presented in this thesis.

4.4 LOAD LOCK

Tips, samples and other tools or devices may be brought into the vacuum through a load lock. The load lock is pumped by a turbomolecular pump. After about $30 - 45$ minutes of pumping, it allows for a transfer into the experimental system without breaking the vacuum. The load lock is equipped with a stage for resistive heating of tips which are newly introduced to the UHV. The tip holders are slit into the stage on the transfer unit. Once in place, the stainless steel plates of the tip holder are electrically connected from the sides with copper beryllium springs. This way, a current can be passed through the cross connection between the two stainless steel plates, heating both, the cross connection and the suspended tip to an orange glow. This removes water and oxide that might have been attached to the tip and thus allows for maximum conductivity and stability.

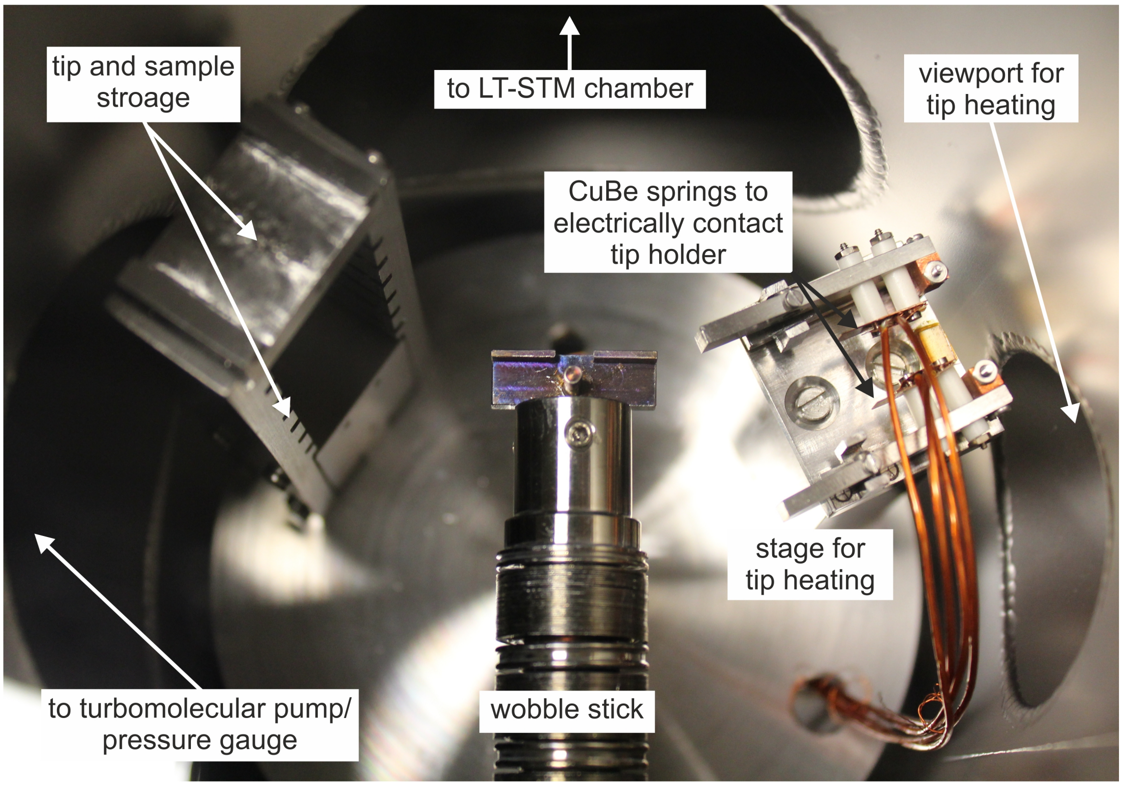

Figure 30: View into the load lock. With the help of the load lock, tips, samples and tools may be brought into the experimental system without having to break the vacuum. Pumping time from ambient conditions until transfer is around 45 minutes. The load lock is equipped with a stage to store several tips and samples as well as a stage to contact the tip carriers for direct resisitive heating of the tips. This way, water and oxides may be removed from the tip before introducing them to the STM.

4.5 PREPARATION CHAMBER

The preparation chamber yields various possibilities to clean e.g. noble metal crystals by ion bombardment and annealing (see chapter 5) or to prepare e.g. silicon samples by direct current heating. In subsequent preparation steps, thin metallic or organic layers may be grown.

4.5.1 *Ion Bombardment*

Ion bombardment (also called sputtering) is used to remove the first few layers of a sample in order to provide a clean surface. Here, Argon (Ar) was used as a sputtering gas. The gas is ionized inside the sputter gun and the Ar^+-ions are accelerated towards the sample with a high voltage of around a few kV. For the experiments presented here, two kinds of sputter guns were used: one realizing the ionisation of the Ar-atoms by applying a high voltage (cold cathode ionization) and another one ionizing the Ar through impact ionization with electrons emitted from a filament and subsequently accelerated by a high voltage.

4.5.2 *Evaporators*

Currently, the chamber is equipped with a single Knudsen cell evaporator used for growing thin Bi films, an electron beam evaporator currently used for growing thin cobalt films, a commercial 4-cell Knudsen evaporator (Kentax), and a homebuilt 3-cell Knudsen evaporator. The latter are filled with organic molecules such as PTCDA, C_{60}, copper-phthalocyanine (CuPc), or iron-octaethyl-porphyrin (FeOEP). One cell is additionally filled with sodium chloride (NaCl) in order to provide thin insulating layers to decouple molecules from e.g. noble metal surfaces for future STM-LE experiments.

The preparation chamber is equipped with a Balzers QMH 410 quadrupole mass spectrometer (QMS). The QMS has a detection range up to $2048 amu$. It allows for a precise monitoring of evaporation rates, e.g. during the growth of thin organic layers. The QMS-signals are ion-currents that correspond to a certain atomic mass. Using e.g. STM data, the magnitude of the ion-current signals can be correlated with the evaporation rates of certain species in ML per time. Further, the QMS may provide information whether organic molecules coming from the evaporators may be fragmented or not. Also, it can be used for residual gas analysis. Due to the high range of detectable masses the QMS may also be utilized to obtain thermal desorption spectra, e.g. of organic layers. However, the latter method was not applied during the experiments conducted for this thesis.

4.5.3 *Sample Heating and Cooling*

Within the preparation chamber the samples are placed on a manipulator. The latter is used to transfer samples between the preparation chamber and the photoelectron spectroscopy/LEED unit and to place samples in front of the respective evaporators.

The manipulator is equipped with a $50W$ filament positioned directly underneath the samples which can be used for annealing up to temperatures of about $900K$. For

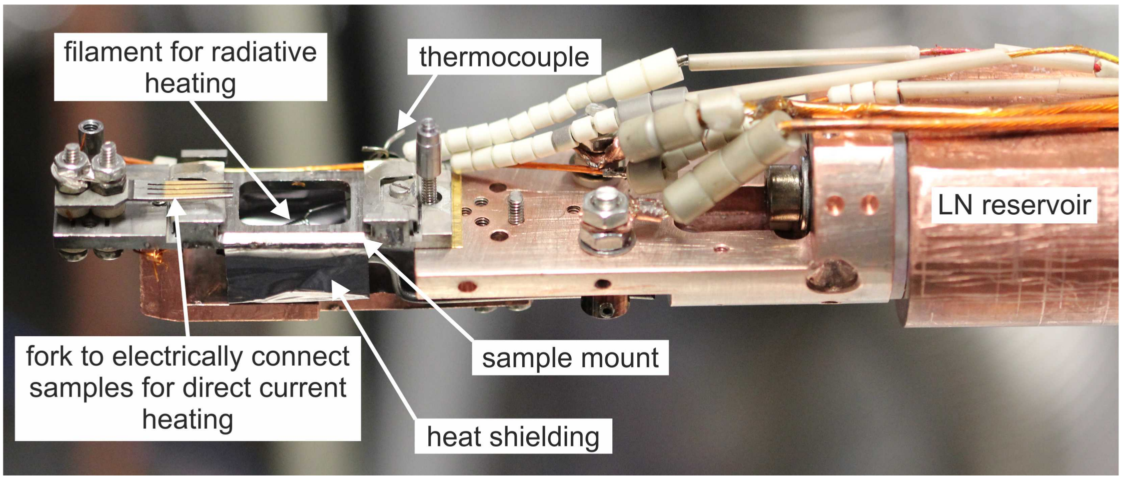

Figure 31: Preparation chamber transfer rod. On the transfer rod, samples may be electrically connected for direct current heating of e.g. silicon samples. Additionally, a filament allows for radiative heating of samples. Counter cooling of the transfer rod prevents excessive desorption of residual gas particles during heating.

higher temperatures, as e.g. needed for the preparation of silicon samples, especially designed sample holders may be electrically connected for direct current heating.

Additionally, the manipulator may be cooled using liquid nitrogen. This may be used during the preparation of various sample systems to obtain ideal preparation parameters for thin Bi-film growth on silicon e.g. following the recipe of Nagao et al. [182] or Bobisch et al. [183].

The cooling of the manipulator including the sample mount during the heating of samples may prevent the excessive desorption of residual gas from the manipulator surface. This assures maximum cleanliness at the best possible vacuum conditions. For sample preparation at very high temperatures, e.g. needed for of silicon samples, it further prevents the melting of manipulator parts.

4.6 PHOTOELECTRON SPECTROSCOPY/LEED CHAMBER

Another chamber of the experimental setup is equipped with an electron spectroscopy unit. This yields the opportunity to conduct x-ray photoelectron spectroscopy (XPS) or ultraviolet photoelectron spectroscopy (UPS). However, these techniques were only rarely used in the course of the work for this thesis.

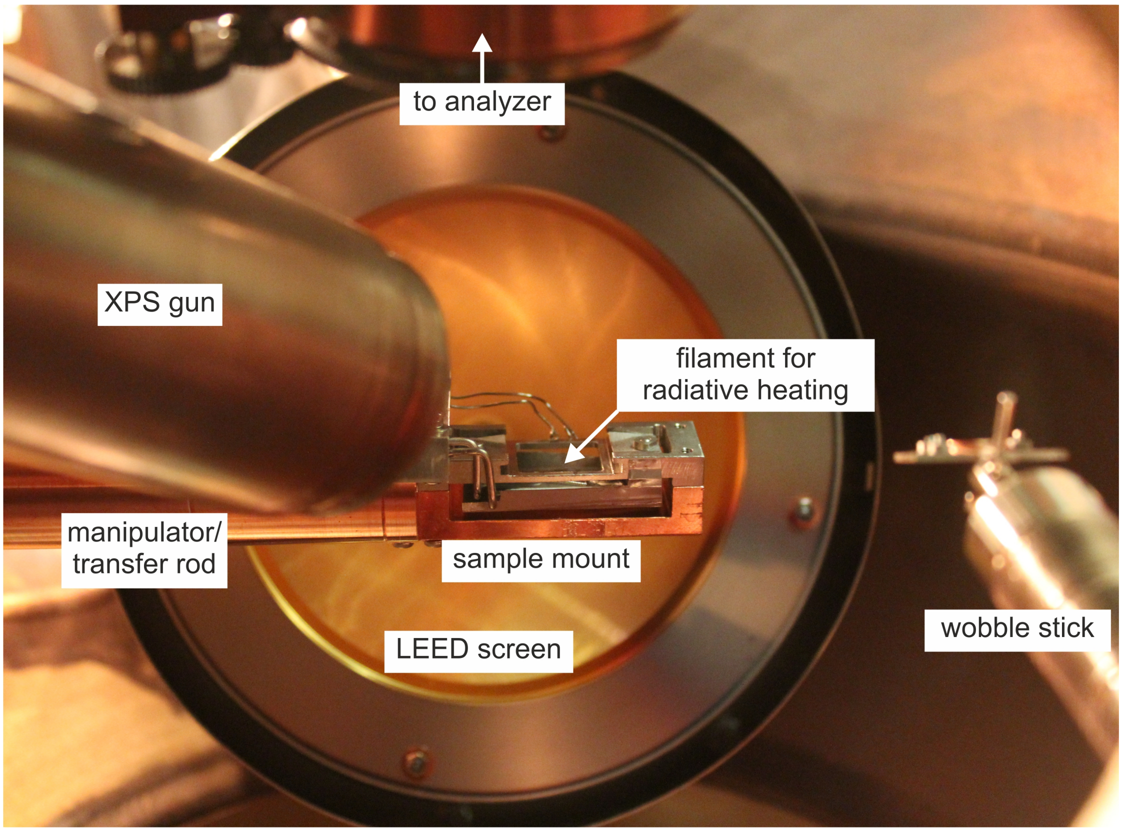

Figure 32: View into the photoelectron spectroscopy/LEED unit through a flange window. The unit allows for XPS and UPS experiments. In the image, the UPS gun is hidden behind the XPS gun. The LEED setup was quite regularly used to check the sample quality after preparation. Also, it was used to reveal the dominating ordered structures on the surface as a complementary information to local STM data.

However, the low energy electron diffraction (LEED) setup, also located in the same vacuum chamber, was frequently used to check the sample quality before performing further preparation steps or the STM analysis. It allows to gather information about the long range ordered structures on the sample to complement the local STM data.

The photoelectron spectroscopy/LEED chamber exhibits a manipulator that, similarly to the manipulator in the preparation chamber, offers the possibility of radiative sample heating and cooling with liquid nitrogen.

4.7 SOFTWARE AND ELECTRONICS

The STM control and signal processing is realized using homebuilt modular electronics along with a Soft dB MK3-Signal Ranger DSP[6]-board. The modular electronics allow for an easy extension and adaption of the experimental capabilites. This way, modules featuring custom designs for new experimental opportunities can be easily included into the electronic setup. E.g. a *Scanning Noise Microscopy* module [184] enables the experimental setup to detect and analyze the noise in the tunneling current simultaneously to regular STM and STS experiments. The analysis of the frequency, amplitude and duty cycle of the noise in the tunneling current can yield valuable information e.g. about inelastic excitations of the sample [168].

The Signal Ranger DSP-board used to control the STM is addressed using the open source Gnome x Scanning Microscopy (GxSM) software [185]. Princeton Instrument's WinSpec software [186] is used to record and process the spectra of emitted light detected by the spectrograph.

The subsequent data analysis for the data presented here was performed using the open source Windows Scanning x Microscopy (WSxM) software [187]. The processing of all spectroscopic data additionally involved OriginPro software [188]. For the further vizualization of the data, CorelDraw [189] was used.

For the typesetting of this thesis, LaTeX in conjunction with the classicthesis package by André Miede was used [190].

---

[6] digital signal processing

5

TIP AND SAMPLE PREPARATION

5.1 PT-IR-TIPS

The tunneling tips used in the scope of this work were mechanically cut from $0.1\mathrm{mm}$ diameter Platinum Iridium wire (90% Platinum, 10% Iridium) and spot welded onto the cross connection of the tip carrier (see Fig. 24). The wire was cut at an angle of around 30°. While cutting, a slight pulling on the wire causes a ripping of the material. Therefore, the produced tip surfaces do not directly come into contact with the wirecutter, reducing the amount of possible contamination.

Even though tips produced in such a fashion appear a lot duller than electrochemically etched tips on a macroscopic scale, the produced microtips have been proven to exhibit high resolution and stability in STM experiments.

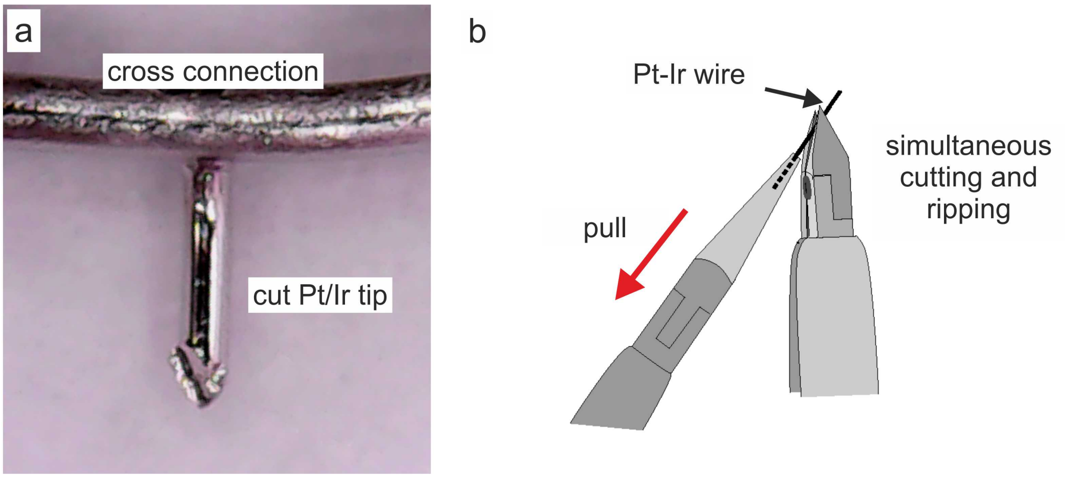

Figure 33: Pt-Ir tip preparation by cutting. a) Closeup image of a cut Pt/Ir-tip. b) Scheme of the Pt/Ir-tip preparation by a mixture of cutting and ripping the wire [191]. Even though macroscopically the tip looks rather dull, the sharp microtips that are produced by the mixture of cutting and ripping the wire usually yield nicely resolved STM data.

Before being introduced into the STM-chamber, the tips are resistively heated in a specially designed heating stage in the load lock at vacuum conditions of about $1 \times 10^{-6}\mathrm{mbar}$. A current of roughly $4-5\mathrm{A}$ is passed through the cross connection on which the tip is suspended, heating both to an orange glow. This procedure removes adsorbates and non-conductive oxide layers resulting from the exposure of the tip to ambient conditions and ensures maximum cleanliness and conductivity.

Before STM-LE experiments, once being introduced into the STM, the tips are brought into controlled mechanical contact with an Ag sample to cover the tip with Ag atoms. This enhances the plasmonic excitability of the tips and thus the photon yield in STM-LE experiments due to the characteristic dielectric function of Ag which exhibits a low internal damping [19], [90].

The induced photon yield as well as the spectral fingerprint of tips in STM-LE experiments are known to be very sensitive to tip changes [11]. To enhance their stability, after being indented into the Ag surface, the the tips are field emitted at around $50\mu A$ at $400V$ for at least $15min$ up to several hours.

The tips are characterized for their topographic resolution and induced photon yield on a well known material, e.g. Ag(111) before being used in STM-LE experiments on more complex material systems, e.g. Bi/Cu(111) or organic layers.

5.2 SUBSTRATES

5.2.1 *Ag(111) single crystals*

Ag(111) single crystals were prepared by several cycles of Ar^+-ion bombardment and subsequent annealing. The ion bombardment was conducted at an Ar-base pressure of 5×10^{-5} at $2.6kV$ and a sputtering current of about $30\mu A$[1]. To ensure flat samples with terrace sizes of some hundreds of nm, Ag-samples were annealed by radiative heating with a tungsten filament for at least $45min$ at $20W$.

5.2.2 *Cu(111) single crystals*

Cu(111) single crystals were prepared by several cycles of Ar^+-ion bombardment and subsequent annealing. The ion bombardment was conducted at an Ar-base pressure of 5×10^{-5} at $2.6kV$ and a sputtering current of about $30\mu A$. In the following Cu(111) samples were annealed by radiative heating with a tungsten filament at $30W$ for $10min$.

5.2.3 *Ultrathin Bi films on Cu(111)*

For the preparation of ultrathin Bi films on Cu(111), a Cu(111) single crystal was prepared as described above. Before applying Bi to the surface by evaporation from a Knudsen cell, the single crystals were preheated to around $400K$ for several minutes. Bi was evaporated at a rate of about $0.75 - 2ML$ per minute. Subsequently, LEED was used to ensure sample quality and to determine the dominating Bi-induced surface structures.

5.3 ORGANIC MOLECULES

The organic molecules C_{60}, PTCDA, and CuPc were evaporated from Knudsen cells. During evaporation of the organic species, the samples was held at room temperature.

Prior to the UHV experiments, PTCDA was cleaned from unwanted fragments by gradient sublimation. After bakeout, all molecular species were degassed at a temperature slightly below the sublimation temperature of the molecules for several hours until the base pressure in the preparation chamber was hardly effected by the operation of the molecular evaporators. This way, unwanted contaminations and fragments of the molecules were removed.

---

[1] Estimating a size of $1cm^2$ for the sputtered area, this corresponds to a current density of about $30\mu A/cm^2$

Part IV

RESULTS AND DISCUSSION

6

GENERAL REMARKS AND DEFINITIONS

In the following chapters, the results of STM-LE experiments on different systems will be presented and discussed. In order to facilitate the determination of the respective discussed quantities, this chapter introduces general terms that will be used throughout this thesis. Further, some general experimental details will be given.

6.1 OVERALL PHOTON YIELD, NORMALIZED DI/DV-SPECTRA, AND RELATIVE Z-DISPLACEMENT

6.1.1 *Overall Photon Yield*

To measure the intensity of the emitted light simultaneously to STM-imaging and spectroscopy, an avalanche photodiode (APD), sensitive to wavelengths between $400\mathrm{nm}$ and $1060\mathrm{nm}$, i.e. photon energies of $3.10\mathrm{eV}$ to $1.17\mathrm{eV}$, was used. This quantity will be referred to as the *overall photon yield*, the *emission yield* or the *(overall) emission intensity*. The photon detection efficiency of the APD is about 5% at $400\mathrm{nm}$, 65% at $650\mathrm{nm}$, 45% at $830\mathrm{nm}$, and 2% at $1060\mathrm{nm}$ [61]. The collection efficiency of the setup is in the order of 10^{-4}.

The integration time per pixel during the STM imaging and photon mapping was usually approx. $2-5\mathrm{ms}$ per pixel. For the spectroscopic measurements, the integration times per pixel were usually around $10-30\mathrm{ms}$.

6.1.2 *Normalized dI/dV-Spectra*

The imaging as well as the spectroscopic measurements were performed at constant current. This way, the rate of incident electrons was kept constant.

To yield dI/dV-data comparable to conventionally gathered constant distance STS, the data was normalized by multiplying with the bias voltage V (see chapter 2.5.1). In the labeling of graphs, the dI/dV·V-signal will be referred to as the *normalized dI/dV-signal*. In the description and discussion of the data, the dI/dV·V-signal is usually referred to as plainly the dI/dV-signal for simplicity.

6.1.3 *Relative z-Displacement*

During the spectroscopic measurements, the *relative z-displacement of the tip*, i.e. the change in the tip-sample distance, versus the applied bias voltage was recorded as an additional data channel.

Note, that the recorded value is a relative z-displacement of the tip. The absolute value of the z-displacement of the tip (i.e. the voltage applied to the piezo crystal) may change in the course of the experiment. Slow changes in the absolute z-displacement of the tip may e.g. be caused by drift effects. Further, if e.g. the sample is mounted slightly tilted, a change in the lateral position of the tip above the sample yields a different z-displacement, etc..

To compare between according curves of relative movement of the tip, the absolute positions of the z-displacement curves were aligned to coincide at their starting points. This was done despite of changes in the LDOS, e.g. tunneling above a molecular layer instead of the bare substrate or tip changes, which may result in different absolute tip-sample distances, i.e. different absolute values of the electric field strength in the tip-sample junction.

6.2 SPECTRA OF THE EMITTED LIGHT

Integration times for the *spectra of the emitted light*, also referred to as *emission spectra*, were usually in the order of $5\mathrm{min}$.

During the data acquisition, an automatic cosmic ray removal was applied to the data[1]. Remaining erratic spikes in the data that were falsely not removed by the software were removed manually. Dark spectra were subtracted manually from the gathered data.

To correct for random jumps in the background intensity caused by the automated signal processing by the detection software, when comparing spectra of the emitted light in the following chapters, the spectra were manually aligned to overlap for photon energies larger than the respective quantum cutoff energy, i.e. the tunneling energy eV_{Bias}.

6.3 MISCELLANEOUS

The base pressure during the experiments was better than $5 \cdot 10^{-10}\mathrm{mbar}$. LEED data was gathered at room temperature. STM experiments were performed while both, the sample and the entire scanning unit including the tip were held at 80K. All given bias voltages refer to voltages applied to the sample.

Since mostly not needed for the discussion of the data presented here, both, the overall photon yield and the spectra of the emitted light, were not corrected for the respective detector efficiencies except stated otherwise.

---

[1] Cosmic ray hits on the CCD detector may lead to an excessive creation of electron hole pairs in individual pixels. This leads to erratic spikes in the data. These false signals were identified and automatically removed by an algorithm provided by the Winspec Software [186].

7

STM-INDUCED LIGHT EMISSION ON NOBLE METALS: AG(111)

As a first archetype system for our newly built setup, we revisited the (111)-oriented surface of silver (Ag) [25, 192]. Due to their characteristic dielectric functions, noble metals may support strong plasmonic modes [30]. The dielectric function of silver (Ag) exhibits an especially low imaginary component. The resulting low internal damping bares the potential for high count rates, especially when both, the tip and sample are made from Ag.

The presented data will serve as first examples to discuss the general light emission characteristics from the tunnel junction of an STM. Especially, the role of the tip and the effect of archetype organic molecules adsorbed on the surface will be addressed. The presented experiments were also part of the master thesis by Ebru Özen [193].

7.1 LATERAL DISTRIBUTION OF THE EXCITATION EFFICIENCY

First, we want to concentrate on the lateral distribution of the excitation efficiency, i.e. the overall photon yield, induced on the Ag(111)-surface.

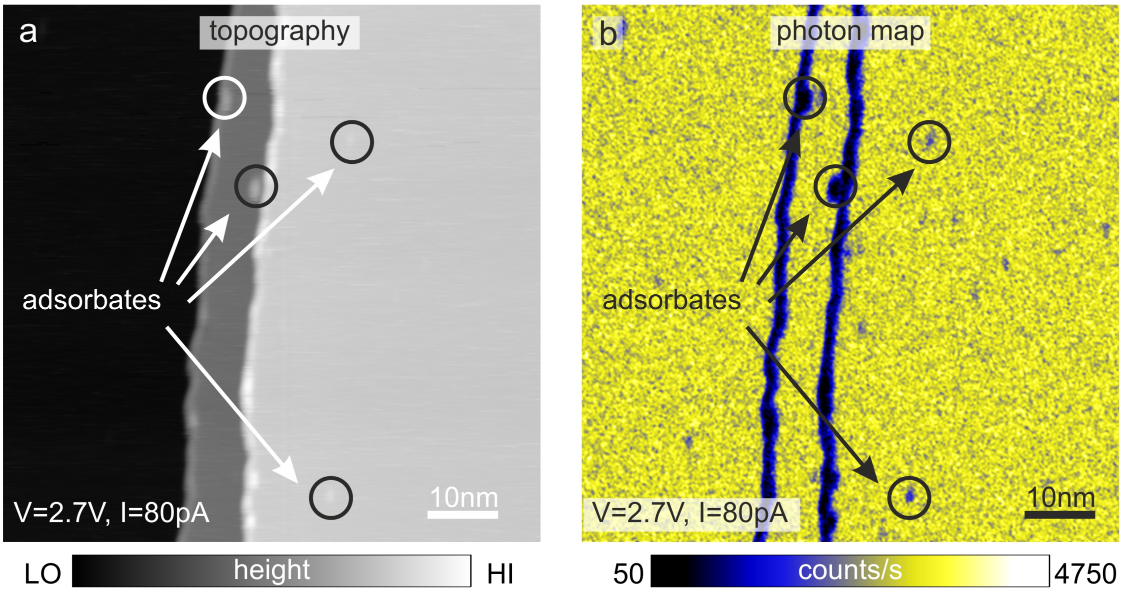

Figure 34: Overview of the lateral distribution of the overall photon yield induced on the Ag(111) surface. a) Topography, and b) simultaneously acquired photon map. Two step edges run vertically through the imaged area. The circles exemplary indicate adsorbates which appear as protrusions in the topography. The count rates given on the intensity scale were corrected for the dark count rate. $V_{sample} = 2.7V$, $I = 80pA$, $T = 80K$.

Fig. 34 a shows the topography of a representative Ag(111) surface area. The imaged area exhibits two step edges running vertically through Fig. 34.

Fig. 34 b shows the corresponding photon map. For the given bias voltage of 2.7V, the overall photon yield induced on the Ag-terraces is laterally uniform and equally high on each terrace. However, some small spots with a reduced emission intensity can be found on the terraces. The positions of the reduced photon count correspond to the postions of surface defects, e.g. adsorbates which appear as protrusions in the topography. Some of these adsorbates are examplary indicated in Fig. 34. Even more pronounced is the drop in the emission yield at the step edges. Also for other positive bias voltages, the emission yield was generally reduced at the Ag(111) step edges.

Step edges are archetype examples for one dimensional surface defects. To further examine the effect of Ag(111) step edges on the emission yield, photon maps were gathered for a set of different positive and negative bias voltages (see Fig. 35).

During the recording of the topographies and photon maps shown in Fig. 35, the bias voltage was ramped from −4V to 4V. With changing bias voltage, small changes in the appearance of the step edges in the topography can be observed (Fig. 35 a and c). E.g. at positive bias voltage, a small bump arises on the respective upper terraces of the step edges. This bump could originate from a rise in the LDOS due to an edge state, as it was e.g. reported for Cu(111) [25, 194].

For the photon maps (Fig. 35 b and d), the influence of the changing bias voltage is quite strong. Most obviously, the photon count rate induced on the Ag(111)-terraces at positive bias voltages is significantly higher than at negative bias voltages. However, additionally, also the contrast evoked by the surface defects in the photon map changes considerably when changing the bias voltage. This is most obvious for the step edges.

At large negative bias voltages, the contrast between step edges and terraces is rather low (see Fig. 35 b and d). The emission yield is slightly enhanced at the step edges until at smaller negative bias voltages than about −3V, the emission yield starts to exhibit a slight drop at the position of the step edges. At positive bias voltage, the relative drop of the light emission intensity at step edges is even larger. In consequence, the resulting contrast between the step edges and the Ag(111) terraces is substantially more pronounced for positive bias voltage.

Bias voltages from −1.2V to 1.2V were exempt from the imaging, since the these tunneling energies are not sufficient to induce detectable light emission[1].

At the positions of the surface defects, the feedback loop has to actively react to changes in the topographic structure and chemical nature (LDOS)of the surface. Here, an overshooting or a too slow adjustment of the feedback loop may cause artifacts in the photon maps due to fluctuations of the tunneling current. To rule out artifacts from the feedback loop, the topographies and photon maps were acquired in both, forward and backward scanning direction. Fig. 35 a and b were recorded in forward scanning direction (left to right), while 35 c and d were acquired in backward scanning direction (right to left). In both cases, the emission yield shows the same behavior at the step edges. Thus, we may faithfully exclude artifacts from the feedback loop as possible the cause of the observed contrasts in the photon maps.

---

[1] Photons with a corresponding energy, i.e. 1.2eV or below, are out of the detactable energy range for the used APD.

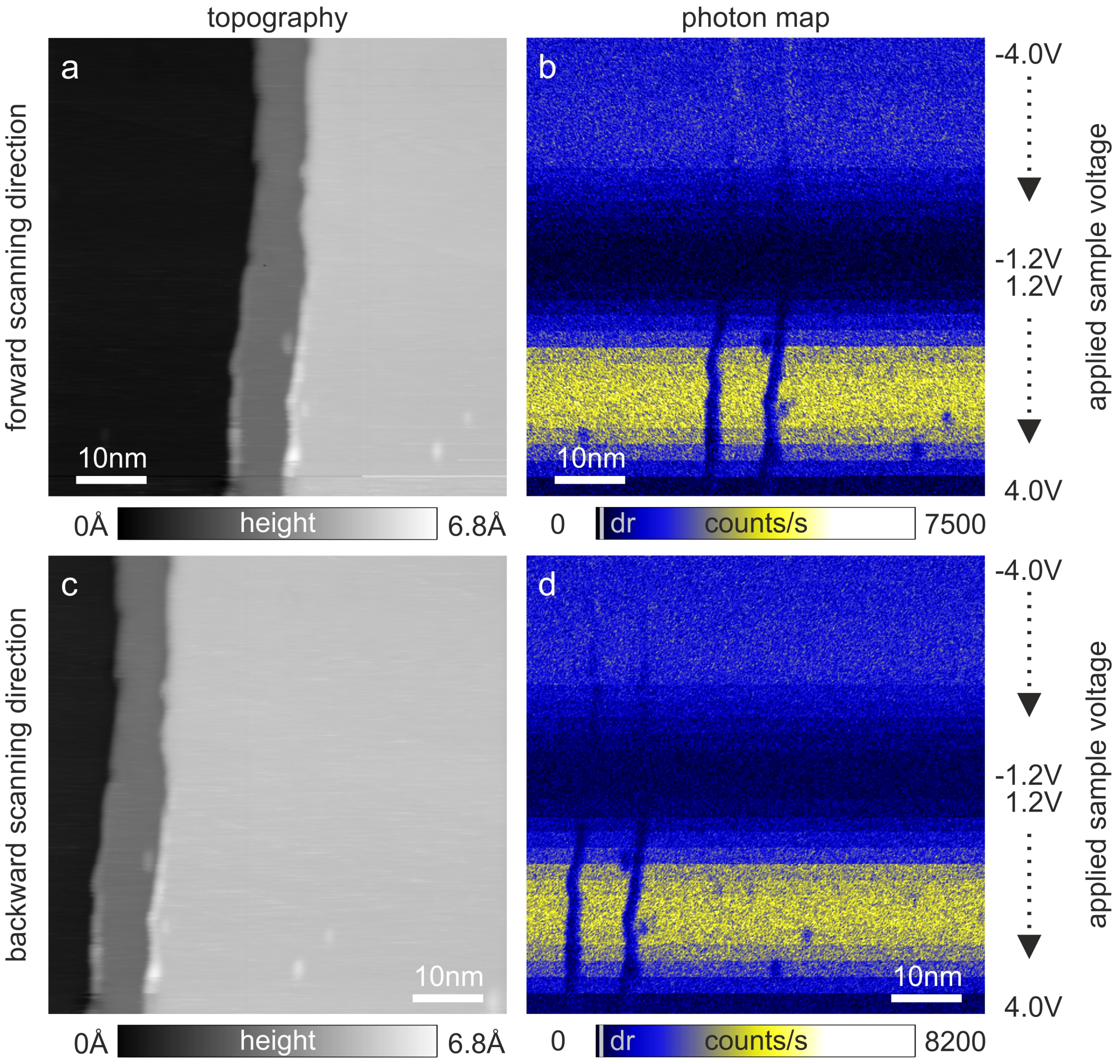

Figure 35: Tunneling energy resolved surface scan of a Ag(111)-surface exhibiting two step edges. During the scan, the applied sample voltage was ramped from $-4V$ to $4V$ in steps of $0.2V$. a) Topography and b) simultaneously acquired photon map in forward scanning direction (left to right). c) Topography and d) simultaneously acquired photon map in backward scanning direction (right to left). Vertical lines on the intensity scales of the photon maps indicate the dark count rate (dr). Bias voltages between $-1.2V$ and $1.2V$ were exempt from the imaging, since the these tunneling energies are not sufficient to induce light emission within the detectable range. $I = 80pA$, $T = 80K$.

7.2 BIAS VOLTAGE DEPENDENCY OF THE EXCITATION EFFIENCY

Even more precisely than with the help of photon maps, the bias voltage dependency of the emission yield can be examined by recording spectra of the overall photon yield simultaneously to regular dI/dV-spectroscopy.

7.2.1 *Spectra of the Overall Photon Yield on Terraces*

Exemplary spectroscopic data acquired on a Ag(111) terrace for positive and negative bias voltage are shown in Fig. 36. The range of $\pm 0.1V$ around the Fermi energy was excluded in order to prevent tip-sample collisions as the spectroscopy was performed at constant tunneling current.

Fig. 36 a shows dI/dV-data. Below 3V, the dI/dV-spectrum at positive sample voltage (probing the LDOS of empty sample states), exhibits a relatively flat progression with a slight increase towards the Fermi energy. This increase can be assigned to the Ag(111) surface state. The surface state onset lies in the excluded bias voltage range at $\approx -65meV$ [195]. At a bias voltage of approx. $+3.7V$, the LDOS exhibits a steep increase.

The overall photon yield (Fig. 36 b) at positive bias polarity exhibits an onset at about $+1.3V$. The spectrum shows a distinct single peaked structure. Maximum emission intensity occurs around 3.1V. A rapid drop of the light emission intensity occurs simultaneously to the steep rise of the LDOS. The rise of the LDOS may be correlated to the onset of the upper sp-band of the surface projected electronic band structure of Ag(111) [196]. The increasing LDOS leads to a steep retraction of the tip from the sample starting around 4V (see Fig. 36 c).

At negative bias, the LDOS exhibits larger variations. Here, the progression of the overall photon yield throughout the examined voltage range is flatter than at positive bias voltage. However, the values of the dI/dV-signal, i.e. the LDOS, are generally higher at negative bias voltage comparing the LDOS at equal absolute values of the bias voltage of opposite sign up to around $\pm 3.7V$.

The steeper increase of the integrated LDOS at negative bias polarity leads to a stronger retraction of the tip within equally large bias voltage ranges at positive and negative bias polarity. The difference Δz_{rel} between the relative tip retraction in the bias voltage range from $-0.1V$ to $-3V$ and $0.1V$ to $3V$, respectively, is indicated in Fig. 36 c.

The the overall photon yield induced at negative bias voltage has an onset at about $-1.25V$. The maximum induced photon yield in the examined voltage range is around three times smaller compared to the peak intensity at positive bias polarity. A first maximum occurs around $-3V$. The subsequent drop of the emission intensity is followed by a second rise towards more negative bias voltages starting around $-4.5V$.

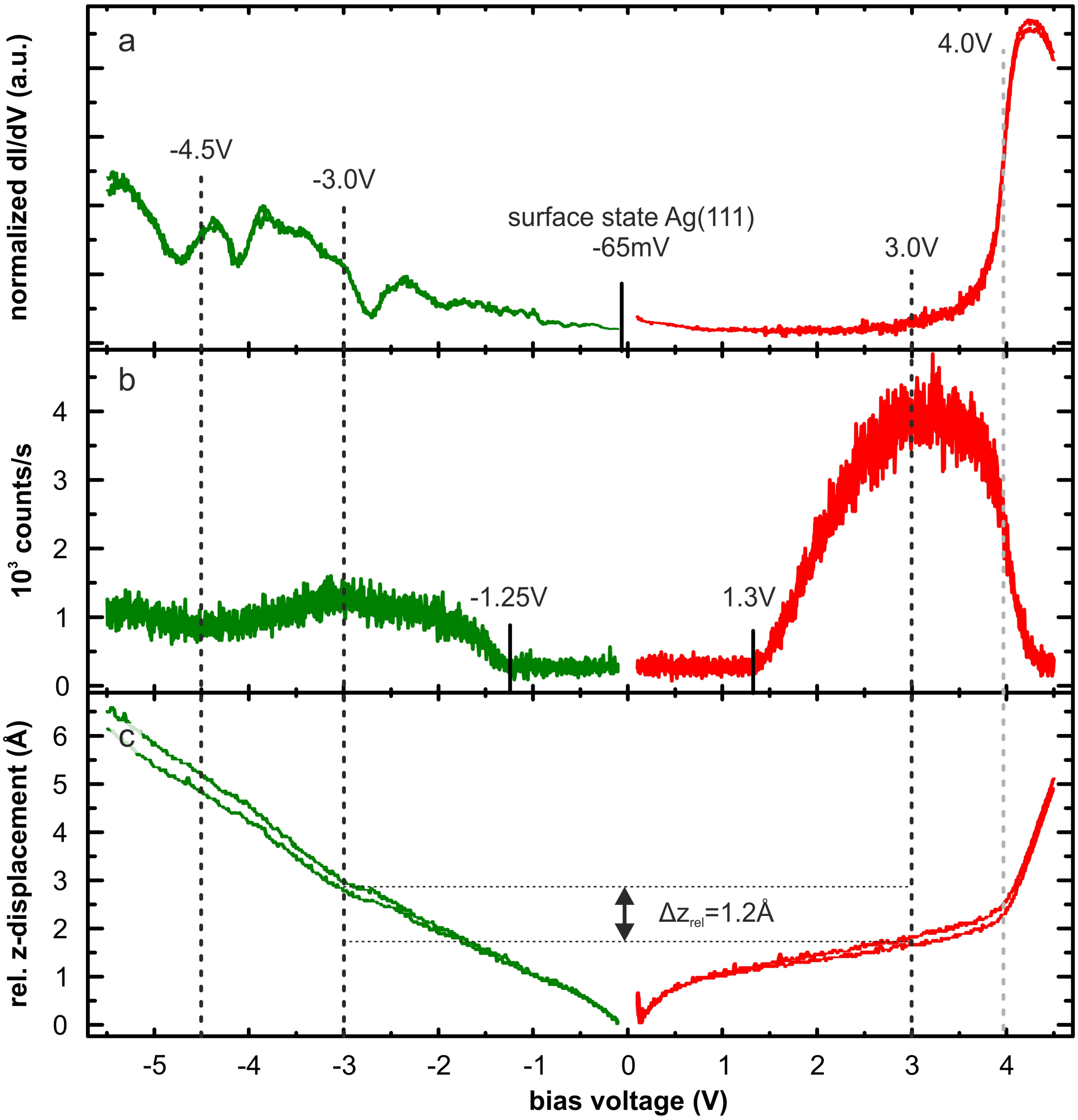

Figure 36: Set of spectroscopic data for positive and negative bias voltages on a Ag(111) terrace. a) Normalized dI/dV-data, b) simultaneously acquired spectra of the overall photon yield, and c) relative z-displacement of the tip during the recording of the spectra. The bias voltage range of ±0.1V around the Fermi energy was excluded in order to prevent tip sample collisions. $I = 80pA$, slope: $0.2V/s$, $T = 80K$, 800 points.

7.2.2 *Spectra of the Overall Photon Yield at Step Edges*

Fig. 37 shows a series of dI/dV-spectra along with simultaneously acquired spectra of the overall photon yield. The positions at which the spectra were taken were approaching a Ag(111) step edge. Due to rather unstable tunneling conditions, the spectra were smoothed in order to obtain easily comparable data.

Approaching the step edge, changes in the LDOS (Fig. 37 a) along with a reduction of the peak intensity in the spectra of the overall photon yield (Fig. 37 b) can be observed. For bias voltages from roughly 0.75V to about 3.7V, the LDOS probed close to the step edges is larger than that on the Ag(111)-terraces. This is in good agreement with e.g. the findings made in dI/dV-maps (not shown), where an increased LDOS is found at the step edges for several positive tunneling energies. It further corresponds to the bump observed in the topographies shown in Fig. 35, that also points to an elevated LDOS at the step edge in the according energy range.

All spectra of the overall photon yield (Fig. 37 b) exhibit roughly the same onset. However, the subsequent rise of the overall photon yield with increasing energy is much steeper when the light emission is induced on the terrace as compared to positions close to the step edge. In accordance to the findings for the energy resolved photon maps presented in Fig. 35, the overall photon yield induced close to the step edges is always lower than on the terraces.

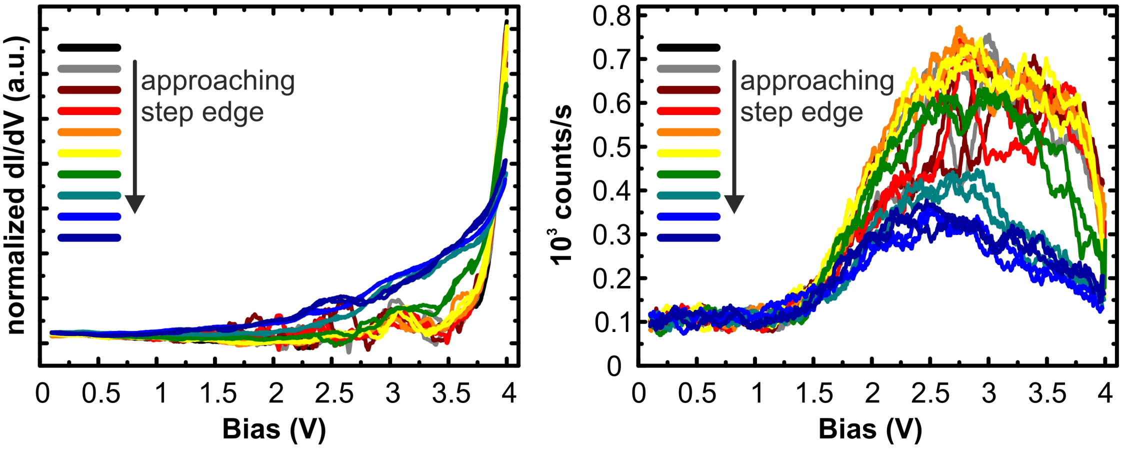

Figure 37: Series of spectra taken at positions approaching a Ag(111) step edge. a) Normalized dI/dV-spectra and b) simultaneously acquired spectra of the overall photon yield. I = 80pA, 0.2V/s, T = 80K, 800 points. The data were smoothed using a 30 point moving average smooth.

7.2.3 *Spectral Distribution of the Emitted Light*

A further characteristic of the light emission induced on a surface is the spectrum of emitted photons. For a comprehensive data set, a bias voltage resolved study was conducted.

7.2.3.1 *Spectra of the Emitted Light at Positive Sample Bias*

A series of spectra of the emitted light, recorded for different positive sample voltages ranging from 1.4V to 3.5V, is displayed in Fig. 38. The graphs were vertically offset for clarity.

The applied bias voltage V defines a quantum cutoff energy $h\nu_{max} \leqslant eV$ for the emitted photons. Here, $h\nu$ is the energy of the photons, e is the elementary charge and V is the bias voltage. The respective cutoff energies for each spectrum are indicated by vertical lines.

A tunneling bias of 1V is not sufficient to induce photon emission in the depicted energy range. The depicted spectrum recorded at this tunneling energy serves as an example for the dark rate fluctuations in the spectra. In the following spectra, starting as a bias voltage of 1.4V, the intensity is already elevated at the low energy edge of the depicted range so that no clear low-energy onset for the spectra can be observed. For bias voltages up to 1.8V, the detected photon energies are almost uniformly distributed from the low energy edge to the respective cutoff energies. At higher tunneling energies, additionally, a peak evolves in the spectra, which extends from photon energies around 1.75eV (700nm) and to around 2.25eV (550nm). A second, significantly smaller peak can be found around 2.5eV (500nm).

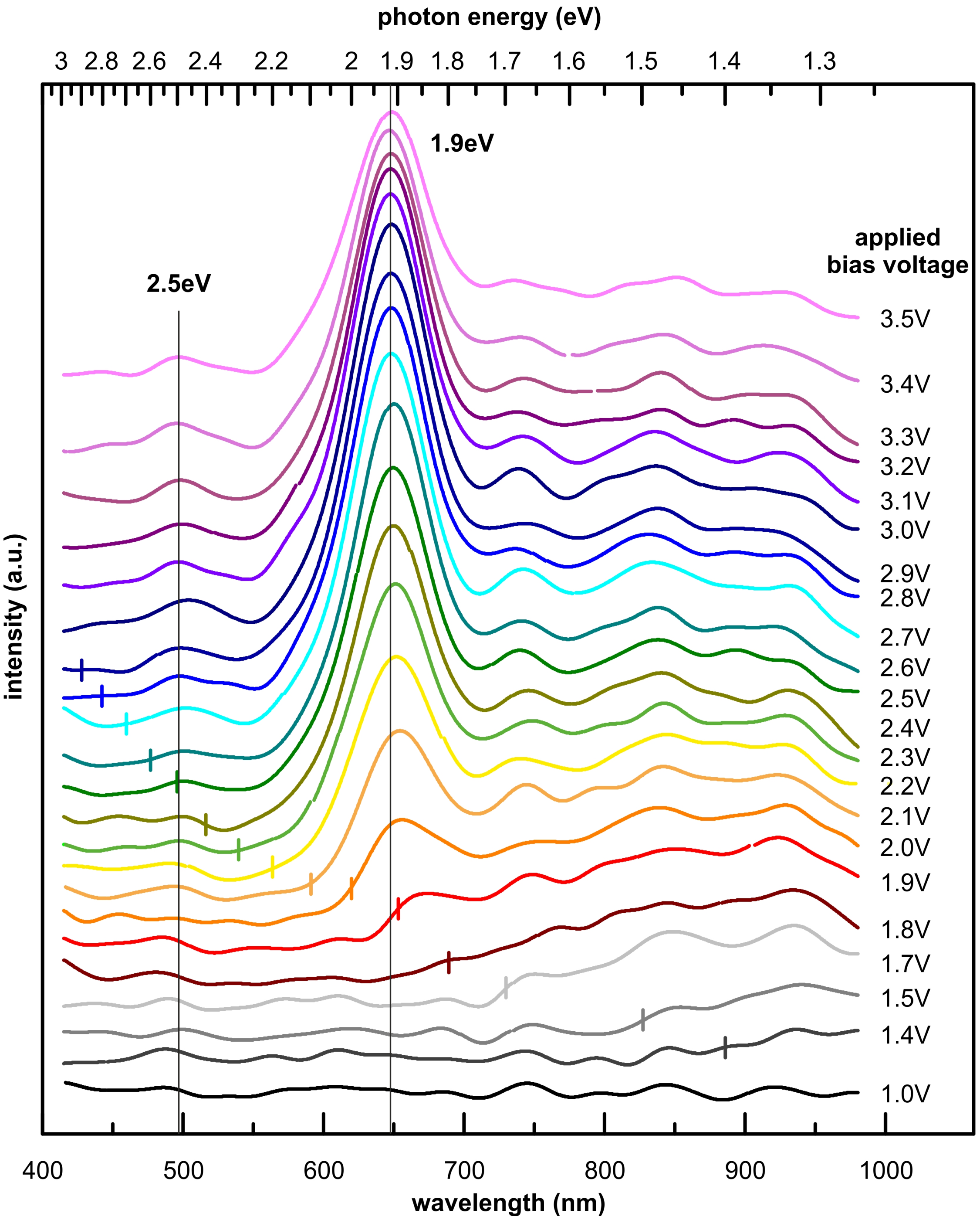

Figure 38: Series of spectra of the emitted light recorded while tunneling above a Ag(111)-terrace at different applied bias voltages in between 1V and 3.5V. The graphs were vertically offset for clarity. Vertical lines in the individual spectra mark the respective quantum cutoff eV_{Bias}. The spectrum at 1V bias voltage serves as an example for variations in the dark count rate. Please note that the spectra of the emitted light shown here were acquired with a different tip than the spectroscopic data shown in Fig. 36. For spectra of the overall photon yield recorded with the same tip, refer to Fig. 41. I = 80pA, acquisition time t = 300s, T = 80K, 1340 points. The spectra were smoothed using a 40 point FFT-smooth.

7.2.3.2 *Spectra of the Emitted Light at Negative Sample Bias*

Now, we want to compare spectra of emitted light recorded for the same positive and negative sample bias. Fig. 39 shows spectra of the emitted light acquired at bias voltages ±3V. The spectra were acquired with a different microscopic tip than the spectra shown in Fig. 38. The different tip yields a significantly different spectrum of the emitted light (see section 7.3). In this case a peaking of the light intensity for photon energies around 1.4eV is observed.

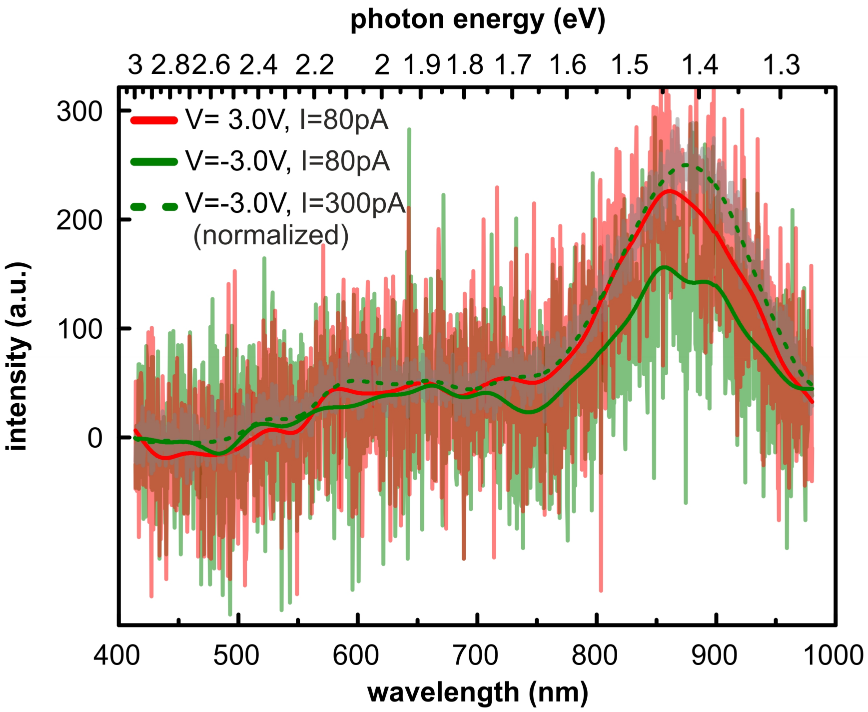

Figure 39: Comparison of spectra of emitted light acquired for positive and negative bias voltage, respectively. The green dashed spectrum was normalized to account for the higher tunneling current. V = ±3V, I = 80pA (solid green and red spectra), I = 300pA (dashed green spectrum), acquisition time = 300s, T = 80K, 1340 points. The spectra were smoothed using a 40 point FFT-smooth. The respective raw data is shown in transparent colors.

The green spectra were acquired at −3V. The solid green spectrum was recorded with a tunneling current of 80pA. Here, the intensity peak around 1.4eV appears split. However, the split appearance may merely be the result of the high noise level in the tunneling junction. Comparing this spectrum to a normalized[2] smoothed spectrum acquired at 300pA at a later point in time, the peak does not appear split any more (dashed green line). The difference in the spectral shapes may be assigned to e.g. a mild tip change, which also affected the emission intensity, i.e. the peak height. Such mild tip changes happened quite frequently at negative bias, due to the generally more unstable tunneling conditions.

The red spectrum was recorded at +3V. The spectral shape shows large coincidence to the spectra acquired at negative bias voltage. The spectra exhibit no significant differ-

---

[2] The spectrum was normalized for the higher set current.

ences that may clearly be assigned to the different bias polarities at which the spectra were recorded.

7.3 THE EFFECT OF TIP CHANGES

Even though the emission spectra presented in Fig. 38 and Fig. 39 were both recorded with the same macroscopic Ag covered Pt/Ir-tip above a Ag(111) surface, the emission spectra shown in both figures are significantly different.

The light emission characteristics induced in an STM-LE experiment, sensitively depend on the used tunneling tip. When talking about a different tip in this context, this does not necessarily mean that a different macroscopic tip was used. Here, we rather refer to microscopic changes of the tip on the nanometer or Ångstrøm scale. Such microtip changes were observed at several occasions in the course of the STM-LE experiments on the Ag(111)-surface presented here.

7.3.1 *Tip Changes through Tip Preparation*

Tip changes that are particularly invasive to the microscopic tip geometry are e.g. evoked by an intentional *in situ* preparation of the tip. During the latter, the tip is e.g. indented into a noble metal surface, here Ag, and subsequently formed by field emission at parameters of a few hundred V and several ten μA for some minutes up to several hours. *In situ* tip preparation was performed quite regularly, e.g. to recover the light emission intensity of the tip-sample system after an unwanted tip-sample collision.

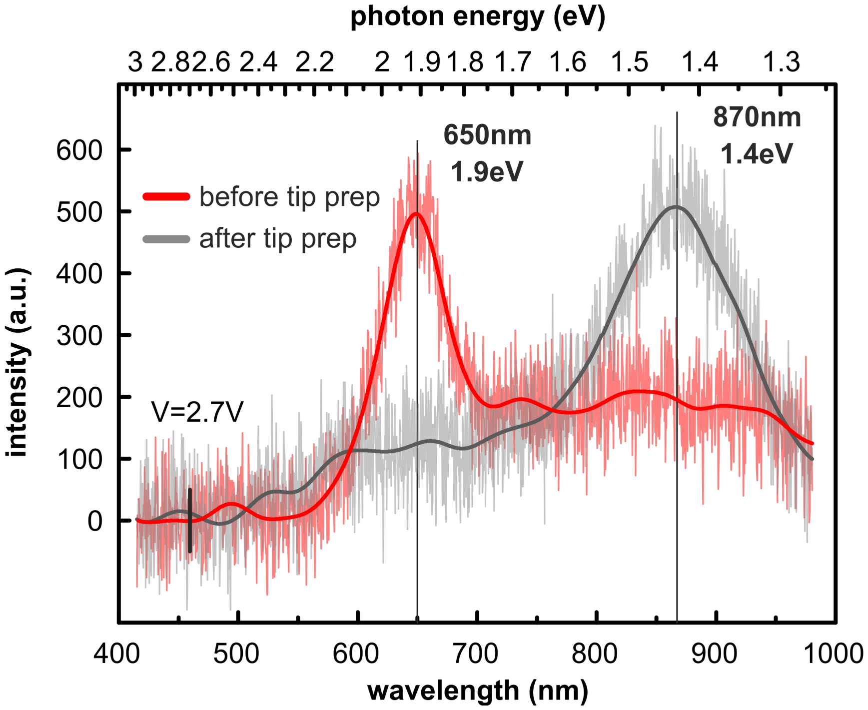

Figure 40: Comparison of spectra of the emitted light recorded before (red) and after (gray) the *in situ* preparation of the tip by indentation into a Ag-sample and subsequent field emission. Both spectra were acquired at equivalent tunneling parameters. $V = 2.7V$, $I = 80pA$, acquisition time $t = 300s$, $T = 80K$.

7.3.1.1 *Effects on the Spectra of Emitted Light*

A tip preparation as described above generally widely effected the light emission characteristics. In fact, the change in emission spectra between the spectra presented in Fig. 38 and Fig. 39 were evoked by an *in situ* tip preparation by field emission. The applied parameters in this case were 12μA at 140V for approximately 90 minutes.

Fig. 40 shows spectra of the emitted light recorded at the same tunneling parameters (2.7V, 80pA) before and after the tip preparation. Both spectra exhibit completely different spectral shapes and photon energies of maximum light intensity.

7.3.1.2 *Effects on the Overall Photon Yield*

Also the spectra of the overall photon yield are significantly affected by such a significant tip change. Fig. 41 depicts the spectroscopic changes in the dI/dV-data and the overall photon yield evoked by the tip preparation.

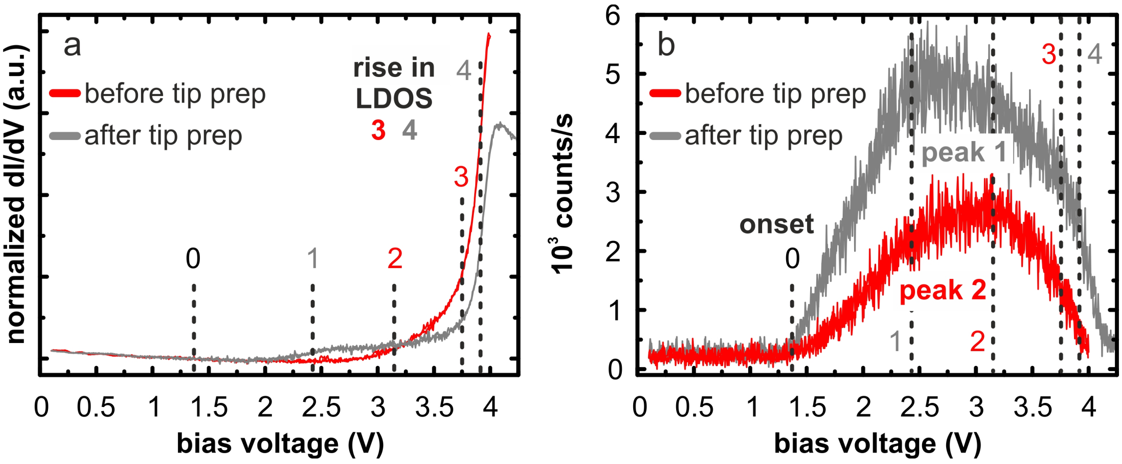

Figure 41: Spectroscopic data recorded with the same macroscopic tip, before (red) and after (gray) the *in situ* preparation of the tip by indentation into a Ag-sample and subsequent field emission. a) Normalized dI/dV-spectra and b) corresponding spectra of the overall photon yield. I = 80pA, 0.2V/s, T = 80K, 800 points.

Slight changes can be observed in the dI/dV-spectra (Fig. 41 a) for bias voltages higher than 2.0V. Most obvious, however, are the slightly different energetic positions for the steep increase of the LDOS which govern the retraction of the tip from the sample at constant current (labeled "3" and "4"). After the tip preparation the increase of the LDOS lies at a slightly higher bias voltage.

The changes in the spectroscopic characteristics of the overall photon yield (Fig. 41 b) are more significant. While the onsets of both spectra roughly coincide at around 1.3V (position "0"), the spectrum acquired after the tip preparation exhibits a considerably steeper increase of the light emission intensity. The shape of the spectra of the overall photon yield differs significantly for both microscopic tips. The overall photon yield induced after the tip preparation is generally higher. Also, the peaking of the spectra occurs at significantly different bias voltages, i.e. 2.4V vs. 3.2V (positions "1" and "2").

In particular for the gray spectrum of the overall photon yield after the tip preparation, a sudden drop of the light emission intensity can be observed simultaneously to the steep increase of the LDOS around 3.9V.

7.3.2 *Random Tip Changes during the Experiment*

Also during an STM-experiment, the tip may unintentionally change, e.g. by picking up an adsorbate or by the rearrangement or falling off of a front atom. Especially when performing spectroscopic measurements, i.e. when the bias voltage is ramped and the tip sample distance is lowered at small bias voltages, the probability for such tip changes rises. Also during regular STM imaging, such tip changes that lightly influenced the light emission intensity are observed. Sometimes the effect may be even quite drastic, i.e. the count rate almost vanishes or may be drastically increased. However, extreme tip changes are usually only observed for unstable tips or if mobile adsorbates are present on the sample surface.

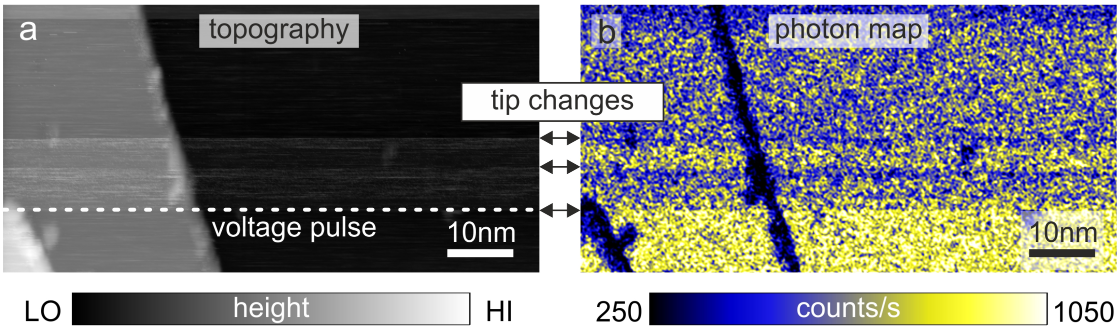

Figure 42: a) Topography and b) corresponding photon map illustrating the effects of tip changes which happen randomly during the scanning of the surface. The positions of the tip changes are indicated by arrows. The last indicated tip change was evoked by a purposely applied voltage pulse which stabilized the tip. The count rates given on the intensity scale were corrected for the dark count rate. $V = 3.0V$, $I = 80pA$, $T = 80K$.

Fig. 42 shows a topography and the simultaneously acquired photon map of the Ag(111)-surface. Here, the surface scan exhibits some disturbances probably resulting from changes of the tunneling tip and associated instabilities in the tunneling conditions. These appear as horizontal lines and a noisy segment in the topography. At equivalent positions in the photon map, changes in the overall photon yield can be observed. Even though the tunneling tip is stable over wide parts of the experiment, such tip changes may happen, e.g. when performing spectroscopy at negative bias voltage, where the tunneling conditions were significantly less stable than at positive bias voltage.

A voltage pulse that was applied in the bottom third of the images stabilized the tip. Here, e.g. an adsorbate may have been detached.

7.3.2.1 *Spectra of the Emitted Light*

Even though random tip changes during an experiment may significantly influence the overall emission intensity, the spectra of the emitted light are usually only mildly affected. Spectra of the emitted light recorded along with the series of spectra displayed in Fig. 44 are shown in Fig. 43. (The chosen colors in Fig. 43 do not reflect any direct affiliation to spectra shown in Fig. 44.)

In contrast to the severe changes in the emission spectra evoked by the field emission of the tip (see Fig. 40), the emission spectra before and after the random tip change during the experiment looked at here only exhibit small variations. For example, the black and the red spectrum show a splitting of the intensity peak around 1.4eV (885nm). The non-split peaks of the green and blue spectrum are slightly shifted with respect to the gray dashed spectrum by roughly 0.02eV. Still, the overall spectral shape is widely conserved.

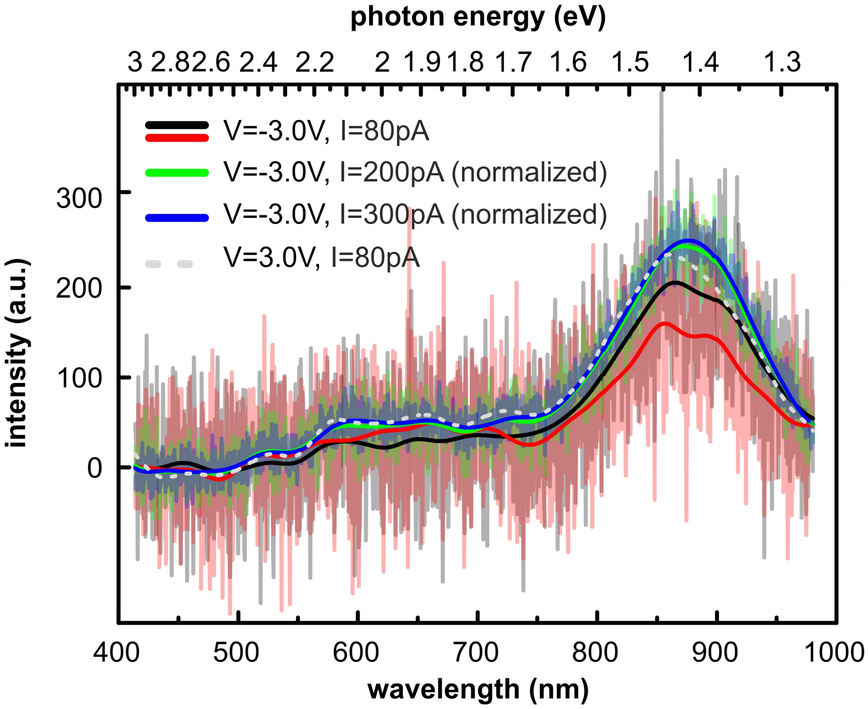

Figure 43: Spectra of the emitted light recorded during one experimental session at the same tunneling energy. The spectra were acquired in between the spectroscopic measurements of the overall photon yield depicted in Fig. 44. For comparison to the spectra acquired at $V = -3V$, a spectrum acquired the same tunneling energy but at positive bias voltage is shown (gray dashed line). $V = -3V$ $I = 80pA, 200pA, 300pA$, acquisition time $t = 300s$, $T = 80K$. The spectra recorded at 200pA and 300pA were normalized to account for the higher current. The data was smoothed using a FFT-smooth. Raw data is shown in transparent colors.

7.3.2.2 *Effects on the Spectra of the Overall Photon Yield*

To further illustrate the effects of such random tip changes on the overall photon yield, several spectra taken above the same Ag-terrace are displayed together in Fig. 44. The spectra were taken in the course of a series of measurements in which the bias voltage polarity was switched back and forth quite regularly. In between the spectra, tunneling was performed at negative bias voltage for longer periods of several minutes. As a result, in particular the dI/dV-spectra exhibit a higher noise level than data acquired with a freshly prepared tip with which most experimental steps until that point were performed while tunneling at positive bias voltage.

Even though the spectroscopic measurements were performed under equal conditions, the dI/dV-spectra exhibit slight differences from each other (see Fig. 44 a). Also the spectra of the overall photon yield exhibit differences. Interestingly, even though the dI/dV-spectra for the red and green curve exhibit differences for tunneling energies below 1.5eV, the spectra of the overall photon yield for both coincide. These curves also show the largest congruence for the relative z-displacement of the STM tip (see Fig. 44 c).

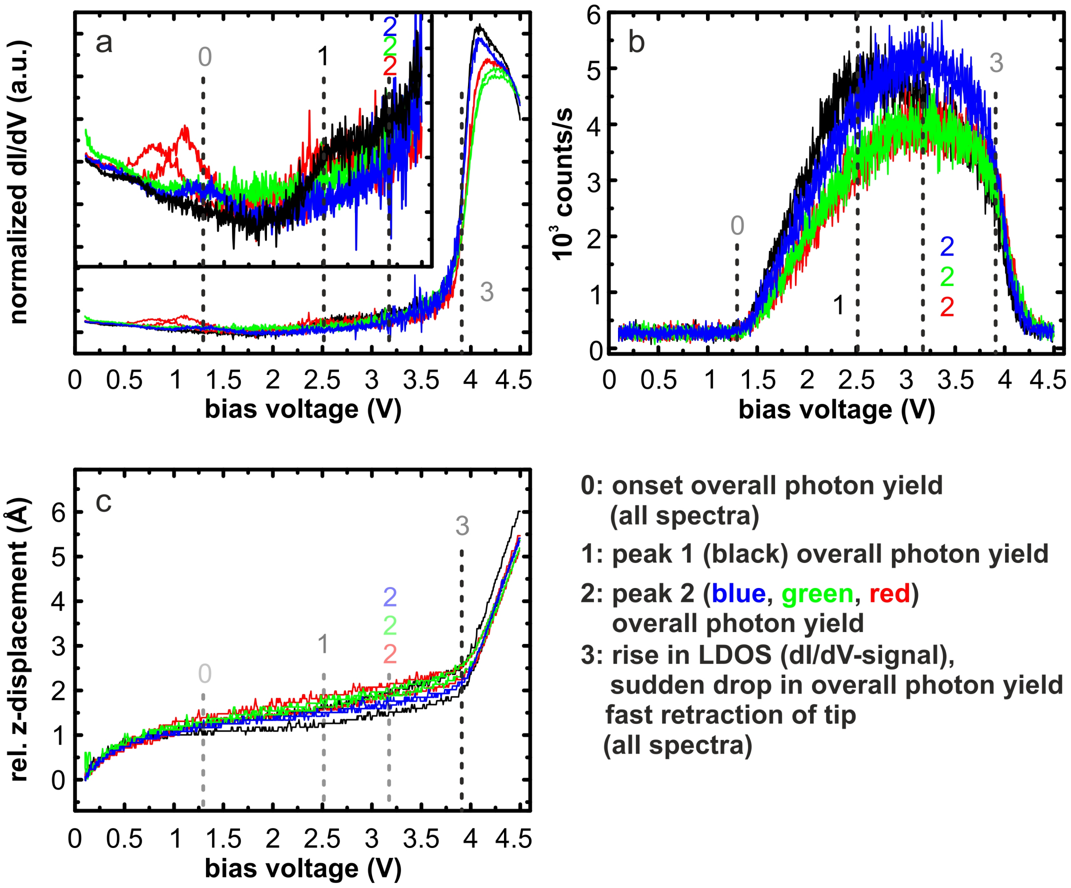

Figure 44: Spectroscopic data recorded with the same macroscopic tip during the same experimental session. a) Normalized dI/dV-signal, the inset shows an enlargement for the bias range from 0 to 3.5V, b) overall photon yield, and c) relative z-displacement of the tip, recorded on the same Ag(111)-terrace. No intentional tip preparation steps were performed in between taking the spectra. I = 80pA, 0.2V/s, T = 80K.

All depicted spectra of the overall photon yield exhibit similar onsets around 1.3V (Fig. 44 b). However, the slopes at which the the photon count increases are slightly different for the different spectra. Also, the bias voltages at which the photon yield peaks vary for the black spectrum and the other spectra, i.e. 2.5V vs. 3.2V. In contrast, the right flanks of all curves, i.e. the rapid decrease of the light emission intensity around 3.7V, coincide. The rapid drop of the light emission intensity cooccurs to the steep increase of the dI/dV-signal. The steeply increasing LDOS induces a sudden retraction of the tip from the sample which can be observed as a kink in the graph of the relative z-displacement (Fig. 44 c).

Depending on the bias voltage at which the light emission is induced, the spectra of the overall photon yield shown in Fig. 44 b exhibit differences in the light emission intensity of up to roughly 40%, e.g. between the green and the black spectrum at 2.5V.

7.3.3 *Drastic Tip Changes during the Experiment*

While the effects of random tip changes presented in Fig. 44 had a considerable effect in particular on the emission intensity, the general shapes of the spectra of the overall photon yield, in particular the number of peaks in the spectra were conserved.

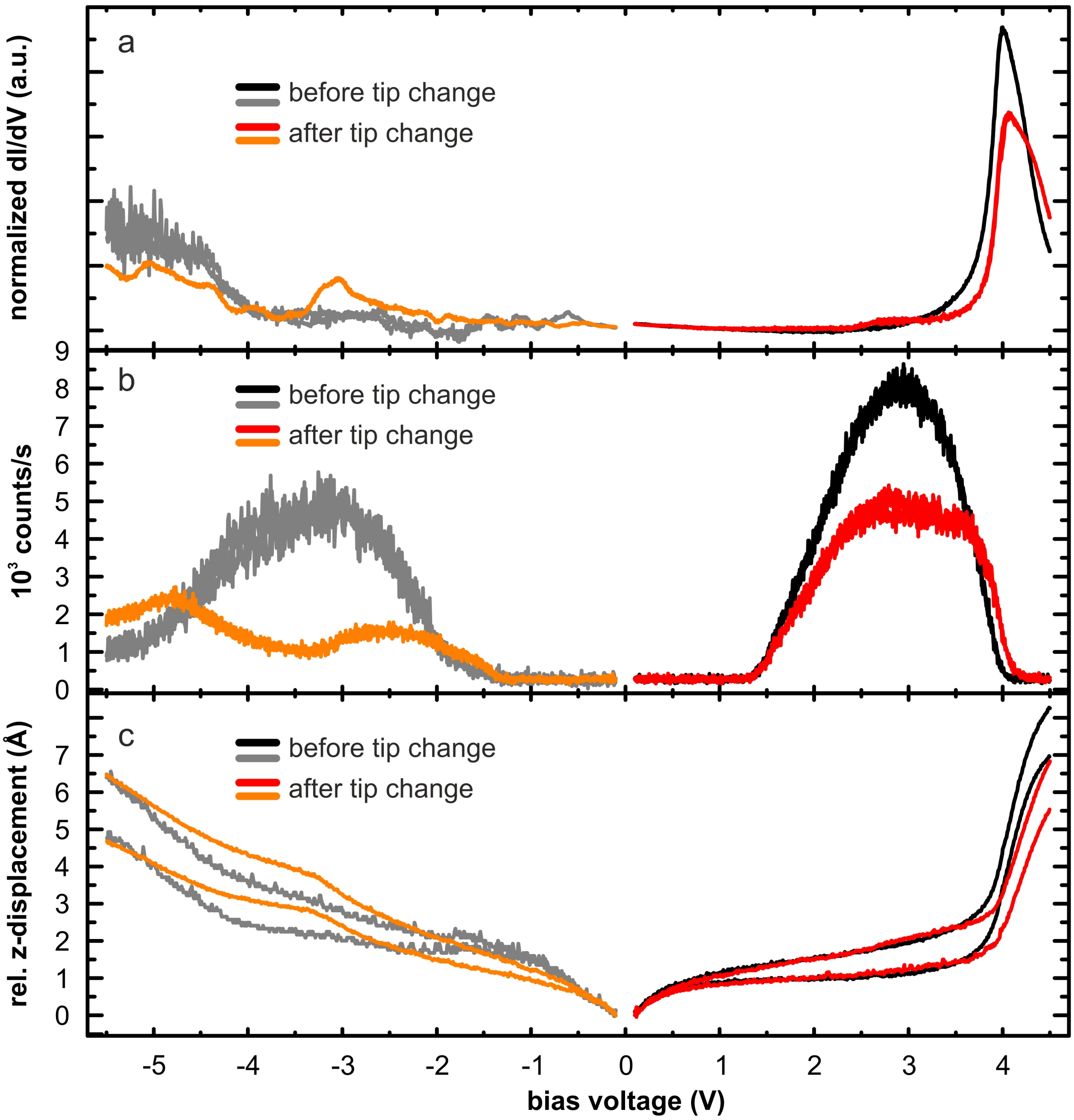

Figure 45: Spectroscopic data for positive and negative bias voltages before and after a severe random tip change. a) Normalized dI/dV-signals, b) simultaneously acquired spectra of the overall photon yield, and c) relative z-displacement of the tip during the recording of the spectra. I = 80pA, 0.2V/s, T = 80K, 800 points.

Fig. 45 exemplary shows the effect of a random tip change with an exceptionally large impact on the spectral shapes of the overall photon yield. The tip change happened during a series of spectroscopic runs performed shortly after the *in situ* preparation of the tip. Here, the tip may still have been unstable promoting an unusually severe random tip change.

Spectra of the normalized dI/dV-signal, the overall photon yield, and the relative z-displacement of the tip, recorded before (black and gray) and after (red and orange) the tip change, are depicted for both bias polarities. The dI/dV-spectrum at positive bias voltage exhibits slight differences in the onset of the rise of the LDOS towards higher tunneling energies. At negative bias voltage, the dI/dV-spectra exhibit significantly larger differences.

The changes in the LDOS result in changes in the tip retraction curves as can be seen in Fig. 45 c.

The spectra of the overall photon yield (Fig. 44 b) exhibit very drastic changes. Both, the maximum overall photon yields as well as the general shapes before and after the tip change differ significantly. For positive bias voltage, both microscopic tips yield a singly peaked spectrum. The maximum overall photon yield is reduced by roughly a factor of two after the tip change. For negative bias voltages, the effect of the microscopic tip change is even larger. The microtip before the tip change yields a single peaked structure, while the spectrum acquired after the tip change exhibits a double peaked structure. Similarly to the situation at positive bias voltage, the maximum photon yield observed at negative is around a factor of two smaller after the tip change.

8

DISCUSSION

Chapter 7 presented exemplary data to analyze general characteristics and correlations between the different measured quantities, e.g. the LDOS, the spectra of emitted light, and the overall photon yield.

The following discussion of our STM-LE results on a well-studied model system serves as a guideline for the interpretation of further STM-LE data. In particular, we want to gain deeper insight into the different contributions of tip and sample properties to the STM-induced light emission.

8.1 THE ROLE OF THE TIP IN STM-LE EXPERIMENTS

The light emission induced on noble metal surfaces like the Ag(111)-surface stems from the radiative decay of collective electronic excitations in the tip-sample junction, so called tip induced plasmons (TIPs), which are excited by inelastically tunneling electrons [25, 27, 91, 92]. The tip acts as a radiating antenna for the emitted light (see Fig. 46 a).

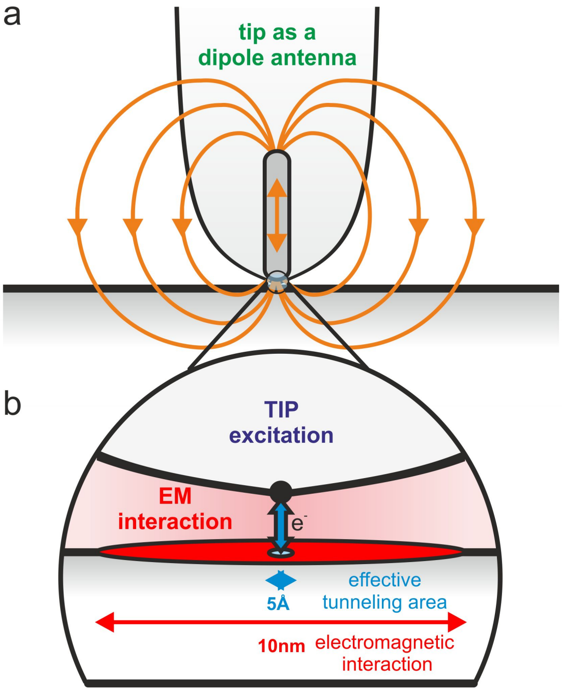

Figure 46: Schematic model of an STM-LE tip-sample junction. a) On a scale of several hundred nm, the tunneling tip acts as radiating dipole antenna. b) The emitted spectrum is defined by the electromagnetic interaction between the tip and the sample on length scales in the order of several nm. The effective tunneling area for the electrons that excite the TIPs is much smaller in the order of some Å.

When considering the intensities and spectra of the emitted light, we have to differenciate between two different length scales. The tunneling current responsible for the TIP-excitation flows through an effective tunneling area at the very front of the tip apex. The size of this area is usually some Å^2. In contrast, the electromagnetic interaction between the tip and the sample happens on a much larger area (see Fig. 46 b), usually a few to some hundred nm^2 [11, 197]. This interaction localizes the charge densities involved in the TIPs. Additionally, the TIP modes experience an electric field enhancement due to the electric field in the junction (see chapter 2.6.2.1).

8.2 SPECTRA OF THE EMITTED LIGHT

The spectrum of TIP modes excited in the particular tip-sample junction is reflected by the spectra of the emitted light. The TIP spectrum depends on the materials and on the geometry of the tunneling junction.

The emission spectra presented in chapter 7 (see e.g. Fig. 38, Fig. 40) exhibit a rather broad intensity-distribution with peaks with a width of some tenths of an eV. Depending on the specific microtip used, the spectra exhibit intensity peaks at different positions.

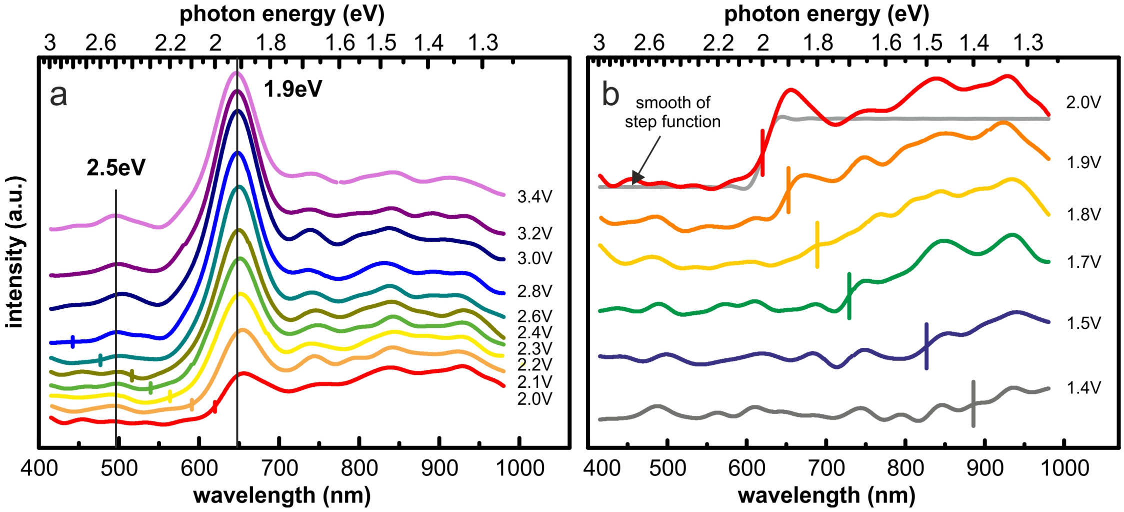

Figure 47: Spectra of the emitted light revisited from Fig. 38. a) Emission spectra acquired for bias voltages between 2.0V and 3.4V. b) Emission spectra acquired at bias voltages between 1.4V and 2.0V. The energy spectrum of the detected photons slightly exceeds the quantum cutoff defined by eV_{Bias} which is indicated by vertical lines. To exclude that the broadening is merely due to the smoothing of the spectra, a step function smoothed with an equivalent smooth as the emission spectra is shown along with the spectrum for a bias voltage of 2V.

Fig. 47 revisits the bias voltage resolved series of spectra of the emitted light shown in Fig. 38. The emission spectra exhibit a prominent intensity peak at photon energies around $1.9eV$ ($650nm$). A second, smaller peak arises around $2.5eV$ ($500nm$).

With rising bias voltage, a slight blueshift of the peaks can be observed (see Fig. 48). Comparing the peak positions of the spectrum taken at 2.0V and the spectrum taken at 3.4V, the peaks shift by around $8nm$ ($30meV$).

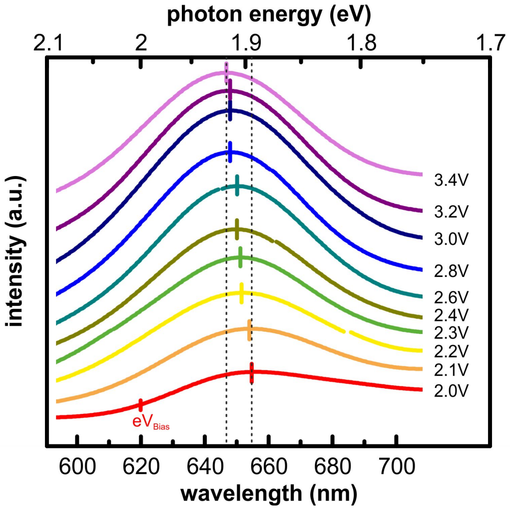

Figure 48: Detail of the series of spectra shown in Fig. 47 for the photon energy range between 1.7eV and 2.1eV. The peaks of the spectra exhibit a small blueshift of around 8nm between the emission spectra taken at 2.0V and 3.4V.

This tendency may be ascribed to a slight increase of the tunneling distance with rising bias voltage which slightly modifies the junction geometry. Here, we observe a retraction of the tip in the order of roughly 1Å when the bias voltage is ramped from 2.0V to 3.5V (see e.g. Fig. 36). For an Au-Au-tunneling junction, changes in the tunneling distance have been shown to shift the TIP-spectrum in the order of a few nm per Å [93]. This roughly corresponds to the shifts observed here. Also the direction of the shift, i.e. a blueshift of the emission spectrum with rising tunneling distance, matches the theoretical predictions and experimental findings reported in literature [93, 198].

In our experiments, we used Ag-coated Pt-Ir-tips. Here we may assume that Ag is a significant part of the tip material governing the TIP spectrum. In fact, the positions of the intensity peaks in our data are similar to those found by Berndt et al. for an Ag tip above a an Ag(111)-surface. Here, the authors observe a large peak at 1.85eV (670nm) and a second, smaller peak at 2.25eV (550nm) [90]. Besides the tip material, the junction geometry strongly influences the TIP-spectrum (see also section 8.3). The strong similarities in emission spectra suggest similar geometries in both experiments.

The rather broad background in our spectra, exemplary indicated for the red spectrum in Fig. 49, may be evoked by the Pt/Ir-trunk of the tunneling tip. Tunneling junctions consisting of an Ir-tip in front of an Ag(111)-surface would be expected to produce a rather broad emission spectrum [55, 56], which is more featureless than that induced by a Ag-tip [56]. Here, influences of both materials, Ag and Pt/Ir, may be reflected in the emission spectra.

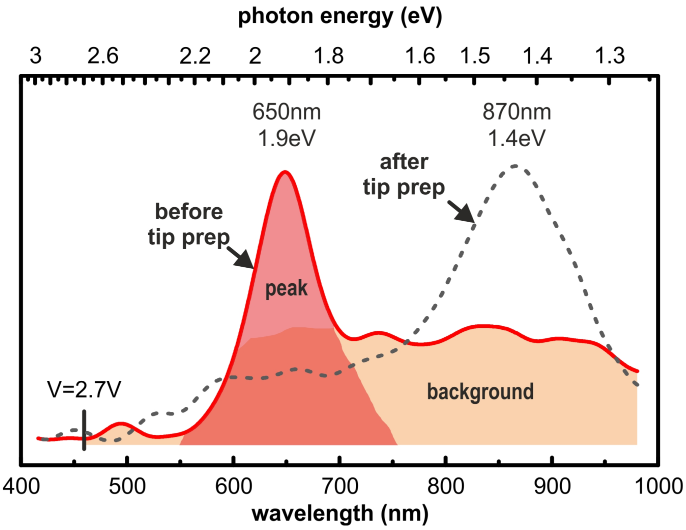

Figure 49: The effects of an *in situ* tip preparation on the emission spectra. Data revisited from Fig. 40. For the emission spectrum before the tip change, the defined intensity peak and the broad background are exemplary indicated. The background may be evoked by the Pt-Ir-trunk of the tunneling tip while the defined peaks would be rather be assigned to the Ag-component of the tip.

8.2.1 *Quantum Cutoff Energies and Natural Linewidth*

The applied bias voltage defines a quantum cutoff energy for the emitted photons. For tunneling currents in the regime up to a few hundred pA as they were used here, we may expect that usually only one electron will be involved in the emittance of a photon [199]. In this case, the quantum cutoff energy for the emitted photons is given by $h\nu_{max} = eV_{Bias}$. However, for higher tunneling currents in the order of $100nA$, also two-electron-photon emission processes have been observed [199–201].

For bias voltages from $1.4V$ to $2.0V$, the spectra of the emitted light presented in Fig. 38 are found to exhibit some faint residual intensity even above the quantum cutoff energy eV_{Bias} (see Fig. 47 b). The emission spectra were acquired at a tunneling current of $80pA$. Even though it cannot generally be excluded, it seems rather improbable that two-electron-photon emission processes play a significant role at such tunneling currents [199]. Also, the emitted light was well focused on the grating spectrograph and the grating was well illuminated. The a broadening of the emission lines due to the experimental setup is much too small to explain the exceedance of the quantum cutoff. Also, the smoothing of the spectra may result in a slight broadening of the emission peaks. Along with the spectrum corresponding to a bias voltage of $2V$, an equivalent smooth of a step function is shown in Fig. 47 b. The broadening of the function due to the smooth is smaller than the exceedance of the quantum cutoff in the emission spectrum.

Rather than the effects mentioned above, the natural linewidth of the emission peaks, may be assumed to play a role here [57]: The lifetime of the TIPs for an Ag-Ag-tunneling junction may be expected to lie in the order of $10fs$ [57]. In terms of Heisenberg's uncertainty principle, this leads to a linewidth in the order of $0.25eV$. This value corresponds nicely to the peakwidth observed in our spectra. The photon energies in our emission spectra exceed the quantum cutoff energy by around 0.05eV which is well within our estimate for the natural linewidth. Therefore, the intrinsic nature of the emission process itself explains the effect observed here.

8.2.2 *Changes in the Emission Spectra*

In literature, it is widely reported that different tips on the same surface may yield significantly different emission spectra. The tip material is crucial for the emission characteristics induced on a surface [56]. However, even for tips that are fabricated from the same material, the emission spectra acquired on the same surface may be completely different [202]. Such differences in the emission characteristics are usually ascribed to different tip geometries. The shape of the tip on a nm-length scale affects the geometry of the tip-sample junction defining the spectrum of available TIP-modes.

In our experiments, we observe a considerable change of the emission spectrum after the *in situ* preparation of the tip (see Fig. 40). During the preparation, the tip was indented into a Ag-crystal followed by the field emission of the tip. The main intensity peak for the resulting new microtip lies to around 1.4eV (870nm). Corresponding emission spectra before and after the tip change recorded at equivalent tunneling parameters are revisited in Fig. 49.

A tip preparation as described above can alter the tip shape on a length scale of several hundred nm. Additionally, since the tip that we used in our experiments was not entirely fabricated from the same material, the tip preparation might have also slightly changed the material composition of the significant part of the tunneling tip.

Both emission spectra, before and after the tip preparation, exhibit a broad background and a defined intensity peak. Probably, the latter was in both cases evoked by the Ag-component of the tip. The significant change in the peak position indicates, that a large part of the changes in the emission spectrum may be assigned to changes in the tip geometry.

8.3 EFFECTS OF THE TIP GEOMETRY

In our data presented in chapter 7.3, the effect of tip changes on the light emission characteristics can be observed. Besides the changes in the characteristic emission spectra after the intentional preparation of the tip discussed in section 8.2.2, changes of the emission intensity without a significant effect on the characteristic emission spectrum are found to happen randomly during the experiment. There are several hints which imply that these changes in the emission intensity are also connected to a geometric change of the tunneling tip. The changes in the emission intensity, e.g. observed during photon mapping (see Fig. 42), are abrupt, i.e. the overall photon yield changes from one scanned line to another, rather than a gradual change of the intensity. Also, the changes in the emission intensity are usually associated with changes in the topographic images, e.g. small changes in the contrast. Such behavior is well known for microscopic tip changes.

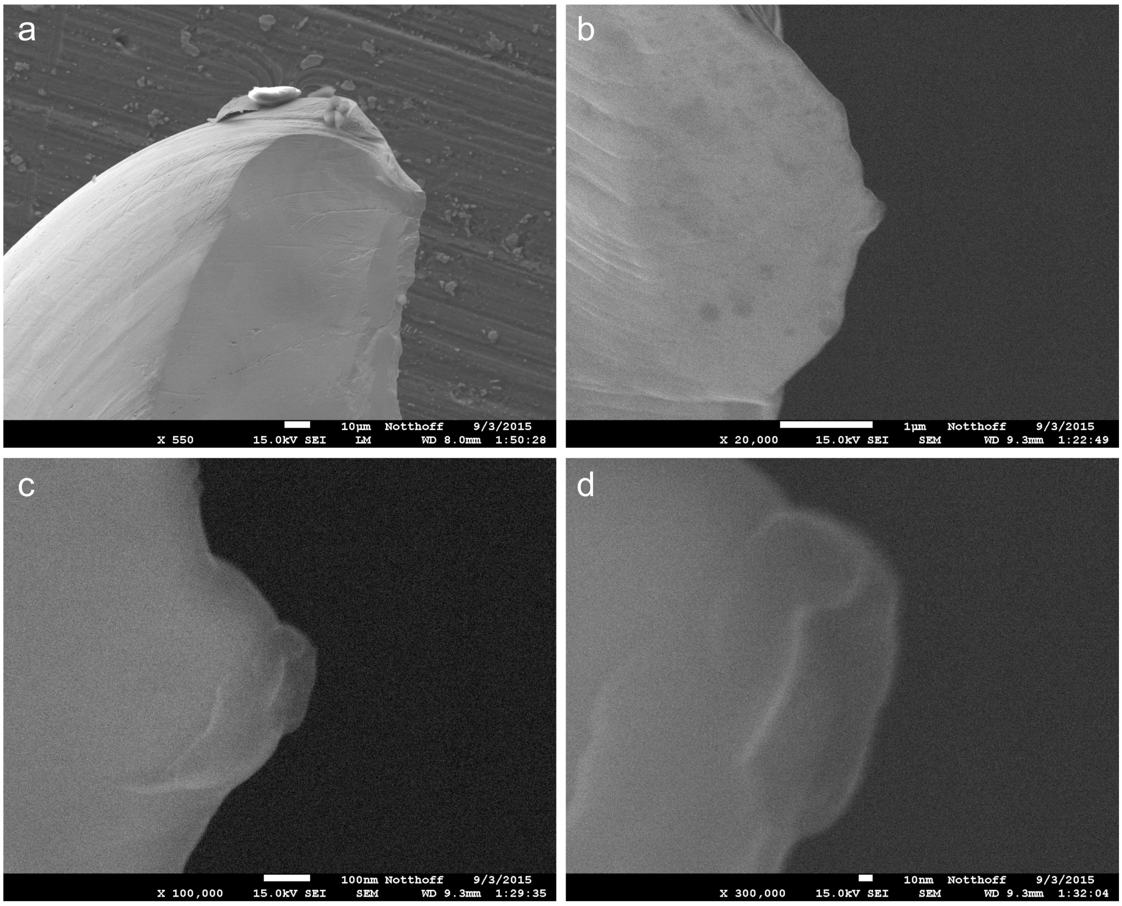

Figure 50: SEM images of a tunneling tip similar to the ones used in the experiments presented here. From a) to d) the magnification is increased. Scale bars have lengths of a) $10\mu m$, b) $1\mu m$, c) $100 nm$, and d) $10 nm$. The SEM data was acquired in collaboration with Christian Notthoff.

The accessibility of the microscopic tip shape is a general problem in STM-LE experiments so that it usually remains unknown. Additionally, the tips used in our experiments probably exhibited a quite irregular shape on a microscopic scale. Fig. 50 shows scanning electron microscopy (SEM) images of a Ag-indented cut Pt/Ir-tip to give an idea of a typical tip shape.

The qualitative influence of the tip geometry on the light emission characteristics has been studied by various authors. One way to learn about the influence of the tip geometry in STM-LE experiments is to conduct experiments with double tips. When imaging the same surface structures with different microapecies of the same tip, the resulting changes in the emission characteristics may be assigned to the tip geometry. Maurel et al. observed significantly different emission spectra for two different microapecies of the same tip [203]. This complemented previous findings with double tips by Hoffmann et al. [204]. Other experiments by Dawson and Boyle showed a correlation between the size of the apecies and the induced emission yield [202].

For etched tunneling tips, the approximate radius of curvature R of the part of the tunneling tips responsible for the electromagnetic interaction may be estimated e.g. by using SEM [197, 202]. Also, in experiments with multi-tips, the relative sizes of the microtip apecies may be estimated from the relative size of the same surface structure imaged in the topography [202]. The latter method may be applied also for cut tips. This way, clear correlations between the tip geometry and the emission spectra could be experimentally verified [197, 202].

In fact, the experiments referred to above relied on model calculations of the emission spectra which were compared to the experimental data. From the early days of STM-LE on, model calculations for the light emission from the tunneling junction of an STM have been applied by a variety of authors [11, 55, 56, 197, 204]. Modifications of the model parameters for the tip geometry within plausible ranges yield shifts and intensity changes in the TIP spectra that qualitatively match experimental observations for different tips [11, 197, 204].

As becomes evident from Fig. 50, realistic tip shapes may be much more complex than the model geometries used in such calculations. Still, having a closer look at the different model geometries used in theoretical considerations may help to better understand the nature of the tip changes observed in the experiments presented here. These will be discussed in the following.

8.4 MODELING OF STM-LE TIP-SAMPLE JUNCTIONS

Two different models for the tip geometry dominate the literature on modeling STM-LE tunneling junctions. In simple considerations, the tip is modeled as a sphere [55, 56, 197]. More sophisticated calculations describe the tip as a hyperboloid [11, 93]. Both models are schematically depicted in Fig. 51.

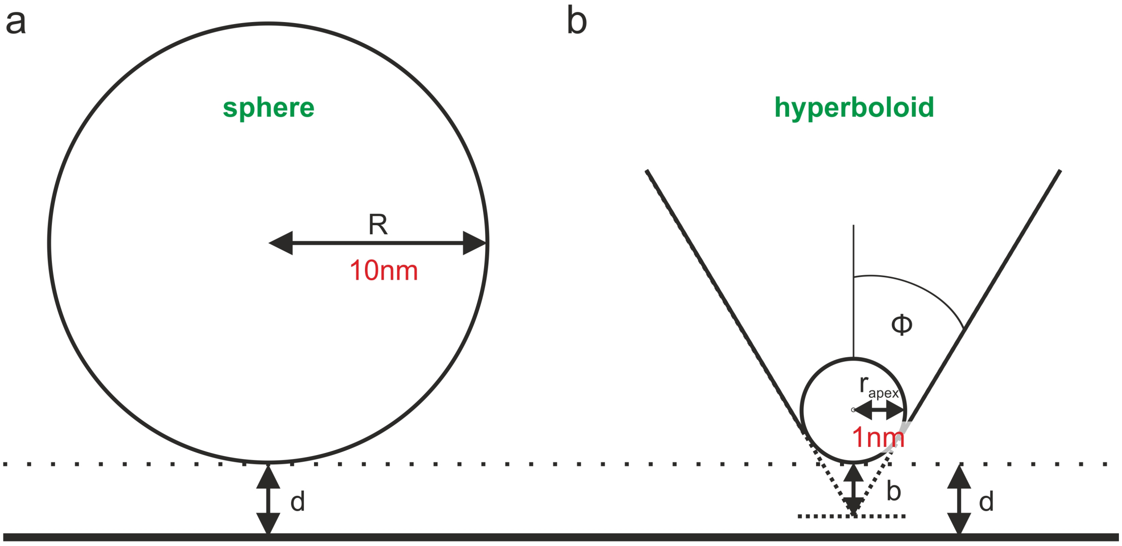

Figure 51: Different models used to calculate STM-LE emission spectra. a) Sphere-plane model, where the variable geometry parameters for the tip are the radius R of the sphere and the tunneling distance d. b) Hyberboloid model, where the variable geometry parameters for the tip are the ratio b/d defining the apex curvature and the aperture angle Φ.

8.4.1 *Modeling of the Tip as a Sphere*

One of the most simple ways of modeling the tunneling junction in an STM is to describe the tip as a sphere in front of a plane. Such a model was e.g. presented in the fundamentals chapter to make some general important statements about the tunneling current in an STM. Also for the calculation of emission spectra obtained in STM-LE experiments, the sphere-plane model has been widely applied [55, 56, 197].

Note, that the radius of curvature R used in these models refers to the part of the tip relevant for the electromagnetic interaction between the tip and the sample. Thus, the radii assumed for the spheres in this case are much larger than the radii considered to calculate the effective tunneling areas (see section 8.1).

Already before the invention of the STM, Rendell and Scalapino used this model to calculate the localized plasmonic modes and associated light emission from tunnel junctions [205, 206]. Changes in the tip radius on a scale of several ten nm have been calculated to considerably shift the TIP spectrum in the order of a few tenths of an eV and further affect the emission intensity [55, 56, 197].

The change of the emission spectra after the tip preparation observed in our experiments may be explained within this model. Changes in the radius of curvature of the tip evoked by indenting the tip into the sample and the subsequent field emission may plausibly lie in the order of several ten nm. However, in calculations with the sphere model, changes in the tip geometry always evoke simultaneous changes in the overall emission intensity and in the peak positions of the emission spectra. This is in contradiction to our findings for random tip changes during the experiment (see chapter 7.3.2). Here, we observe significant changes of the emission intensity while the spectral shape of the emission spectra remains widely unaffected. To understand the effect of these tip changes on the emission characteristics, we need a more elaborate model of the tip geometry.

8.4.2 *Modeling of the Tip as a Hyperboloid*

Such a model for STM-LE junctions was established by Aizpurua et al. [11]. Instead of as a sphere, the authors discribe the tip as a hyperboloid.

In the sphere model, the tip is only characterized by a single parameter, namely the radius R of the sphere. This parameter simultaneously impacts the effective tunneling area as well as the electromagnetic interaction area between the tip and the sample. The hyperboloid model applied by Aizpurua et al. yields the advantage of two different model parameters, the apex curvature and the larger scale aperture angle Φ (see Fig. 51). In their calculations, Aizpurua et al. express the apex curvature through the ratio $\frac{b}{d}$, where d is the tunneling distance and b is the distance from the front of the tip apex to the imaginary end of a perfectly conical tip (see Fig. 51). This allows for dedicated considerations revealing the role of different tip portions for the emission spectra [11].

Figs. 52 and 53 visualize the effect of the changes on different length scales. They show schematics of different tip geometries with different apex curvatures for the same aperture angle (Fig. 52) and different aperture angles (Fig. 53) for the same apex curvature along with emission spectra calculated by Aizpurua et al.. The calculations were conducted for a fixed tunneling distance. The spectra were normalized by the tunneling current [11].

8.4.2.1 *The Role of the Tip Apex*

In the hyperboloid model, the apex curvature mainly has an effect on the electric field enhancement. Tips with sharper apecies provide a larger field enhancement. In consequence, sharp tips yield higher emission intensities due to the larger field enhancement as compared to more blunt tips. Geometric changes of the very tip apex barely influence the localization of the charge densities of the TIPs and only have a weak impact on the spectrum of TIP-modes (see Fig. 52) ([11] all this paragraph).

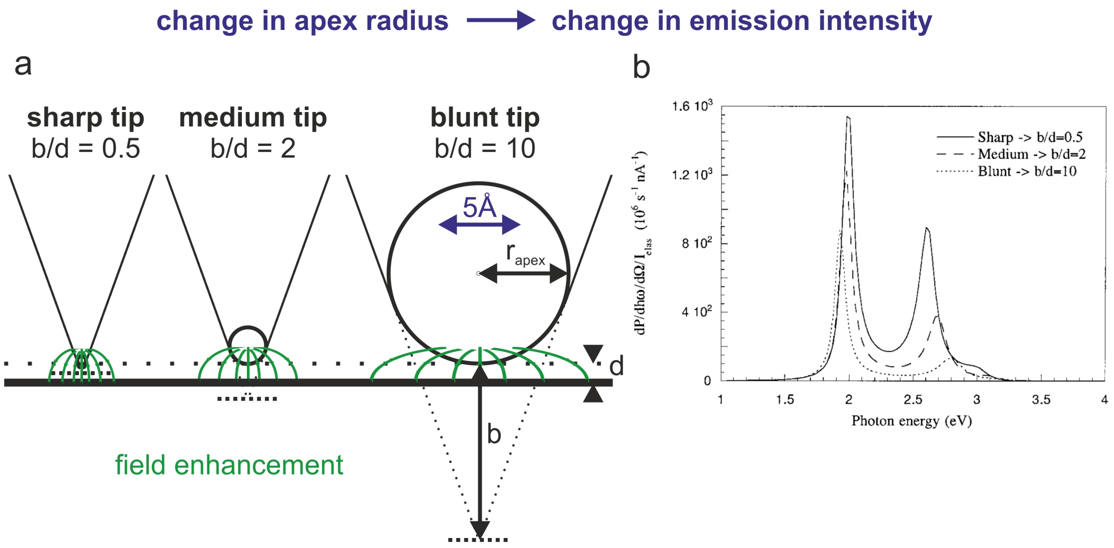

Figure 52: The effect of changes in the apex curvature defined by the parameter b/d at constant tunneling distance. a) Schematics of three tips with different ratios b/d and the same aperture angle. b) Calculated emission spectra for three different Ag tips with different apex curvatures at a given tunneling distance and aperture angle and a Ag sample. (b) Reprinted with permission from [11]. Copyright 2000 by the American Physical Society.

8.4.2.2 *The Role of the Tip Shaft*

The aperture angle of the tip shaft mainly determines the electromagnetic interaction area between the tip and the sample and thus the localization of the involved charge densities. It therefore governs the spectral distribution of the TIP-modes. Calculated emission spectra for different aperture angles at a fixed apex radius and tunneling distance exhibit similar emission intensities (see Fig. 53) ([11] all this paragraph).

The calculations by Aizpurua et al. [11] reveal a further interesting effect of the tip geometry. Depending on the aperture angle of the tip, different surface charges are involved in the TIP modes. For rather sharp tips with aperture angles $< 45°$, the interactions of surface charges of mainly the tip dominate the physics of the TIP modes. For rather blunt tips with aperture angles $> 45°$, the surface charges of both, the tip and the sample contribute.

8.4.3 *Classification of Tip Changes*

The model calculations referred to above were conducted for rotationally symmetric tips. The irregular shape of the tips used in our experiments further prevent a straightforward simple modeling that may yield an accurate calculated emission spectrum. Still, the general findings for the influence of the very tip apex and the larger scale tip shaft are well reproduced in our data. Here, we may classify the tip changes into to kinds:

Random tip changes during the experiment can be assumed to only mildly affect the tip geometry. In particular, they usually only alter the tip apex, e.g. by the rearrangement of one or several frontmost atoms. This may affect the electric field enhancement

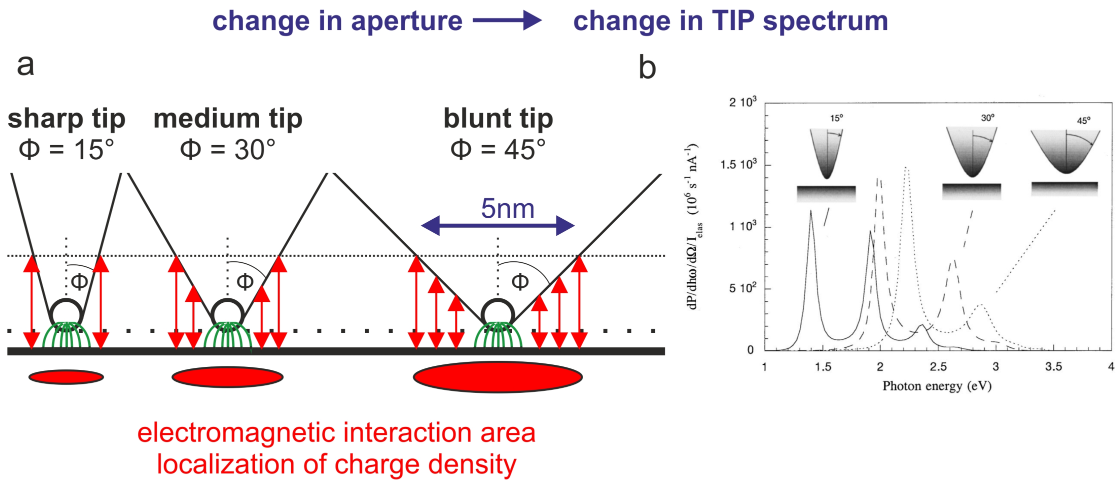

Figure 53: The effect of changes in the aperture angle Φ at constant tunneling distance. a) Schematics of three tips with different aperture angles Φ and the same apex radius. b) Calculated emission spectra for three different Ag tips with different aperture angles at a given tunneling distance and apex curvature and a Ag sample. (b) Reprinted with permission from [11]. Copyright 2000 by the American Physical Society.

but not the localization of the charge densities involved in the TIPs. Consequently, they usually only have impact on the emission intensity, leaving the spectra of the emitted light to a large degree unchanged.

The intentional *in situ* preparation of the tip is rather more invasive to the microscopic tip geometry. Here, it is very probable that the preparation changes the tip geometry on a length scale that well exceeds the few very frontmost atoms, altering the shape of the larger tip shaft and therefore the junction geometry relevant for the spectrum and field enhancement of the TIP-modes. This corresponds very well to the changes in the emission spectra that we observe in our data.

8.5 THE LATERAL EXTENT OF THE ELECTROMAGNETIC INTERACTION

In the fundamentals chapter, estimates for the lateral resolution of an STM were given. These relied on model geometries of the tip sample junction for which the effective tunneling area was approximated. In an STM-LE experiment, it is the electromagnetic interaction between the tip and the sample which defines the emission characteristics. The tip geometry influences the electromagnetic coupling and defines the localization of the involved charge densities. It therefore also defines the lateral extent of the electromagnetic interaction area between the tip and the sample.

The portion of the tunneling tip involved in the electromagnetic interaction is much larger than the portion supporting the tunneling current. In a simple sphere-plane model of the tip-sample junction, the length scale for the electromagnetic interaction can be estimated to $L \approx \sqrt{2Rd}$ [205]. Assuming typical parameters, e.g. a distance d of $1\mathrm{nm}$ and a radius of curvature R in between $10\mathrm{nm}$ and $300\mathrm{nm}$ the electromagnetic interaction happens on length scales of approx. $4-25\mathrm{nm}$. The radius of curvature for the tip characterized by SEM shown in Fig. 50 is approximately 100-150nm which would correspond to a lateral extent of the tip modes on length scales between $14\mathrm{nm}$ and $17\mathrm{nm}$.

More sophisticated calculations for the electric field enhancement factor by Mitra et al. yield lateral interaction areas in the same order of magnitude [197]. Note again that the radii of curvature used to model the tip for the electromagnetic interaction are much larger than the radii of curvature used to estimate the effective tunneling area.

Using a hyperboloid model of the tunneling tip, Aizpurua et al. find values for the lateral spatial extent of the charge densities involved in the plasmonic excitations in the range of magnitude between $2\mathrm{nm}$ to $15\mathrm{nm}$ in particular depending of the aperture angle of the tip [11].

In particular, this is important when discussing the lateral resolution achieved in STM-LE experiments. The topographic images of the Ag(111)-surface presented in chapter 7.1 (e.g. Figs. 34 and 35) depict surface areas which exhibit several step edges and adsorbates. These features are also resolved in the corresponding photon maps.

As a representative example, Fig. 54 a and b show details of the topography and the corresponding photon map of the surface area depicted in Fig. 34. The width of the imaged structures in the topography is approx. $2.5\mathrm{nm}$ (see Fig. 54 c). In the photon maps, the surface defects influence the emission intensity on roughly the same length scale.

The appearance of the structures in STM imaging may be influenced by the tip shape. In particular, structures may appear wider than the actual lateral extent of their LDOS when they are imaged with a large tip apex. Here, the apparent size of the structures in the topography gives us an upper limit for the lateral size of the structures. Although they appear larger in the topography, the adsorbates are probably roughly atomic sized defects, e.g. CO-molecules. This is very small compared to the electromagnetic interaction area between the tip and the sample which would be expected in the order of several hundred nm^2.

To evoke changes in the characteristic spectrum of TIP modes, the properties of the tip-sample junction would have to be modified on a length scale similar to the lateral extend of the involved charge densities. However, the structures that evoke the

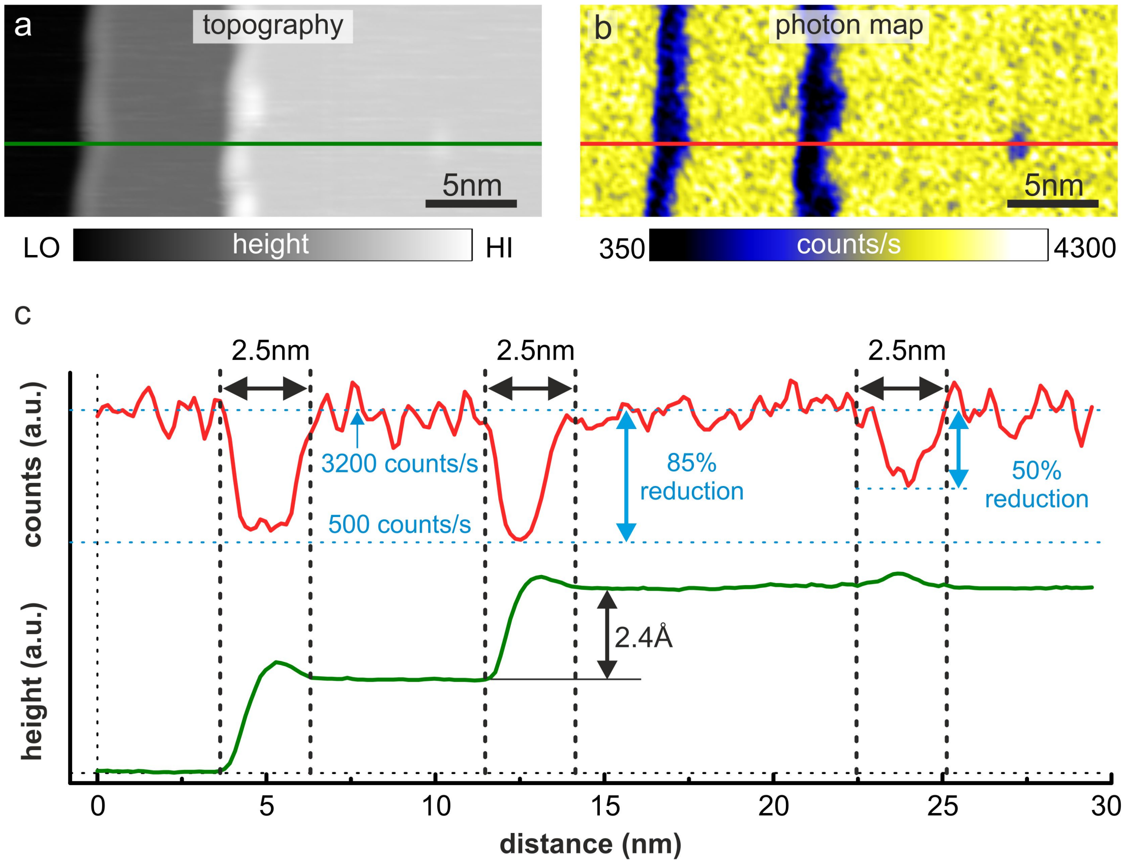

Figure 54: Correlation between the topography and the corresponding photon map at step edges and adsorbates. a) Topography and b) corresponding photon map. The left step edge is partially decorated with adsorbates. Additionally, a singly lying adsorbate on a Ag(111)-terrace can be observed in the right quarter of the imaged area. c) and d) show line profiles through a) and b). $V = 2.7\text{V}$, $I = 80\text{pA}$, $T = 80\text{K}$.

contrasts in the photon maps here are much smaller. Thus, they are not expected to affect the TIP-spectrum significantly. This suggests that to interpret the contrasts in the photon maps, we have to instead concentrate on variations in the excitation efficiency.

8.6 CONTRASTS IN PHOTON MAPPING

A variety of contrast mechanisms has been proposed for the photon maps of metallic surfaces [25, 91, 92, 202, 207, 208].

In our data, the contrasts are evoked by structures with a size much smaller than the lateral extent of the TIP modes (see section 8.5). Thus, in our discussion here, we concentrate on variations in the excitation efficiency of the TIP spectrum.

8.6.1 *Changes in the Direction of the Tunneling Current*

Berndt et al. discussed, if a change in the direction of the tunneling current, i.e. the orientation of the k-vectors of the inelastically tunneling electrons, at surface defects might play a role for the reduced intensity in the photon maps [92].

The excitation of the TIPs is driven by the tunneling current parallel to their dipole moment. When tunneling on a flat surface, the majority of the tunneling electrons usually possesses k-vectors perpendicular to the surface, i.e. along the surface normal.

At adsorbates or step edges, an increased number of tunneling electrons may also contain a nonzero momentum parallel to the surface (see Fig. 55). The orientation of the dipole moment of the TIPs which is governed by much larger scale factors, is maintained. In consequence, a different portion of the tunneling current is oriented parallel to the dipole moment of the TIPs and the effective excitation of the latter may be altered [92].

For the dipole moment of the TIPs oriented normal to the surface as shown in Fig. 55, the fraction of the driving current parallel to it is reduced at step edges. However, the orientation of the dipole moment of the TIPs is defined by the specific tip. In particular for asymmetric tips, it might exhibit a certain angle to the surface normal. Thus, depending on the specific tip, a change in the direction of the tunneling current might also lead to a larger fraction of the driving current oriented parallel to the dipole moment of the TIPs. Thus, also an increase of the TIP excitation efficiency might be evoked by this effect.

The contrast observed in our data depends on the bias polarity (see. e.g. Fig. 35). At negative bias voltage, the contrast in the photon maps, especially for step edges, is significantly reduced. This is not in contradiction to an effect of the orientation of the k-vectors of the tunneling electrons: In addition to geometric factors, the fraction of electrons tunneling with a nonzero momentum parallel to the surface depends on the band structure of the substrate and may therefore be bias dependent [209].

However, the size of the drop in the intensity at step edges and defects at certain bias voltages is considerably large, e.g. approx. 85% at the step edges and 50% at the defect at a bias voltage of 2.7V (see Fig. 54). In a simple geometric consideration, Berndt et al. estimate the fraction of inelastically tunneling electrons, i.e. the TIP excitation efficiency, by $\cos^2\alpha$, where α is the angle between the surface normal and the tip axis [92]. For Cu(111) double steps and the dipole moment of the tip oriented parallel to the surface normal, the authors calculate a reduction of the emission intensity by about 30% at the step edges. While this matches the experimental data that Berndt et al. obtained on the Cu(111)-surface, the effect is much too low to explain the reduction in our case. Thus, we have to consider additional effects that may influence the emission efficiency in our case.

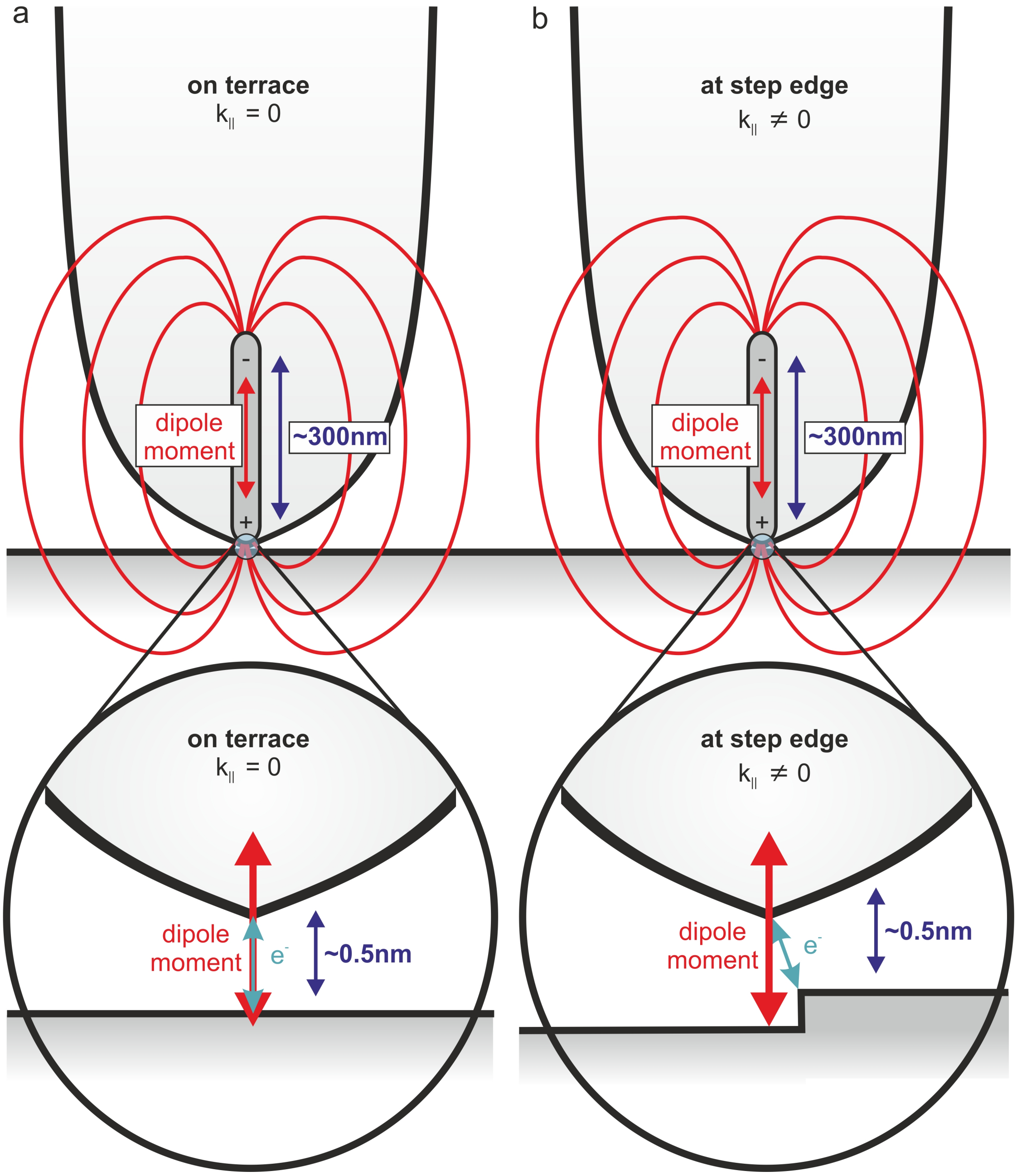

Figure 55: Schematic of the change in the tunneling current direction at step edges. The tip acts as a dipole antenna on a length scale of several hundred nm. a) When the tip is located on a terrace, the k-vectors of the tunneling electrons are oriented along the surface normal direction. When approaching a step edge, electrons may also tunnel with a nonzero momentum parallel to the surface. The orientation of the TIP modes is governed by much larger scale geometries which remains widely unaffected by the presence of the step edge. However, the fraction of the driving inelastic current parallel to the TIP modes changes. This may alter the excitation efficiency and thus the light emission efficiency.

8.6.2 *Changes in the Local Field Enhancement*

The electric field in the tip-sample junction provides a local field enhancement that significantly influences the emission intensity. The strength of the electric field scales with the separation distance s between the electromagnetically interacting parts of the tip and the sample like $1/s$ [192].

The electromagnetic interaction area between the tip and the sample is usually much larger than the effective tunneling area. Thus, the "interaction distance" for the electromagnetic interaction is not the same as the tunneling distance. In particular, it may change even without a change of the tunneling distance, e.g. in the vicinity of a surface defect (see Figs. 56 and 57).

When tunneling above a small protrusion, e.g. the adsorbate in Fig. 54, the "interaction distance" is increased (see Fig. 56). The resulting decrease of the electric field enhancement might cause a reduction of the excitation efficiency.

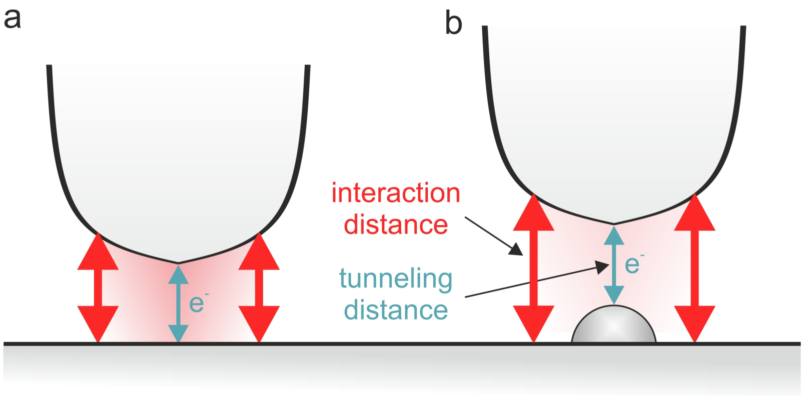

Figure 56: Effect of an adsorbate on the separation distance between electromagnetically interacting parts of the tip and the sample. When tunneling on the terrace (a), the separation between the electromagnetically interacting parts of the tip and the sample is smaller than when tunneling above a defect (b).

A similar contrast mechanism was proposed to be responsible for the resolution of atomic rows in photon maps of the (2×1)-reconstruction on Au(110) [24]. The rows are separated by roughly 8Å with a corrugation of 0.7Å. In this case, the emission rate is increased for the lower trenches between the rows. The authors assigned this effect to the smaller interaction distance when tunneling above the trenches.

For our experiments presented here, the tunneling distance can faithfully be estimated to be well above 4Å [210]. Taking this value for a very conservative estimate for the interaction distance, a change by the apparent height of the adsorbate in Fig. 54 (approx. 0.5Å) may only evoke a reduction of the field enhancement by around 10%. However, the emission intensity in the photon map at the position of the adsorbate studied here is reduced by roughly 50% with respect to the terrace value. Assuming that the field enhancement term enters the the photon emission intensity quadratically [13], a reduction of the emission yield by 20% at the most might be explained. In fact, the larger the interaction distance, the smaller the possible effect on the field enhancement. Thus, the increased tip-sample separation cannot be the only cause of the drop in intensity.

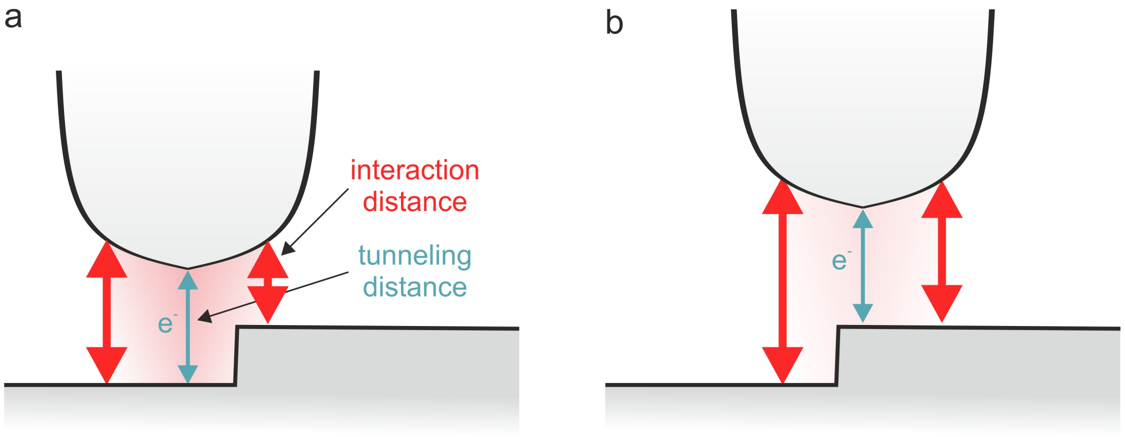

Figure 57: Effect of step edges on the electric field enhancement. a) When the tip is tunneling on the lower terrace close to the step edge, parts of the tip can already electromagnetically interact with the upper terrace at a smaller interaction distance. b) Conversely, when the tip is tunneling close to the step edge on the upper terrace, the interaction distance for parts of the tip is increased.

Further, the emission intensity profile at step edges is not in consistent with a pure effect of an altered field enhancement (see Fig. 54). If only the field enhancement were responsible for the variations in the emission intensity, the emission intensity would be increased when the tip is tunneling close to the step edge on the lower terrace, since at these positions, the interaction distance for parts of the tip is decreased (see Fig. 57 a). Conversely, the increased interaction distance when tunneling close to the step edge on the upper terrace should lead to a reduced intensity (see Fig. 57 b). Consequently, the resulting intensity profile at a certain bias voltage would contain emission intensities that were higher and lower than the terrace values, respectively. This is not what we observe in our data.

In our bias voltage resolved study presented in Fig. 35, with changing bias voltage, we find significant differences in the relative emission intensity on step edges and terraces. Fig. 58 shows details of the corresponding topography and photon map in forward scanning direction focusing on the step edges. The depicted photon maps were normalized by a global intensity profiles from the terraces to obtain "contrast maps" which highlight the relative changes of the emission intensity at the step edges. The remaining variations in the terrace value that occur especially for low bias voltages may be assigned to the increased effect of fluctuations in the close-to-zero count regime. Vertical lines indicate the position of the step edge in the "contrast maps".

Over a wide range of positive bias voltages, a reduction of the photon count is observed at the step edges. The reduction is mainly observed when tunneling near the step edge on the upper terrace. This is in agreement to the assumption of a decreased field enhancement, however, no increase of the emission intensity is observed for the lower terrace. Even though the bumps observed in the topography would correspond to a slightly more increased interaction distance at positive bias voltage, the effect on the field enhancement should be small (see discussion for the point defect above).

Also, there is a very faint increase of the emission intensity observed at large negative bias voltages which also occurs on the upper terrace. In terms of alternations of the field enhancement by the step edges, an increase could be only explained on the lower terrace. Consequently, we have to consider additional contrast mechanisms that may be held responsible for the observed intensity variations.

With rising absolute values of the bias voltage, the tunneling distance is slowly increased (see e.g. Fig. 36). Consequently, the relative change in the interaction distance caused by the step edges becomes smaller. This may monotonically reduce the contrast towards higher absolute values of the bias voltage. However, in our data, e.g. between 1.6V and 2.5V, we observe a clear increase of the contrast (see e.g. Fig. 58). This is not consistent with a dominating role of the field enhancement for the contrast.

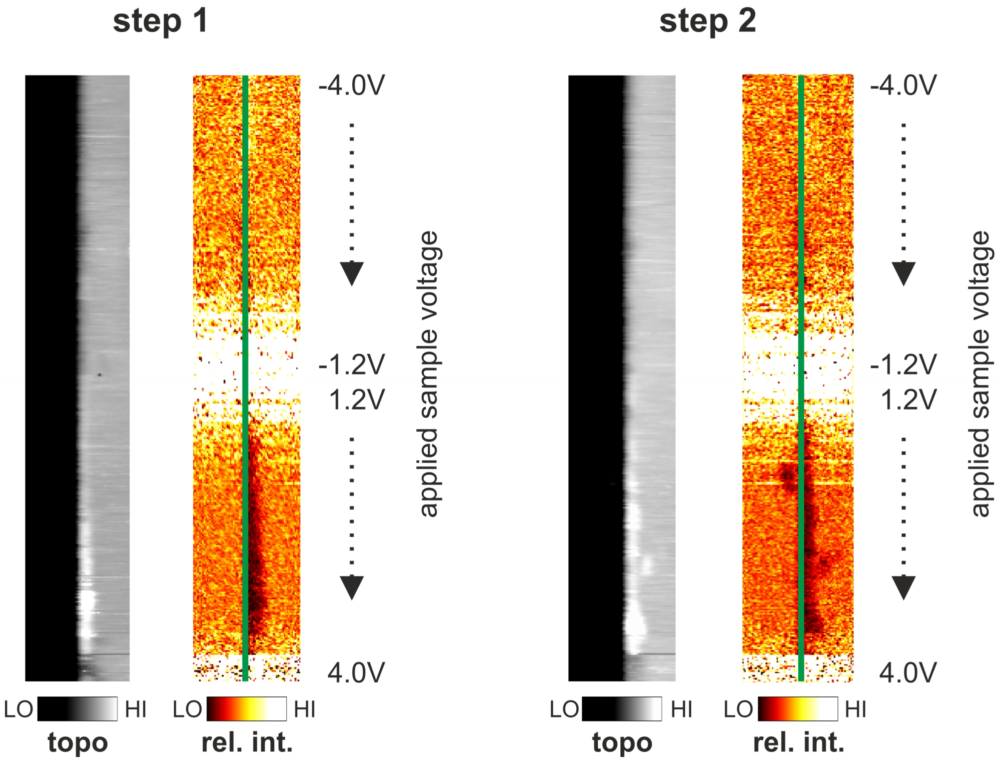

Figure 58: The evolution of the contrast in the photon maps at step edges with the bias voltage. Topography and corresponding "contrast map". The data was extracted from the bias voltage resolved data shown in Fig. 35. To obtain the "contrast map", the photon map was normalized with a global intensity profiles of the terraces. The positions of the step edges in each scanned line were aligned to allow for an easy comparability of the data gathered at different bias voltages.

8.6.3 *Additional Excitation Channels*

As discussed above, the increased emission intensity for step edges at elevated negative bias voltages cannot be explained through differences in the electric field enhancement (section 8.6.2). Instead, a local opening of additional excitation channels may lead to the increase of the emission intensity.

Such an effect was proposed by Uehara et al. to explain the intensity differences observed in photon maps for the atomic structure of the (2×1)-reconstructed Au(110)-surface [208]. The authors acquired spectra of the emitted light on the rows and trenches with atomic scale precision. In their data, the authors observe an additional peak which they claim to be the result of an additional electronic excitation that only occurs when tunneling in the trenches.

However, the authors also mention a clear modification of the surface structure while recording the spectra at elevated bias voltage. Thus, it seems likely that, instead of an additional excitation channel, a tip change may have evoked the changes in the emission spectra. This is further corroborated by later results by Hoffmann et al. who, in a similar experiment on Au(110), do not observe any differences in the shape of the emission spectra for rows or trenches [25]. These authors rather propose that the differences in the emission intensity observed in photon maps are related to a different excitation efficiency of the TIP-modes. They suggest that the lateral distribution of the LDOS results in a branching ratio of elastic and inelastic tunneling channels. This effect may likewise explain both, an increase and decrease of the emission intensity and seems rather more probable than a local additional excitation mechanism also in our case. The effects of local variations in the LDOS on the emission yield will be discussed below.

8.6.4 *Changes in the LDOS*

The role of the LDOS for the inelastic tunneling probability can be better understood when looking at the energy diagram shown in Fig. 59. It schematically illustrates the elastic and inelastic tunneling channels for tunneling at positive and negative sample bias.

At positive sample bias, electrons tunnel from the tip to the sample (Fig. 59 a). Most tunneling electrons are injected with an initial energy close to the Fermi energy of the tip[1]. The elastic portion of the tunneling current tunnels into final states with the same energy as the initial state energy of the electrons in the tip. Thus, the elastic tunneling probability is governed by the LDOS of the sample at this energy $E_{\mathrm{final\,elastic}} = E_{\mathrm{initial}} \approx E_{\mathrm{F,\,tip}} = E_{\mathrm{F,\,sample}} + eV_{\mathrm{Bias}}$, where e is the elementary charge and V_{Bias} is the bias voltage. The elastic part is by far the largest fraction of the overall tunneling current.

The inelastic portion of the tunneling current specifically depends on the availability of final states for the inelastic transitions and thus probes the LDOS of the sample at energies defined by $E_{\mathrm{final\,inelastic}} = E_{\mathrm{initial}} - h\nu$, where $h\nu$ is the energy of the emitted photons, i.e. the energy of the excited TIP modes [92, 192].

Lateral variations of the LDOS, e.g. at surface defects, may result in a changing ratio of the sample LDOS at energies $E_{\mathrm{final\,elastic}}$ and $E_{\mathrm{final\,inelastic}}$ and may thus lead to variations in the fraction of inelastic tunneling events and consequently the emission intensity [92].

Our spectroscopy data presented in Fig. 37 revealed changes in the dI/dV-spectra when approaching a step edge. Here, the dI/dV-spectra gathered on the Ag-terraces exhibit a particularly flat progression. Close to the step edges, the increase of the LDOS with rising bias voltage is significantly steeper. The elevated LDOS may be associated to electronic edge states as e.g. reported for the step edges on Cu(111) [25, 194].

---

[1] The tunneling current depends exponentially on the square root of the barrier height (see fundamentals chapter) yielding a sharp decay of the tunneling probability on the energy scale.

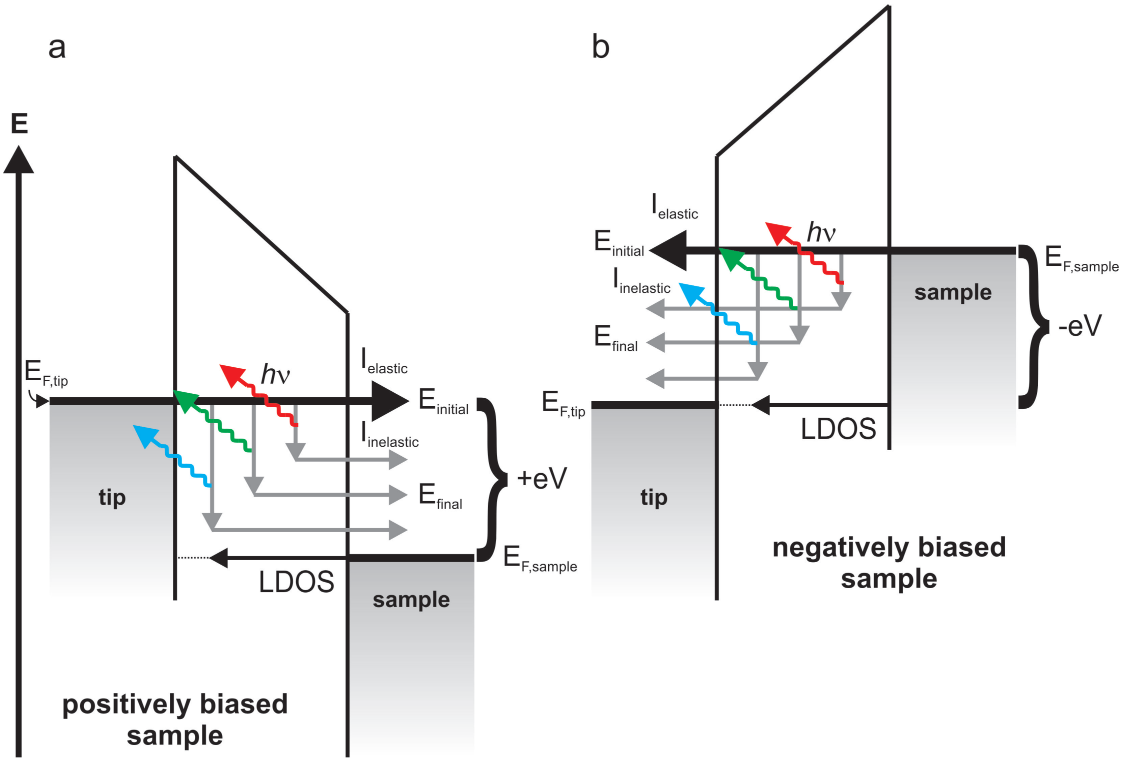

Figure 59: Schematic diagram for the inelastic tunneling processes happening at positive and negative bias polarity. a) Tunneling from the filled states of the tip to the empty states of the sample at positive sample bias and b) tunneling from the filled states of the sample to the empty states of the tip at negative sample bias. For the first case a), the LDOS of the sample provides final states. When tunneling to the tip b), the final states are provided by the LDOS of the tip.

For typical bias voltages which are associated to a strong drop of the emission intensity at step edges, the dI/dV-spectra exhibit a significantly increased LDOS for elastic tunneling close to the step edges. Also the corresponding final state LDOS for inelastic processes is increased for the step edges as compared to the spectrum for the terraces. However, the differences between the parts of the spectra providing the respective final state LDOS for inelastic processes at terraces and close to the step edges are not as drastic.

Here, the step edges provide an increased number of elastic tunneling channels while the number of inelastic tunneling channels as compared to the terraces changes less. In consequence, the fraction of inelastically tunneling electrons is reduced, explaining the reduced emission intensity.

A variation in the fraction of inelastically tunneling electrons is also in agreement with the reduced contrast in the photon maps at negative bias voltage. Here, the electrons tunnel from the sample into empty states of the tip (Fig. 59 b). Only the sample LDOS close to the Fermi energy of the sample is involved, defining the initial states for the inelastic processes. The final states are provided by the LDOS of the tip and are thus independent of the sample.

In their STM-LE study of Ag(111) step edges, Hoffmann et al. quantify the effect of the LDOS on the light emission intensity using line profiles through topographies of the surface [25]. STM topographic images represent contours of constant integrated LDOS up to the applied bias voltage. Thus, they give a measure of the available tunneling channels. Topographies acquired at different bias voltages may be used to estimate the number of elastic and inelastic tunneling channels.

The topography at a given bias voltage V represents the contour for the elastic tunneling current. The corresponding topography recorded at a bias voltage $V - \frac{h\nu}{e}$, where $h\nu$ is the dominating energy of the emitted photons, may be used to approximate the contour of the inelastic tunneling current. From the difference between both contours, the authors calculate the change in the relative inelastic current. The resulting contour shows large agreement to the contour of the emission intensity.

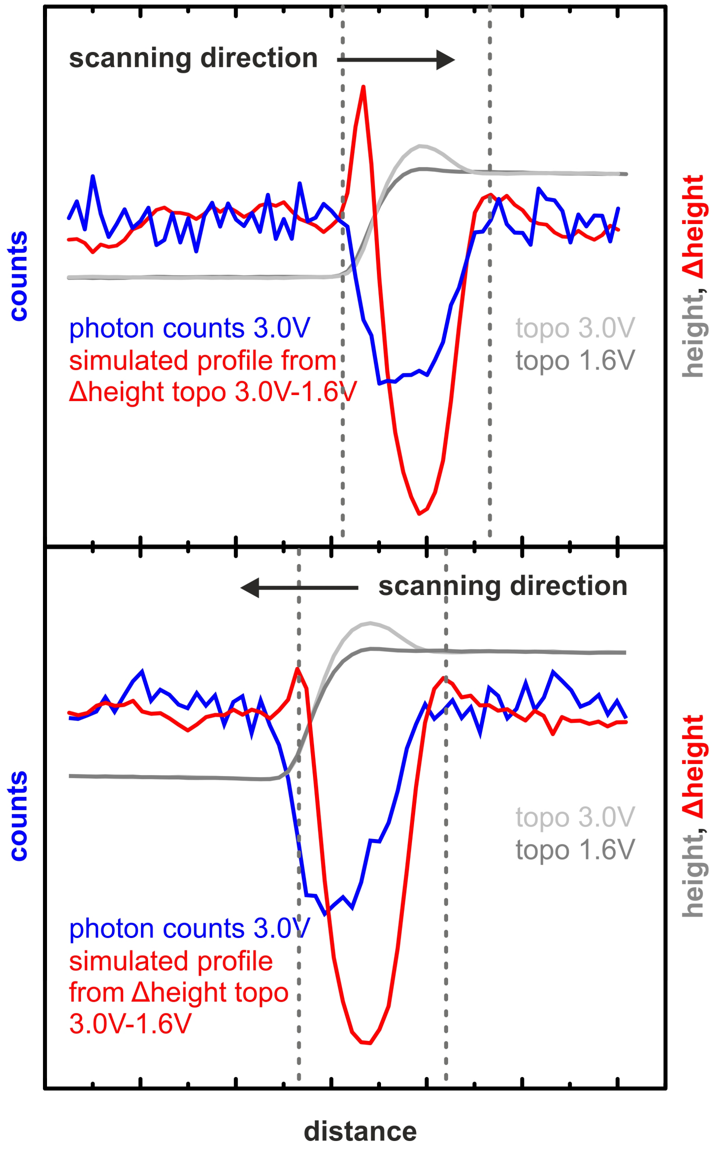

Figure 60: Simulation of the drop in photon emission intensity by estimating the contours of elastic tunneling and the final states of inelastic tunneling by topographic images acquired at $E_{\mathrm{final\,elastic}}$ and $E_{\mathrm{final\,inelastic}}$. In particular the lateral extent of the simulated intensity profile is in good agreement to our simulated data.

Fig. 60 shows a similar analysis of our data. We use the contour of the topography acquired at 3.0V as the elastic contour. As the dominating photon energy, we use $h\nu = 1.4eV$ which corresponds to the peak in our spectra of emitted light. Thus, as the final state contour for the inelastic channels, we subtract the topographic contour at 1.6eV. The inelastic tunneling probability can then be estimated using the function $I_{inelastic}/I_{elastic} = exp(-\kappa\Delta h)$, with $\kappa = 2.04\text{Å}^{-1}$ [25].

In contrast to the data presented by Hoffmann et al., the line profile of the photon map and the inelastic tunneling probability estimated from the elastic and final state contour in our case exhibit some differences. The size of the drop in the emission intensity is not perfectly reproduced by our simulation. In particular, the intensity drop is laterally shifted with respect to the height difference profile. For both scanning directions (left to right and right to left) the drop is extended further towards the lower terrace than it would be expected from our simulation.

Here, the change in the direction of the tunneling electrons' k-vectors at the step edge might evoke an additional reduction of the light emission intensity (see section 8.6.1). However, this could also be connected to the way we obtained the height difference profiles. Here, the positions of the step edges were aligned to coincide. However, the position of the step edge for different tunneling energies may vary, which would result in slightly different height difference profiles.

Hoffmann et al. obtained their data with a liquid helium cooled STM [25]. Here, thermal drift is suppressed to an extent where the differences in the topographic contours may be obtained using subsequent scans without further alignment. This revealed a shift in the positions of the step edge for different tunneling energies that is not straightforwardly accessible in our data. Also, Hoffmann et al. found a general height difference between the terraces imaged at different bias voltages. This difference may have been obscured by the necessary image processing in our case, which would impact the size of the inelastic tunneling probability from our simulation. Considering an additional height offset would bring our simulated data from the height profiles even closer to the relative drop in intensity observed in the photon maps.

However, even with the mentioned uncertainties in our data evaluation, the lateral extent and approximate position of the drop in the emission intensity with respect to the changes in the topography observed in our data let us faithfully conclude a correlation between differences in the LDOS of providing final states for elastic and inelastic tunneling processes and the inelastic tunneling probability.

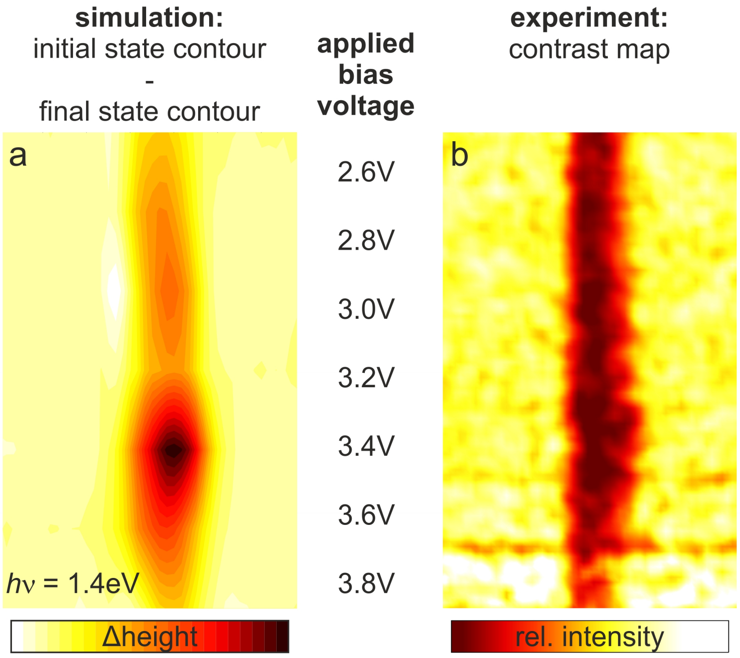

Figure 61: Comparison between experimental and simulated "contrast maps". a) Contour plot of the differences in the topographic height between topographies acquired at the respective indicated bias voltages in between 2.6V and 3.8V and the corresponding "final state contours", i.e. topographies acquired at $V - \frac{h\nu}{e}$. The dominating photon energy in this case was $h\nu = 1.4eV$ as extracted from the spectra of the emitted light. b) "Contrast map" for the same bias voltage range as a).

.

In Fig. 35, we presented a bias resolved study of the light emission induced on step edges. We extracted averaged line profiles of the topography for bias voltages from 2.6V to 3.8V as the elastic tunneling current contours. Corresponding line profiles of the topography for 1.2V to 2.4V served as final state contours. Fig. 61 a shows the resulting map of deviations of both contours. Fig. 61 b shows the corresponding experimental data. Once again the photon map data was normalized with the terrace value to yield a contrast map. The general behavior of the light emission intensity is reproduced. The contrast first increases and then drops again towards higher bias voltage.

In our case, the broad background of the TIP spectrum yields a variety of final state energies for the inelastic transitions which prevents a simple exact quantitative modeling, however, our bias voltage resolved data shows a nice qualitative correspondence between the the differences in the LDOS and the drop in the emission intensity at step edges.

8.7 SPECTRA OF THE OVERALL PHOTON YIELD

Generally, photon maps give insight into the lateral distribution of the overall photon yield at a certain tunneling energy. This allows us to study the effect of certain sample structures and their physical properties (e.g. their geometry or LDOS) on the light emission. Further, photon maps in which the bias voltage is ramped during the imaging also bare information about the tunneling energy dependency of the excitation efficiency. A more detailed set of information about this matter is given by the spectra of the overall photon yield.

As discussed above, the overall photon yield at a given tunneling energy depends on the specific TIP-spectrum, i.e. the energetic modes that are available for excitation. Also, the enhancement provided by the electric field of the particular tip-sample junction plays a role (see section 8.3). These properties depend on the specific tip which is used in the experiment.

In contrast, the excitation of the TIPs happens on a very local scale through the inelastic part of the tunneling current. Section 8.6.4 stressed the importance of the LDOS involved in the elastic and inelastic transitions for the inelastic tunneling probability. Thus, the spectra of the overall photon yield also contain valuable information about the electronic structure of the sample and its particular impact on the excitation efficiency. However, the different contributions of the tip and sample properties are entangled in the spectra.

Fig. 62 - Fig. 65 exemplary revisit data presented in chapter 7. Here, we want to discuss several characteristic points in the spectra of the overall photon yield. These allow an insight into the specific involvement of the different contributions in the excitation efficiency.

8.7.1 *The onset*

A very characteristic feature in the spectra of the overall photon yield is the onset. It marks the first opening of relevant inelastic tunneling channels, i.e. the lowest tunneling energy that is needed to excite TIP modes which decay radiatively in the detectable range.

The APD used here is sensitive to photon energies down to approximately $1.2eV$ which is very close to the onset observed in the spectra. Thus, for the data on Ag(111) presented here, also the detector range and efficiency may play a role a non-negligible role for the onset in the overall photon yield, as the used APD is only sensitive to photon energies down to approx. $1.2eV$.

However, generally, the onset energy directly depends on the TIP-spectrum which is specific to each tunneling junction and microtip. Also, it depends on the energetic positions of the lowest final states available for inelastic transitions. Here, we want to exemplary discuss the influence of these factors. Especially for more complex systems, e.g. involving molecular layers as presented and discussed in chapters 12 and 13, we will be able to see their influence more clearly.

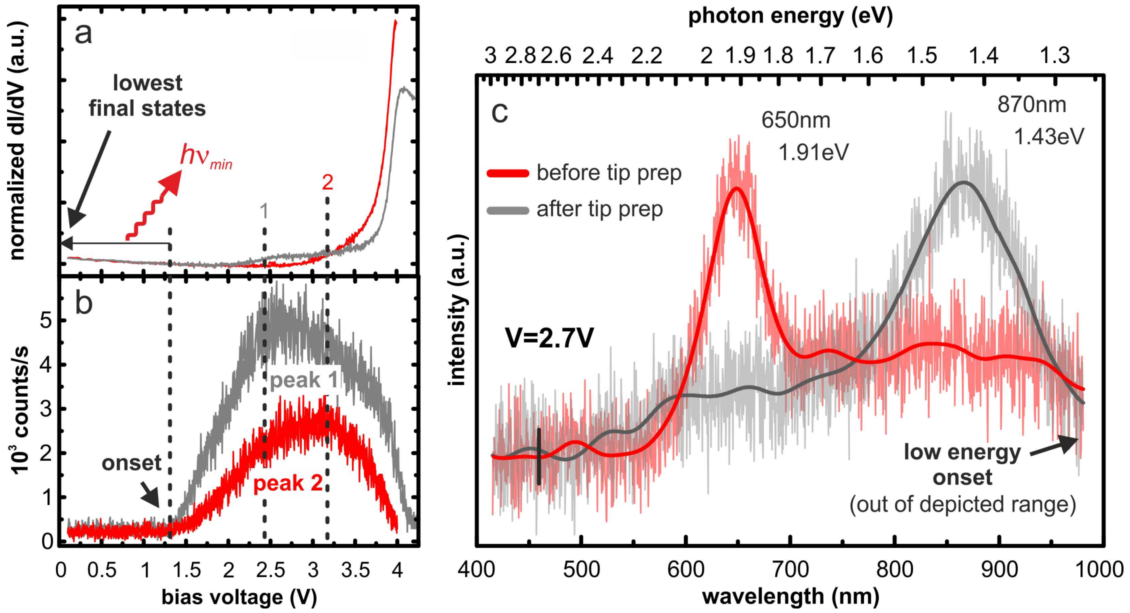

Figure 62: Characteristic spectroscopic data before and after a tip change through *in situ* tip preparation. a) Normalized dI/dV-spectra, b) spectra of the overall photon yield and c) spectra of the emitted light recorded at a bias voltage of $V = 2.7\mathrm{V}$. Data revisited from Figs. 40 and 41.

8.7.1.1 *The Role of the LDOS*

The energetically lowest final states involved in the inelastic transitions are expected at an energy $E_{\mathrm{final\,min}} = eV_{\mathrm{Bias}} - h\nu_{\mathrm{max}}$. This is true as long as the highest energy of emitted photons is not limited by the specific TIP spectrum. For the bias voltage resolved spectra of the emitted light presented in Fig. 38 (see also section 8.2, Fig. 47), the spectrum of TIP modes limits the emission intensity above approx. 2.2eV. For bias voltages up to 2.1V, we find that the spectra exhibit significant intensity up to photon energies of $h\nu_{\mathrm{max}} \approx eV_{\mathrm{Bias}}$, where e is the elementary charge and V_{Bias} is the bias voltage. Thus, we may identify the lowest final states provided by the Ag(111)-sample to lie roughly around the Fermi energy. At this energy, final states for inelastic tunneling may be provided by the Ag(111) surface state which has an onset slightly below the Fermi energy.

8.7.1.2 *The Role of the TIP Spectrum*

We find that for most random tip changes during the experiment the TIP spectrum is not affected. In consequence, we do not observe any changes in the onset of the spectra of the overall photon yield (see Fig. 44 in chapter **??** or Fig. 62 in this section).

For the tip change through tip preparation, a slight change in the onset energy might vaguely be discerned, however, the effect of the tip change in the onset is very minor (see Fig. 62 b). In both cases, the onset of the overall photon yield lies roughly around 1.3V. Knowing that the lowest final states for inelastic transitions lie close to the Fermi energy, we have to compare the availability of TIP modes around 1.3eV. Here, the spectra of the emitted light before and after the tip change exhibit almost equal intensities at photon energies of 1.3eV (see Fig. 62 c). This explains the similar onset energies.

Our spectra of the emitted light reveal excitable TIP modes down to the low energy edge of the recorded spectral range ($\approx 1.25eV$). Thus, also lower energy transitions which are not detectable may be involved here. As stated above, the detector range and efficiency may play a significant role for the onset here.

8.7.1.3 *Differences in the Onset at Positive and Negative Bias Voltage*

Comparing spectra of the overall photon yield acquired with the same microscopic tip for positive and negative bias voltage (Fig. 36, figure revisited in Fig. 63), a slight difference in the onset energies for both bias polarities by roughly $0.05 - 0.1eV$ may be observed. This slight difference might be connected to two different phenomena.

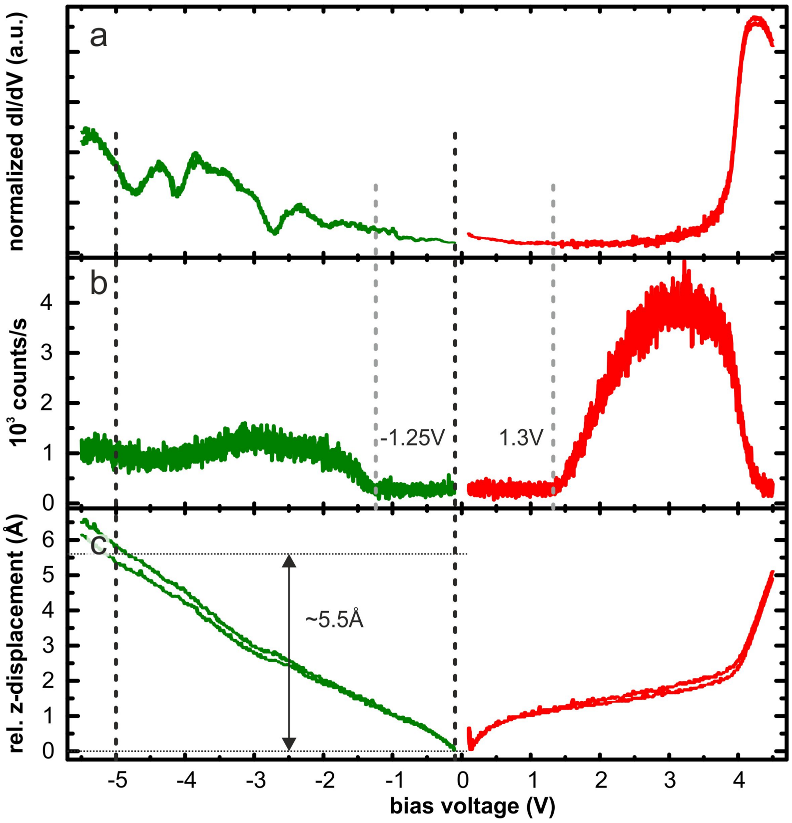

Figure 63: Spectra of the overall photon yield at positive and negative bias voltage revisited from Fig. 36. From the data, an estimation of the difference between the tunneling distance at the onset voltages of the overall photon yield at positive and negative bias voltage can be derived.

1) A shift in the TIP spectrum: The dI/dV spectra shown in Fig. 63 reveal a slightly higher LDOS for tunneling energies around $-1.3eV$ than at $1.3eV$. This would be associated to a slightly larger tunneling distance when tunneling at the onset energy at negative bias polarity. This modification of the overall junction geometry might induce a small shift in the TIP spectrum leading to the slightly shifted onset.

Shifts in the emission spectra as the result of changes in the tunneling distance have been reported experimentally [93, 198] and are also supported by theory [93]. However, an increase of the tunneling distance would rather be associated to a blueshift of the emission spectrum. Here, this would be expected to lead to an onset at higher instead of lower tunneling energies for negative bias voltage. For a Au(111)-tip above a Au(111) sample, the shift is found to occur roughly linearly at a rate $r = \mathtt{shift}/\Delta d$ of $3nm/\text{Å}$, where d is the tunneling distance [93]. Also for different tip materials on Au(111)[2], similar results were reported [198]. The order of magnitude of the difference in the tunneling distance between positive and negative bias voltage may be estimated from the tip retraction curves during spectroscopy (see Fig. 63). Even the considerably large increase of the LDOS in the bias voltage range from $-0.1V$ to $-5V$ only leads to a retraction of the tip of around 5.5Å. The difference between the LDOS up to approx. $-1.3V$ and $+1.3V$ is clearly smaller than the increase of the LDOS from $-0.1V$ to $-5V$. In consequence, also the change in the tunneling distance would be expected to be smaller, i.e. a few Å at the most. Thus, the impact of a shift in the TIP-spectrum on the onset of the overall photon yield would be negligibly small here.

Our spectra of the emitted light for positive and negative sample bias presented in Fig. 39 show no clear tendency for a spectral shift as the result of the inversed bias voltage. In this case, even very minor tip changes may overrule the effect of the different tunneling distances and slightly shift the spectra in one direction or the other. Thus, a different effect elaborated below is much more likely to cause the difference in the onset.

2) A different LDOS of initial and final states: When the bias polarity is reversed, the tunneling direction of the electrons is reversed. At negative bias voltage, the electrons tunnel from initial states in the sample to final states in the tip (see Fig. 59 b). In this case, different LDOS provide the initial and final states for the inelastic tunneling processes, which may evoke a shift of the onset.

Taking all the above considerations into account, the second effect is most likely responsible for the small shift in the onset of the overall photon yield observed in our experiments.

---

[2] However, the tip may have possibly been indented into the Au(111) surface during tip preparation and therefore have been covered with Au.

8.7.2 *Spectrum above the Threshold*

The spectrum of the overall photon yield above the threshold (the onset), is governed by the competition of factors which increase and those which reduce the inelastic tunneling probability. Here, again, the specific tip is involved providing the particular energetic distribution and intensity of the TIP modes. However, for the overall photon yield versus the bias voltage, the LDOS provided by the sample is a crucial factor [192, 211].

8.7.2.1 *Ratio of Elastic to Inelastic Tunneling Channels*

The inelastic tunneling probability is given by the fraction of inelastically tunneling electrons with respect to the overall tunneling current. The latter is the sum of the inelastic and the elastic current (see Fig. 64).

The fraction of inelastically tunneling electrons is very small. Thus, when looking at the ratio of inelastic and elastic tunneling processes, the overall tunneling current may be approximated by the elastic tunneling current.

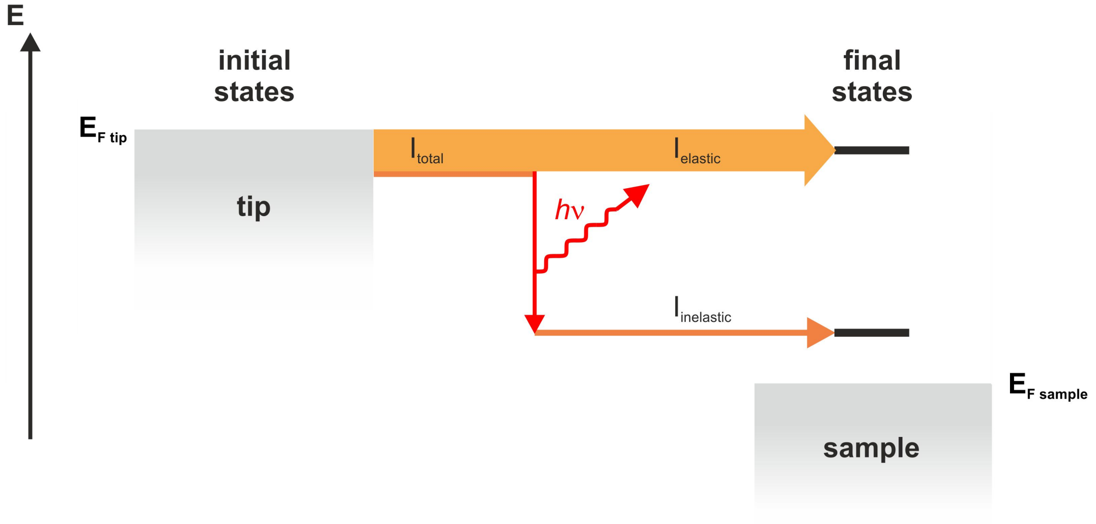

Figure 64: Inelastic tunneling scheme for tunneling from the tip to the sample. The total tunneling current splits up into an elastic and an inelastic component. The ratio of both depends on the number of final states provided by the sample for the respective tunneling channels.

With rising bias voltage, a larger number of final states for elastic and inelastic transitions become available. Consequently the amount of possible elastic and inelastic tunneling channels grows. The number of elastic tunneling channels at a certain bias voltage V is influenced by the LDOS of the sample up to the tunneling energy $E_{\mathrm{initial}} = E_{\mathrm{final\,elastic}} = eV_{\mathrm{Bias}}$. The fraction of inelastically tunneling electrons depends on the availability of final states provided by the LDOS up to $E_{\mathrm{final\,inelastic}} = eV_{\mathrm{Bias}} - h\nu$ (see Fig. 59 and section 8.6.4) [211].

As the number of inelastic and elastic channels available at a certain bias voltage depends on the integrated LDOS over different energetic ranges, they may change with the bias voltage at different rates. In consequence, their ratio and consequently the fraction of inelastically tunneling electrons changes.

8.7.2.2 *Influence of the Tip-Sample Distance*

In literature, additionally an effect due to the decrease of the electric field enhancement with the retraction of the tip has been proposed to affect the spectra [192]. However, experiments in which the current was tuned over a range of several orders of magnitude at a given bias bias voltage point against such a contribution. They reveal a widely linear increase of the countrate versus the current in spite of a changing tunneling distance [212], [14] (supporting info). However, the strength of the electric field enhancement particularly depends on the specific tip used and the impact of changes in the overall photon yield on the photon yield depends on the interaction distance. Thus, the effect might vary depending on the tip.

8.7.2.3 *The Role of the TIP Spectrum and Field Enhancement*

At positive bias voltage, the onset is followed by a roughly linear rise of the overall photon yield. For different microtips, the slope of the increase differs significantly (see e.g. Fig. 62 and 65).

With rising bias voltage, further energetically higher modes from the tip spectrum can be excited. For tips that provide different TIP-spectra, e.g. after tip preparation, the different slopes for the increase may easily be understood through changes in the TIP spectrum. For the example given in Fig. 62, the microtip after tip preparation provides a greater number of excitable TIP-modes at lower energies, corresponding to a steeper increase of the emission intensity in the spectrum of the overall photon yield.

However, also random tip changes without a significant impact on the TIP spectra may evoke changes in the slope of the rise of the overall photon yield (see e.g. Fig. 65). These changes might alter the electric field enhancement provided by the tip and therefore affect the emission intensity.

8.7.3 *Characteristic Features in the Spectra*

The LDOS of Ag(111) is rather featureless at low positive bias voltages. The dI/dV-signal increases slowly until a steep rise of the LDOS around 3.8V. In our experiments, for the microtip before the tip preparation, the overall photon yield at this bias voltage had already dropped significantly. Consequently, no clear effect of the steep rise in the LDOS can be distinguished in the spectra of the overall photon yield acquired with this tip. In contrast, the spectra recorded with the microtip after the tip preparation exhibit a quite considerable photon yield at 3.8V. For these spectra, the rise in the LDOS may be associated to a sudden drop in the light emission intensity.

The peaking of the spectra of the overall photon yield occurs when the opening of further inelastic channels is overruled by the opening of further elastic channels. For spectra that were all acquired with a tip exhibiting the same TIP spectrum, different peak positions of the overall photon yield may be correlated to different rises of the dI/dV-spectra as indicated by vertical lines in Fig. 65.

Besides the availability of final states in the LDOS for elastic and inelastic transitions, the specific number of radiative inelastic channels depends on the availability of TIP modes. Thus, the exact peak positions of the spectra of the overall photon yield depend on the specific tip. Still, the different positions of the maxima observed in our spectra for the tip before and after preparation by field emission may also be correlated to different increases of the LDOS up the corresponding bias voltage as indicated by vertical lines in Fig. 62.

8.7.4 *Spectra at Positive and Negative Bias Voltage*

At negative bias voltage, the electrons tunnel from the sample to the tip. The final states for the inelastic transitions at this bias polarity are provided by the tip.

The overall photon yield at negative bias voltages e.g. shown in Fig. 63 is significantly reduced as compared to positive bias voltages. The tip-retraction curves at this bias voltage (see e.g. Fig. 63 c) are significantly steeper than for positive bias voltage. This is associated with a faster increase of the number of elastic tunneling channels which would explain a decreased ratio of inelastically and elastically tunneling electrons and the resulting smaller photon yield.

As opposed to the spectrum at positive bias voltage, the overall photon yield at negative bias voltage shown in Fig. 63 does not exhibit a distinct singly peaked structure. Instead several small peaks appear in the spectra. This may be explained by the larger variations in the LDOS that modulate the ratio of elastic to inelastic channels at negative bias voltage.

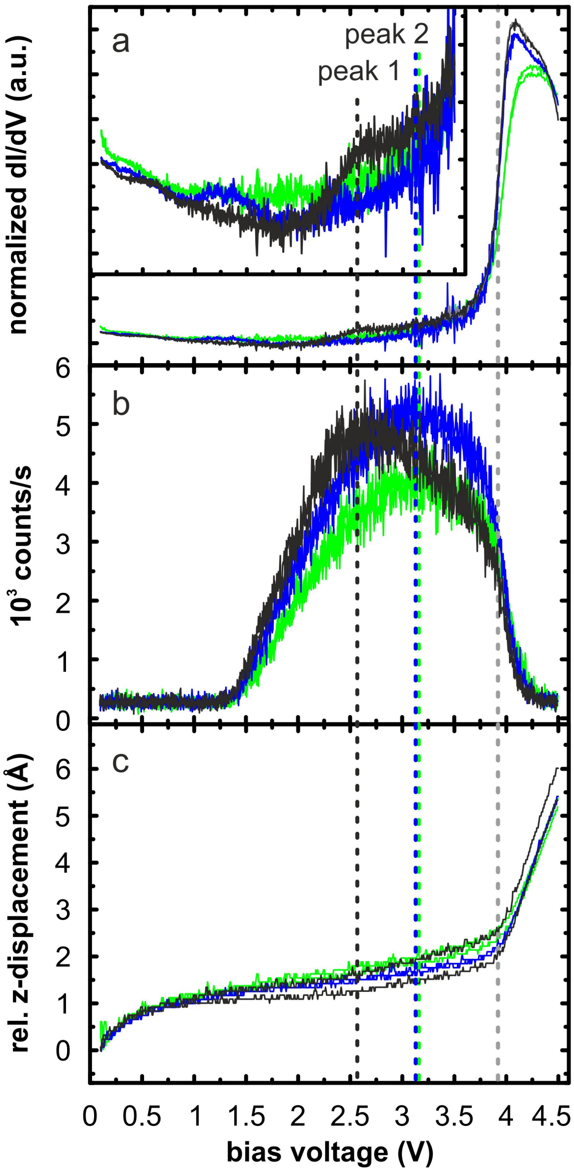

Figure 65: Spectroscopic data recorded with the same macroscopic tip revisited from Fig. 44. While the spectra exhibit some differences, the TIP-spectrum was not affected. The black, blue and green vertical lines indicate a possible correlation between the a rise in the LDOS and an earlier peaking of the black spectrum. The gray vertical line indicates a clear correlation between the steep rise of the LDOS around 3.9V and a drop of the light emission intensity.

8.8 SUMMARY

In this chapter, we exemplary discussed the characteristics of the STM-induced light emission on Ag(111). In particular, we gained insight into the contrast mechanisms in photon mapping and the different factors that govern the spectra of the overall photon yield.

After a careful consideration of the different effects, we may assign a dominating role for the contrasts evoked in photon maps by step edges and other surface defects to lateral variations in the LDOS. The differences in the distribution of the LDOS affect the ratio of inelastic to elastic tunneling channels and therefore the inelastic tunneling probability.

This contrast mechanism can fully explain our experimental data. This includes the size of the observed drops in the emission intensity which are too large to be explained only by geometric factors, e.g. a change in the direction of the tunneling current.

The influence of the ratio of inelastic to elastic tunneling channels can also be observed in the spectra of the overall photon yield. With the dedicated analysis of data acquired with different microtips, we may partially disentangle the interwoven contributions of tip related effects and the LDOS of the sample to the light emission. This understanding provides us with the prerequisites to interpret the data gathered on more complex sample systems presented in the following chapters.

9

LIGHT EMISSION INDUCED ON MOLECULES ON AG(111)

Particularly with regard to possible technological applications, the influence of adsorbed organic molecules on the induced light emission is a topic of interest. Here, a brief overview of our STM-LE experiments on different archetype molecules adsorbed on Ag(111) will be given. We chose the perylene derivative 3,4,9,10-perylenetetracarboxylic-dianhydride (PTCDA) and the fullerene C_{60} at submonolayer coverage as archetype organic layers. As an example for singly adsorbed molecules, copper-phthalocyanine (CuPc) molecules were deposited at submonolayer coverage. At a significantly higher coverage, the same molecules will serve as an example for a molecular multi-layer structure.

9.1 MONOLAYER DOMAINS AND INDIVIDUALLY ADSORBED MOLECULES

Fig. 66 shows the topographic images and simultaneously acquired photon maps of Ag(111)-samples with submonolayer coverages of the different organic molecules adsorbed. The Ag(111)-sample depicted in the STM images shown in Fig. 66 a exhibits a low submonolayer coverage (< 0.1ML) of PTCDA. Similar to a variety of other metallic substrates, the PTCDA molecules assemble into highly ordered domains in which they assume a so called "herringbone structure" [150]. Within this structure, the molecules are assembled in a braid-like arrangement, with their negatively polarized short edges facing the positively polarized long edges. In addition, PTCDA molecules are also found to decorate the Ag(111)-step edges.

Fig. 66 c shows the topography of another Ag(111)-sample. Here, submonolayer coverages of two different organic species, C_{60} (≈ 0.1ML) and CuPc (< 0.1ML), were deposited subsequently onto the Ag(111)-substrate. The C_{60} molecules are assembled into densely packed hexagonally ordered domains. Further, they are found to decorate the Ag(111)-step edges (see Fig. 67). At the given sample temperature of 80K, the CuPc molecules are found to adsorb individually on the pristine Ag(111)-terraces[1]. Due to charge-transfer between the molecules and the substrate, the CuPc molecules experience an intermolecular repulsion which at low coverages drives them into this dilute phase [166].

---

[1] At higher temperatures, e.g. room temperature, individual CuPc are mobile on flat crystalline metal surfaces [164].

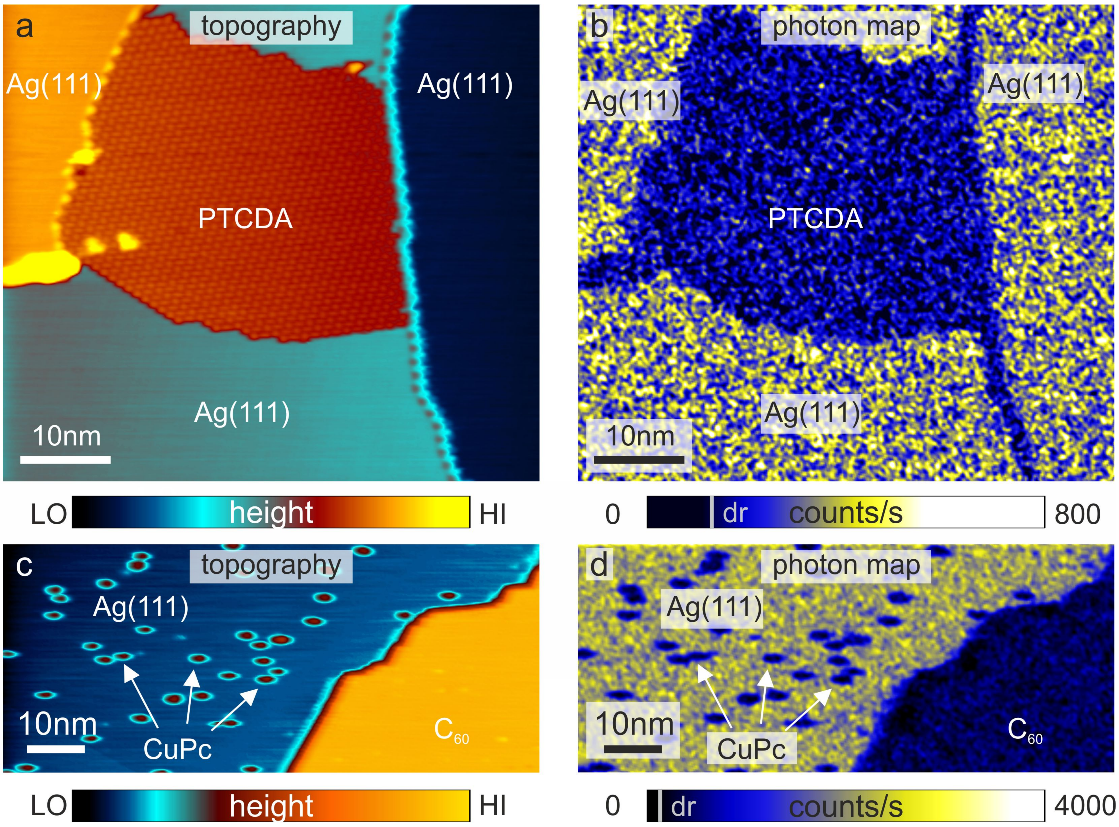

Figure 66: Topographic images and simultaneously acquired photon maps of different organic molecules on Ag(111). a) Topography and b) corresponding photon map of a Ag(111) sample with a submonolayer coverage (< 0.1ML) of PTCDA. c) and d) Topography and corresponding photon map of a Ag(111)-sample exhibiting a coverage of roughly 0.1ML monolayer C_{60} and a submonolayer coverage clearly below 0.1ML of CuPc. Vertical lines on the intensity scale of the photon maps indicate the dark count rate (dr). $V = 2V$, $I = 30pA$, $T = 80K$.

In the photon maps (Fig. 66 b and d), the induced light emission is quenched almost completely when tunneling above the molecular species. The data shown in Fig. 66 were recorded at a bias voltage of 2V. Also further photon maps acquired at higher bias voltages of e.g. 2.7V and 3V, showed a similarly significant quenching of the light emission intensity for the molecules.

9.2 CONTRASTS IN THE PHOTON MAPS AT POSITIVE AND NEGATIVE BIAS VOLTAGE

As discussed in chapter 8, at negative bias polarity, the contrasts in the photon maps evoked by step edges and other defects on the Ag(111)-surface are significantly reduced (see e.g. Fig. 35). A similar behavior was also found for the contrast evoked by the molecular-domains. Fig. 67 shows two topographic images and the corresponding photon maps of the same area of a partially C_{60} covered Ag(111)-surface. The respective images were acquired for bias voltages with the same absolute value, however opposite bias polarities. At the positive bias voltage, the photon yield induced on the C_{60}-domain is significantly reduced (see Fig. 67 b). At negative bias polarity, the contrast almost vanishes so that the C_{60} domains and decorated step edges can hardly be discerned in the photon map.

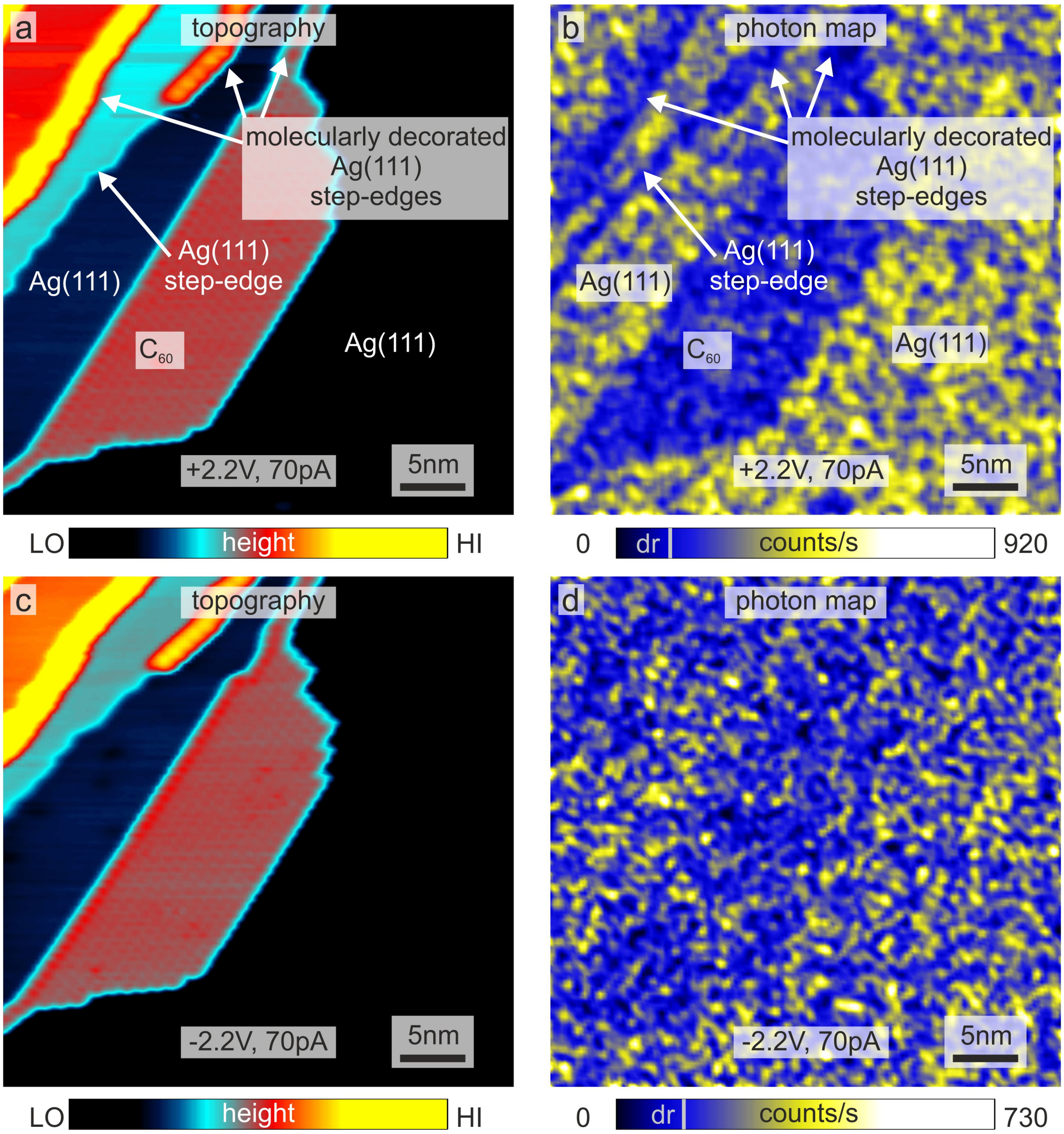

Figure 67: Topographies and corresponding photon maps of the same partially C_{60}-covered Ag(111)-surface area recorded at opposite bias polarities. a) and b) were recorded at $V = +2.2V$. c) and d) were recorded at $V = -2.2V$. Both sets of images were acquired at equally large tunneling currents. Vertical lines on the intensity scale of the photon maps indicate the dark count rate (dr). $I = 70pA$, $T = 80K$.

9.3 MULTILAYER DOMAINS VS. SINGLE LAYERS

For the sample shown in Fig. 66 c and d, the CuPc-coverage was further increased in an additional deposition step. After this additional deposition of molecules, the examined surface area was entirely covered with molecules. Fig. 68 shows the topography and the corresponding photon map of the resulting sample surface containing both, C_{60} and CuPc covered areas.

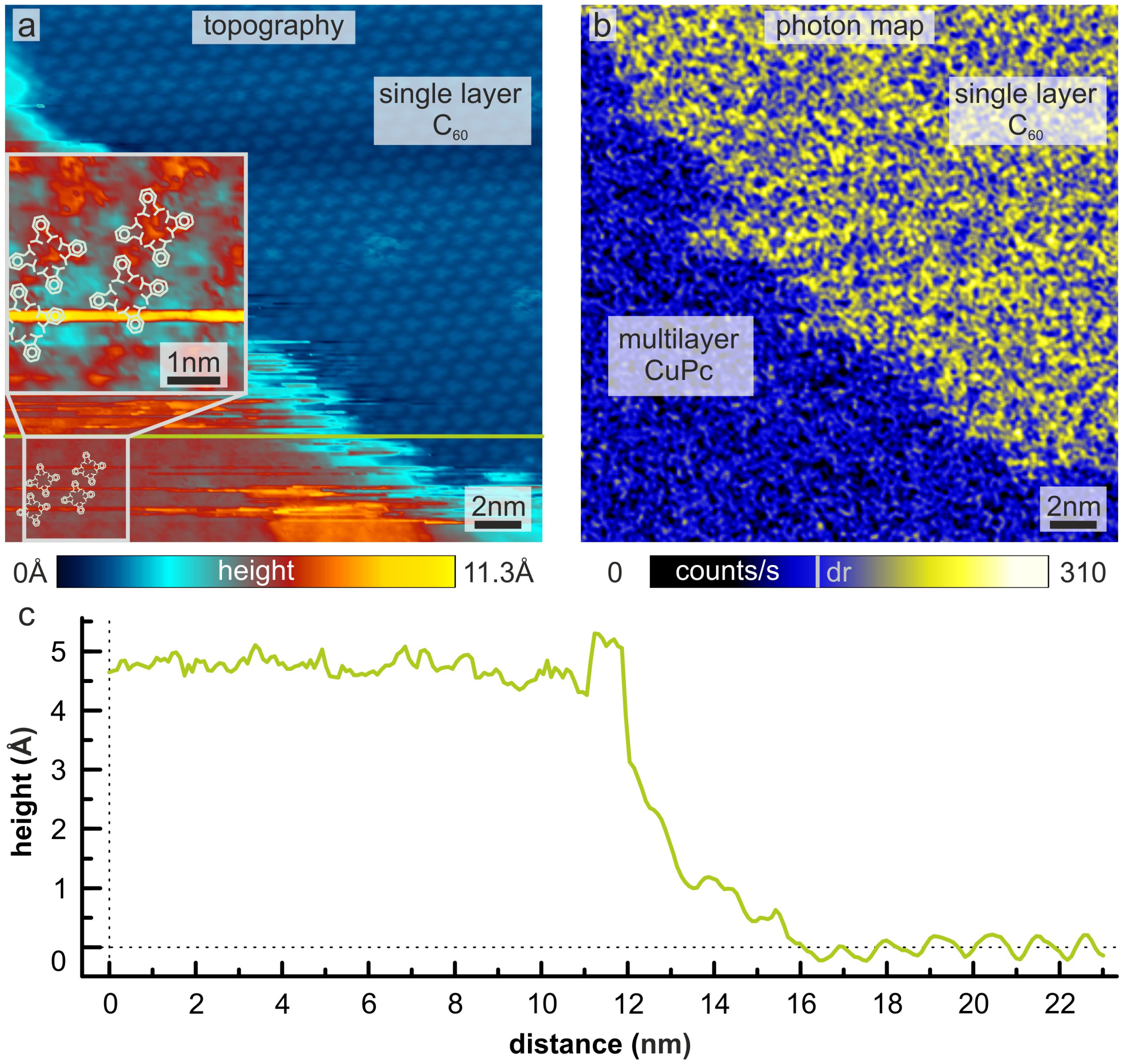

Figure 68: Molecular domains of CuPc and C_{60} on Ag(111). a) Topography and b) corresponding photon map of the sample shown in Fig. 66 c and d after the CuPc-coverage was further increased. c) Height profile, indicated in (a) by the green line. A vertical line on the intensity scale of the photon map indicates the dark count rate (dr). $V = 2.5V$, $I = 15pA$, $T = 80K$.

The upper right part of the imaged area is covered with densely packed C_{60}-molecules. For the subsequent deposition of C_{60} and CuPc onto a coverage of about 1ML in total on Au(111), Stöhr et al. found that the domains of both molecular species coexist without a significant intermixing. Also if the CuPc coverage was slightly increased, the CuPc molecules were not found to diffuse underneath the C_{60}-domains [137]. We faithfully assume that similar to the case of Au(111), the C_{60}-domains are not affected by the subsequent deposition of CuPc. Thus, also at this CuPc-coverage, we presume that the C_{60}-molecules are still adsorbed in first layer directly on the Ag(111)-substrate.

The lower left part of the imaged area exhibits a CuPc-domain. At this higher coverage, the CuPc molecules are assembled into a densely packed ordered structure. The CuPc-domain appears higher than the adjacent C_{60} covered area in the topography (see Fig. 68 a). A line profile, indicated by the green line in Fig. 68 a, is shown in Fig. 68 c. The difference in height between the C_{60} covered area and the CuPc-domain measures about $4.5\text{Å} \pm 1\text{Å}$.

The adsorption height of CuPc on Ag(111) at submonolayer coverage is about 3Å [165, 167]. Roughly the same height was found for steps between the third and the second layer of CuPc on Ag(111) [213]. From this, we may assume that at least up to this thickness, the molecules lie flat within the layers with a layer thickness of about 3Å. The height difference between the CuPc- and the C_{60}-domain may additionally be associated with one or multiple steps in the Ag(111) surface. The step height of a Ag(111) monoatomic step measures about 2.4Å [73].

The height of a single layer C_{60}-domain on Ag(111) is about 7Å (see Fig. 71). Thus, the height difference of roughly 4.5Å between the C_{60}-domain and the CuPc-domain indicates a height difference of roughly $11 - 12\text{Å}$ between the top of the CuPc-layer and the Ag(111)-surface underneath the C_{60}. Thus, at least a triple-atomic step in the Ag(111) surface would be required in order to model the height difference between both molecular domains without having to assume the CuPc growing on top of any other molecular layer (CuPc or C_{60}). Consequently, it is very likely that the CuPc covered area in Fig. 68 exhibits molecules adsorbed in a higher layer.

Several noisy areas are found in the topography of the CuPc-domain, i.e. parts of the image are blurry. This is the result of unstable tunneling conditions which may be evoked e.g. by mobile CuPc molecules or weakly bound clusters. The CuPc molecules in higher layers may be only weakly bound by van der Waals interactions between molecular layers. Thus, they are likely to be moved when the STM tip is scanned across them. Also, a reduced conductivity of the multi-layer film may have caused tip-sample collisions. These instabilities, which have also been observed for multi-layer films of CuPc on Au(111) [214], prevented a further detailed STM study of the ordered CuPc area.

A tentative model for the molecular order is indicated in Fig. 68 a. However, no unambiguous determination of the molecular orientation can be given. In particular, the CuPc molecules in the topmost layer may also be inclined with respect the the surface parallel direction. Such a behavior was e.g. found for the third layer of CuPc on Cu(111) [215] and may also be expected for higher layers of CuPc on Ag(111) due to the increasing decoupling of the molecules from the substrate. Further, the first layer of CuPc on C_{60} on Ag(111) was found to also exhibit an incline with respect to the surface parallel direction [125, 216].

Instead of on the particular molecular ordering, here, we want to concentrate on the effect of this thicker molecular layer on the induced light emission. The photon map in Fig. 68 b reveals that the emission induced on the CuPc covered area is virtually completely suppressed. In contrast, for the C_{60}-domain some residual light intensity is detected.

9.4 MOLECULAR RESOLUTION IN PHOTON MAPPING

Now, we want to concentrate more closely on the light emission induced on the C_{60}-domain. The photon map shown in Fig. 68 exhibits a distinct modulation of the light emission intensity which roughly corresponds to the lateral modulation of the C_{60}-layer in the topography.

9.4.1 *Exclusion of Experimental Artifacts*

Besides real physical phenomena, also experimental perturbations may have an effect on the STM induced light emission. In particular, despite the STM is operated in constant current mode, an overshooting or a too slow adjustment of the feedback loop may result in variations of the tunneling current e.g. during the acquisition of the photon maps. To exclude variations of the tunneling current as the origin of the molecular resolution in the tunneling current, the relative variation in the light emission intensity may be compared to the relative variation in the tunneling current. This was done in Fig. 69.

Fig. 69 a shows a detailed view of the molecularly resolved C_{60}-domain in the photon map shown in Fig. 68. Fig. 69 b shows the corresponding map of the tunneling current. After a tip change, the periodic modulation in the photon map that is already faintly discernible in Fig. 68 b is now very clearly visible.

Line profiles, indicated by colored lines in Fig. 69 a and b, were taken through the photon map and the corresponding map of the tunneling current (see Fig. 69 c-f) . The variations in the photon yield are found to measure up to around 60% of the mean count rate (75% for another profile direction), while the variations in the tunneling current lie in the range of only 15% (8%) of the set value. Most importantly, the relative fluctuations in the photon yield are much larger than the fluctuations observed in the tunneling current. Here, it can be assumed that the photon yield scales roughly linearly with the tunneling current. The periodic modulations in the photon images are therefore clearly not only related to fluctuations in the tunneling current, e.g. due to overshooting effects of the feedback loop, but seem to be the result of intrinsic modulations of the characteristic light emission in which the C_{60}-molecules are somehow involved. This is worth to be further looked at.

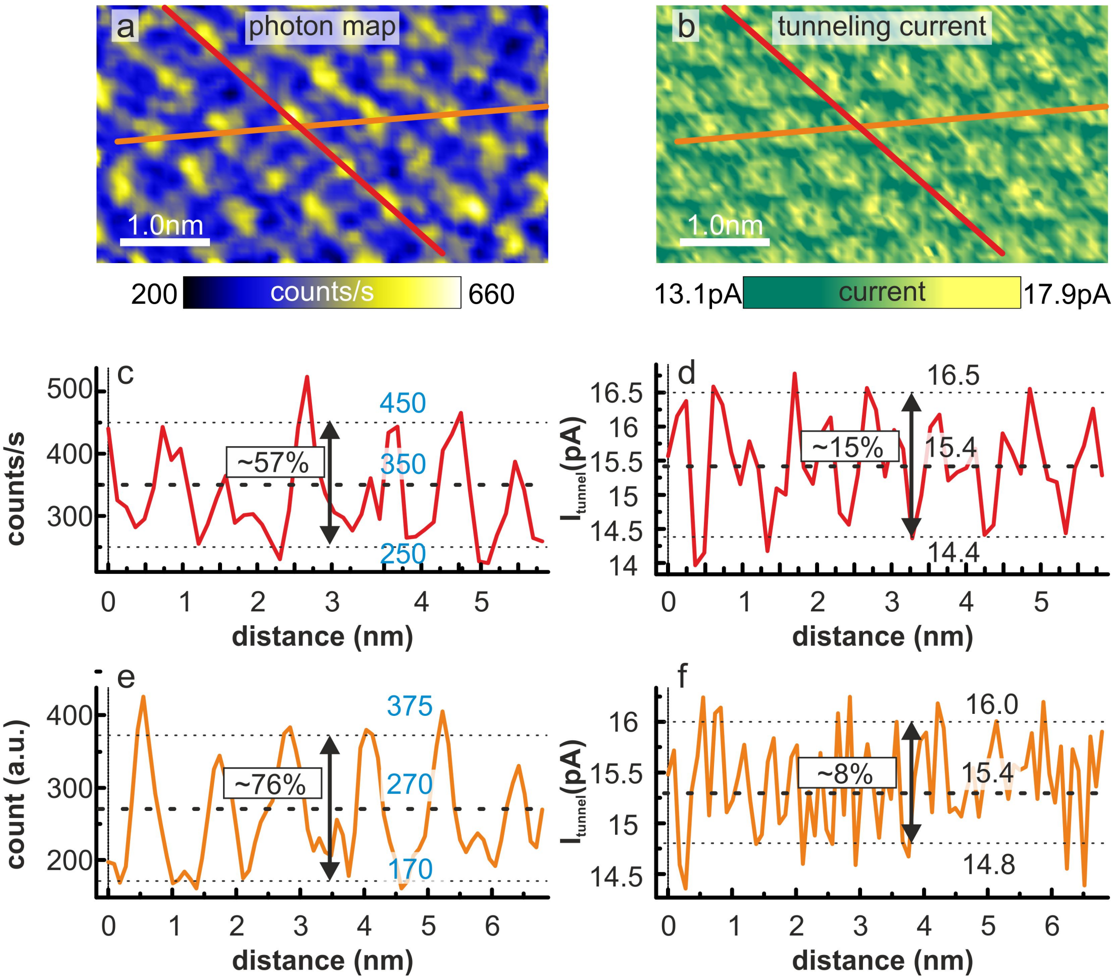

Figure 69: Analysis of the relative variations in the light emission rate and the tunneling current. Details of a) a photon map and b) the corresponding map of the tunneling current acquired on the C_{60}-domain depicted in Fig. 68. c-f) Line profiles through a) and b) as indicated by the colored lines in the images. The given count rates were corrected for the dark count rate. V = 2.5V, I = 15pA, T = 80K.

9.4.2 *Correlation between the Topography and the Photon Map*

Fig. 70 shows the Fourier transforms of the topography (Fig. 70 a) and photon map (Fig. 70 c) of the C_{60} covered area depicted in Fig. 68. When superimposing both Fourier transforms (see Fig. 70 b), the reflexes for the photon map lie on top of those for the topography. Thus, we may clearly correlate the modulation in the photon map to the molecular layer.

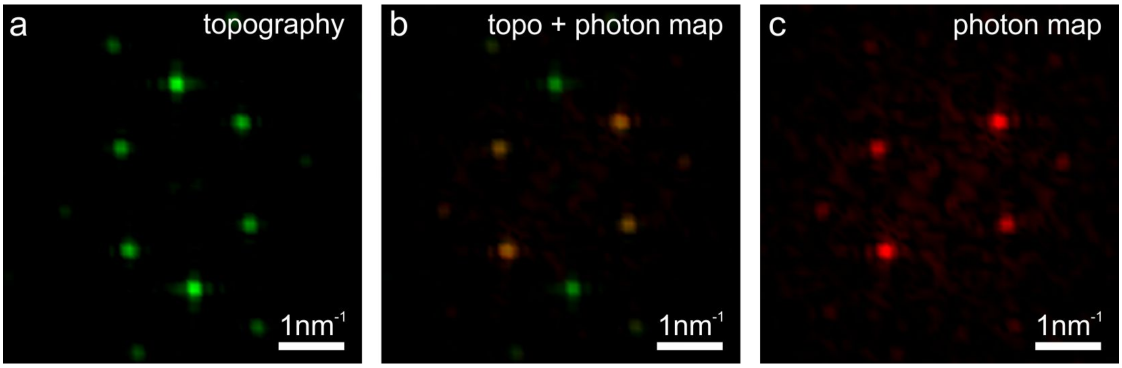

Figure 70: Fourier transforms (FTs) of a) the topography and c) the molecularly resolved photon map of a C_{60}-domain on Ag(111). b) Superposition of both FTs.

As one would expect, the Fourier transform of the topography yields a sixfold set of intensity peaks ("reflexes")[2]. Surprisingly, in contrast, in the Fourier transform of the photon map two distinct reflexes are missing.

---

[2] The intensity peaks in the FT yield a distorted hexagon. C_{60} on Ag(111) forms hexagonal domains [129]. The distortion results from a distortion of the STM images due to different gains of the piezo voltages in x- and y-direction. These were not corrected, as here, they do not affect any of the discussed matters.

10

DISCUSSION: LIGHT EMISSION INDUCED ON MOLECULES ON AG(111)

The analysis of the light emission on organic adlayers and singly adsorbed molecules presented in chapter 9 was a purely qualitative analysis based on laterally resolved photon mapping. The photon yield induced on the molecules was significantly lower than on the substrate at all examined bias voltages and for all archetype molecular species. However, the light emission was not fully attenuated on all molecular layers. Some residual emission intensity was induced, e.g. on the single layer C_{60}-domains. For this residual photon emission, a periodic modulation of the light emission intensity by the molecules, i.e. molecular resolution in the photon maps, was observed.

10.1 REDUCTION OF THE PLASMONIC LIGHT EMISSION

In literature, a reduction of the STM-induced light emission on molecules directly adsorbed on metal surfaces has been widely observed [58, 59, 94, 140, 217]. Different effects may be involved here which will be discussed in this section.

10.1.1 *Changes in the TIP spectrum*

Fig. 68 presented a photon map of a C_{60}-domain and an adjacent CuPc-domain. While the C_{60}-molecules were presumably adsorbed in first layer directly on the Ag(111)-substrate, CuPc-molecules most likely were not. Judging from the height difference between the C_{60} and the CuPc-domain, the topmost CuPc-layer was presumably part of a multi-layer molecular film with either one or several layers CuPc or a single layer C_{60} underneath. This multi-layer domain may have likely been thicker than the adjacent single layer C_{60}-domain.

In the photon map, we find an approximately full attenuation of the light emission intensity for the CuPc-domain. In contrast, for C_{60} some residual induced emission intensity can be detected.

The molecular layers increase the tip-metal distance and therefore influence the geometry of the tip-sample junction. Here, the effect of higher-layer CuPc-domain would be expected to be larger. Further, the different molecular species and layer thicknesses might affect the dielectric constant in the junction. This might have an effect on the TIP-spectrum which would in turn affect the emission intensity at a certain bias voltage.

However, a significant effect of changes in the TIP spectrum may be excluded here. The lateral transition of the light emission intensity in the photon map between both molecular domains is rather sharp. In chapter 8.5, we have learned that the electromagnetic interaction between the tip and the sample is at least several nm^2 large, probably in our case even several ten to hundreds of nm^2. If changes in the TIP spectum had a considerable influence, we would expect a gradual change in the emission intensity.

However, in our data, we observe a sharp transition of the emission intensity between both domains.

Also between the Ag(111)-substrate and the C_{60}- and PTCDA-domains a sharp transition of the emission intensity is observed in the photon map. Further, singly adsorbed CuPc molecules, much smaller than the electromagnetic interaction area are clearly resolved in the photon maps. Thus, no significant influence of a possible change in the TIP spectrum on the emission yield is expected here. Instead, as in the discussion for the contrast mechanisms for the photon maps of pristine Ag(111)-surfaces, we have to look for factors that locally affect the excitation efficiency.

10.1.2 *Increased Tip-Sample Separation*

In literature, the reduction of the light emission intensity induced on organic adlayers on metal surfaces is often assigned to the increased tip-metal distance and the resulting weakened coupling between the two [58, 140, 218]. Such an effect of organic layers, e.g. C_{60} on Au(111), is also supported e.g. by calculations by Tao et al. [218]. The authors show that the induced charge densities with and without the dielectric molecular layer are very similar, however, the increased tip-metal distance when tunneling on the molecules leads to a significantly weaker electromagnetic coupling. The calculated emission intensities are decreased by about 50% [218].

Fig. 71 shows line profiles though the topographic images and corresponding photon maps of Ag(111) surfaces covered with the different archetype molecules. The sample addressed in Fig. 71 a and b exhibits both CuPc- and C_{60}-molecules. The singly adsorbed CuPc-molecules lie flat on the surface. Their height of about 3Å is significantly lower than that of the C_{60}-domains (about 7Å) (see Fig. 71 a). Still, the reduction of the photon yield observed in the photon maps for both molecular species is very similar. In both cases, the emission intensity is attenuated by around 85%. The remaining light emission induced when tunneling above the molecules is still slightly above the dark count rate.

Fig. 71 addresses a sample with a submonolayer coverage of PTCDA measured with a different tip. The PTCDA domains on Ag(111) exhibit an apparent height of 1.7Å (see Fig. 71 c). Here, the photon signal is attenuated almost completely. Even though the heights of the molecular structures are significantly different, the relative reduction of the photon yield in all three cases is similarly large (around $85-95\%$, see Fig. 71 b, d).

The impact of an effect regarding the tip-metal distance might in particular depend on the overall strength of the coupling between the tip and the metal as well as on the specific tunneling distance and might therefore be tip dependent. However, even with an uncertainty of around 10%, the large similarities of the relative reductions of the emission intensity for CuPc and C_{60} observed in 71 b cannot be explained by a pure spacing effect of the molecules, e.g. a reduced field enhancement. If the molecules would act as a pure spacer layer, a significantly larger reduction of the light emission intensity e.g. by the higher C_{60}-domains would be expected. This is not the case here.

Further, several findings in literature oppose a mere effect of the molecules as a spacer layer. Geng et al. present a detailed study of one and two layer thick C_{60}-domains on Au(111) [58]. The authors find a clear decrease of the emission intensity

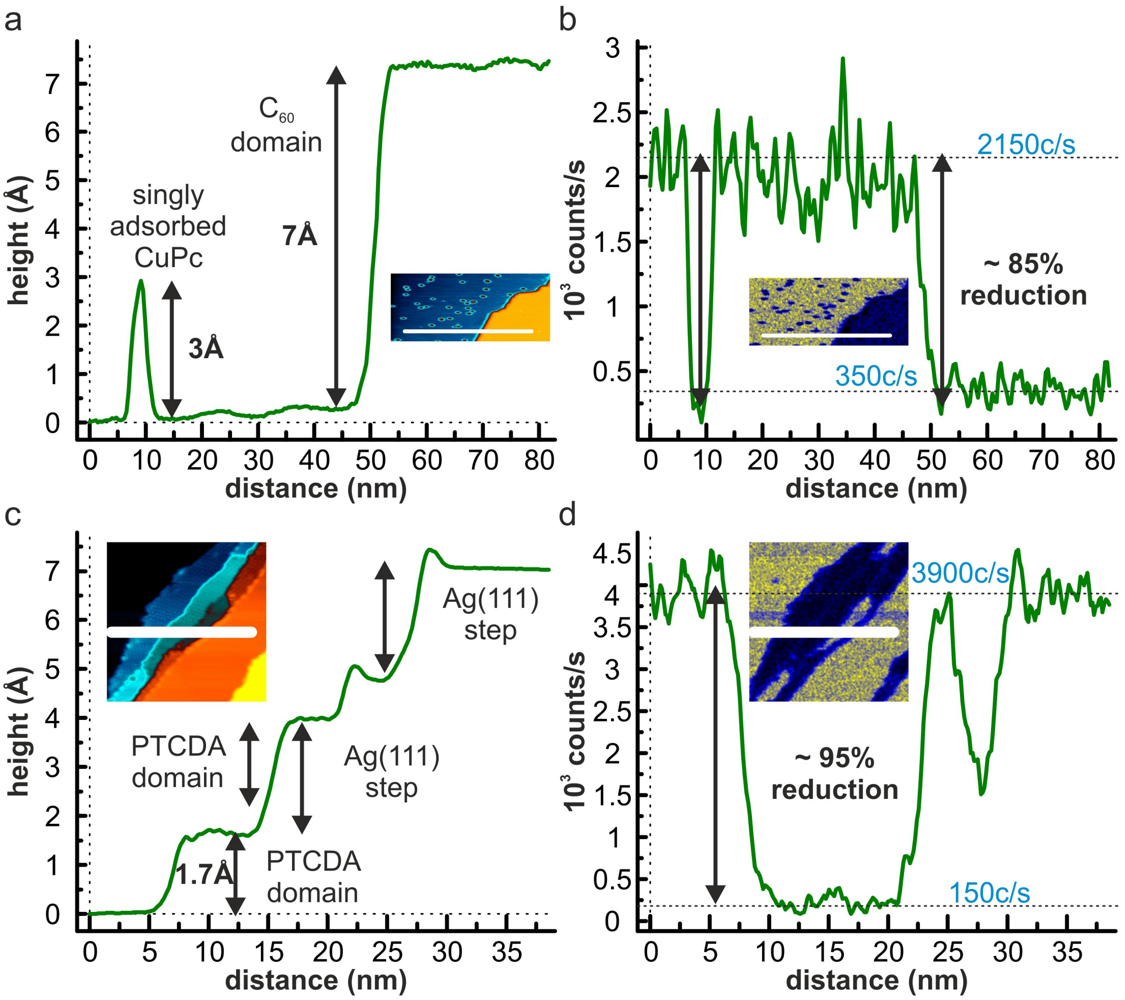

Figure 71: The effect of different archetype molecules on Ag(111) on the induced photon yield. Line profiles through a) the topography and b) the corresponding photon map for a Ag(111) sample covered with dense C_{60}-domains and singly adsorbed CuPc-molecules. c) and d) line profiles for a Ag(111) sample exhibiting several PTCDA domains. The given count rates were corrected for the dark count rate. a), b) $V_{sample} = 2V$, $I = 30pA$, $T = 80K$; c), d) $V_{sample} = 2V$, $I = 100pA$, $T = 80K$.

on the molecular layers. However, the presented spectra of the photon yield show approximately equally high maximum induced emission yields occurring at different bias voltages for one and two layers C_{60}. If a decreased coupling due to the increased tip-metal distance would play a dominating role here, a lower emission yield for the double-layer would be expected.

Further, Hoffmann et al. and Dong et al. present data of porphyrin molecules adsorbed on Cu(111) and Cu(110) surfaces, respectively [198, 219]. Here, the molecules "stand up" on tilted functional groups, so that their core is lifted from the substrate. The molecules definitely increase the tip-metal distance. However, the photon yield above the molecules is even increased as compared to the substrate.

This cannot be understood when assigning a dominating role to the tip-metal distance and the associated field enhancement. Rather, our findings and several observations made in literature propose some additional active role of the molecules that influences the light emission yield.

10.1.3 *The LDOS of the Molecules*

In chapter 8.6 and 8.7, we discussed that the LDOS of final states available for elastic and inelastic transitions provided by the sample impacts the ratio of inelastic to elastic tunneling channels and therefore the inelastic tunneling probability. Organic molecules adsorbed on a surface modify the LDOS of the sample.

E.g. in the calculations by Tao et al. [218] that stress the leading role of the weakened electromagnetic coupling due to the increased tip-metal distance for the reduced light emission efficiency, the LDOS of the molecules was not considered.

However, since the tunneling probability scales exponentially with the barrier width (see fundamentals), with a high probability, the electrons tunnel into the LDOS of the molecules. A ballistic tunneling through the molecules directly into the Ag(111)-substrate is relatively unlikely [58] and would be expected to yield only a maximum of a few percent of the overall tunneling current [132]. This suggests an active involvement of the LDOS of adsorbed molecules in the inelastic tunneling processes that excite the TIPs as has been shown in several experiments [13, 14, 58] (see also chapters 12 and 13). Indications that the molecular states serve as final states for inelastic tunneling can e.g. be observed in form of high energy cutoffs in the spectra of the emitted (see also chapter 13.2 in this thesis).

Thus, the different sample LDOS provided by the molecules might change the ratio of elastic and inelastic tunneling channels in favor of a decrease of the inelastic tunneling probability as compared to the substrate. However, for molecular layers adsorbed on noble metal surfaces without further decoupling, generally a reduction of the photon yield is observed [58, 59, 94, 140, 217]. Upon further decoupling, also higher count rates as compared to the substrate have been induced on the molecules [198, 219]. Such correlation between the induced emission intensity and the coupling strength between the molecules and the substrate points to another effect of the molecules on the TIP excitation efficiency (see section 10.1.4 below).

10.1.4 *Coupling of the Molecules to the Substrate*

In an electromagnetic picture, the molecules may be viewed as dynamic dipole oscillators which are driven by the inelastic tunneling current. Here, the coupling between the molecules and the substrate may damp these oscillations by non-radiative energy transfer and reduce the coupling to the TIP-modes leading to the general attenuation of the emission intensity ([220] all this paragraph).

There are several possible ways of non-radiative energy transfer between the molecules and substrate. Adsorbed directly on metallic substrates, the coupling between the molecules and the substrate e.g. allows for charge transfer. Further, dipole-dipole interactions may play a role [220]. These two effects also quench the light emission from direct electronic excitations of the molecules [57, 59] (see below).

The lifetime of the inelastic electrons within the molecules further affects the efficiency with which the dynamic dipole of the molecules may be driven. For molecules that exhibit a strong coupling to the substrate, fast charge transfer to the substrate reduces the dipole oscillation probability [220]. For molecules directly adsorbed on noble metals such as Ag as for the data presented here, a rather strong coupling between the molecules and the substrate is expected, matching the observed attenuation of the emission intensity.

10.2 THE ORIGIN OF THE LIGHT EMISSION INDUCED ABOVE THE MOLECULES

Even though the induced light emission is significantly reduced above the molecules, some residual light emission intensity may still remain. For example, this is clearly observed for the C_{60}-domain shown in Fig. 68. The origin of this residual light emission induced above the molecules used to be a highly discussed topic. In early publications, direct molecular fluorescence was proposed to play a role even for single layer organic domains adsorbed directly on metallic substrates [217, 221]. However, under these circumstances, the lifetimes of the tunneling electrons within the molecular electronic states are too short to induce electronic transitions within the molecule. As elaborated above, a variety of non-radiative decay channels, e.g. charge transfer and dipole-dipole interaction, provide a fast energy transfer to the substrate and quench molecular fluorescence [59, 222].

Light emission from the direct radiative decay of electronic excitations of the molecules can only be observed if the lifetime of the electrons within the molecules is prolonged by a sufficient decoupling from the metallic substrate by a spacer layer of some sort, e.g. a thin layer of salt [15, 19] or oxide [16, 18], or several layers of organic molecules [223]. For thin organic layers adsorbed directly on metallic substrates, instead, more recent publications faithfully assign the induced light emission to the radiative decay of TIP-modes which are purely excited by inelastically tunneling electrons [13, 14, 30, 31, 198].

In the following, we want to analyze the lateral variation of the residual light emission in more detail.

10.3 MOLECULAR RESOLUTION IN PHOTON MAPPING

For the C_{60}-domain, a periodic modulation of the light intensity was observed in the photon maps (see Fig. 68, Fig. 69, Fig. 72). Fig. 69 demonstrated that these modulations are not the mere result of fluctuations in the tunneling current. Rather, the light emission intensity seems to be modulated by the molecular layer in some more intrinsic way.

10.3.1 *Correlation between the Topography and the Overall Photon Yield*

In Fig. 70 the Fourier transforms of the corresponding molecularly resolved areas in the topography and the photon map were superimposed. The observed periodicities for the photon map correspond to those of the topography. To allow for a correlation between the lateral distribution of the induced overall photon yield and the topographic structure of the molecular domain, in Fig. 72 also the topographies and respective photon maps were superimposed.

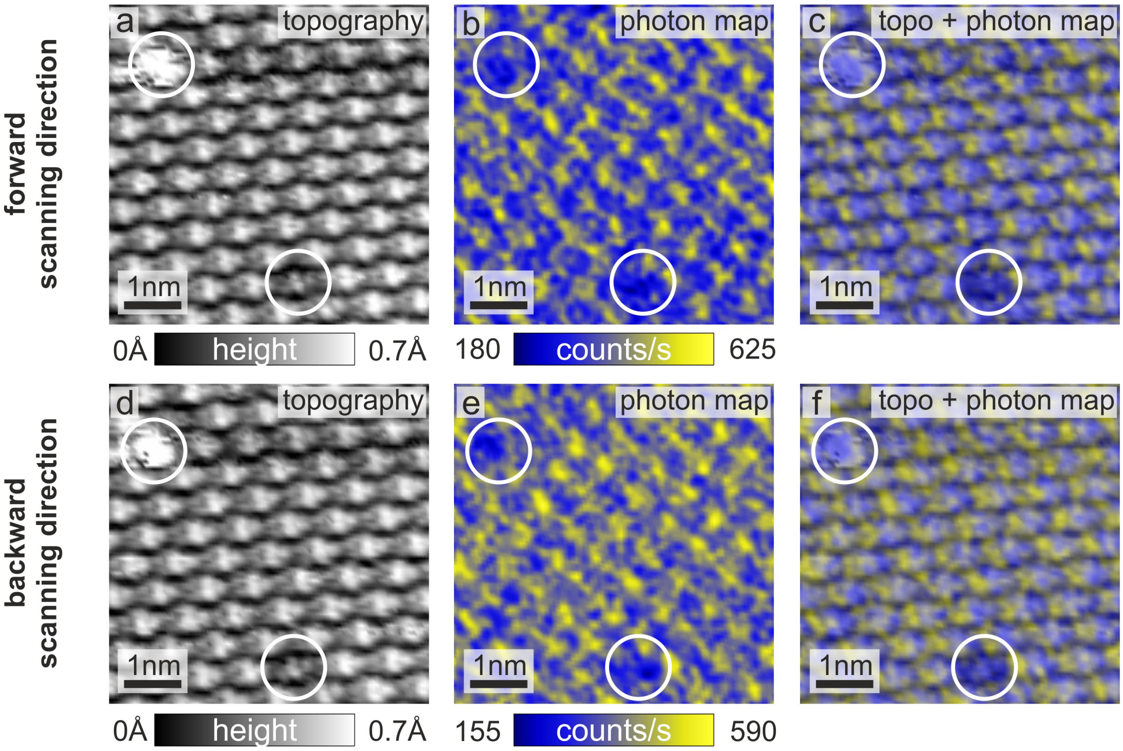

Figure 72: Lateral correlation between the topography and the induced photon yield. a) Detail of the topography and b) the corresponding simultaneously acquired photon map of a C_{60}-domain acquired in forward scanning direction (left to right). c) Superimposed image of both. d-f) Corresponding data recorded in backward scanning direction (right to left). The white circles indicate two defects in the molecular layer. The count rates given on the intensity scales of the photon maps were corrected for the dark count rate. $V = 2.5V$, $I = 15pA$, $T = 80K$.

The modulation of the overall photon yield can be clearly correlated to the topographic structure of the molecular layer. However, the positions of the highest induced emission yield are found to lie asymmetrically with respect to centers of the molecules.

For both scanning directions (left to right, see Fig. 72 a-c, and right to left, see Fig. 72 d-f) the maxima of the overall photon yield equally occur upon excitation above the respective left flank of each molecule. This further proves that the observed effect is not an artifact e.g. due to the feedback loop.

Molecular resolution in photon mapping of C_{60}-domains has been observed before by other groups [14, 58, 140, 217]. One of the earliest works treating the light emission from molecule covered surfaces was published by Berndt et al. in the early 1990's. The authors present molecularly resolved photon maps of a C_{60}-layer on Au(110) [140, 217]. Cross sections reveal that the maxima of the emission yield in the photon map cooccur to maxima in the topography.

A rather recent work by Geng et al. analyzes the light emission from C_{60} on Au(111) [58]. The authors present molecularly resolved photon maps which show an inverse correlation between maxima in the topography and maxima in the photon yield.

In our data, the largest emission yield is neither induced on the centers, nor in the valleys in between the molecules. In order to understand this behavior and the deviations from the results of other groups, we will first discuss possible origins of the molecular resolution in more detail.

10.3.2 *Modulation of the Tip-Metal Distance*

When the tip is scanned across the molecules in constant current mode, the tip follows the contour of the molecular layer. Thereby, the distance between the tip and the metal substrate underneath the molecules is modulated. Geng et al. hold the resulting modulation of the local field enhancement responsible for the observed molecular resolution in their case [58]. This well matches their data, where highest photon intensity is induced in the valleys in between the molecules.

As for our case, the correlation between the topography and the molecular layer is not as straightforward which becomes immediately clear when looking at the superposition of the topography and the photon map depicted in Fig. 72. Also, the part of the C_{60} layer imaged in Fig. 72 exhibits two surface defects. The defect in the upper left corner of the images appears as a protrusion in the topography. In contrast, the defect at the bottom of the imaged area is a molecule which appears slightly indented into the layer. For both defects, we observe a general reduction of the photon yield. At the right edge of the defect that appears as a protrusion, the photon yield is additionally enhanced. This further points against a leading role of the modulation of the tip-metal distance in our case. Here, we have to consider further factors that play into the variations of the emission intensity.

10.3.3 *Lateral Variations of the LDOS*

For the contrast mechanisms in photon maps acquired on Ag(111), we were able to assign a dominating role to lateral variations in the LDOS which cause a variations in ratio of inelastic to elastic tunneling channels (see chapter 8.6.4). As pointed out in section 10.1.3, the molecules provide final states for the elastic and inelastic tunneling. Thus, lateral variations of the LDOS provided by the molecules, i.e. the shape of different molecular orbitals providing final states for elastic and inelastic transitions, would be a likely cause for the molecular resolution observed in the photon maps.

In particular, when the tip follows the elastic contour, i.e. the topography, the overlap with the LDOS providing final states for inelastic tunneling and the ratio of inelastic to elastic tunneling channels may be altered resulting in a modulation of the photon emission intensity.

In their study, Geng et al. apply site specific dI/dV-measurements in which they find the LDOS of final states for inelastic transitions to be nearly equal on top and in between the molecules [58]. The small variations in the LDOS which the authors observe reveal a slightly increased LDOS at the energies for final states on top of the molecules. This would rather support an increased inelastic tunneling probability at these positions. Still, the opposite tendency is found for the emission yield in the photon maps. In consequence, Geng et al. exclude a major contribution of the LDOS to the molecular resolution. However, the authors neglect the effect of variations in the elastic tunneling channels. The excursion of the tip observed in the topography indicates a clear decrease of the number of overall (mainly elastic) tunneling channels in between the molecules which might in fact significantly modulate the inelastic tunneling probability when the LDOS providing inelastic channels does not follow the exact same contour.

10.3.3.1 *Photon Mapping at Constant Current vs. Constant Height*

A different group of authors, Lutz et al., study the same system as looked at in this thesis, a monolayer C_{60} on Ag(111) [14] (and supporting information). These authors mainly treat the case of tunneling from the sample to the tip. This is the opposite tunneling direction as for the photon maps presented here and by Geng et al. in Ref. [58].

Constant current photon maps shown in the supplementary information to Ref. [14] by Lutz et al. exhibit significantly different intensity distributions for data recorded at ± 3V, respectively (see Fig. 73). In the topography, the C_{60}-molecules appear as protrusions at both bias voltages. While at -3V highest intensity in the photon map is found in between the molecules, at $+3$V the highest intensity is observed somewhere on the molecules. This contradicts a leading role of the tip-metal separation and is another factor that supports an influence of the LDOS of the molecules for the molecular resolution.

As opposed to Geng et al., Lutz et al. also propose that the lateral variation of the LDOS of the molecules does in fact modulate the inelastic tunneling probability. To disentangle the influence of the tip excursion, the authors gather both, dI/dV-maps and photon maps at constant height. They find a correlation between the shape of the C_{60}-molecular orbitals in the dI/dV-maps and the shapes of the features in the photon map.

Here, it is important to note that when photon maps are recorded at constant height, the resulting changes in the tunneling current when scanning above the molecule will naturally modify the number of incident electrons. This will in consequence also modulate the number of inelastic tunneling processes. To obtain incontrovertible data, the according photon maps would have to be normalized by maps of the tunneling current. The authors of the publication discussed above state that the interpretation of their results still applies after such normalization [47].

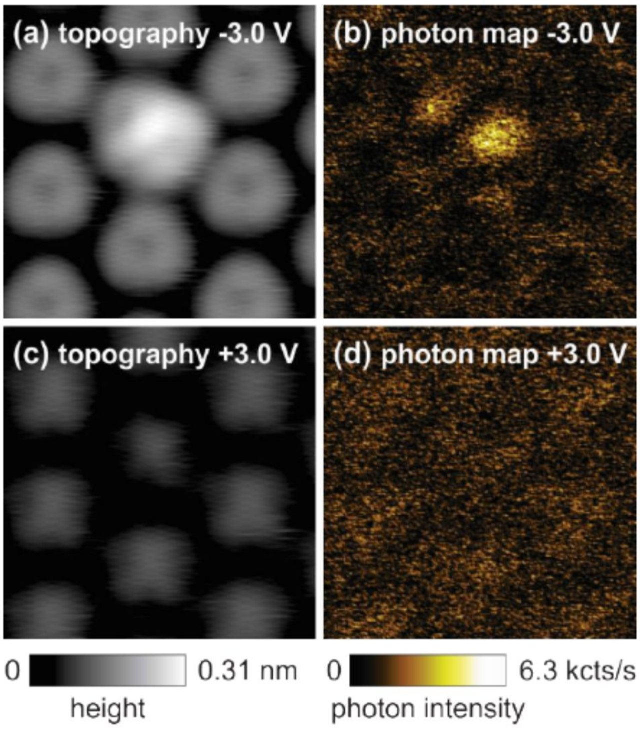

Figure 73: Topographies and corresponding photon maps for a monolayer of C_{60} on Ag(111) reported by Lutz et al.. The data were recorded at constant current for a bias voltage of ±3V, respectively. In the middle of the imaged area a different organic molecule is adsorbed on top of the C_{60}-layer. It is also present for the images acquired at +3V, however, it is "invisible" in the topography at this bias voltage. For the purposes of our discussion here, the effect of this additional molecule may be ignored. Reprinted with permission from the supplementary information to Ref. [14]. Copyright 2013 American Chemical Society.

The molecularly resolved data presented in this thesis was gathered at constant current and thus shows entangled information about the lateral distribution of the different molecular LDOS providing final states for elastic and inelastic tunneling.

10.3.4 *Asymmetries between the Topographic Structure and the Photon Maps*

One striking fact when correlating the overall photon yield to the topography that still needs to be discussed is the asymmetry of the lateral distribution of the overall photon yield with respect to the center of the molecules with the topography. Here, two different factors might play a role.

10.3.4.1 *Orientation of the Molecules within the Molecular Layer*

One effect that might play into the asymmetry is the orientation of the molecules with respect to the substrate [47]. For the molecularly resolved data presented in chapter 9, the electrons tunnel from the tip to the sample. Final states for the inelastic transitions may e.g. be provided the LUMO of the C_{60} [58] or the LUMO+1 depending on the tunneling energy, i.e. the initial state energy of the tunneling electrons.

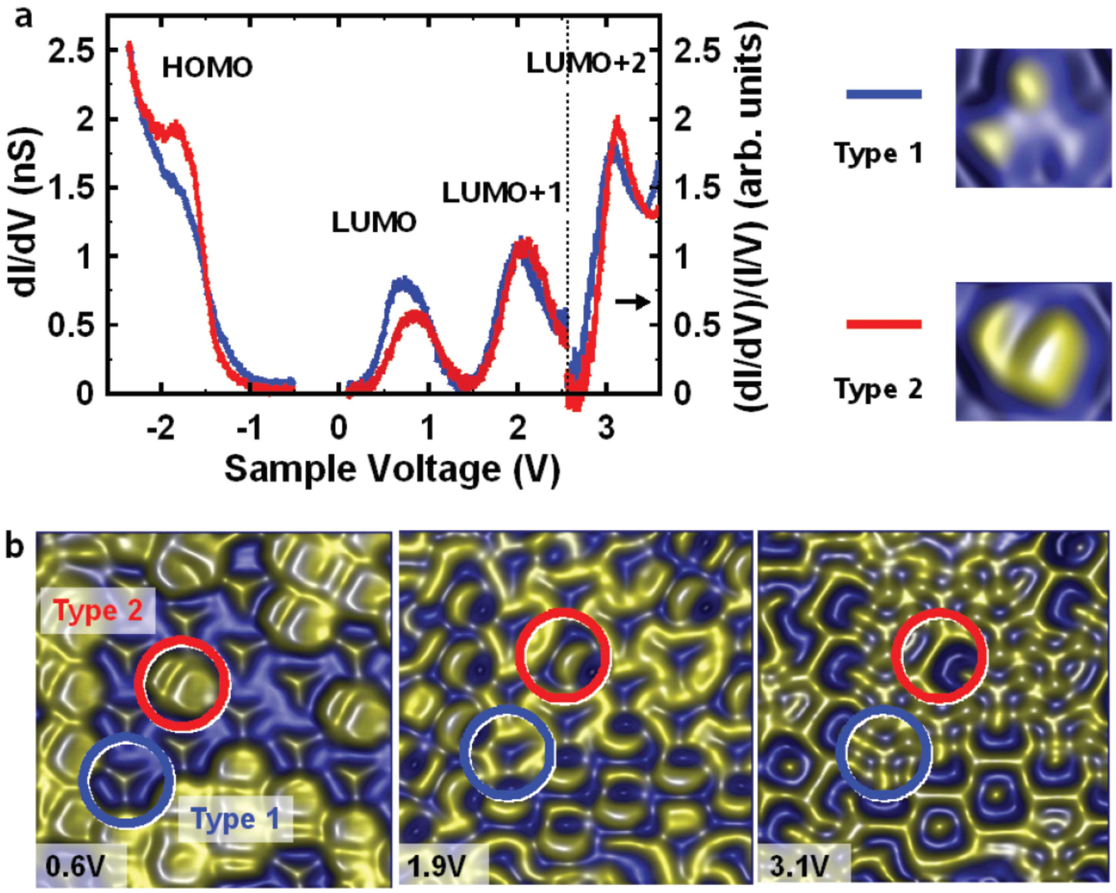

Figure 74: dI/dV-data for C_{60} with different adsorption orientations on Au(111). a) dI/dV-spectra. b) dI-dV-maps for different bias voltages applied to the sample as indicated in the images. The molecular shape in the images varies depending on the adsorption configuration of the molecules with respect to the substrate. In particular, two different orientations are found in the imaged area: C_{60} adsorbed with a hexagon facing down (type 1) and C_{60} adsorbed on a double bond between two adjacent hexagons (type 2). Reprinted from Ref. [133] under the creative commons license [224]. Copyright 2008.

Schull et al. showed for C_{60}-domains on Au(111), that depending on the orientation of the C_{60}-molecules within the molecular layer, the lateral distribution of the LDOS provided by the C_{60} molecular orbitals may be quite different [133, 225]. Data from Ref. [133] is shown in Fig. 74. For the molecules adsorbed with a hexagon facing down, the LUMO has a trifold star-like shape (type 1 in Fig. 74), for the molecules adsorbed on a double bond between two adjacent hexagons, the LUMO resembles a twofold split ellipse (type 2 in Fig. 74) [133]. In particular, for the second configuration, the LDOS exhibits a more uniform lateral distribution. Similar effects may also occur on Ag(111). Thus, depending on the orientation of the molecules, the lateral modulation of the density of final states for elastic and inelastic transitions, and in consequence of the inelastic tunneling probability, may be modulated.

Different orientations of the molecules within the domains studied in the experiments presented in this thesis as well as by Geng et. al [58] and Lutz et al. [14], might result in a different influence of the LDOS for the lateral modulation of the light emission intensity and alter the effects observed in the photon maps.

An asymmetric distribution of final states, similar to the case e.g. found for the C_{60}-LUMO adsorbed on the double bond between two adjacent intramolecular hexagons on Au(111) (see Fig. 74, type 2) [133], may manifest itself in the photon map and might explain the asymmetry between the topography and the photon map in our data. At closer look, a certain asymmetry between the left and the right flanks of the C_{60}-molecules is already visible in the topography. This would support such a claim. A combination of the different symmetries of the molecular orbitals supporting the elastic and inelastic tunneling channels may also explain the symmetry reduction between topography and photon map observed in Fig. 70.

10.3.5 *Distribution of the k-Vectors of the Inelastically Tunneling Electrons*

The lateral distribution of the overall photon yield with respect to the centers of the C_{60} is approximately equal for all molecules depicted in Fig. 72. To explain the asymmetric distribution of the photon yield by the orientation of the molecules alone would require that the entire domains of C_{60}-molecules would exhibit the same orientation to the surface.

An effect independent of the molecular LDOS and the orientation of the molecules that might additionally play into the molecular resolution are changes in the direction of the tunneling current. Depending on where the tip tunnels above the molecules, the direction of the k-vectors of the inelastically tunneling electrons may change. A different fraction of electrons tunneling with a momentum parallel to the dipole moment of the TIPs may affect the coupling strength between the inelastically tunneling electrons and the plasmonic excitation as discussed in chapter 8.6.1 for the contrasts in photon maps for Ag(111). While this effect alone is too small to explain the variations up to 75% in the overall photon yield induced on the C_{60}-layer, it might still be an additional factor modulating the emission intensity.

In particular, the orientation of the dipole moment of the TIPs depends on the specific tip, e.g. for asymmetric tips it may not be exactly parallel to the surface normal. This may result in different portions of the tunneling current that are oriented parallel to the dipole moment of the TIPs on opposing flanks of the molecules as observed in our data (see Fig. 75).

Irregularly shaped tips have been reported to yield asymmetric photon maps [16]. In the experiment presented here, a cut Pt-Ir tip was used. The tip was indented into the Ag surface several times in order to cover its surface with Ag. Thus, the tip was very likely of rather asymmetric shape which lets an impact of the described effect seem quite probable.

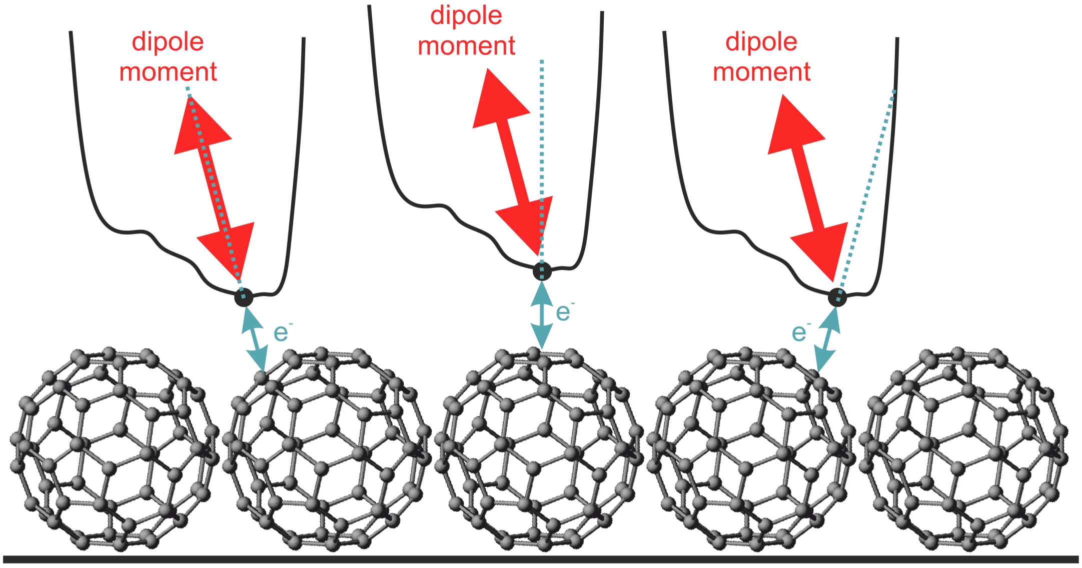

Figure 75: Schematic indicating the possible effect of a changing distribution of k-vectors of the tunneling electrons on the TIP-excitation efficiency. Depending on the position of the tip above the molecules, the k-vektors of the electrons may possess a different direction. The orientation of the dipole moment of the TIPs is governed by much larger scale geometries and stays unaffected. This changes the fraction of the inelastic tunneling current oriented parallel to the dipole moment of the TIPs. Note that the drawing is not to scale. In particular, the relative size of the tip responsible for the electromagnetic interaction with respect to the molecules is much larger than depicted here.

10.3.6 *Comparison to Complementary Techniques: BEEM*

Bannani et al. used ballistic electron emission microscopy (BEEM) to study the ballistic electron transport through monolayer thick C_{60} layers on Bi(111)/Si(100) [132]. The BEEM technique can be viewed as a partially complementary technique to STM-LE. It analyzes the ballistic fraction of the tunneling current, i.e. the tunneling electrons which do not loose energy due to interaction with the sample either during the tunneling process itself or during their subsequent transport through the sample[1]. In the BEEM-maps, the authors observe a donut-like shape of the molecules. They find the highest fraction of ballistic electron transport to occur at rotationally symmetric positions on the sides of the molecules. The lowest fraction of ballistic current is found when tunneling above the centers of the molecules.

Intuitively, the fraction of ballistic transport channels would be expected to be inversely correlated to the excitability of the sample at a specific site. Thus, if plasmonic excitations were the dominating channel of energy loss for the tunneling electrons, an inverse behavior of the intensity in BEEM- and photon maps would be expected. Here, this would correspond to the case observed by Berndt et al., where the photon emission intensity is greatest upon excitation in the center of the molecules. However, the BEEM is sensitive to all processes of energy loss which the electrons may encounter, e.g. molecular excitations that decay non-radiatively but also other forms of scattering during transport within the metal layer.

10.3.6.1 *Defects Within the Molecular Layer*

Fig. 76 displays a detail of the molecularly resolved C_{60}-domain in our data. It reveals a defect in the molecular layer which is marked by a circle. In the topography (Fig. 76 a), this defect appears as a slight indentation of a single C_{60} molecule into the molecular layer. No severe effects related to this defect have been observed in the simultaneously acquired dI/dV-map or the image of the tunneling current (not shown). However, the drop of the emission intensity observed at the according position in the photon map (Fig. 76 b) is quite significant.

Here, a change in the LDOS of final states for the excitation may explain both, the appearance of the defect in the topography and the reduced intensity in the photon image. Such a change in the LDOS may e.g. be induced by a doping of the C_{60}-molecule.

In their BEEM study of C_{60} on Bi(111)/Si(100) [132], Bannani et al. specifically address such a specific C_{60}-molecule within a molecular island. This molecule also appears slightly indented in the topography, very similar to the case observed here. The ballistic transport through this specific molecule is found to be greatly enhanced. The authors suggest that the molecule may have been doped, e.g. by an alkaline atom in the vicinity. The associated shift of the electronic states of the molecule would lead to an increased coupling to the substrate. For our case, an increased number of ballistic transport channels would in turn mean a reduced fraction of excitation channels. Further, the increased coupling between the molecules and the substrate would also favor non-radiative energy transfer between both and therefore reduce the photon yield.

---

[1] In BEEM-experiments this is a thin metal film on a semiconducting substrate.

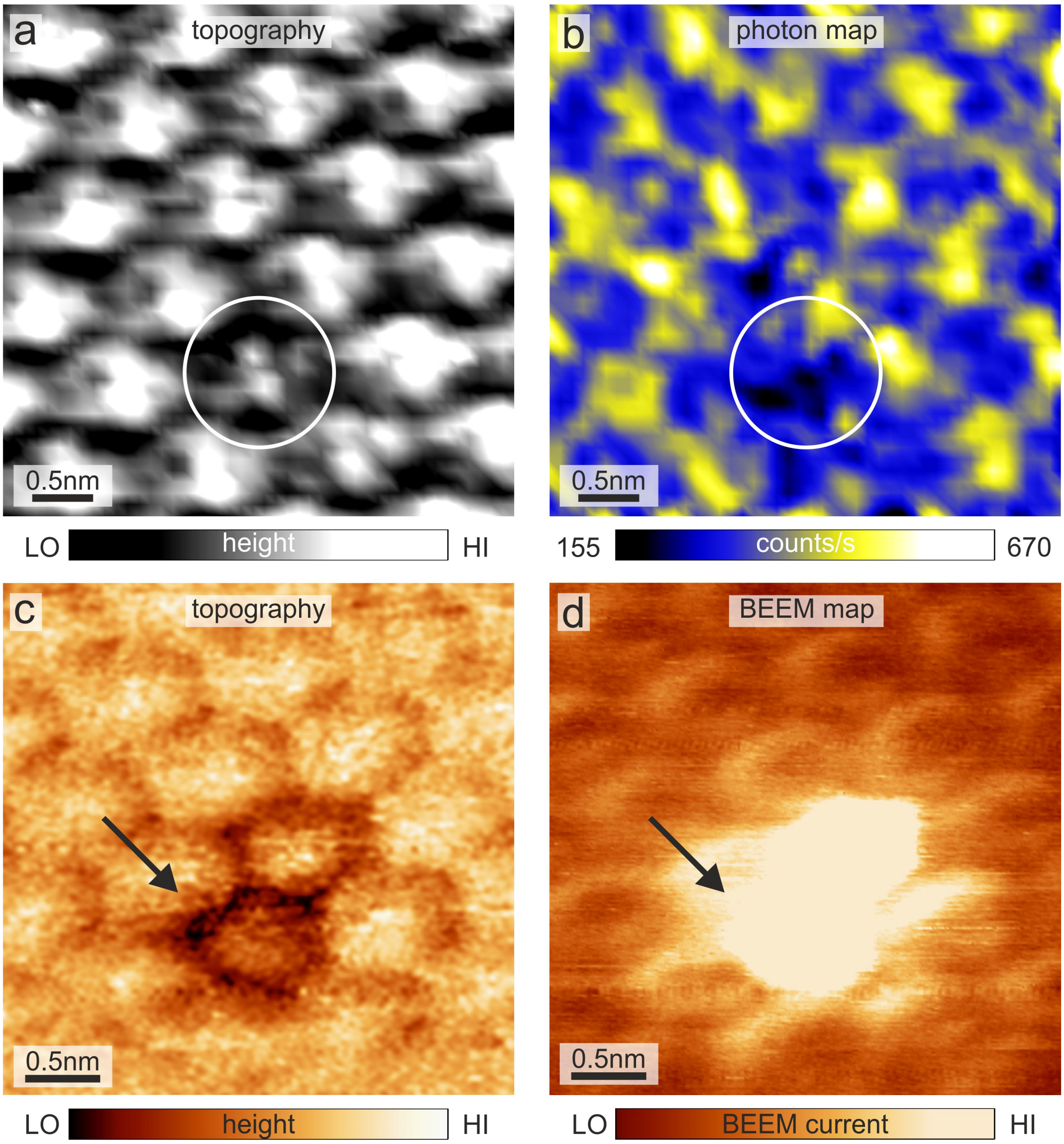

Figure 76: Comparison between STM-LE and BEEM data. a) Topography and b) corresponding photon map focusing on a defect in the C_{60} molecular layer on Ag(111) in our experimental data. $V = 2.6V$, $I = 15pA$, $T = 80K$. c) Topography and d) BEEM-map for C_{60} on Bi/Si(100). Defects in the C_{60} layers are indicated by circles and arrows. BEEM data courtesy of C.A. Bobisch, A. Bannani, and R. Möller. $V = 2.1V$, $I = 40pA$, $T = 150K$. c) and d) similarly published in [132], [226].

10.4 SUMMARY

In chapters 9 and 10, we presented and discussed photon maps of Ag(111)-surfaces which were partially covered with different archetype organic molecules. We were able to show that our newly built STM-LE setup is capable of performing powerful state-of-the-art measurements including highly resolved photon mapping. The data reveal a considerably reduced photon yield induced on the molecules as compared to the substrate. Despite the general reduction of the emission intensity induced on molecular layers on Ag(111), the photon map of the residual light emission induced on a monolayer thick C_{60}-domain yielded molecular resolution. Here, we discussed the impact of different effects on the overall photon yield for which several effects might play a role.

Our data shows that the role of the molecules goes beyond that of a mere spacer layer increasing the separation distance between the tip and the metal. The LDOS of the molecules is actively involved in the excitation of the TIPs. In particular, the molecular LDOS may manipulate the ratio of inelastic to elastic tunneling channels. This may lead to a decrease of the inelastic tunneling probability.

Further, the coupling between the molecules and the substrate may damp the TIP excitation by non-radiative energy transfer leading to the general attenuation of the emission intensity induced on the molecules.

The molecular resolution observed in the photon maps may be explained by variations in the inelastic tunneling probability due to lateral variations in the LDOS of the molecular layer providing final states for elastic and inelastic transitions.

Additionally, a change in the direction of the k-vectors of the electrons when tunneling above the molecules may modify the TIP excitation yield by changing the fraction of electrons tunneling parallel to the dipole moment of the tip. The latter effect would depend on the specific tip used in the experiment and might explain differences between our data and data presented in literature. Additionally, this might explain the asymmetric distribution of the maximum induced photon yield with respect to the centers of the molecules revealed by the superposition of our topographic data and photon maps.

The fundamental understandings gained in the discussion here will serve as a prerequisite to interpret data acquired on more complex molecule-covered substrates which will be presented in the following chapters.

11

LOW COVERAGES OF BISMUTH ON CU(111)

The previous chapters presented STM-LE data on pristine and molecularly covered Ag(111) surfaces. They gave an introduction into the interpretation of STM-LE-data. Now, we want to address a more complex sample system, the initial monolayer of bismuth (Bi) on Cu(111) which will be shown to have rather peculiar properties as a substrate for different archetype organic molecules.

Low coverages of Bi on Cu(111) or Ag(111) have recently attracted a lot of attention due to their peculiar electronic properties [114–116, 119, 227–229]. Even though the species are immiscible in bulk, Bi forms $BiAg_2$- and $BiCu_2$-alloys in the very top surface layer. These surface alloys have been shown to exhibit a giant spin orbit splitting of their surface states [114, 117]. When the Bi-coverage is increased beyond the amount needed for a complete alloyed layer, a gradual dealloying into a monolayer thick Bi-overlayer takes place [230, 231].

In the formation of different surface structures and their general electronic properties, Bi/Ag(111) and Bi/Cu(111) behave mostly analog. Thus, here, we may faithfully rely on the literature for both systems, when discussing the Bi/Cu(111)-data presented in this thesis.

11.1 BI ON CU(111): TOPOGRAPHIC SURFACE STRUCTURE

11.1.1 *The initial growth of Bi on Cu(111) and Ag(111)*

At very low coverage, the Bi-atoms embed into the (111)-ordered Cu- or Ag-surface and form a dilute surface alloy [230, 232]. This incorporation of the larger Bi-atoms is favorable since it relieves tensile stress from the (111)-surface [230, 231, 233]. With increasing coverage, the Bi-atoms order into a dense $\sqrt{3} \times \sqrt{3}$-reconstruction, which is fully developed at a Bi-coverage of about 1/3ML[1]. Upon further increasing the Bi-coverage, the incorporation of additional Bi-atoms would lead to an unfavorable compressive stress, thus a gradual dealloying of $\sqrt{3} \times \sqrt{3}$-reconstruction into a monolayer-thick Bi-overlayer takes place [230–233].

The atomic structure of the $BiCu_2$ surface alloy and the initial Bi-monolayer are schematically depicted in Fig. 77.

Once the dealloyed Bi-monolayer is closed, Bi-domains with a height of multiples of one bilayer start to form [230, 231].

---

[1] Here, we use the convention that the coverage is given in units of Cu(Ag)(111) surface atoms. The $\sqrt{3} \times \sqrt{3}$-ordered surface alloy has a chemical composition of $BiCu_2$ ($BiAg_2$), i.e. when the surface is fully covered with the $\sqrt{3} \times \sqrt{3}$-reconstruction every third Cu(Ag)-surface atom is replaced by a Bi atom. In literature, the Bi-coverage is sometimes also given in units of an atomic Bi(110)-layer (9.3×10^{14} atoms per cm^2 [231]). The density of this layer is significantly smaller than that of the (111)-ordered Cu(Ag)-surfaces (e.g 1.38×10^{15} atoms per cm^2 for Ag(111) [231]). Therefore, a Bi-coverage of 1/3ML in terms of Ag(111) surface atoms corresponds to a higher value of 0.5ML in therms of Bi(110) atomic layers.

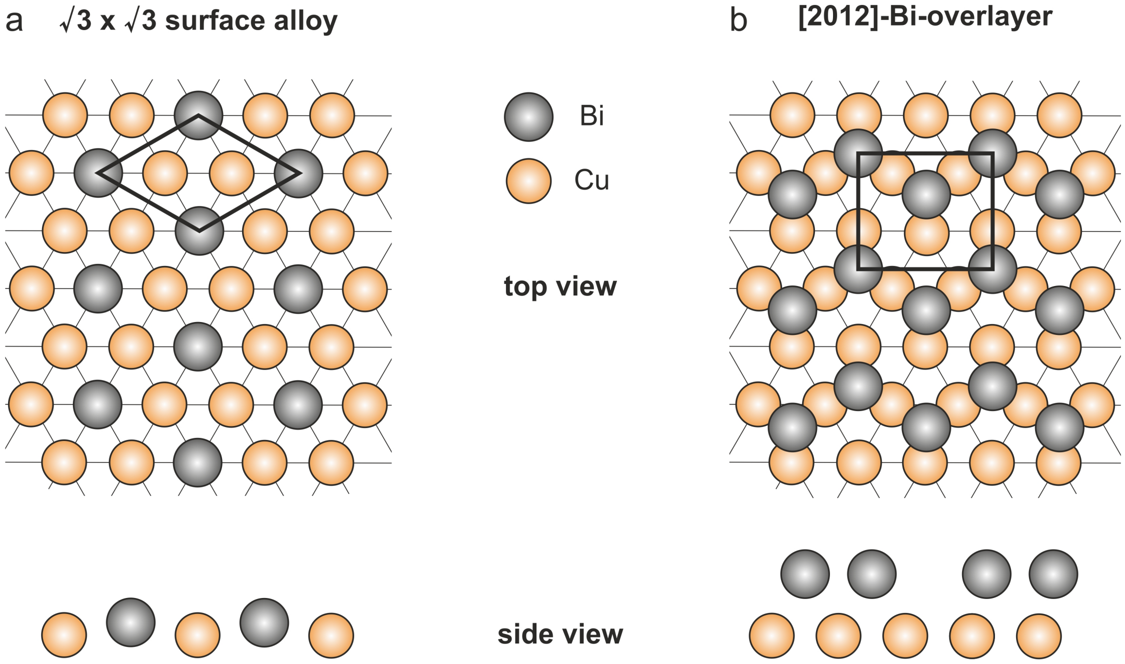

Figure 77: Schamatics of the atomic structure of the BiCu$_2$ $\sqrt{3} \times \sqrt{3}$-ordered surface alloy (a) and the initial dealloyed $\left(\begin{smallmatrix}2 & 0\\ 1 & 2\end{smallmatrix}\right)$-ordered Bi-monolayer (b).

11.1.2 *The initial Bi-Monolayer on Cu(111)*

The experiments presented in chapter 12 focus on the initial Bi-monolayer on Cu(111) as a substrate to organic molecules. In literature, the monolayer thick dealloyed Bi-overlayer phase is also referred to as the $p \times \sqrt{3}$-reconstruction [231, 234]. For Bi/Ag(111), the layers have $\sqrt{3}$-periodicity along the Ag[11$\bar{2}$]-direction but are incommensurate in the orthogonal direction [231]. With the $p \times \sqrt{3}$-denomination, the authors follow the nomenclature used in earlier publications where Bi was electrodeposited on Ag(111) [235] and the parameter p was found to depend on the deposition potential [231].

Within the dealloyed monolayer of Bi on Cu(111), the Bi atoms assume a $\left(\begin{smallmatrix}2 & 0\\ 1 & 2\end{smallmatrix}\right)$-ordering [230, 233].

For the experiments presented in this and the following chapters, we deposited an amount of slightly more than 0.5ML[2] on a Cu(111) single crystal. Fig. 78 shows topography images of this Bi/Cu(111)-sample. At this coverage, the surface is entirely covered with a closed dealloyed Bi-monolayer. In the topography images, the Bi/Cu(111) surface exhibits a striped appearance that is due to a surface corrugation in the order of a few tenth of an Å. The width of these stripes is approximately 2.5nm (see Fig. 78 d). On most terraces, the stripes do not run straight but exhibit a certain curvature, i.e. "wavyness" (see e.g. Fig. 78 a and b).

This wavy-striped appearance deviates from the STM topographic images of the dealloyed monolayer of Bi on Ag(111) and Cu(111) reported in literature. For Bi/Ag(111) the topographies exhibit stripes with a width of around 0.9nm [231, 232]. The modulation amplitude of the layers is roughly 0.1Å [232] - 0.2Å [231]. In both references, the stripes run very straight. Also in earlier experiments on Bi/Ag(111) conducted in our

---

[2] in terms of Cu(111)-surface atoms

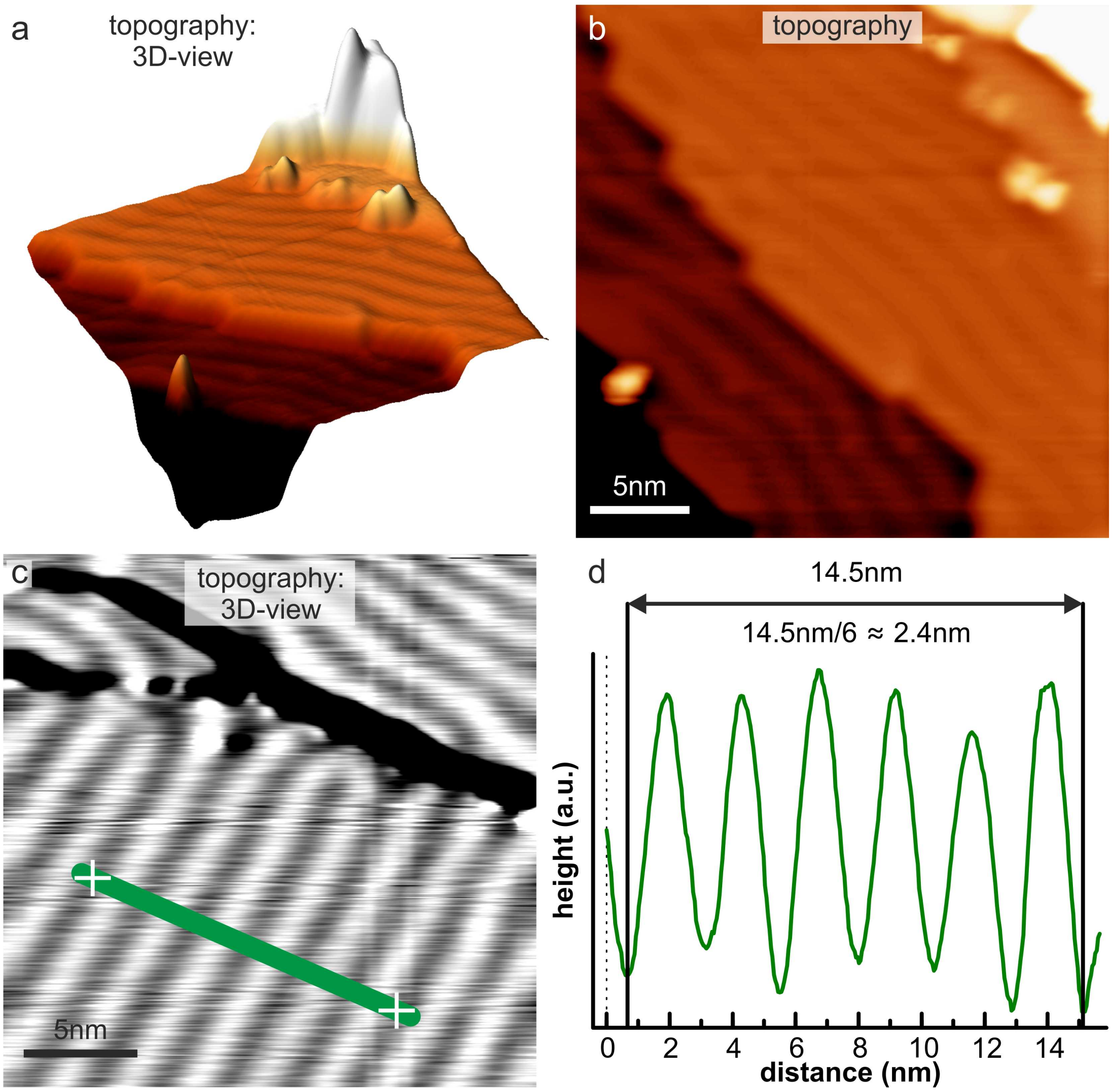

Figure 78: Bi/Cu(111) sample with a Bi coverage of slightly above 0.5ML. a)-c) Topographies. a, b: $V = 2.6V$, $I = 300pA$, $T = 80K$; c: $V = 2.1V$, $I = 200pA$, $T = 80K$. d) Line profile through c). The Bi-overlayer exhibits a wavy striped structure. The stripes have a width of about 2.4Å.

group, we observed a similar structure to this literature data for the monolayer thick dealloyed Bi/Ag(111)-phase (see chapter3.2.1, Fig. 16).

The authors of Ref. [231] assign the stripes to a moiré pattern due to the interference between the Bi-overlayer and the Ag-substrate. Since the unit cell sizes of Ag(111) and Cu(111) are different, i.e. $0.409\mathrm{nm}$ (Ag) vs. $0.362\mathrm{nm}$ (Cu) [232], so that a moiré pattern causing the stripes might look significantly different as observed in our case. The authors of Ref. [232] propose the ordering of the atoms in a $\begin{pmatrix} 3 & 0 \\ 1 & 2 \end{pmatrix}$ rectangular Bi/Ag(111)-unit cell. They suggest that herein, the Bi-atoms assume threefold, nearly twofold and nearly on top-positions on the Ag(111)-surface, where the Bi-atoms on the latter two positions are slightly higher, resulting in the surface corrugation.

For Bi on Cu(111), the $\begin{pmatrix} 2 & 0 \\ 1 & 2 \end{pmatrix}$-ordering of the dealloyed Bi-monolayer has been confirmed by LEED [236], x-ray diffraction (XRD) [233], and atomically resolved STM-images [230]. In the $\begin{pmatrix} 2 & 0 \\ 1 & 2 \end{pmatrix}$-Bi/Cu(111)-layer, all Bi-atoms assume positions close to the threefold Ag(111) hollow-sites [233]. For this structure, surface roughness was found to be negligible [233].

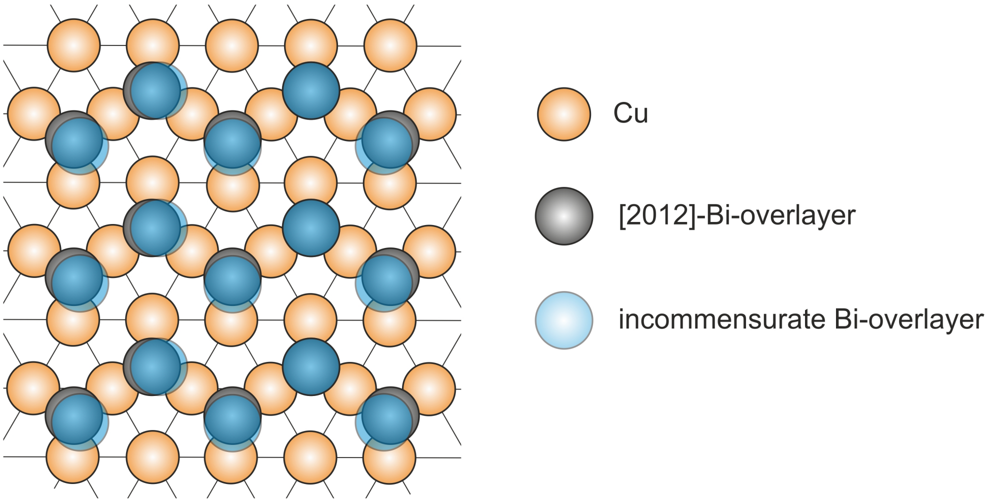

Figure 79: Schematic of the atomic structure of the $\begin{pmatrix} 2 & 0 \\ 1 & 2 \end{pmatrix}$-ordered and the compressed initial Bi-monolayer on Cu(111). The Bi-atoms for the $\begin{pmatrix} 2 & 0 \\ 1 & 2 \end{pmatrix}$-ordered overlayer are shown in gray. The slightly displaced Bi-atoms in the compressed monolayer are shown in blue. On the basis of [233].

However, in their XRD-study, Kaminsiki et al. observe a structural change of the Bi-overlayer when the coverage is slightly increased above the fully dealloyed $\begin{pmatrix} 2 & 0 \\ 1 & 2 \end{pmatrix}$-Bi-monolayer [233]. As additional atoms are incorporated into the layer, the Bi-atoms rearrange into uniaxial-incommensurate overlayer. This layer is commensurate along the $[\bar{1}10]$-direction but incommensurate along the $[10\bar{1}]$ direction of the Cu(111)-surface. The new unit cell size in the incommensurate direction is about 5% smaller as compared to that of the the non-compressed $\begin{pmatrix} 2 & 0 \\ 1 & 2 \end{pmatrix}$-Bi/Cu(111)-overlayer (4.848Å vs. 5.112Å). For the commensurate direction, the unit cell size is found to be almost perfectly conserved (4.431Å vs. 4.427Å). Due to the compression of the layer, the Bi-atoms are displaced from the threefold-coordinated hollow-sites into different positions. They now assume a variety of different positions with respect to the Cu(111)-surface, some of which are close to twofold-coordinated bridge-positions. A schematic model of the atomic structure of this compressed monolayer is displayed in Fig. 79. The displacement of the Bi-atoms results in a surface rumpling which Kaminski et al. find to be in the order of 0.4Å. The ideal coverage for this phase is given as 0.53ML.

A uniaxially compressed phase as reported by Kaminski et al. well corresponds to our experimental findings. Similar to Kaminiski et al. in their XRD-experiments, we observe three rotational domains of the Bi-monolayer as confirmed by our LEED-data. A compression of the closed Bi-monolayer due to a slight overcoverage would also explain the "wavyness" of the stripes, e.g. observed in Fig. 78 a and b.

11.2 BI ON CU(111): ELECTRONIC STRUCTURE

In the following scope of the experiment, we characterized the electronic structure of the compressed Bi-monolayer by dI/dV-spectroscopy. Fig. 80 a shows representative data. At low tunneling energies, the LDOS is relatively low. The spectrum exhibits a continuous rise with two weakly distinguishable shoulders at approx. 2.2eV and 2.4eV. At 2.6eV the spectrum exhibits a well defined peak followed by a second smaller peak at 2.9eV.

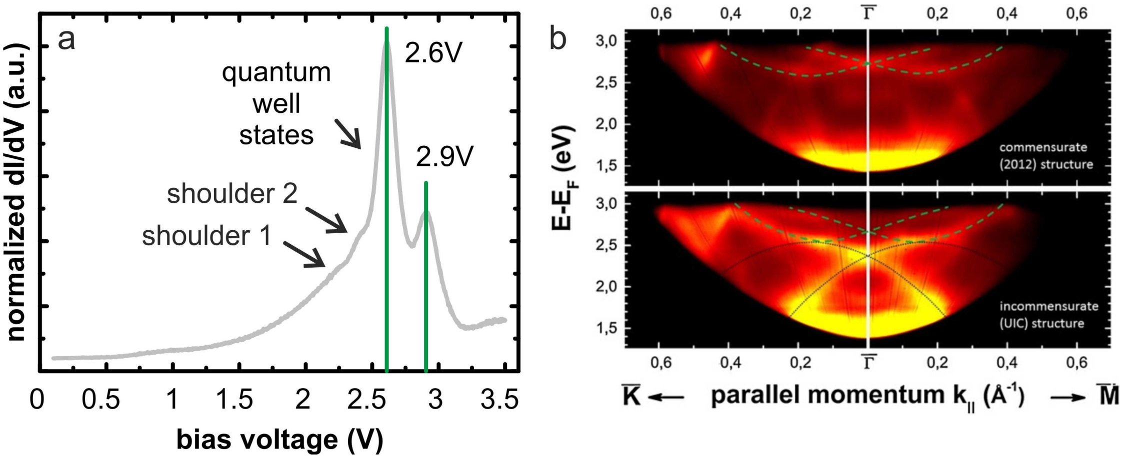

Figure 80: Electronic structure of the initial monolayer of Bi on Cu(111). a) Normalized dI/dV-data gathered on the compressed Bi-monolayer as depicted in Fig. 78. 0.2V/s, $I = 60pA$, $T = 80K$. b) Literature data for the unoccupied electronic band structure of the commensurate $\left(\begin{smallmatrix}2 & 0\\ 1 & 2\end{smallmatrix}\right)$-ordered and the incommensurate uniaxially compressed Bi monolayer as determined by two-photon-photoemission (2PPE). The dashed green line is a guide to the eye for the free-electron like quantum well state with a Rashba crossing point at 2.76eV, while the black dotted lines are a guide to the eye for the hole-like quantum well state located at 2.36eV. Reprinted from Ref. [120], Copyright 2015, with permission from Elsevier.

Here, our data nicely corresponds to two-photon-photoemission (2PPE) experiments, supported by density-functional theory calculations reported by Mathias et al. [119] and Jacobs et al. [120] (see Fig. 80 b). The authors assign the electronic states to quantum well states that form within the initial Bi-monolayer on Cu(111) [119]. These quantum well states are found at energies of 2.33eV[3] (2.1eV[4]) and 2.76eV (2.7eV) with respect to the Fermi level. These values slightly differ from the peak positions in our dI/dV-data. However, the energetic spacing and relative intensity of the peaks qualitatively match the 2PPE-data.

11.2.1 *Spin-Splitting in Bi-Containing Surfaces*

Differently oriented Bi-surfaces have received considerable attention in literature for the electronic properties of their surface states [99–101, 108, 109, 237]. E.g. the surface states of Bi(111), Bi(110), and Bi(110) exhibit a notably large spin orbit splittings [102,

---

[3] experiment
[4] theory

238]. These splittings result from spin-orbit interaction and the symmetry break at the surface. The resulting potential gradient in the surface normal direction leads to a Rashba-type splitting of the surface state bands [238].

An even larger spin-splitting has been found for the surface state bands of the $\sqrt{3} \times \sqrt{3}$- ordered Bi/Ag(111) [114] and Bi/Cu(111)-surface alloys [116, 239]. In the formation of the $\sqrt{3} \times \sqrt{3}$-reconstruction, the Bi-atoms are incorporated into the (111)-surface structure. The Bi atoms are larger than the Ag or Cu atoms, therefore, the Bi-atoms are displaced out of the surface plane by around 0.6Å. Due to the rumpling between the different atomic species, an in-plane potential gradient occurs and leads to an unusually large spin splitting of the surface state bands [114, 117]. The splitting is up to 6 times larger than the Rashba-type splitting e.g. for Bi(111) [114]. It therefore is also referred to as "giant spin-orbit splitting".

11.2.2 *Spin-Splitting in the initial Bi-monolayer*

Also for the initial monolayer of Bi on Cu(111) addressed in this thesis, a considerably large spin orbit splitting has been observed [119, 120]. Here, the splitting occurs for the unoccupied quantum well states addressed in Fig. 80 ($3-5$ times the size of the Rashba splitting of Bi(111)) [102, 119]. The Rashba-type spin-orbit splitting is larger than that of the $\sqrt{3} \times \sqrt{3}$-Bi/Cu(111) surface alloy [239] (see table 2) and occurs for both, the $\left(\begin{smallmatrix}2 & 0\\ 1 & 2\end{smallmatrix}\right)$-ordered monolayer and the compressed monolayer [119, 120].

While in first 2PPE-experiments the Rashba-type splitting was assigned to an out-of-plane potential gradient [119], later spin-resolved experiments showed that for both layers also an in-plane potential gradient plays a role [120]. As expected from the larger surface roughness of the uniaxially compressed monolayer, this effect is shown to be more prominent for this phase.

The large spin splitting makes these systems very interesting for spintronic applications. The Bi/Cu(111)-monolayer is the first quantum well system to exhibit such a large spin-orbit splitting [119]. It is particularly interesting, since here, a Rashba-type-splitting of such order of magnitude occurs in electronic states other than surface states.

The electronic structure of the quantum well states is governed by the confinement between the surface and the Bi/Cu-interface. Therefore, they may be modified by the film thickness. For Bi on e.g. Si(111) the electronic structure of thin Bi-films has been shown to crucially depend on the layer thickness [240]. This opens a route to easily engineer such electronic states. This possibility to selectively tune electronic properties, along with the giant spin-orbit splitting, makes the Bi/Cu(111)-system an attractive candidate for spintronic applications.

Table 2: Rashba parameter α_R for Au(111) and different Bi-containing materials.

Material	Type of State	α_R (eVÅ)	Reference
Au(111)	surface state	0.33	[114] (and references therein)
Bi(111)	surface state	0.56	[114] (and references therein)
Bi/Ag(111) surface alloy	surface state	3.05	[114]
Bi/Cu(111) surface alloy	surface state	0.85	[239]
Bi-monolayer on Cu(111)	quantum well states	1.47-2.48	[119]

11.3 LIGHT EMISSION FROM THE INITIAL LAYER OF BI ON CU(111)

In our experiments, we focused especially on the STM-induced light emission from the Bi/Cu(111)-surface. Fig. 81 a-c shows photon maps that depict the lateral distribution of the overall photon yield for the compressed initial monolayer. Fig. 81 a shows the topography of a surface area exhibiting several steps. Fig. 81 b and c depict corresponding photon maps acquired at tunneling energies of 2.6eV and 2.1eV, respectively. Even though the the overall photon yield induced on the Bi/Cu(111) terraces is significantly higher at 2.1eV, the contrast evoked by the step edges is stronger in the photon map recorded at 2.6eV. The opposite effect is observed for the adsorbates attached to the step edges, that almost cause any contrast in the photon map acquired at 2.6eV, while they evoke a considerable drop of the emission intensity at 2.1eV. Especially, in contrast to the situation observed for step edges on the Ag(111)-surface (see chapter 7.1), here, the photon yield induced in the proximity of the step edges is clearly higher than on the terraces.

Here, we see the contrast mechanisms discussed in chapter 8.6 at work. Particularly, the change of the relative light emission intensities induced on the terraces, step edges and other surface defects with the bias voltage (compare Fig. 81 b and c) underlines that in particular the LDOS of the sample may modulate the efficiency of the TIP excitation on a very local scale. The bright appearance of the step edges in the photon maps which has been observed for several microtips, may e.g. point to the existence of some edge state, modifying the LDOS is this region.

Fig. 81 d-f exemplary show a spectroscopic data set for the compressed Bi-monolayer on Cu(111). For the given tip and corresponding TIP spectrum, the onset for the light emission lies around 1.4V (see Fig. 81 e). The induced photon emission intensity rises until it peaks at 2.1eV. The subsequent drop of the photon emission intensity may be attributed to the the increasing ratio of elastic to inelastic tunneling channels (see Fig. 81 d) as discussed in chapter 8.7.

In our experiments, the spectra of the emitted light change considerably for different microtips similar to the case of Ag(111) discussed in chapter 8. This is a strong indication that also for the initial monolayer of Bi/Cu(111), the light emission is dominantly excited by inelastically tunneling electrons. If further, e.g. electronic, excitations of the Bi/Cu(111)-surface were involved in the TIP-excitation, these would be expected to cause features in the emission spectra which were independent of the tip. We did not observe such features in our data.

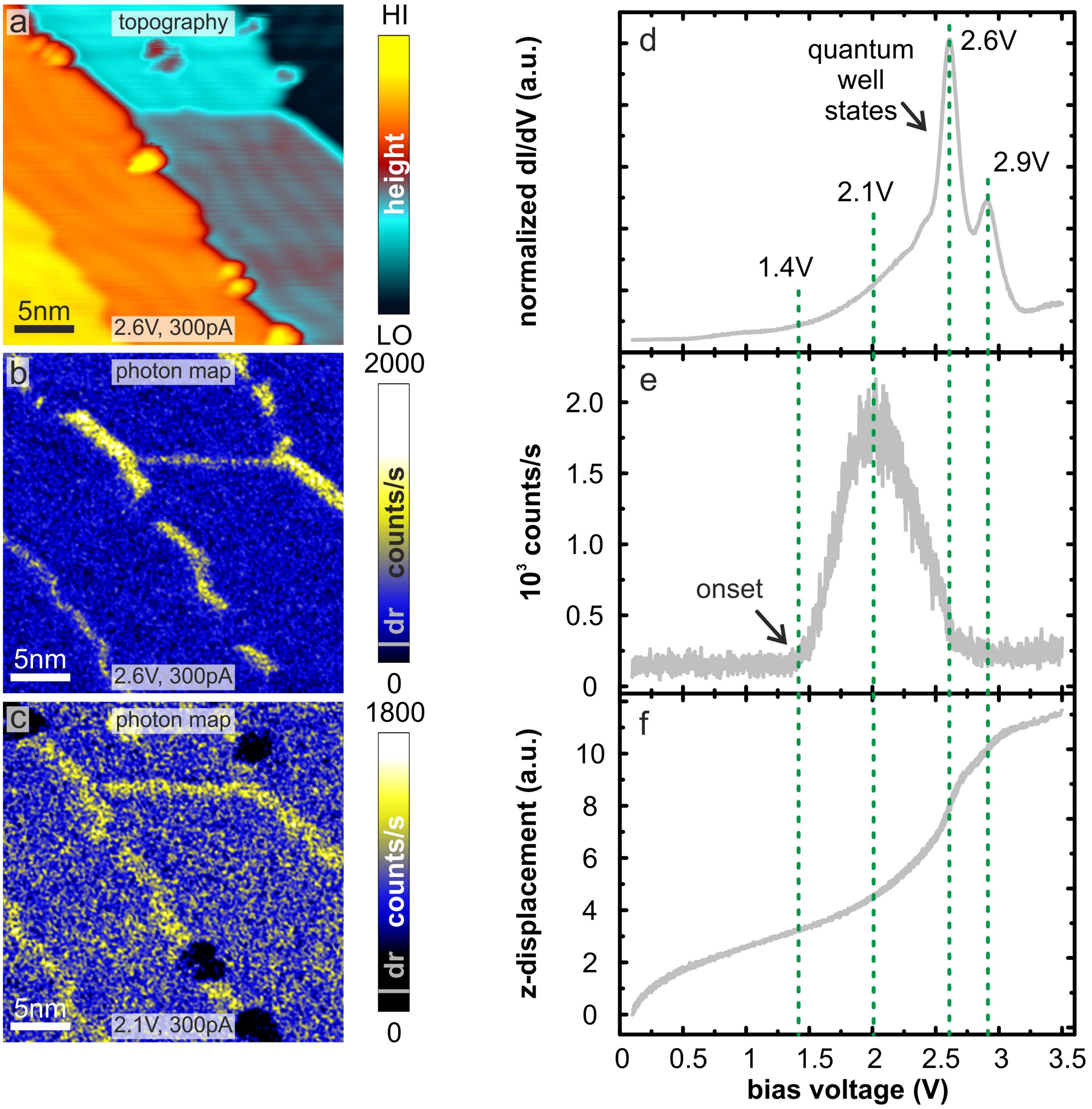

Figure 81: Light emission induced on the initial monolayer of Bi on Cu(111). a) Topography, and b) corresponding photon map. $V = 2.6V$, $I = 300pA$, $T = 80K$. c) Photon map of the same surface area acquired at a tunneling bias of 2.1eV. d)-f) Comprehensive spectroscopic data set. d) Normalized dI/dV-spectrum, b) corresponding spectrum of the overall photon yield, c) spectrum of the relative z-displacement of the tunneling tip. $I = 60pA$, $0.2V/s$, $T = 80K$.

11.4 SUMMARY

Chapter 11 gave a brief introduction to the topographic and electronic structure, as well as the general light emission characteristics of the compressed initial monolayer of Bi on Cu(111). The system has peculiar electronic properties. In particular, it exhibits quantum well states that are also observed in our dI/dV-data. These electronic states have been found to show an exceptionally large Rashba-type spin splitting which makes the system an interesting candidate for spintronic applications.

Like the light emission induced on Ag(111), the photon emission for the initial monolayer of Bi on Cu(111) is induced by inelastic tunneling into states of the surface. Laterally resolved photon maps reveal an increased emission yield induced near the step edges for different microtips. The contrast evoked in the photon maps by step edges and other surface defects is again found to depend on the applied bias voltage. This supports the findings for Ag(111) discussed in chapter 8.6, section and 8.6.4, that local variations in the LDOS of the sample affect the emission intensity.

In the following chapters, a comprehensive study of the induced light emission will be presented in which we use this uniaxially-compressed Bi-monolayer as a substrate for different kinds of archetype organic molecules.

12

MOLECULARLY ENHANCED LIGHT EMISSION: ORGANIC MOLECULES ON BI/CU(111)

Chapter 11 illustrated the promising electronic properties of ultrathin Bi-films on Cu(111). In the experiments conducted in the course of this thesis, a special focus lay on the effects of organic adlayers on the light emission induced on surfaces.

As shown in chapter 9, organic molecules adsorbed on noble metal surfaces usually reduce the induced plasmonic light emission yield. However, for technological applications, it is desirable to be able to selectively tune electroluminescence properties beyond such attenuation.

The suppression of the induced light intensity is associated with molecule substrate interactions (see chapter 10.1). To overcome the attenuation of the emission intensity, the molecules need to be decoupled from the metal substrate. This decoupling may be achieved e.g. by introducing a thin insulating layer [16, 59] or by selecting molecules that exhibit a certain decoupling due to their geometry, e.g. their core is lifted from the substrate by "decoupling legs", i.e. functional groups [34, 198, 219].

Here, we want to achieve an intrinsic decoupling by our choice of substrate. For the $\sqrt{3} \times \sqrt{3}$-surface alloy of Bi/Ag(111), we could show in ARPES experiments, that the electronic surface state is very inert to organic overlayers [118] (see appendix A). Surprisingly, the surface state bands were not altered by the organic overlayers, even when the coverage was increased to a few monolayers. Also the electronic states of the molecules were only minimally affected by the adsorption. The results give rise to the assumption, that also other Bi-induced structures on Ag(111) or Cu(111), e.g. the initial layer of Bi on Cu(111) might exhibit a similarly weak interaction when used as a substrate for organic molecules.

In this chapter, we want to analyze the light emission induced on molecules adsorbed on the initial monolayer of Bi on Cu(111). Apart from revealing the peculiar properties of Bi/Cu(111) as a substrate, our detailed spectroscopic study gives insight into the correlation between the electronic structure of the molecules providing states for inelastic transitions and the induced light emission.

12.1 OVERVIEW

As archetype organic species for our study, we once again chose C_{60} and PTCDA. C_{60} is a commonly used organic material and serves as an example for a rotationally symmetric molecule which, when adsorbed, exhibits a relatively large extent in the surface normal direction. In contrast, the perylene based PTCDA-molecules are planar and adsorb flat on most surfaces.

Here, we subsequently deposited a submonolayer coverage of both molecules onto the uniaxial compressed initial Bi-monolayer on Cu(111). The compression of the Bi-monolayer indicates the complete dealloying of the Bi/Cu(111). Further, an STM-analysis of the sample before the deposition of the molecules revealed exclusively areas covered with the dealloyed Bi-monolayer.

C_{60} and PTCDA both form dense, highly ordered domains on the Bi/Cu(111)-substrate. No intermixing of the organic species was observed. All molecular domains were found to be single layers directly adsorbed on the substrate. The sample was first studied when only C_{60}-domains were present on the surface. A comparison of these data to data for which both organic species were present on the surface, showed, that the C_{60}-domains are not influenced by the subsequent deposition of PTCDA.

Besides the molecular domains, the sample still exhibits areas of the pristine Bi/Cu(111)-substrate. This allows for a direct comparison between the light emission characteristics induced on the organic layers and the underlying substrate.

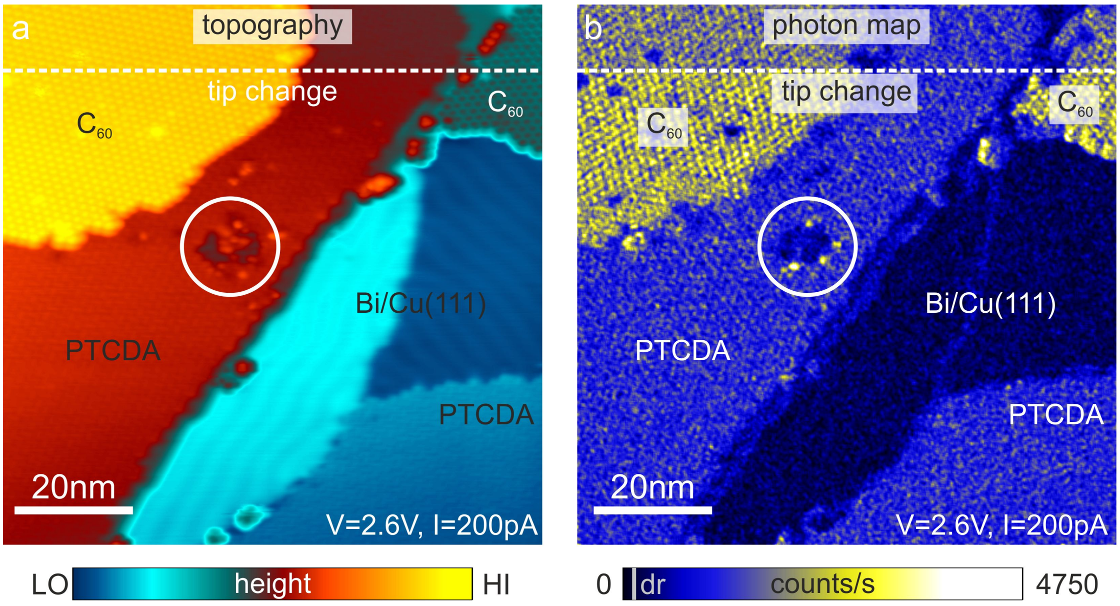

Figure 82: Light emission induced on C_{60}- and PTCDA-domains adsorbed on the initial Bi-mononlayer on Cu(111). a) Topography and b) simultaneously acquired photon map. A vertical line on the intensity scale of the photon map indicates the dark count rate (dr). The dashed horizontal line indicates a minor tip change which does not significantly change the emission spectrum of the tip. The white circle indicates a hole in the PTCDA island probably caused by a tip-sample collision during a spectroscopic measurement. $V_{sample} = 2.6V$, $I = 200pA$, $T = 80K$.

Fig. 82 a shows the topography of a representative area on the according sample. The imaged area exhibits C_{60}- and PTCDA-domains as well as the bare Bi/Cu(111)-

substrate. For simplicity, these three different sample structures will also be referred to as sample species in the following.

Similar to the ordering, e.g. on Ag(111) (see chapter 9), the C_{60}-molecules are hexagonally ordered within the molecular domains. In the PTCDA-domains, the molecules assume a so called herringbone structure. This ordering is commonly observed for PTCDA on a variety of substrates [150] and resembles the ordering observed on Ag(111) (see chapter 9).

When looking at the corresponding photon map in Fig. 82 b, the peculiar properties of the Bi/Cu(111) substrate become obvious: In contrast to the reduction of the induced light emission found for molecules adsorbed on Ag(111), here, all molecular domains exhibit a higher photon yield.

The emission yield for different domains of the same organic species is roughly the same. However, between the C_{60}- and PTCDA domains a significant difference between the induced emission yields is found. The highest yield at the given tunneling energy (2.6eV) is found for the C_{60} covered areas.

The photon map exhibits molecular resolution for both, the C_{60} and the PTCDA islands.

The dashed horizontal line in Fig. 82 a and b marks a tip change. The tip change has a slight influence on the resolution in the topography. In the photon map, the tip change does not only influence the molecular resolution, best visible for the molecular resolution of the left PTCDA-domain, but also affects the overall photon yield, which is especially obvious for the C_{60} islands. However, the tip change did not have any significant influence on the emission spectra. Such behavior is in accordance to tip changes that particularly influence the very front tip apex as discussed in chapter 8.3.

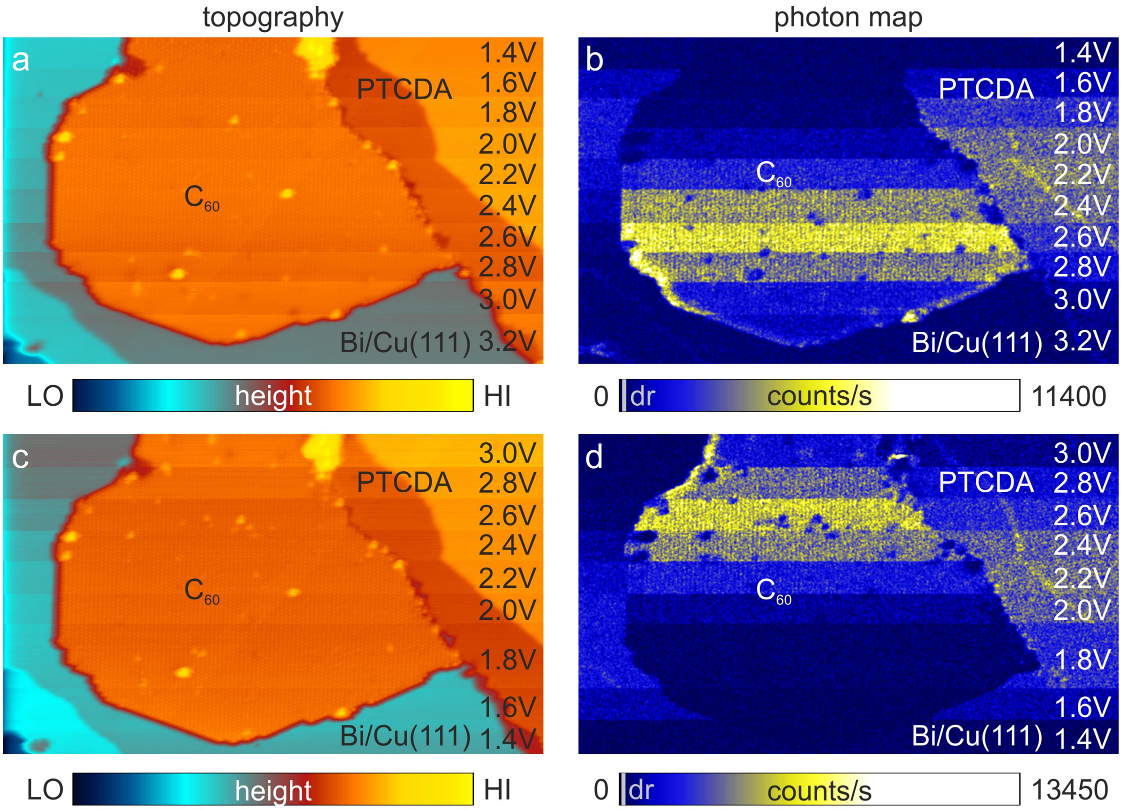

Figure 83: Evolution of the overall photon yield versus the bias voltage (tunneling energy) in the photon maps. a) Topography and b) simultaneously acquired photon map. During the recording of the images, the bias voltage was varied between 1.4V and 3.0V in steps of 0.2V. The respective applied bias voltage is indicated in the images. For c) and d) the bias voltage was conversely varied between 3.0V and 1.4V. Vertical lines on the intensity scales of the photon maps indicate the dark count rate (dr). $V_{sample} = 1.4V...3.0V$, $I = 60pA$, $T = 80K$.

Fig. 83 exemplary reveals the evolution of the overall photon yield in the photon maps when varying the bias voltage. The images were recorded with the fast scanning direction from left to right and the slow scanning direction from top to bottom. About every 50 lines the bias voltage was changed in steps of 0.2V. In Fig. 83 a and b the bias voltage, i.e. the tunneling energy, was varied from 1.4V to 3.2V. In Fig. 83 c and d the bias voltage was conversely varied from 3.0V to 1.4V to exclude artifacts from possible tip changes. Both scans reveal a clear evolution of the overall photon yield as a function of the bias voltage.

The bias voltages at which the onsets and maxima for the induced light emission on the respective molecular species occur are clearly different. This points to an active involvement of the molecules in the excitation of the tip-sample junction. The following detailed spectroscopic analysis will shine further light into the matter.

12.2 SPECTROSCOPIC CHARACTERIZATION: TIP 1

We performed a detailed spectroscopic analysis with two different microtips. The TIP spectra yielded by these microtips were significantly different. Comparing the data gathered with both tips allows us to better separate the influence of the tip from the intrinsic properties of the sample. The different microtips will in the following be referred to as tip 1 and tip 2.

12.2.1 *Spectra of the emitted light*

Tip 1 yields a rather broad spectrum of TIP modes. Fig. 84 shows a set of spectra of the emitted light acquired on PTCDA and C_{60} for different bias voltages from 1.6V to 3.8V. The spectra were vertically offset for clarity.

At low bias voltage, first, only the evolution of a broad peak in the spectra of the emitted light acquired on the PTCDA is observed. Up to 2.0V, the intensity for the spectra recorded on the C_{60}-domains almost vanishes. From 2.2V on, also the light emission induced on C_{60} exhibits a clear evolution of a single broad peak in the emission spectra.

At high applied bias voltages, e.g. 2.8V, the peaks in the emission spectra are fully developed for both molecular species. Both, PTCDA and C_{60}, exhibit very similar, broad, singly peaked emission spectra with a low energy onset at photon energies around 1.3eV and maximum intensity around 1.6eV. The peak extends to around 2.1eV. At these higher photon energies, the spectra roughly only differ in intensity.

In Fig. 84, the quantum cutoffs eV_{Bias} for the respective spectra are indicated by vertical lines. In the evolution of the emission spectra at low bias voltages, the high energy cutoffs for the PTCDA spectra lie at photon energies close to the expected quantum cutoffs. In contrast, the high energy cutoffs of the emission spectra for C_{60} lie at significantly lower photon energies than eV_{Bias}.

A major tip change prevented an equally detailed spectroscopic characterization of the Bi/Cu(111)-substrate with the same tip.

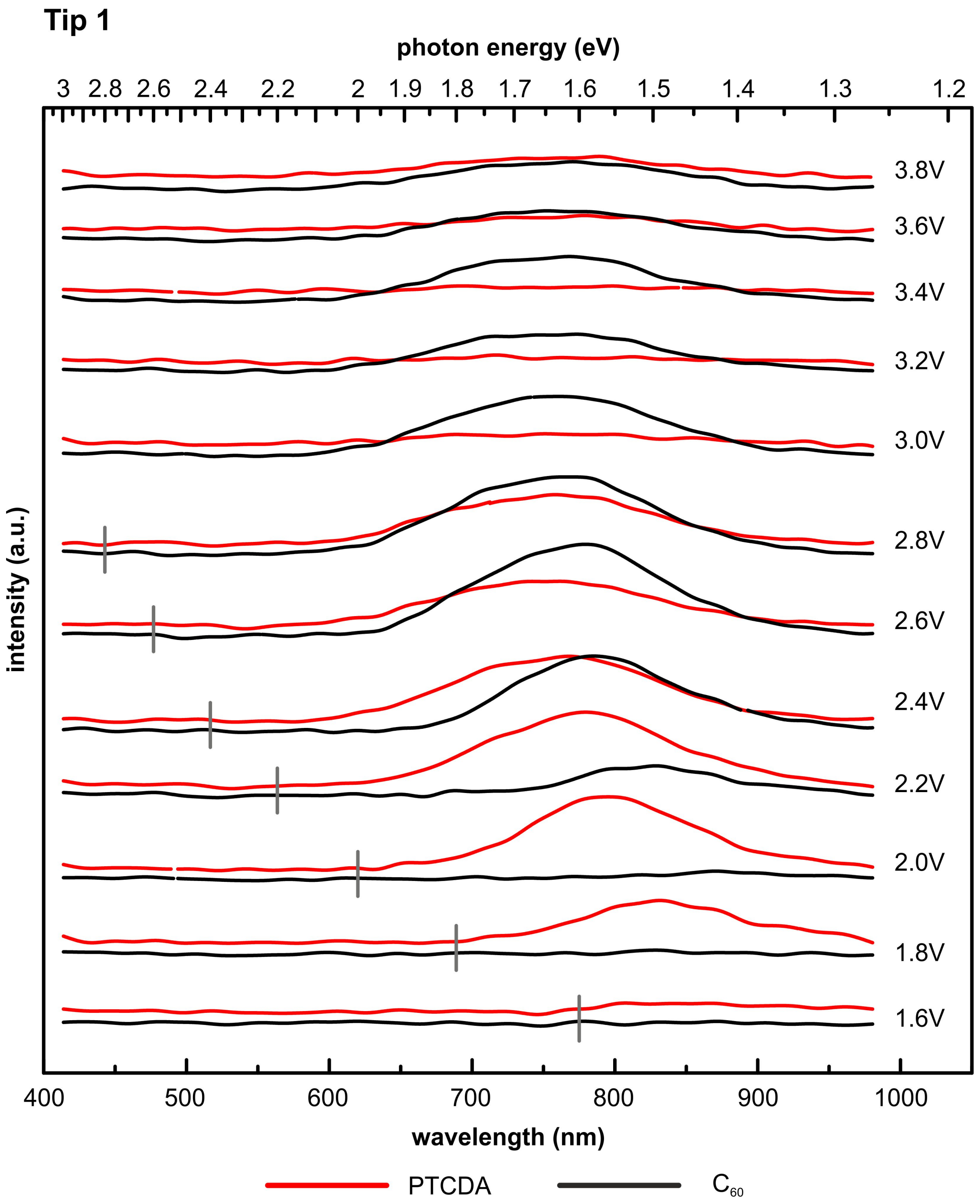

Figure 84: Series of smoothed spectra of the emitted light collected with tip 1 at different bias voltages between 1.6V and 3.8V on the PTCDA- and C_{60}-domains. The spectra were vertically offset for clarity. The quantum cutoff energies eV_{Bias} are indicated by vertical lines where applicable. $I = 60pA$, acquisition time: 300s.

12.2.2 *Spectra of the overall photon yield*

The spectra of the emitted light depicted in Fig. 84 show that the light emission induced on both molecular species mainly differs in its intensity, i.e. the efficiency of the TIP excitation and the subsequent radiative decay. Now, we want to get a more detailed insight into the bias voltage dependence of the emission intensity for each sample species by looking at the spectra of the overall photon yield.

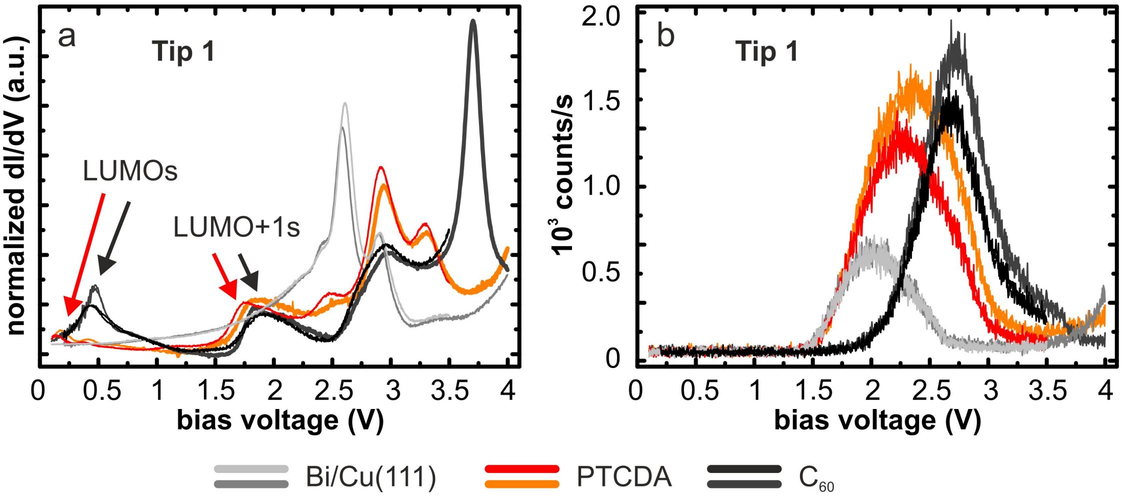

Figure 85: Set of spectroscopic data gathered with tip 1 on all different sample species . a) Normalized dI/dV-spectrum, b) spectrum of the overall photon yield. Two spectroscopic runs, indicated by different colors, are shown for each sample species to demonstrate typical variations in the spectra for different runs. I = 60pA, slope: 0.2V/s, T = 80K, 800 points.

Fig. 85 shows a representative set of spectroscopic data acquired with tip 1. The results of two spectroscopic runs are depicted for each sample species, i.e. the molecular overlayers and Bi/Cu(111)-substrate. This gives an idea of the size of the effect of small fluctuations during the experiment, which may also include minor changes in the very front tip apex. However, the changes might also be evoked by slightly different positions on the molecules at which the spectra were taken.

The spectroscopic data for the Bi/Cu(111) substrate has been described in detail in section 11.2. Here, we will focus on the spectra for the molecules.

The dI/dV-data for the PTCDA exhibits two small peaks around 0.15V and 0.35V above the Fermi level. These peaks are tentatively assigned to the lowest unoccupied molecular orbital (LUMO) of the adsorbed PTCDA-layer. A distinct shoulder at 1.7V is tentatively ascribed to the second lowest unoccupied molecular orbital (LUMO+1). Further peaks in the dI/dV-spectrum of the PTCDA arise around 2.5V, 3.0V, and 3.3V. In fact, the last three features exhibit some similarity to the spectrum of the Bi/Cu(111)-substrate, however shifted to higher energies.

The dI/dV-spectra for the C_{60} exhibit a peak at 0.4V, that we tentatively assign to the LUMO. This peak is significantly higher than the peaks ascribed to the LUMO of the PTCDA. The peak that we tentatively assign to the LUMO+1 of the C_{60} approximately coincides with the LUMO+1 for the PTCDA around 1.7V. Further peaks are observed at 3.0V and 3.8V.

The onset of the spectra of the overall photon yield for the PTCDA lies very close to that of the Bi/Cu(111)-substrate around $1.3\text{V} - 1.4\text{V}$. The initial rise of the overall photon yield almost coincides with the spectrum for the substrate. However, while the spectrum of the Bi/Cu(111) already peaks around 2.0V, the photon yield for the PTCDA further rises and peaks around 2.2V. The maximum induced photon yield for PTCDA is significantly higher than that of the substrate. The peak in the PTCDA spectrum extends over significantly wider bias voltage range than that for the substrate.

For the C_{60}-domains, the onset of the light emission is found at significantly higher bias voltages around 1.75V. The spectra peak around 2.7V. The maximum induced photon yield even exceeds that for the PTCDA. Also here, the bias voltage range in which a significant light emission yield is induced is again wider than that for the substrate and extends to about 3.75V.

12.2.3 *Reference Spectra*

A full comparability of the spectra of emitted light is only granted when the spectra on the different species are gathered with the same microscopic tip (see chapter 8.3). To check if the tip changed, reference spectroscopic measurements of the overall photon yield along with dI/dV-spectra were performed before, during and after the recording of the sets of emission spectra. The results of the respective reference measurements are shown in Fig. 86.

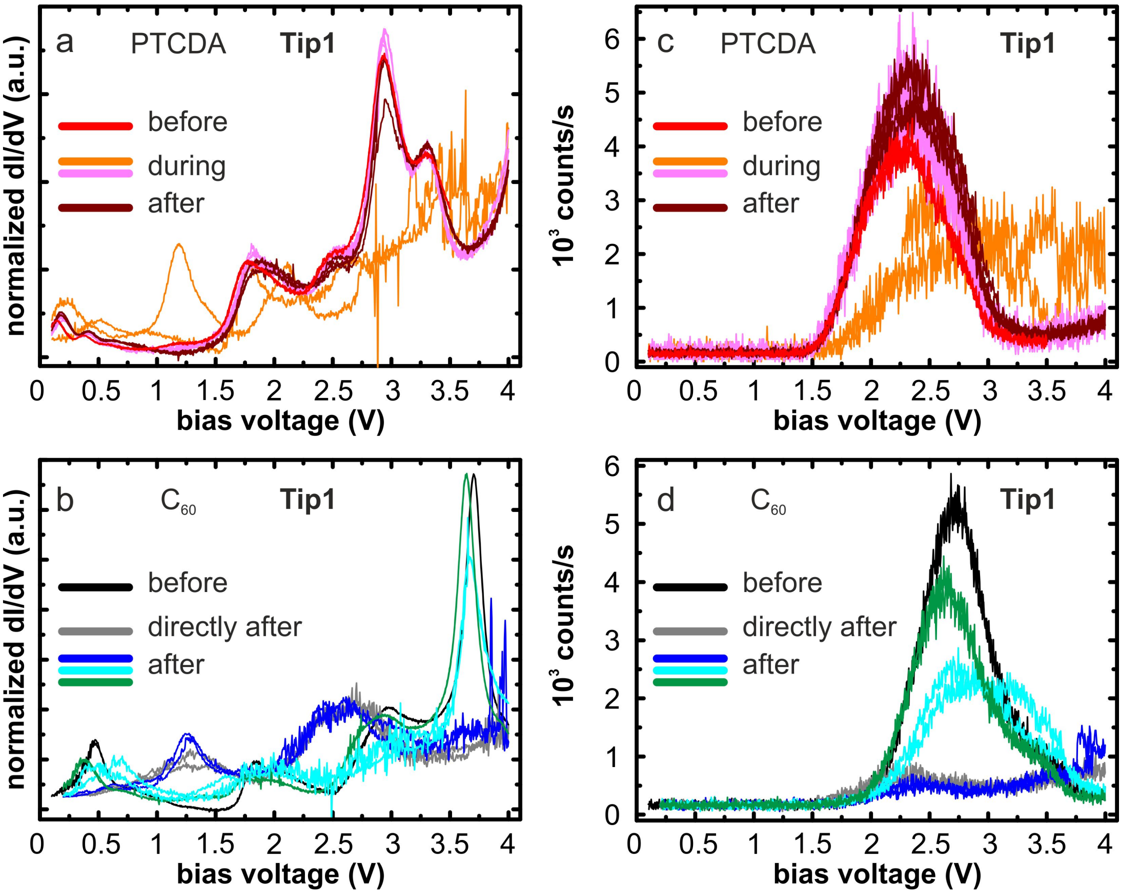

Figure 86: Reference spectra taken before, during and after the recording of the series of spectra of emitted light presented in Fig. 84. a,c,e) Normalized dI/dV-spectra and b,d,f) simultaneously acquired spectra of the overall photon yield. I = 60pA, slope: 0.2V/s, T = 80K, 800 points.

Unfortunately, the reference measurements reveal changes in the spectra of both, the LDOS and the overall photon yield for both series of spectra of emitted light. For PTCDA, one reference measurement taken in the middle of the series of spectra of emitted light (orange in Fig. 86 a and b) differs completely from the spectra which were regularly observed for this sample spieces. After the lateral tip position above the PTCDA layer was slightly altered, the obtained reference spectra (pink) show the usual spectral shape except for a slight shift in the dI/dV-spectrum and a small change in the peak width and the maximum peak height of the overall photon yield.

The unusual and very unstable orange reference spectrum may be the result of the drifting of the tunneling tip above a surface defect, e.g. an adsorbate. Also, an invasive change of the structure of PTCDA domains has been observed as the result of extensive spectroscopy. Also such a change in the sample structure may explain the altering reference spectra. The reference spectrum taken after the series of spectra of the emitted light (brown) exhibits slight instabilities. However, in good approximation it coincides with the spectra taken in the middle of the spectral series, indicating that the conditions during this part of the measurement (at least applied bias voltages from 1.4V to 2.4V) were stable.

The spectra of the emitted light recorded directly before this reference spectrum was acquired were the ones taken at highest bias voltages presented in Fig. 84. These emission spectra exhibit a slight increase of the emission intensity. The changes revealed in the reference spectra have no significant influence the shape of the emission spectra.

The slight changes between the very first (red) and the last (red) reference spectrum for PTCDA may be due slightly different lateral positions of the tip above the molecular layer. Also, a minor tip change may be involved. However, the influence of this tip change may be considered to be rather small and the general emission characteristics, in particular the spectrum of TIP-modes, are widely conserved.

For the case of the reference measurements obtained on C_{60}, the changes in the dI/dV-spectra and spectra of the overall photon yield are quite considerable. The reference measurements recorded after the series of spectra of emitted light exhibit a severe drop of the overall light intensity (gray and dark blue). Also after the lateral position of the tip was altered (cyan) the reference spectra exhibit instabilities and still vary from the usual spectral shapes. Only after a couple of further spectroscopic runs performed at different positions on the sample, the spectra return to the usual spectral shape (dark green). Slight changes in the dI/dV-data and the spectrum of the overall photon yield remain. This kind of behavior points to a tip change which may have happened e.g. in form of the attachment of an adsorbate, maybe even a C_{60} molecule, to the tip. Also here, the general shape of the emission spectra, i.e. the spectrum of TIP-modes, was not significantly affected (see Fig. 84).

The changes in the reference spectra of the overall photon yield indicate that the tip change was associated with a severe drop of the emission intensity. In the series of emission spectra shown in Fig. 84, a drop of the emission intensity is not observed until rather high bias voltages, e.g. 3.6eV. This suggests, that the tip change may have happened as the result of the elevated applied bias voltages. Thus, we may still plausibly assume a certain comparability for the emission spectra acquired at significantly lower bias voltage.

In the discussion of the data in chapter 13.4, we will draw general conclusions from the shape of the emission spectra that are not affected by these changes elaborated here. We will keep in mind, that small changes in the emission spectra may be associated to minor tip changes. For the discussion of the emission intensity, we refer to characteristic spectra of the overall photon yield to obtain a reliable, comprehensive data set.

12.3 SPECTROSCOPIC CHARACTERIZATION: TIP 2

A mayor tip change resulting in a loss of stability and light emission properties occurred before a complete set of spectroscopic data on all sample species could be acquired with tip 1. The same macroscopic tip was newly prepared by indention into a Ag-substrate and subsequent field emission at parameters of approximately $50\mu A$ and $200 - 300V$. This resulted in a major change of the light emission characteristics. The resulting microtip will be referred to as tip 2.

12.3.1 *Spectra of the emitted light*

Fig. 87 shows a series of spectra of the emitted light acquired at different tunneling energies for all three sample species acquired with tip 2. The shape of the emission spectra, i.e. the spectrum of excitable TIP modes, significantly differs from those for tip 1. Instead of a single broad peak, here, the spectra of the emitted light exhibit two main narrower peaks located at photon energies around $1.7eV$ and $1.35eV$. The peaks extend over a range of about $0.2 - 0.3eV$. Additionally, several smaller peaks may be observed, e.g. around $1.95eV$ and $1.27eV$.

For tip 2, also emission spectra recorded on the substrate are available for comparison. The shapes of the emission spectra for the molecules and the substrate are very similar. None of the peaks are exclusive to any sample species.

The TIP spectrum provided by tip 2 allows for an easy comparison between the light intensities induced in different spectral regions: For the same bias voltage but different sample species, the relative height of the two main peaks in the spectra varies. For example, the emission spectra for PTCDA and C_{60} recorded at a bias voltage of $3.0V$ exhibit a roughly equal intensity of the low energy peak. However, the higher energy peak is significantly higher in the emission spectrum for the C_{60}.

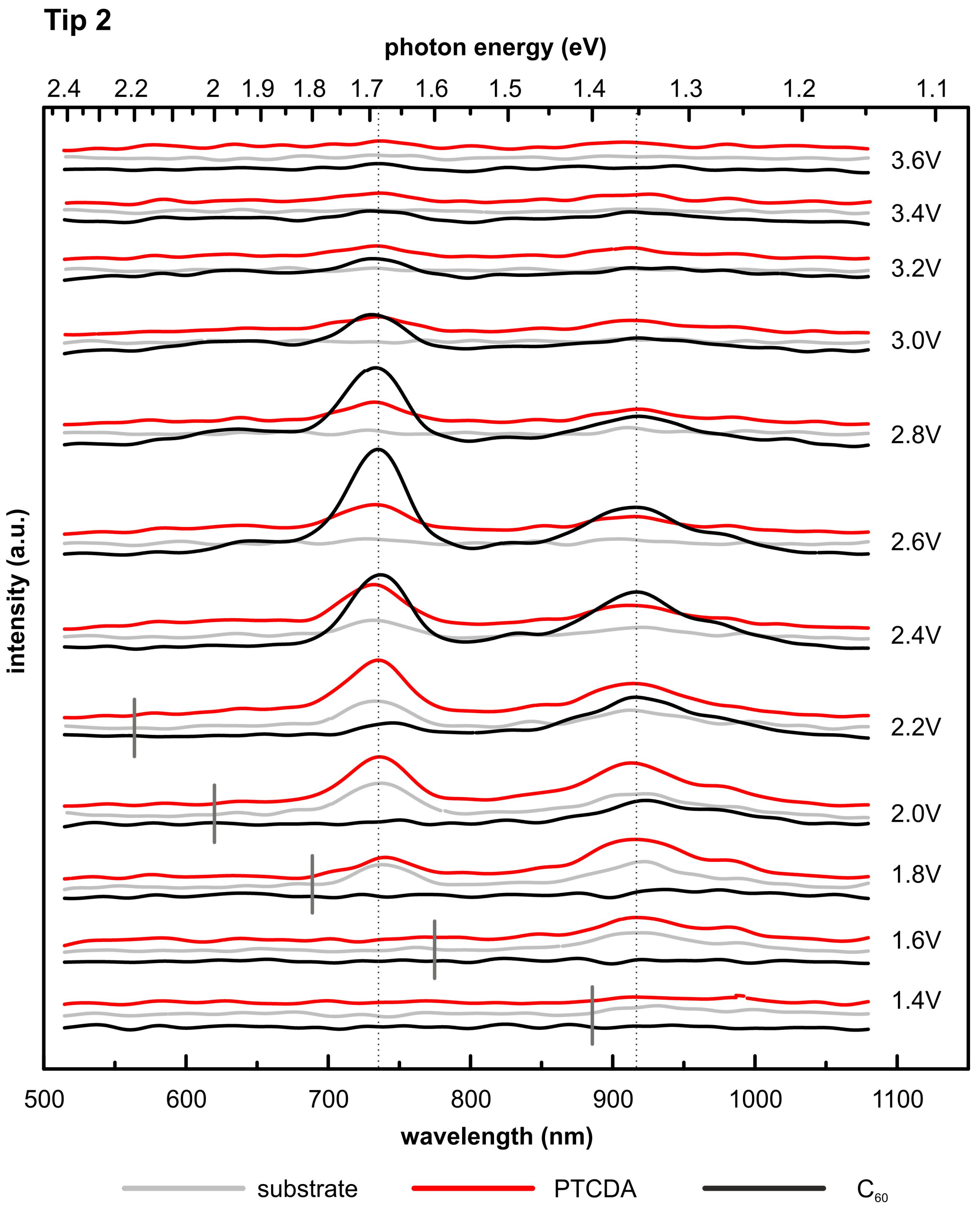

Figure 87: Series of smoothed spectra of the emitted light collected with tip 2 at different bias voltages for all sample species. As a result of the tip preparation through field emission, the emission characteristics of the tip have changed considerably. The spectra were vertically offset for clarity. The quantum cutoff energies eV_{Bias} corresponding to the respective bias voltages are indicated by vertical lines where applicable. $I = 200pA$, acquisition time: 300s.

12.3.2 *Spectra of the overall photon yield*

Fig. 88 compares sets of STS-data for tip 1 and tip 2. The dI/dV-spectra acquired with both tips only show minor variations (see Fig. 88 a).

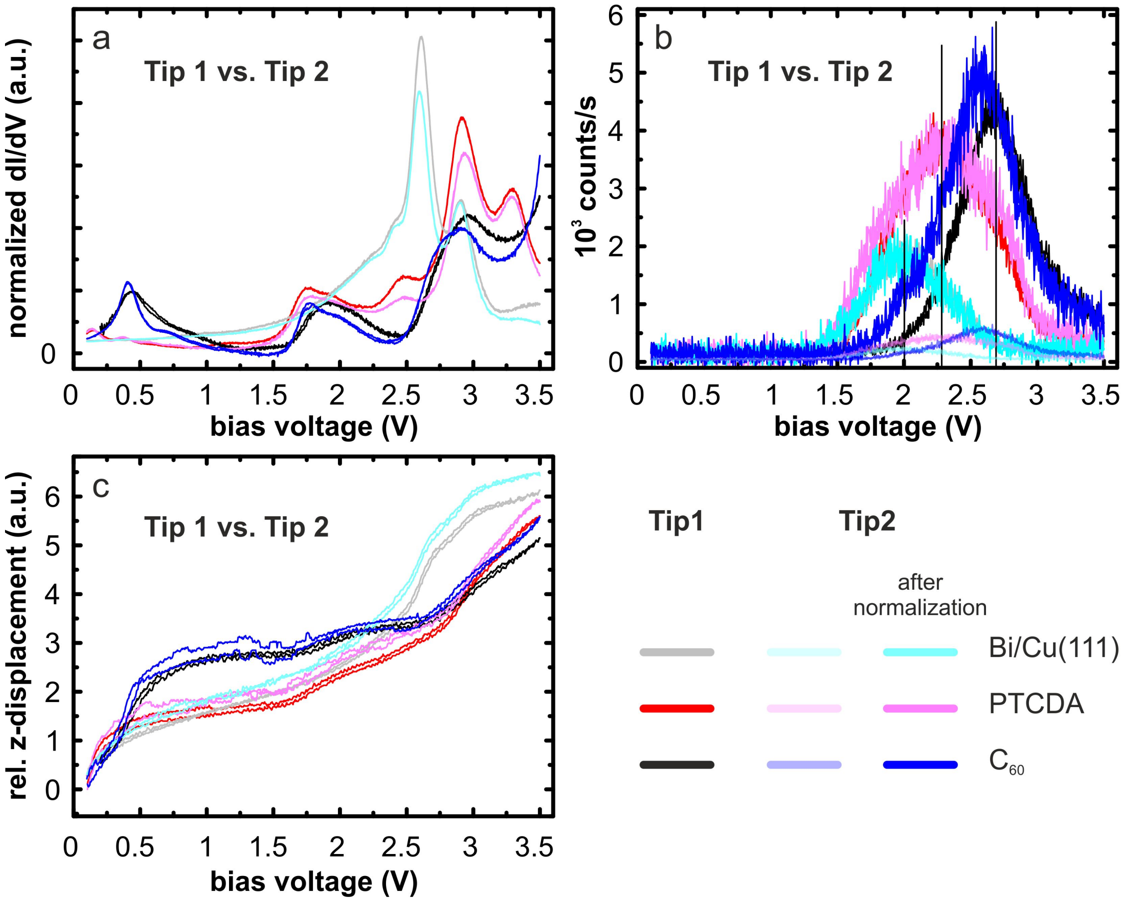

Figure 88: Comparison of spectroscopic data gathered with tips 1 and 2. a) Normalized dI/dV-spectra, b) simultaneously acquired spectra of the overall photon yield, and c) the relative z-displacement of the tip. The spectroscopic data were acquired at a higher tunneling current with tip 1, the dI/dV-data were normalized accordingly for comparability. The spectra of the overall photon yield were normalized for similar intensities (by a factor of 9.3), to account for the significantly smaller emission yield induced with tip 2. The original data is shown in lighter colors. The peak positions for tip 1 are indicated by vertical lines. I = 60pA (tip 1) and 200pA (tip 2), 0.2V/s, recording 800 points within the bias range. T = 80K.

In contrast, the impact of the different tips on the overall photon yield is quite more drastic. The count rates induced with tip 2 are significantly reduced. Even at significantly higher tunneling currents, the count rates lie well below the ones induced with tip 1. In Fig. 88 b, the spectra depicted in lighter colors were normalized[1] for the same tunneling current as the spectra acquired with tip 1. The count rates for these spectra are about a factor of 9 smaller than the corresponding spectra gathered with tip 1. The spectra shown for tip 2 in darker colors were normalized with a factor that yields equal

---

[1] In the tunneling current regimes looked at here, a roughly linear scaling of the overall photon yield with the tunneling current may be assumed [241].

intensity for the spectra of the Bi/Cu(111)-substrate. After this intensity normalization, the spectra of the overall photon yield show for tip 1 and 2 exhibit surprisingly strong similarity.

Fig. 88 c displays the corresponding relative z-displacement curves for tip 1 and 2. These curves reflect the movement of the tips as they follow the energetic distribution LDOS with changing bias voltage. For both tips, the relative z-displacement versus the bias voltage is very similar.

Fig. 89 revisits the normalized spectroscopic data for tip 1 and 2. This time, the spectra were vertically offset for clarity.

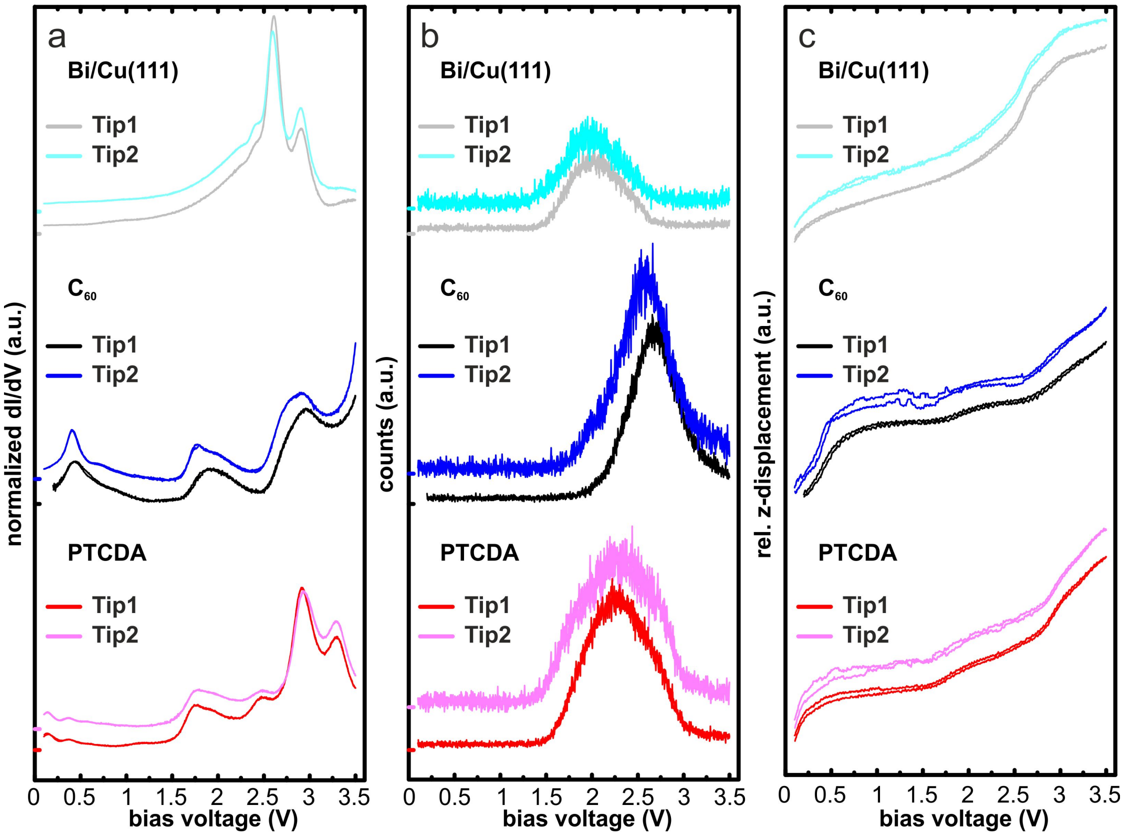

Figure 89: Normalized spectroscopic data revisited from Fig. 88. a) Normalized dI/dV-spectra, b) simultaneously acquired spectra of the overall photon yield, and c) the relative z-displacement of the tip. The spectra were vertically offset for clarity.

12.3.3 *Reference spectra*

Also for this series of spectra, reference spectra were taken to check the comparability of the respective data sets. The results are displayed in Fig. 90.

The reference spectra for the Bi/Cu(111)-substrate and C_{60} confirm the stability of the tip during the respective series of measurements.

In the case of the Bi-monolayer substrate, the reference spectra were recorded at different set tunneling currents. After normalization with the tunneling current, the dI/dV-spectra almost perfectly coincide. Also the overall photon yield was normalized for the different tunneling current. Except for the higher noise level caused by the normalization of the spectrum before the series of emission spectra, the spectra of the overall photon yield also exhibit large coincidence.

Very striking however, are the reference spectra for the measurement series taken for PTCDA. The spectra recorded before as well as after the series of emission spectra differ significantly from the usually observed spectral shape. The spectrum taken at the beginning of the series of spectra of the emitted light still exhibits some weak features, however much less pronounced than the peaks observed in the usual spectra taken on PTCDA. The spectra taken subsequently to the series of spectra of emitted light are almost featureless.

For comparison, reference data displaying the regularly observed spectra for the PTCDA are additionally shown in light red in 90 c and d. Both exhibit significant differences to the displayed reference spectra for PTCDA. Thus, an accidental misplacement of the tunneling tip above another sample species, e.g. due to thermal drift, can be excluded as an explanation for the irregularly shaped spectra. Topographic images of the surface confirm a change of the PTCDA-layer at the position where the series of emission spectra was taken (see Fig. 82). This change of the sample structure, e.g. due to strong tip-sample interactions, seems to be the cause for the changed reference spectra.

When comparing the reference spectra for PTCDA to the usually observed STS data (displayed light red in Fig. 90), the dI/dV-spectra exhibit clear deviations. Also the shape of the spectra of the overall photon yield is slightly altered, this may be easiest observed on the descending flank of the spectrum. The overall emission intensity is slightly smaller than the photon yield induced on regular, non-altered PTCDA domains. However, it is still clearly larger than that induced on Bi/Cu(111).

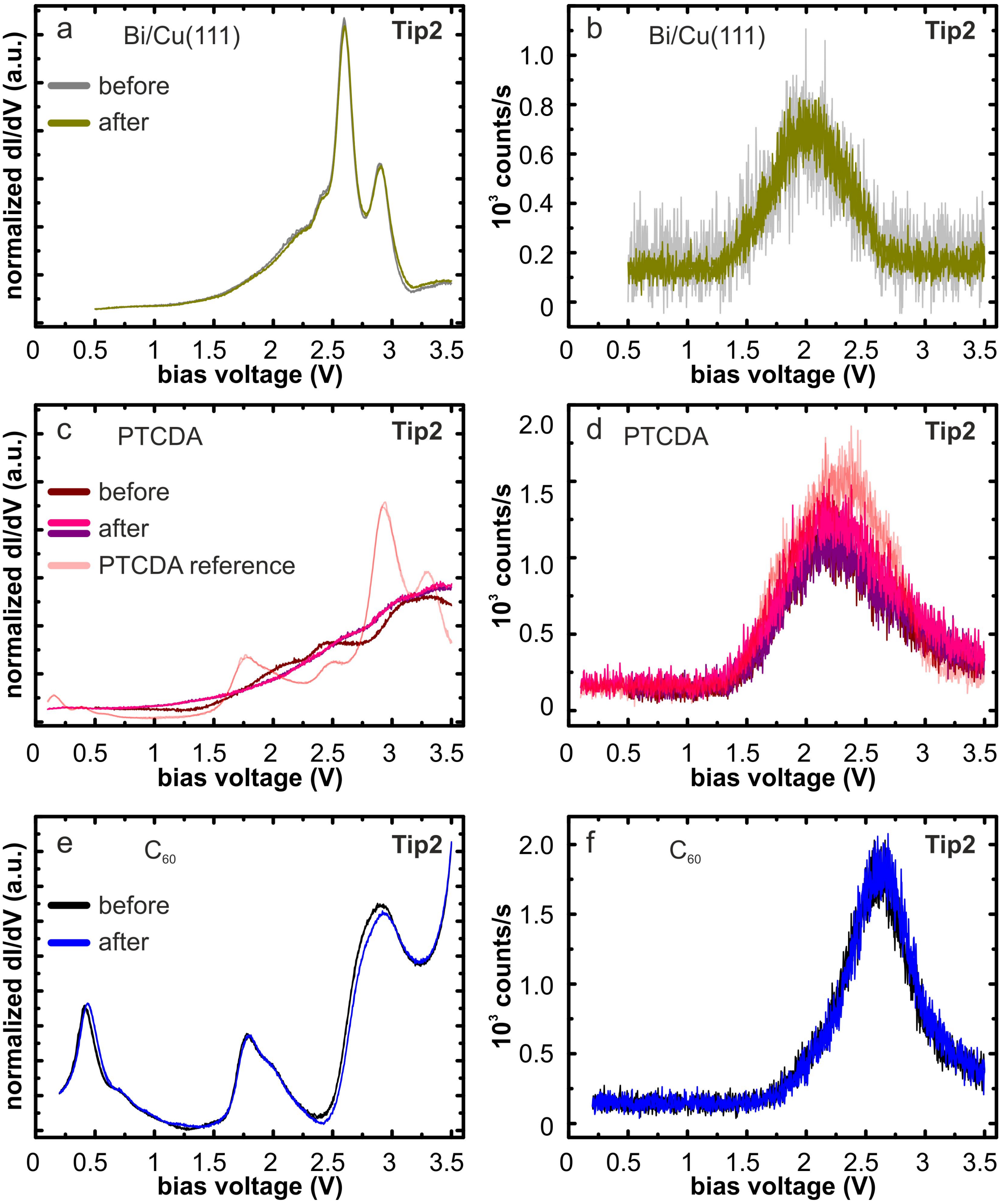

Figure 90: Reference spectra taken before and after the recording of the series of spectra of emitted light presented in Fig. 87. a,c,e) Normalized dI/dV-spectra and b,d,f) simultaneously acquired spectra of the overall photon yield. One of the reference spectroscopic runs for the Bi-monolayer substrate was recorded at 100pA instead of 200pA like the rest of the spectra. The spectra were normalized accordingly. I = 200pA (100pA), slope: 0.2V/s, T = 80K, 800 points.

12.4 LIGHT EMISSION INDUCED AT NEGATIVE BIAS VOLTAGE

The main part of the study presented here focused on the light emission induced at positive bias voltage, i.e. inelastic tunneling from initial states in the tip to final states provided by the sample. We completed the data set acquired with tip 2 with a set of spectroscopic data gathered at negative bias voltage.

12.4.1 *Spectra of the overall photon yield*

At negative bias voltage, the tunneling conditions were much more unstable, especially when performing spectroscopic measurements at constant current in which the tunneling distance was varied. This resulted in a significantly reduced signal to noise ratio. Up to now, all dI/dV-data and spectroscopic data of the overall photon yield was raw data. Here, the data shown in Fig. 91 were smoothed for clarity.

The high noise level in the dI/dV-spectra at negative bias voltage (see Fig. 91 a) makes it hard to distinguish clear features in the data for PTCDA and the substrate. For PTCDA, the weakly discernible peak in the LDOS around -2.0V is tentatively assigned to the highest occupied molecular orbital (HOMO). The second highest molecular orbital (HOMO-1), is assigned to the peak around -3.3V. Both features are rather weak and were identified with the help of further spectra (not shown). For C_{60}, the HOMO is more clearly distinguishable with an onset around -1.3V.

As opposed to the spectra of the overall photon yield acquired at positive sample bias, the onset of the light emission induced at negative sample bias around -1.25V is the same for all sample species. The maximum overall photon yields observed at negative sample bias are in the same order of magnitude as for positive sample bias. However, they occur at slightly larger tunneling energies. In particular, no clear peaking of the overall yield is observed in the examined negative bias voltage range.

Further, the relative intensities of the emission yield for the different sample species have changed. At negative bias voltage, the spectra for the overall photon yield roughly coincide for the substrate and the PTCDA. Here, also the progression of the dI/dV-spectra were similar (see Fig. 91 a). The overall photon yield, induced around -3.5V is comparable to the maximum overall photon yield induced for C_{60} at positive bias voltage.

In comparison to the overall photon yield induced at negative bias voltage on PTCDA and Bi/Cu(111), the emission yield induced at negative bias voltage on C_{60} is significantly lower, i.e. around 50% of the value of that for the other sample species. The corresponding dI/dV-spectra reveal a significantly higher LDOS for the C_{60} than for PTCDA and the substrate.

The relative retraction of the tip from the sample is generally less at this bias polarity (see Fig. 91 c).

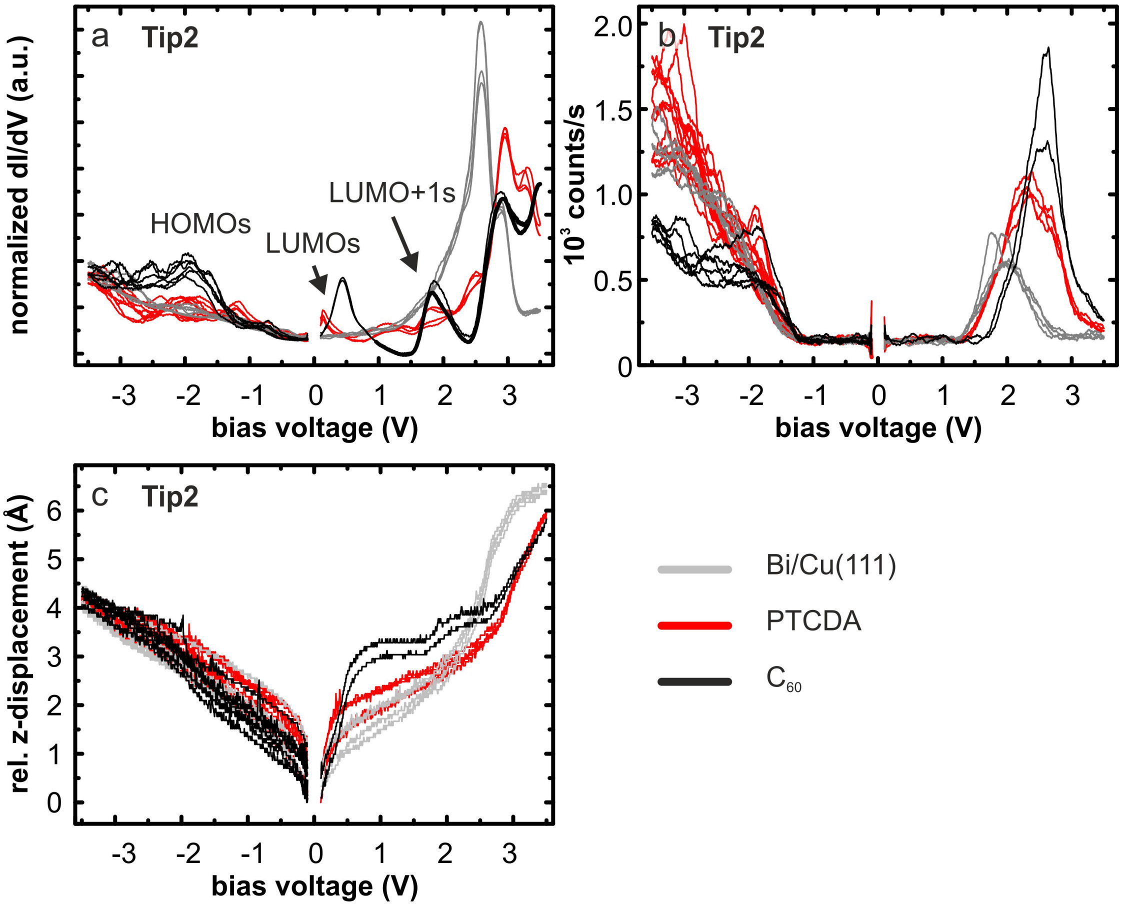

Figure 91: Comparison of spectroscopic data for positive and negative bias voltage. a) Normalized dI/dV-spectra, b) spectra of the overall photon yield, and c) relative z-displacement of the tip. Due to the high noise level, only smoothed data are shown. $I = 100\text{pA}$, slope: 0.2V/s, $T = 80\text{K}$, 800 points.

12.4.2 *Spectra of the emitted light*

The instabilities during the spectroscopic measurements at negative bias voltage also affected the noise level in the subsequent spectroscopic runs at positive bias voltage. This indicates, that during spectroscopy at negative bias voltage, e.g. an adsorbate was attached to the tip.

However, these presumed tip changes, did not affect the general peak positions of the spectra of the emitted light, as can be seen in Fig. 92.

Just as in the case of positive sample voltage, the emission spectra exhibit two peaks around photon energies of roughly $1.35eV$ and $1.68eV$. Generally, the high energy peak seems to be more pronounced at this bias polarity.

Further, at negative bias voltage, the emission intensities induced on the PTCDA-domains and on the substrate are very similar (see Fig. 91 b). This allows for an easy comparison between the peak positions for both sample species in Fig. 92. The high energy peak for the PTCDA is located at around $0.02eV$ higher photon energies at the corresponding intensity peak for the spectra of the substrate. The low energy peak is too broad to distinguish any clear peak shifts.

For high bias voltages, when the emission spectrum is fully developed, i.e. $-2.4V$ and above, the according peak in the emission spectra for C_{60} rather corresponds to the peak position of PTCDA than to that of the substrate.

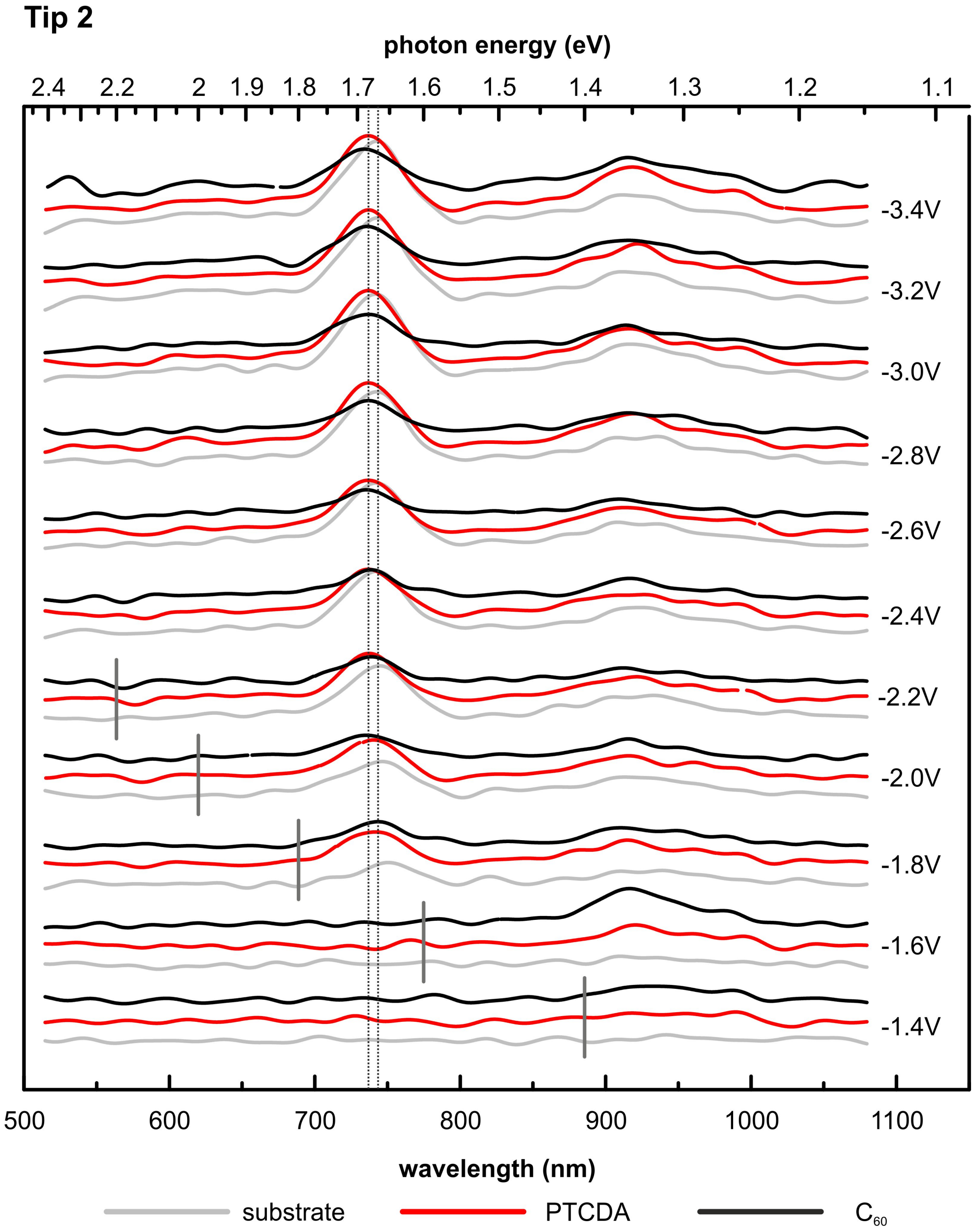

Figure 92: Series of spectra of emitted light for the different sample species acquired at different negative bias voltages with tip 2. The spectra were vertically offset for clarity. The quantum cutoff energies eV_{Bias} corresponding to the respective bias voltages are indicated by vertical lines where applicable. Dashed vertical lines indicate a small shift between the peaks of the spectra for the substrate and the molecular species. $I = 100pA$, $T = 80K$, acquisition time $t = 300s$.

12.4.3 *Reference Spectra*

Once again reference spectra were taken to assure the comparability of the spectra of emitted light. Regarding the high noise level of the raw data, the data taken on the Bi/Cu(111) substrate and the C_{60} in good approximation coincide.

In the reference spectra for the series of spectra of emitted light for PTCDA, once again changes can be observed. For the spectra of the overall photon yield, these changes almost vanish in the noise level but can be vaguely distinguished in the smoothed spectra. In the dI/dV-spectra the changes are even better distinguishable. However, as becomes evident from Fig. 87, the changes were minor enough not to change the spectrum of emitted photons.

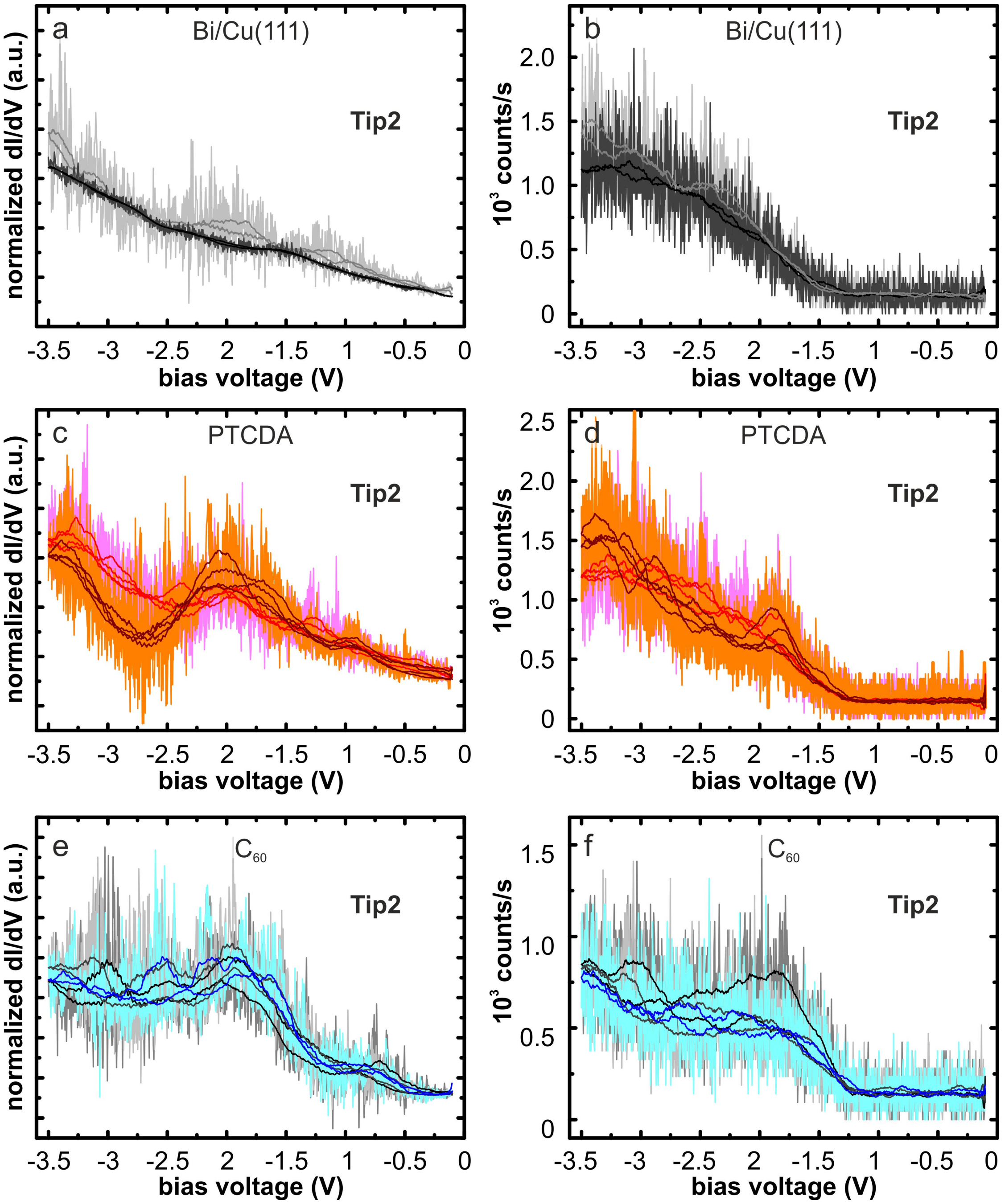

Figure 93: Reference spectra recorded before and after the series of spectra of emitted light shown in Fig. 92. a,c,e) Normalized dI/dV-spectra, b,d,f) simultaneously acquired spectra of the overall photon yield. The data exhibit a very high noise level. For easier comparability, smoothed data is additionally displayed. I = 100pA, slope: 0.2V/s, T = 80K, 800 points.

13

DISCUSSION

In chapters 7 and 8 we presented and discussed STM-LE data for Ag(111). For metallic systems like Ag, the TIPs are exclusively excited by inelastically tunneling electrons. Exemplary data for e.g. PTCDA and C_{60} on Ag(111) were presented and discussed in chapters 9 and 10. Also for such single layers of organic molecules on metal surfaces, without further decoupling, the induced light emission is purely excited by inelastically tunneling electrons. No transitions between electronic states with the molecules are involved in the TIP excitation. Such direct radiative transitions are quenched due to molecule-substrate-interactions (see chapter 10).

The emission intensity of the plasmon-mediated light emission is significantly reduced when tunneling above the organic molecules on Ag(111). This is in agreement to literature findings for organic molecules adsorbed on metallic surfaces without further decoupling [13, 15, 58, 94, 140]. In the discussion in chapter 10.1, we associated the attenuation of the emission yield to the coupling of the molecules to the substrate which provides a number of non-radiative energy dissipation channels and shortens the lifetime of the inelastically tunneling electrons within the molecular states.

In contrast, in our data for molecular layers on the initial monolayer of Bi on Cu(111) presented in chapter 12, we observe a quite different behavior of the emission intensity. For the same molecules for which we observed a quenching of the emission intensity on Ag(111), we find an enhancement of the overall photon yield as compared to the substrate when adsorbed on Bi/Cu(111).

An enhancement of the induced overall photon yield with respect to the underlying substrate has only been observed for molecules that were somehow decoupled. This may be achieved through a spacer layer of some sort, e.g. a thin layer of salt or oxide [16, 59, 242] or organic molecular layers [14, 159]. Also, an enhanced emission intensity has been observed for organic molecules that experienced a certain geometric decoupling from the surface by molecular ligands [31, 198, 219]. In the latter case, the molecules were "standing up" on tilted functional groups lifting their core from the underlying surface.

In our case, the adsorption configurations for PTCDA and C_{60} on Ag(111) and Bi/Cu(111) appear quite similar. Thus, a significant geometric decoupling is improbable here. Instead, the enhancement of the light emission for the molecules adsorbed on Bi/Cu(111) points to a rather low interaction between the molecules and the underlying substrate, i.e. an intrinsic decoupling.

In this chapter, will analyze the induced light emission in further detail. This allows us to shed further light on the enhancement of the emission yield in our case. In particular, we may gain a further understanding of the specific roles of the numbers and lifetimes of the electronic states provided by the molecules in the excitation of the TIPs.

13.1 THE ORIGIN OF THE EMITTED LIGHT

The enhancement of the light emission raises the question whether for molecules on Bi/Cu(111) additional excitation channels apart from inelastic tunneling might be involved in the TIPs excitation. For the plasmonic light emission excited by inelastically tunneling electrons, electrons tunnel inelastically from initial states in the tip to final states in the sample. Thereby, they excite TIPs which decay radiatively. For molecules that are decoupled sufficiently from the substrate, an additional excitation channel becomes available. In this path, a hot electron is injected into the molecule by elastic tunneling. One way of relaxation for this molecular excitation is the transition into an energetically lower state inside the molecule. This path of excitation may couple to the TIPs which enhances the plasmonic light emission [17, 34]. However, if the coupling between the molecule and the substrate is too strong, the electron leaves the molecule before it can traverse into any other molecular state. The molecule-substrate interaction then quenches the light emission from this radiative decay of the molecular excitations.

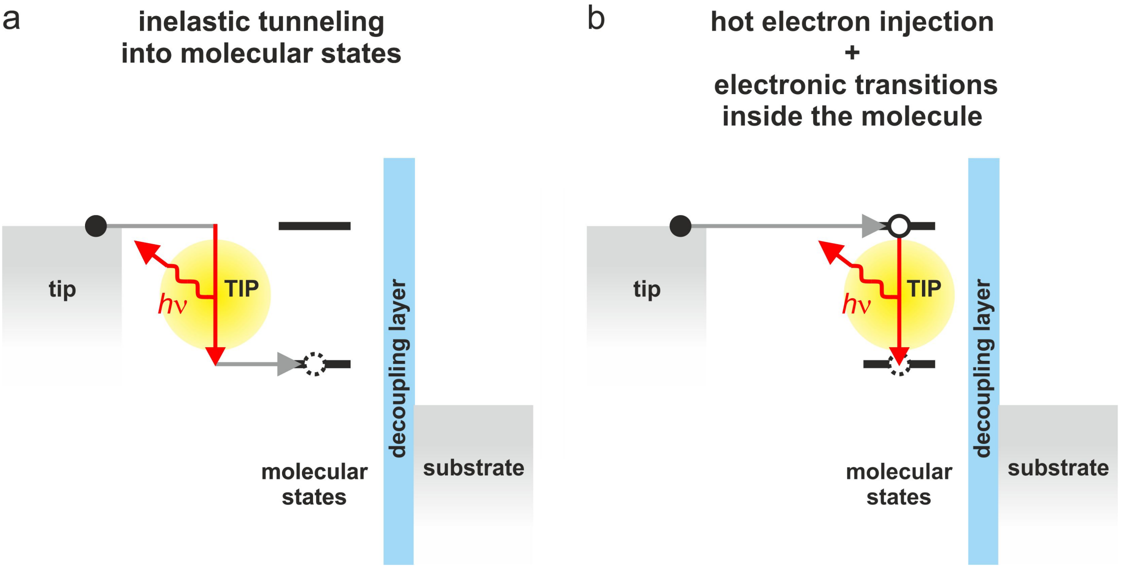

Figure 94: Different paths of excitations by tunneling electrons. a) Inelastic tunneling from initial states in the tip to final states in the sample (here: molecular states). b) Elastic tunneling into molecular states, i.e. hot electron injection, followed by an electronic transition inside the molecule. This excitation channel may couple to the TIPs which enhances the light emission from this channel.

Here, an analysis of the spectra of the emitted light can give further insight into the involved excitation mechanisms. The lifetimes for the electronic excitations that may decay rediatively inside the molecule are in the order of 10ps [33]. This is much longer than the lifetimes of the TIPs which are in the order of 10fs [57]. Consequently, emission lines for the radiative decay of electronic excitations of the molecules would be expected to be sharper than the peaks in the emission spectra observed for metals which purely reflect the TIP-spectrum of the tip-sample junction. However, remaining molecule-substrate interactions may shorten the lifetime of the molecular excitations and broaden the corresponding emission lines.

Electronic transitions inside the molecules couple to the TIPs, so that the TIP-spectrum for the specific tunneling tip significantly also influences the appearance of the molecule-specific features in the emission spectra [17]. However, these features would still be expected at characteristic and molecule specific photon energies, i.e. wavelengths.

In our emission spectra gathered on the molecules on Bi/Cu(111), we do not observe any molecule specific features (see Fig. 95). This allows us to conclude that electronic transitions inside the molecule do not play a significant role here. Instead, we may deduce that the enhancement of the light emission which we observe in our data must be the result of a more efficient excitation of the TIP modes by inelastic tunneling, a reduction of the non-radiative decay channels for the latter or a combination of both.

In the following sections, we further analyze the role of the molecular LDOS for the excitation efficiency (sections 13.2 - 13.4) before we discuss the general role of the molecules for the enhancement of the plasmonic light emission in more detail in section 13.6.

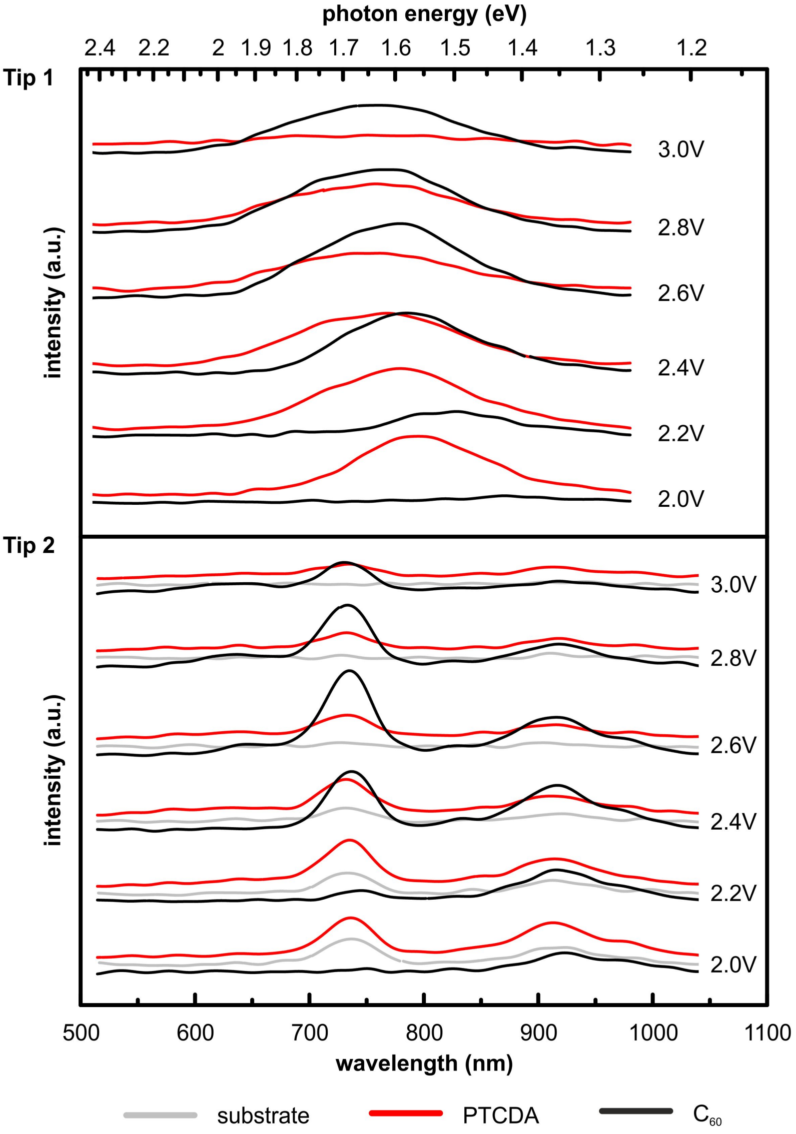

Figure 95: Spectra of the emitted light acquired with tip 1 (top) and tip 2 (bottom). Data revisited from Figs. 84 and 87. The emission spectra show no indication for light emission stemming from the radiative decay of electronic excitations of the molecules.

13.2 THE ROLE OF THE MOLECULAR LDOS FOR THE EXCITATION EFFICIENCY

In chapter 10, we discussed the active role of organic layers directly adsorbed on metal surfaces in providing LDOS as final states for elastic and inelastic tunneling processes. The general influence of the sample LDOS on the emission intensity versus the bias voltage has been exemplary discussed for pristine Ag(111) in chapter 8.7. The discussion yielded that the emission intensity induced at a certain bias voltage is governed by the interplay of the LDOS at different energies providing final states for elastic and inelastic transitions.

In our study of the effect of PTCDA and C_{60} on the light emission induced on Bi/Cu(111), we worked with submonolayer coverages of the organic molecules. This allowed us to gather data sets of the molecular layers as well as on the pristine substrate with the same tip. Even though the characteristic emission spectra exhibit similar shapes for all sample species, i.e. the molecules and the Bi/Cu(111)-substrate, the respective spectra of the overall photon yield exhibit significant differences (see e.g. Fig. 85, Fig. 88).

Even after a significant tip change affecting the TIP-spectrum, the characteristic shapes of the spectra of the overall photon yield, remain widely preserved (see Fig. 89). This underlines the governing impact of the molecular LDOS on the TIP-excitation efficiency.

Our detailed spectroscopic data sets for PTCDA and C_{60} on Bi/Cu(111) allow us to further characterize the particular impact of the molecular LDOS on the TIP-excitation. First, we want to concentrate on the spectra of the overall photon yield and discuss the spectra for each species individually.

Here, we exemplary refer to data recorded with tip 2. The range of possible transition energies, i.e. the energies of the TIP modes, were extracted from the corresponding spectra of the emitted light (see Fig. 87).

13.2.1 *The Overall Photon Yield Induced on Bi/Cu(111)*

Fig. 97 displays a representative spectrum of the overall photon yield (Fig. 97 b) along with the corresponding dI/dV-spectrum (Fig. 97 a) and the tip-retraction curve (Fig. 97 c) for the Bi/Cu(111) substrate.

Up to a bias voltage of approximately 2.3V, the dI/dV-spectrum is relatively featureless (see Fig. 97 a). The LDOS slowly increases until two shoulders at approximately 2.25V and 2.4V, as well as two peaks at 2.6V and 2.9V occur. The peaks may be assigned to spin split quantum well states of the Bi-monolayer as discussed in chapter 11.2.

The corresponding spectrum of the overall photon yield shown in Fig. 97 b possesses a single peak. In the spectrum itself, no other characteristic features can be clearly distinguished. Looking at the derivative of the photon yield accents the changes in the slope of the spectrum. Thus, the bias voltages at which the rate with which the ratio of inelastic to elastic channels changes can be highlighted.

The inelastic tunneling probability depends on the ratio of inelastic to elastic tunneling channels. The overall number of possible final states for elastic or inelastic tunneling is given by the integral over the all states up to the applied bias voltage V_{Bias}

or $V_{Bias} - h\nu/e$, respectively. While the opening of a state providing elastic channels leads to a decrease of the changing rate of the fraction of inelastically tunneling electrons, the opening of a state providing inelastic channels increases the changing rate (see Fig. 96).

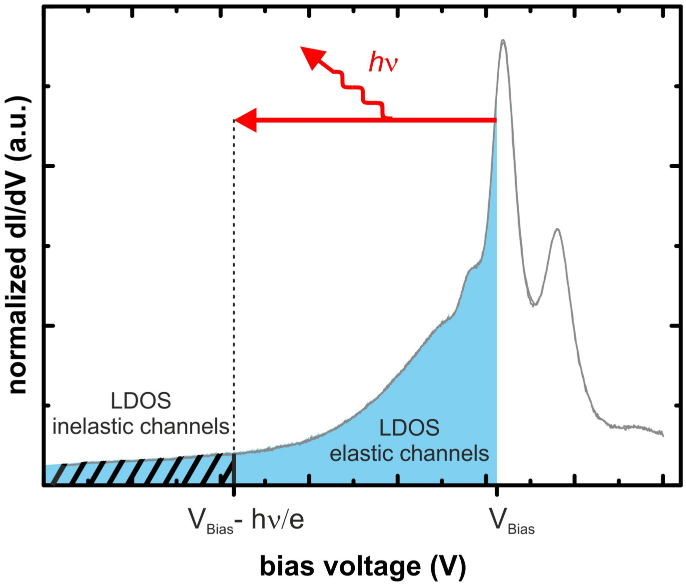

Figure 96: Scheme indicating the energetic ranges (bias voltage ranges) within the dI/dV-spectra that provide final states for elastic and inelastic transitions at a certain applied bias voltage V_{Bias}.

Characteristic changes in the derivative are marked by colored vertical lines. The attached arrows and vertical bars indicate the range of transition energies provided by the TIP spectrum with maxima at 1.35eV and 1.68eV.

The onset of the light emission lies at around 1.2V (light blue line). The spectrum of TIP modes as revealed by the spectra of emitted light reaches down to about 1.2eV (see Fig. 87). Here, we can infer that the final states for the inelastic transitions exciting the TIP modes lie close to the Fermi energy, where the LDOS of the Bi/Cu(111) substrate is uniformly low (see Fig. 97 a). Additionally, some final states provided by the sample might actually lie slightly below the Fermi energy because the Fermi distribution at non-zero temperature also allows some empty states below the Fermi energy.

The derivative of the photon yield, i.e. the change in the ratio of inelastic to elastic channels, increases with an approximately linear slope up to 1.75V. This may be assigned to the opening of inelastic channels with an only moderate increase of elastic channels. Between 1.75V (green line) and 2.2V (dark blue line) the rate of change of the overall photon yield drops and falls below zero. This may be correlated to the rapidly increasing number of elastic channels with an only moderate growth of the number of inelastic channels. This results in a peaking of the overall photon yield. The drop in the changing rate slows down when the range of possible energetic transitions reaches the ascending flank of the dI/dV-spectrum. Here, the number of inelastic channels starts to increase faster than before counteracting the increase of elastic channels more effectively. At 2.6V the peaking of the dI/dV-spectrum marks the beginning of a slower rise of the number of elastic channels. At the same time the number of inelastic channels starts to grow faster so that the drop of the overall photon yield slows down. At 2.75V the changing rate is once again slowed down by the anew opening of an electronic state leading to a faster increase of the elastic channels.

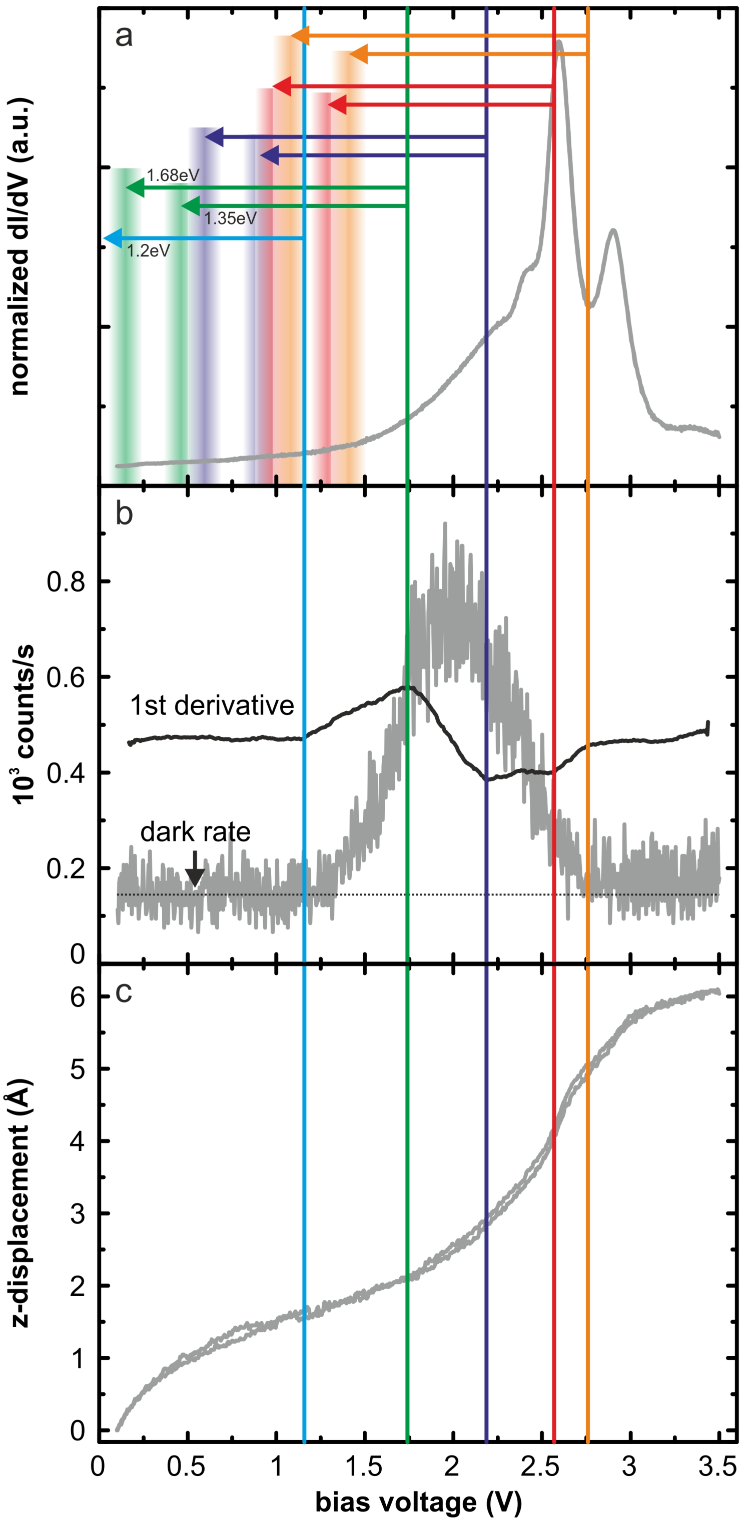

Figure 97: Comprehensive spectroscopic data set for the Bi/Cu(111)-substrate acquired with tip 2. a) Normalized dI/dV-spectrum, b) simultaneously acquired spectrum of the overall photon yield. The derivative of the spectrum is shown in black. Smoothing was applied. c) Relative z-displacement of the tip. Several characteristic points in the derivative of the spectrum of the overall photon yield are marked by vertical lines. The attached arrows and bars indicate the respective range of possible energetic transitions.

The light emission drops to a certain minimum level, which is still slightly higher than the dark count rate (indicated by the horizontal black dotted line). Towards higher bias voltages, a subsequent small increase of the overall photon yield is slightly discernible. Here, the rise in the number of final states for elastic tunneling is rather low, while with rising bias voltage an increasing number of final states for inelastic tunneling becomes available. Thus, for even higher bias voltages than the ones examined here, a second peaking of the light emission intensity would be expected[1].

13.2.2 *The Overall Photon Yield Induced on PTCDA*

The spectra of the overall photon yield for the PTCDA-domains are especially rich in features that may be assigned to the LDOS of the molecular layers. Like for the substrate in section 13.2.1, looking at the first derivative of the overall photon yield helps to identify changes in the slope of the overall photon yield versus the bias voltage and to assign them to the opening of electronic states providing final states for elastic or inelastic tunneling.

Characteristic features in the derivative are indicated by vertical lines in Fig. 98. The attached arrows and vertical bars indicate the range of transition energies provided by the TIP spectrum with maxima at 1.35eV and 1.68eV. For comparison, also dI/dV-data and the corresponding spectrum of the overall photon yield for the substrate are shown in Fig. 98 a and b.

The onset of the overall photon yield induced on PTCDA (gray vertical line) lies slightly above that of the substrate around 1.3V. Thus, also here, the energetically lowest final states for inelastic tunneling are expected close to the Fermi level. In the dI/dV-data for PTCDA, small peaks in the LDOS can be found at bias voltages of 0.15V and 0.35V. These molecular states may be identified as final states for inelastic transitions.

The continuous opening of further inelastic channels leads to an increase of the changing rate up to approximately 1.65V (blue vertical line). At this bias voltage, the opening of the LUMO+1 overrules this effect and leads to a decrease of the changing rate up to 1.8V (green vertical line). Between 1.8V and 2.1V the changing rate is almost constant. At 2.1V (dark blue vertical line) the decrease in the corresponding LDOS providing additional final states for inelastic tunneling is overruled by the significantly higher LDOS responsible for the increase of the number of elastic channels. This leads to a peaking of the overall photon yield around 2.3V.

At 2.65V (red vertical line) the drop of the emission intensity is further accelerated by the opening of an additional state providing elastic channels. The peaking of this state around 2.9V cooccurs with the starting provision of inelastic channels by the LUMO+1. This slows down the decrease of the emission yield (orange vertical line). At 3.1eV (black vertical line) this effect is again counteracted by an anew increase of the LDOS providing further elastic channels.

---

[1] In fact, at elevated bias voltages $>\approx 5$V, an oscillatory behavior of the LDOS is expected due to field emission resonances, i.e. the interference of electron waves due to the reflections at the walls of the vacuum tunneling barrier. These oscillations in the LDOS providing final states for elastic and inelastic tunneling further evoke oscillations in the light emission intensity [192].

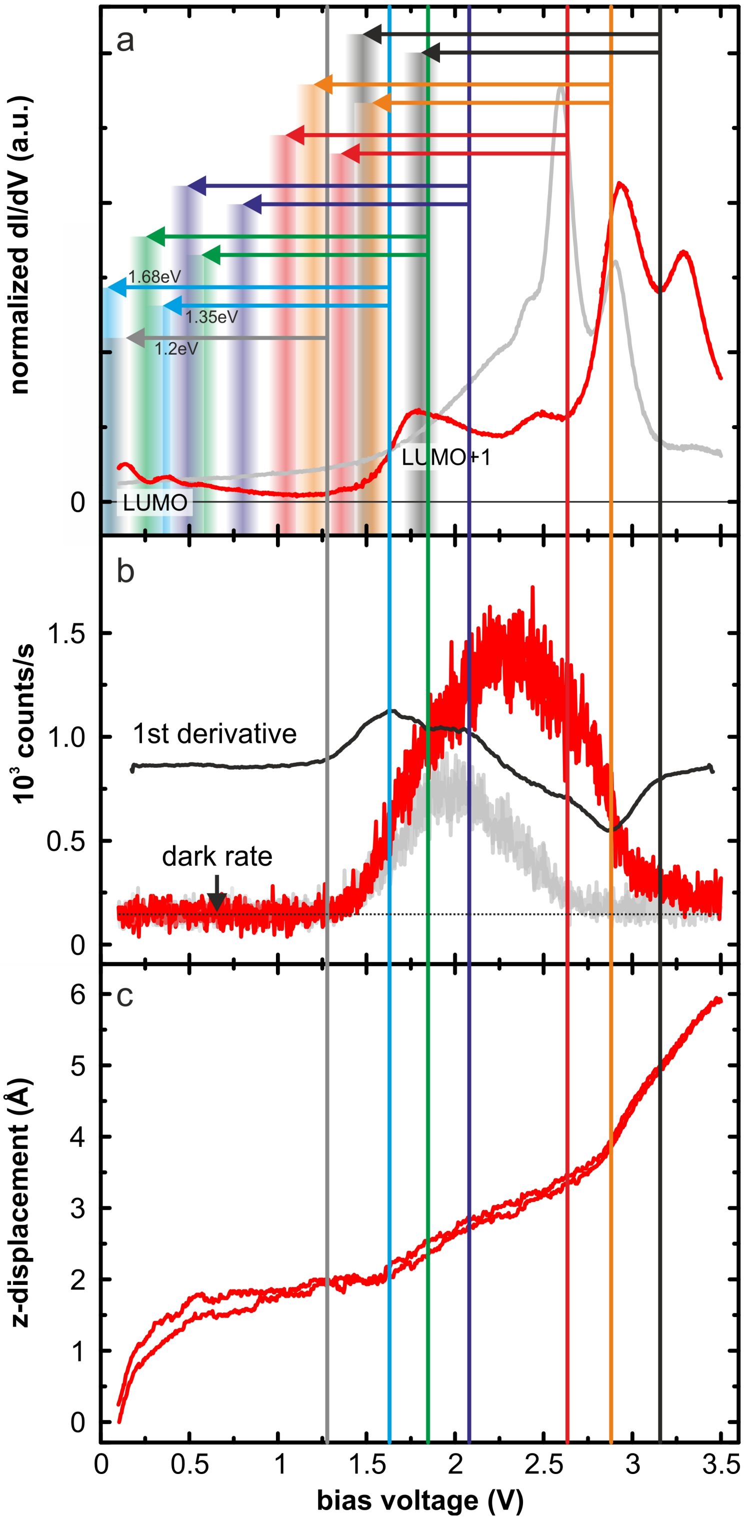

Figure 98: Comprehensive spectroscopic data set for PTCDA on Bi/Cu(111) acquired with tip 2. a) Normalized dI/dV-spectrum, b) simultaneously acquired spectrum of the overall photon yield. The derivative of the spectrum is shown in black. Smoothing was applied. c) Relative z-displacement of the tip. Spectra for PTCDA are depicted in red. For comparison, spectroscopic data for the underlying Bi-monolayer substrate are shown in light gray. Several characteristic points in the derivative of the spectrum of the overall photon yield are marked by vertical lines. The attached arrows and bars indicate the respective range of possible energetic transitions.

13.2.3 The Overall Photon Yield Induced on C_{60}

In the spectra of the overall photon yield for the C_{60}-domains (Fig. 99 b), the shifted onset for the light emission as compared to the substrate and PTCDA is very obvious (blue). It lies around 1.6V which is a shift by roughly $0.2 - 0.3$V towards higher bias voltage as compared to the onset for PTCDA. This nicely corresponds to the onset of the C_{60}-LUMO around 0.3V above the Fermi energy, proposing that this molecular state provides the lowest energy final states for the inelastic transitions.

The overall photon yield increases even faster once the opening of additional elastic channels from the LUMO+1 slows down (green vertical line at 2.1V). The increase in the changing rate is stopped at 2.3V (dark blue vertical line) when the increase in the number of inelastic channels provided by the LUMO is slowed down due to the very low LDOS at $V_{Bias} - h\nu/e$. Also, additional elastic channels become available from the LUMO+2.

The overall photon yield peaks at 2.6V. The rate at which the photon yield decreases is slowed down at 2.8V (red vertical line) when further inelastic channels become available from the LUMO+1. This cooccurs with a slowing down of the increase of the elastic tunneling channels. At 3.25V (orange vertical line) another state providing elastic channels opens which stops this tendency.

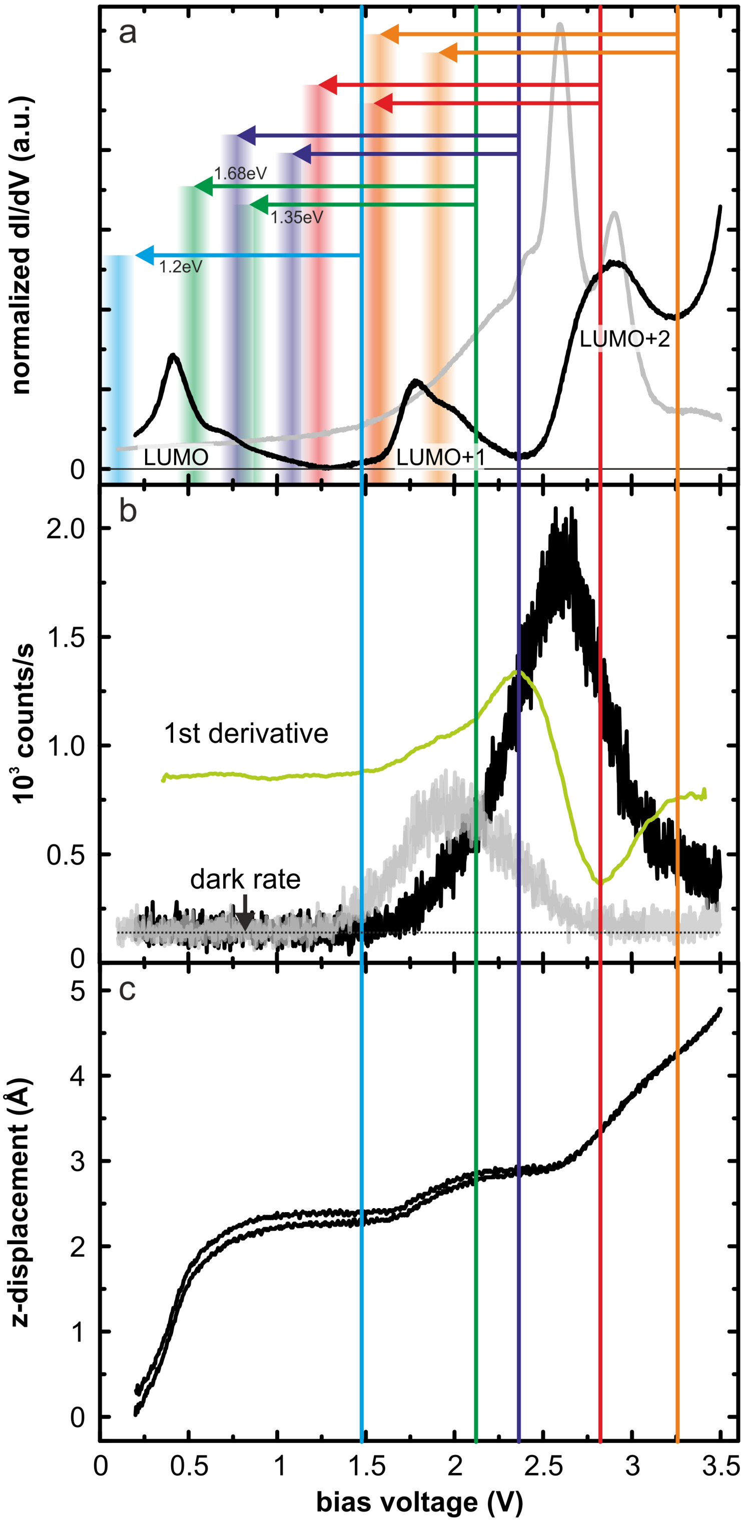

Figure 99: Comprehensive spectroscopic data set for C_{60} on Bi/Cu(111) acquired with tip 2. a) Normalized dI/dV-spectrum, b) simultaneously acquired spectrum of the overall photon yield. The derivative of the spectrum is shown in green. Smoothing was applied. c) Relative z-displacement of the tip. Spectra for C_{60} are shown in black. For comparison, spectroscopic data for the underlying Bi/Cu(111) substrate are depicted in gray. Vertical lines indicate characteristic points in the derivative of the spectrum of the overall photon yield. The attached arrows and bars indicate the range of possible energetic transitions.

13.3 SIMULATION OF THE SPECTRA OF THE OVERALL PHOTON YIELD

The above discussion revealed a clear correlation between features in the LDOS and changes in the rise or fall of the overall photon yield. In this section, we want to apply a simple simulation in order to further demonstrate that the observed changes of the overall photon yield with the bias voltage are indeed dominantly determined by the ratio of the inelastic channels to the overall tunneling channels.

The inelastic tunneling probability is given by the ratio of inelastically tunneling electrons to overall tunneling electrons per time, i.e. the ratio of the inelastic tunneling current to the overall tunneling current. As stated e.g. in chapter 8, section 8.7.2.1, the fraction of inelastically tunneling electrons is very small so that the overall tunneling current may be approximated by the elastic tunneling current. The elastic and inelastic tunneling current are proportional to the LDOS times the respective transmission probability for an electron through the tunneling barrier integrated up to V_{Bias} and $V_{Bias} - h\nu/e$, respectively (see chapter 2.5). Thus, the inelastic tunneling probability $P_{inelastic}$ versus the bias voltage may be approximated by

$$P_{inelastic}(V_{Bias}) \approx \frac{I_{inel}}{I_{el}} \propto \frac{\int\limits_{0}^{V_{Bias}-h\nu/e} LDOS(V) T_{inel}(V, V_{Bias}) dV}{\int\limits_{0}^{V_{Bias}} LDOS(V) T_{el}(V, V_{Bias}) dV}, \tag{13}$$

where $T(V, V_{Bias})$ is the transmission probability of an electron through the tunneling barrier.

Chen et al. used this correlation to simulate their spectra of the overall photon yield using simultaneously acquired dI/dV-data [211]. Here, we want to simulate our data in a similar manner.

Feenstra et al. discussed that the normalized dI/dV-signal gathered at constant distance gives a measure of the LDOS at a certain bias voltage [46]. In contrast to the conventionally applied mode of dI/dV-spectroscopy, the data presented here was gathered in constant current mode. This means that the dI/dV-signal was recorded while the feedback loop continuously adjusted the tunneling distance in order to keep the tunneling current constant (see 2.5). This way, changes in the LDOS with the bias voltage are counteracted by changes in the tunneling barrier width which directly affects the transmission $T(V, V_{Bias})$ through the barrier. As a result of this acquisition method, constant current dI/dV-signals usually exhibit a strong increase towards small bias voltages where the LDOS available for tunneling is rather low and the transmission through the barrier is increased as the feedback loop lowers the tip-sample distance. Conversely, the overall increase of the available LDOS towards higher bias voltages is associated to a decrease of the transmission through the barrier as the tip is gradually retracted from the sample. This is reflected in a rise of the constant-current dI/dV-signal which is smaller than the corresponding relative change in the LDOS. To account for such changes in transmission during the taking of the spectra, in order to yield a signal roughly proportional to the LDOS, the dI/dV-spectra shown in this thesis were normalized by multiplying with the bias voltage. However, this only accounts for a roughly linear decrease of the transmission with the bias voltage which is only a rough approximation. For a more precise normalization of the dI/dV-signal, the data has to be multiplied by a signal proportional to the increase of the tunneling current that would have occurred when tunneling at constant distance, i.e. constant transmission. Such dimensionless factor, in the following referred to as the simulated tunneling current factor I_{sim}, can be calculated from the relative z-displacement curves of the tunneling tip by using

$$I_{sim}(V) = exp^{-2\kappa(z_0+\Delta z_{rel}(V))} = I_0 exp^{-2\kappa\Delta z_{rel}(V)}, \tag{14}$$

with $I_0 = exp^{-2\kappa z_0}$ where z_0 corresponds to the tunneling distance at the lowest bias voltage of the spectrum. κ is the inverse decay length and is in the order of 1Å^{-1} (see chapter 2.2.1). For the simulation shown in the following $\kappa = 1\text{Å}^{-1}$ was assumed. The parameter z_0 was varied to fit the respective experimental data.

Using the normalization with I_{sim}, $P_{inelastic}$ may be approximated from the constant current dI/dV-signal by

$$P_{inelastic}(V_{Bias}) \propto \frac{\int\limits_0^{V_{Bias}-h\nu/e} dI/dV \cdot I_{sim} dV}{\int\limits_0^{V_{Bias}} dI/dV \cdot I_{sim} dV}, \tag{15}$$

where $h\nu$ is the energy of the emitted photons and e is the elementary charge. Here, we simulated data acquired with tip 2 (see e.g. Figs. 97 - 99) and used the sum of the integrals for $h\nu = 1.35eV$ and $h\nu = 1.65eV$. The results of the simulation along with the corresponding experimental data for each sample species are shown in Fig. 100.

Especially for higher bias voltages, i.e. the descending flanks of the spectra, the obtained spectra nicely correlate to the experimental data. However, the initial rise of the simulated spectra is significantly steeper than for the actual data. This might be explained by a systematic error in the simulation. The expression for the inelastic tunneling probability given in eq. (15) contains integrations starting from the Fermi energy. Here, the spectra were recorded at constant current so that the energetic range of $\pm 0.1V$ ($\pm 0.2V$ for C_{60}) around the Fermi energy was exempt from the spectroscopic studies to prevent tip-sample collisions. The higher starting point of the integration, resulted in slightly smaller values of the integrals. With a rising integration range, this error becomes smaller. As the integration range is generally smaller for the integrals associated to the number of inelastic channels, the number of inelastic channels is underestimated more strongly than the the number of elastic channels. The higher the bias voltage, i.e. larger the integration ranges for both, elastic and inelastic transitions, the smaller becomes the error. Given the simplicity of the simulation, the simulated spectra are in nice agreement to the experimental data.

The normalization of the constant current dI/dV-signal applied here includes changes in the transmission due to changes in the tunneling distance. The latter are accounted for by the multiplication by I_{sim}, so that an entity directly proportional to the original LDOS as a function of energy (or voltage V) is obtained. Further changes of the transmission $T(V, V_{Bias})$ with the tunneling energy eV or bias voltage V_{Bias} are neglected in the present simulation. However, the good agreement between the simulation and our experimental data shows that indeed such further changes in the transmission should not play any significant role.

As a result, we may conclude that changes in the inelastic tunneling probability with the bias voltage may be dominantly traced back to changes of the LDOS providing the respective elastic and inelastic tunneling channels. The resulting changes in the ratio of inelastic to elastic tunneling channels manifest themselves in changes of the emission yield with the bias voltage.

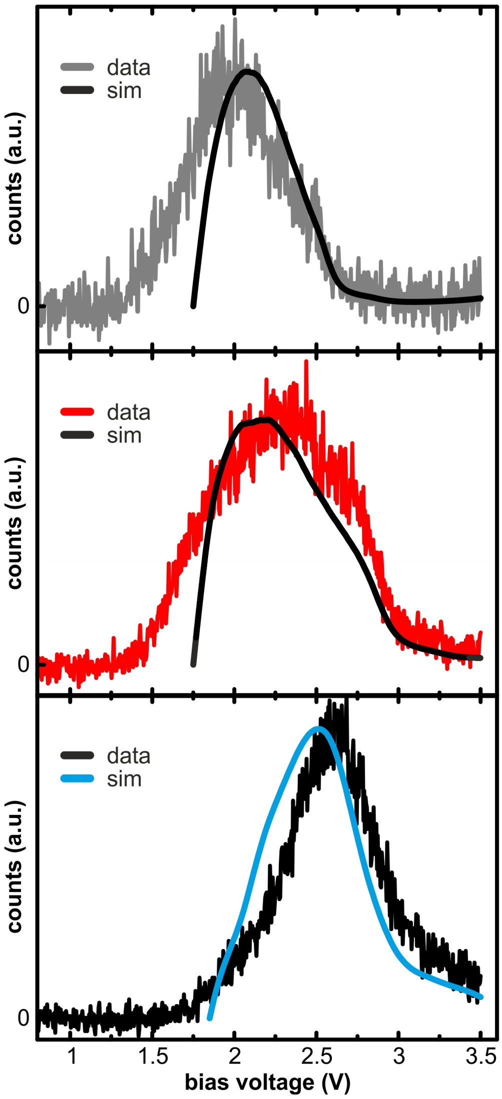

Figure 100: Simulations of the spectra of the overall photon yield. The simulated data were calculated according to equation 15 from dI/dV-data and spectra of the relative z-displacement of the tip.

13.4 THE ROLE OF FINAL STATES FOR INELASTIC TRANSITIONS

In section 13.2, we have identified a variety of features in the spectra of the overall photon yield that can be correlated to the LDOS provided by the molecules. However, changes in the availability of LDOS for final states for elastic and inelastic tunneling channels oftentimes occur simultaneously so that their contributions on the overall photon yield are entangled.

A detailed analysis of the spectra of the emitted light reveals valuable complementary information. In our experiments, we gathered data sets with two different tips that yielded quite different emission spectra. The characteristic shapes of the emission spectra with each tip allow us to focus on different details, respectively.

13.4.1 *High Energy Cutoffs*

The emission spectra reveal the energetic transitions exciting the TIPs. The applied bias voltage defines an upper limit eV_{Bias} for the initial state energy of an inelastically tunneling electron. In turn, the energetic position of the lowest final states available for inelastic transitions defines a lower limit for the final state energy. The difference between the upper and the lower limit is the range of possible transition energies.

For metallic substrates, the lowest final states for inelastic transitions lie close to the Fermi energy. This means the energetically largest possible transitions occur from eV_{Bias} to the Fermi energy. The corresponding maximum energy of the emitted photons is $h\nu_{max} = eV_{Bias}$. If the energetically lowest final states for inelastic transitions lie above the Fermi energy, i.e. at an energy $E_{final\,inelastic\,min} > E_F$, the range of possible energetic transitions becomes smaller. This defines high energy cutoffs $h\nu_{max} = eV_{Bias} - E_{final\,inelastic\,min}$ in the emission spectra.

With rising bias voltage, i.e. rising eV_{Bias}, TIPs with higher energies may be excited by inelastic tunneling. Consequently, the high energy cutoffs $h\nu_{max}$ are shifted towards higher photon energies.

Tip 1 exhibits a rather broad TIP-spectrum spectrum (see Fig. 84). Exemplary spectra are revisited in Fig. 101. This allows to identify high energy cutoffs in the emission spectra.

The range of energetic transitions may be additionally limited by the particular TIP-spectrum. For tip 1, the energetically highest TIP-modes in the examined range reach to about 2.15eV. Since we are interested in the cutoffs defined by the range of inelastic transitions and not by the TIP spectrum, we limit our discussion to high energy cutoffs occuring below this energy.

For PTCDA, the high energy cutoffs lie close to eV_{Bias} (see Fig. 101 a). In contrast, the high energy cutoffs in the emission spectra for C_{60} lie roughly 0.4eV below eV_{Bias} (see Fig. 101 b). With these high energy cutoffs, we may identify the energetically lowest final states for inelastic transitions $E_{final\,inelastic\,min} = eV_{Bias} - h\nu_{max}$. In fact, the dI/dV-spectra for the PTCDA exhibit molecular states close to the Fermi energy. For C_{60}, the lowest molecular state is peaked around 0.4eV.

These findings are in agreement to similar observations for the high energy cutoffs in the emission spectra induced on one and two layer thick C_{60}-domains on Au(111) [58].

Also in this case, the energetically lowest final states were provided by the respective LUMOs of the molecular layers.

Here, our data further supports, that the majority of the inelastically tunneling electrons tunnel into molecular states and not into the substrate.

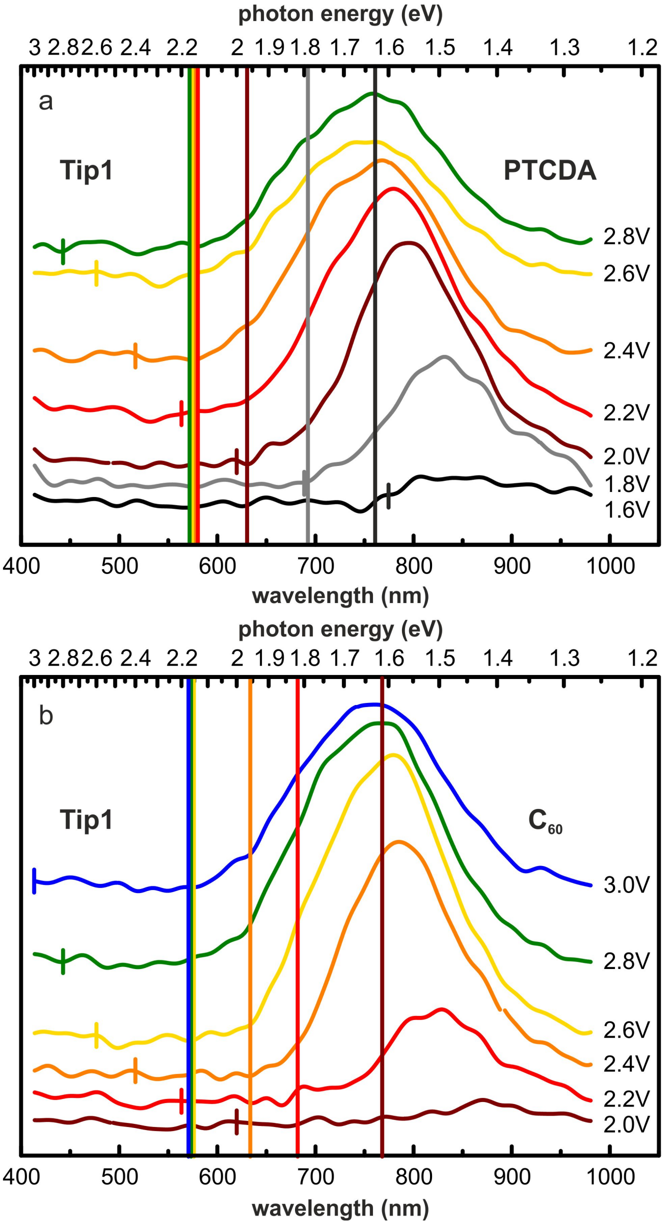

Figure 101: High energy cutoffs in the spectra of the emitted light acquired with tip 1 for PTCDA (a) and C_{60} (b). The applied bias voltages are indicated next to the respective spectra. The high energy cutoffs are indicated by long color coded vertical lines. The short verticals lines indicate the respective quantum cutoff eV_{Bias} for each spectrum where applicable.

13.4.2 *Excitation Efficiencies of Different TIP modes*

In contrast to tip 1, the emission spectra obtained with tip 2 exhibit two dominating peaks with a width of around 0.2eV (see Fig. 87). Emission spectra for PTCDA and C_{60} acquired with tip 2 at positive bias voltage are revisited in Fig. 102. With this spectral shape, the differences in the high energy cutoffs for the different sample species are much harder to distinguish. However, the shape of the emission spectra provided by tip 2 allows us to nicely see the effect of the alternating spectral weights of individual TIP modes. At equal tunneling energies, the relative heights of the intensity peaks around approximately 1.35eV and 1.68eV are significantly different for the different sample species. The peak heights, i.e. the intensities for photon energies of 1.35eV and 1.68eV, yield the excitation efficiencies for the respective TIP-modes.

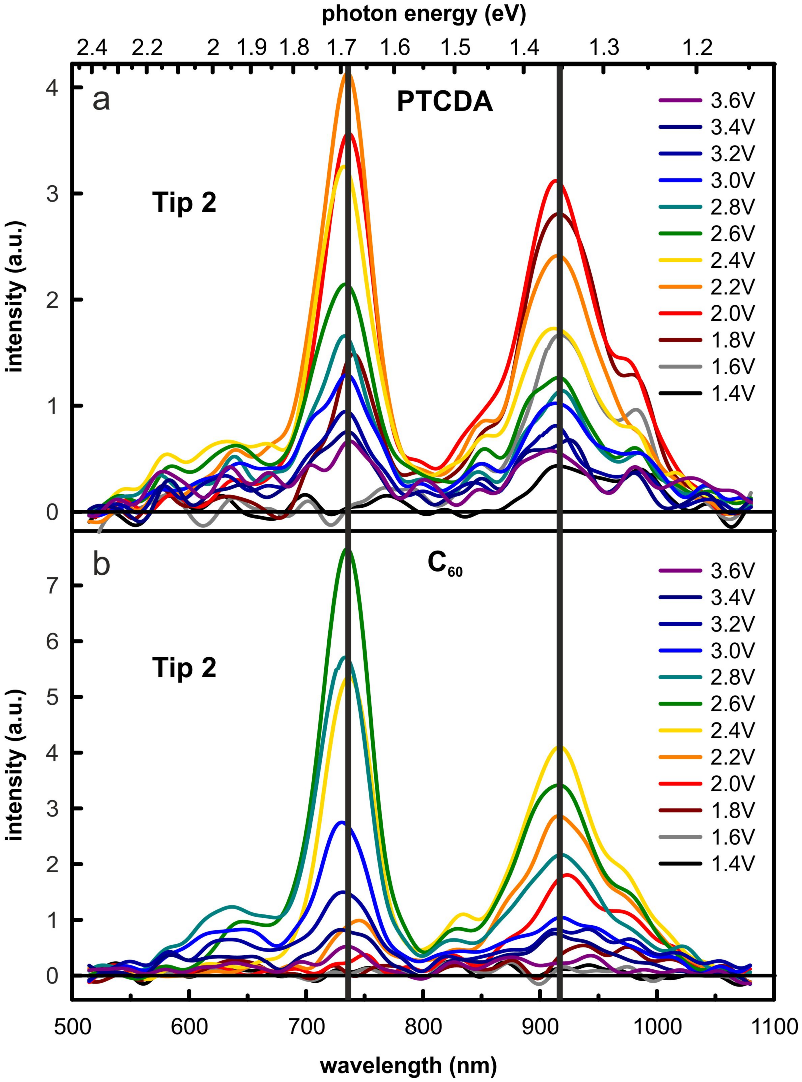

Figure 102: Emission spectra acquired with tip 2 on PTCDA and C_{60}. Data revisited from Fig. 87. The shape of the emission spectra acquired with tip 2 allows us to easily analyze the excitation efficiency for different TIP modes excited at the same bias voltage, i.e. tunneling energy.

The spectra of the overall photon yield discussed in section 13.2 contain information about the entire TIP-spectrum provided by the specific tip. By analyzing the intensity of the emission spectra at a certain photon energy, we can focus on individual transition energies. In Fig. 103, the intensities for characteristic photon energies, 1.35eV and 1.68eV, are plotted versus the bias voltage. Note that in contrast to the spectra of the emitted light shown before, the intensities plotted here were corrected for the efficiency of the used grating[2].

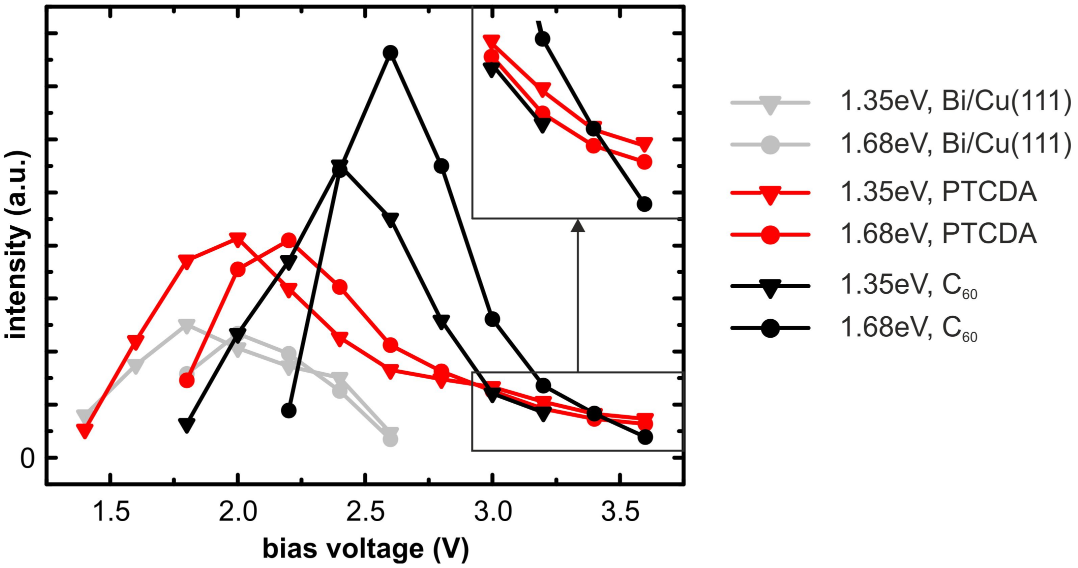

Figure 103: Plot of the emission intensities for two specific photon energies at positive bias voltage. For each sample species, the emission intensites for the 1.35eV and 1.68eV-modes are displayed. The photon energies correspond to the two dominating TIP modes for tip 2. The inset shows a detail of the data for bias voltages from 3.0eV to 3.6eV. The intensities were extracted from the emission spectra displayed in Fig. 87 and further corrected for detection efficiency.

For each bias voltage, the intensities of the two different transition energies for each sample species were extracted from the same emission spectrum. Therefore, the elastic channel is the same for both. Thus, by comparing these two intensities, we can isolate the impact of the availability of final states for inelastic transitions on the emission intensity at a given bias voltage.

As expected, the shape of the intensity plots for each transition energy exhibit close resemblance to the respective spectra of the overall photon yield. Regarding each sample species individually, the onsets and peaks between the 1.35eV and 1.68eV curves are shifted by roughly 0.3eV. This corresponds to the energy difference between the two modes and is in accordance with the later availability of final states which govern the excitation efficiency of the TIPs. Here, e.g. the final states from the LUMO become available for the 1.35eV transitions first, followed by the 1.68eV transitions. Regarding each sample species individually, the shapes of the respective 1.35eV and 1.68eV intensity curves are very similar.

The number of possible final states available for inelastic transitions at an applied bias voltage V_{Bias} is given by the integral over the sample LDOS up to $V_{\text{Bias}} - h\nu/e$

---

[2] This yielded an additional intensity factor of 4/3 for the 1.35eV-peak.

(see section 13.3). Thus, it would intuitively be expected that at a given bias voltage the intensity of the $1.68eV$ mode would always be lower than the intensity of the $1.35eV$ mode. Looking at the data shown in Fig. 103 this is not the case.

This may be understood in terms of a different efficiency with which the respective modes may be excited.

13.5 TUNNELING FROM THE SAMPLE TO THE TIP

At negative bias voltage, the final states for elastic and inelastic tunneling are provided by LDOS of the tip. Thus, the availability of final states is independent of the sample. The sample now influences the tunneling probability by providing initial states for the tunneling.

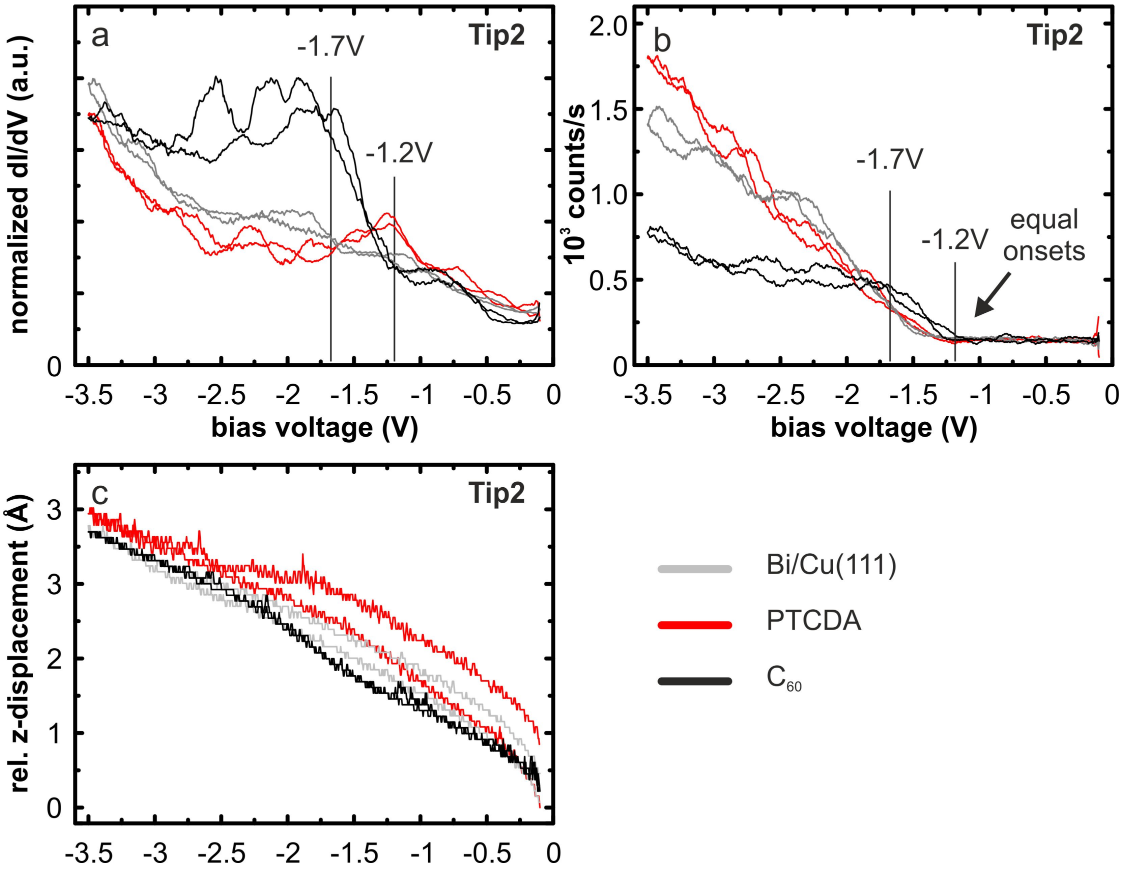

Figure 104: Set of spectroscopic data for negative bias voltages revisited from Fig. 91. a) Normalized dI/dV-spectra, b) spectra of the overall photon yield. Due to the high noise level in the orignial spectra, only smoothed data are shown. c) Corresponding tip retraction curves.

Fig. 104 revisits spectroscopic data for all sample species at negative bias voltage. At this bias polarity, the onset of the overall photon yield occurs at equal bias voltages for all sample species. In section 13.2, we discussed that the different availability of final states for inelastic transitions leads to different onsets of the light emission at positive bias voltage. At negative sample voltage, the tip provides the same LDOS for final states for the inelastic transitions from the molecules as well as from the substrate. The onset lies around 1.2eV which roughly corresponds to the lowest modes of the TIP-spectrum provided by tip 2 in the range detectable by the APD. This points to final states close to the Fermi level of the tip.

Both, PTCDA and the Bi/Cu(111)-substrate exhibit similar overall photon yields at equal tunneling energies throughout the entire spectra of the overall photon yield (see Fig. 104). For these sample species, also the dI/dV-spectra are very similar.

From around 1.7V on, the photon yield induced on the C_{60}-domains is significantly lower than for the other sample species. The corresponding dI/dV-spectra exhibit a rise of the LDOS around this bias voltage.

At negative bias voltage, the sample LDOS provides the initial states for elastic and inelastic tunneling. However, the initial states for the main elastic tunneling channels and the relevant inelastically tunneling electrons inducing the light emission do not necessarily have to be at the same energy [14] (see Fig. 105). At low negative bias voltage, the majority of all electrons tunnel from energies close to the Fermi energy of the sample (see Fig. 105 a). However, when the LDOS from the lower lying states becomes available at higher negative bias voltage, e.g. from −1.3V for C_{60}, the overall, i.e. elastic and inelastic, tunneling channels may be shifted away from the Fermi energy of the sample [14] (see Fig. 105 b). Consequently, the transition energies involved in the corresponding inelastic tunneling processes would not possess sufficient energy to induce light emission in the visible range until the negative bias voltage is increased much further. The resudiual light emission at these bias voltages is induced by inelastically tunneling electrons that have initial states close to the Fermi energy of the sample, i.e. electrons with initial energies different from most elastically tunneling electrons.

This is in agreement with the small kink in the spectrum of the overall photon yield around −2.7V and −3.0V when the transition energies from states close to −1.3V and below would suffice to excite the 1.35eV and 1.68eV TIP-modes.

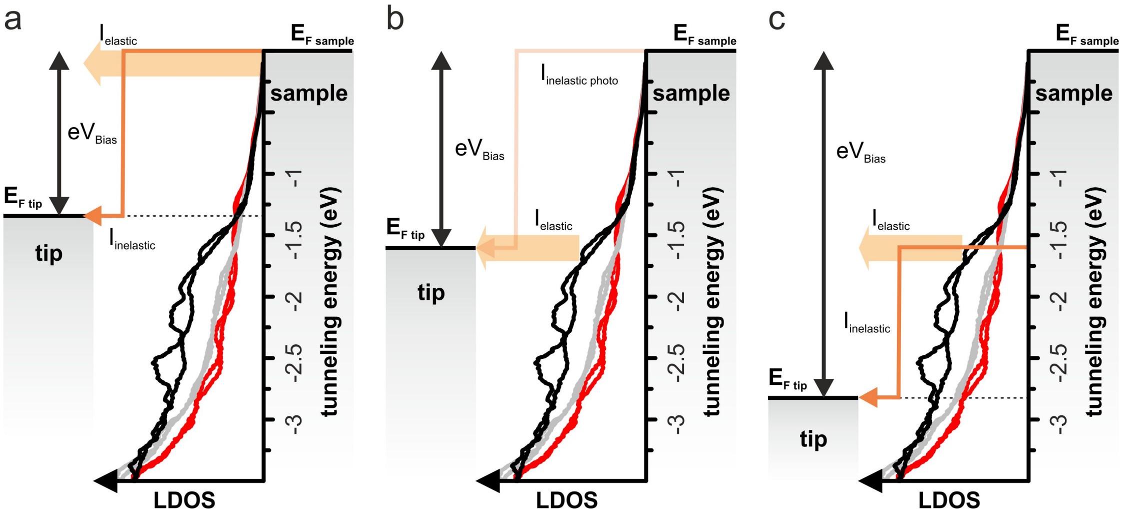

Figure 105: Tunneling scheme for elastic and inelastic channels at negative bias voltage. a) For small negative bias voltages, a lot of electrons tunnel from energies close to the Fermi energy of the sample. This is true for the elastic as well as the inelastic channels. b) When a lot of initial states, e.g. from the HOMO of the C_{60}-layers, become available at a certain applied bias voltage, the majority of the electrons tunnel with initial energies somewhat below the Fermi energy of the sample. However, the inelastic channels that are connected to the light emission still have initial states close to the Fermi energy of the sample. c) When the bias voltage is large enough, the initial state energies of the electrons tunneling at energies below the Fermi level of the sample is sufficient for inelastically tunneling electrons to induce the emission of photons.

Fig. 106 shows the plot of the respective peak heights in the emission spectra, analog to Fig. 103, for negative bias voltages. The intensities of the 1.35eV peak are very similar for all sample species. For the substrate and PTCDA, the 1.68eV-curves are similar and have a larger slope than the 1.35eV-curve. In particular, the 1.68eV-mode always has a higher intensity than the respective 1.35eV-mode. In terms of an integrated density of final states, the intensity of the 1.68eV-modes would generally be expected to exhibit a lower intensity than the 1.35eV mode. Here, a more efficient coupling seems to significantly enhance the 1.68eV-mode in this case.

In contrast, for C_{60}, from −2V on the 1.68eV-curve for C_{60} has a lower intensity and shows a similar slope to that of the 1.35eV-curves. Interestingly, the difference in the overall photon yield seems to be almost exclusively caused by differences in the excitation efficiency for the 1.68eV-peak.

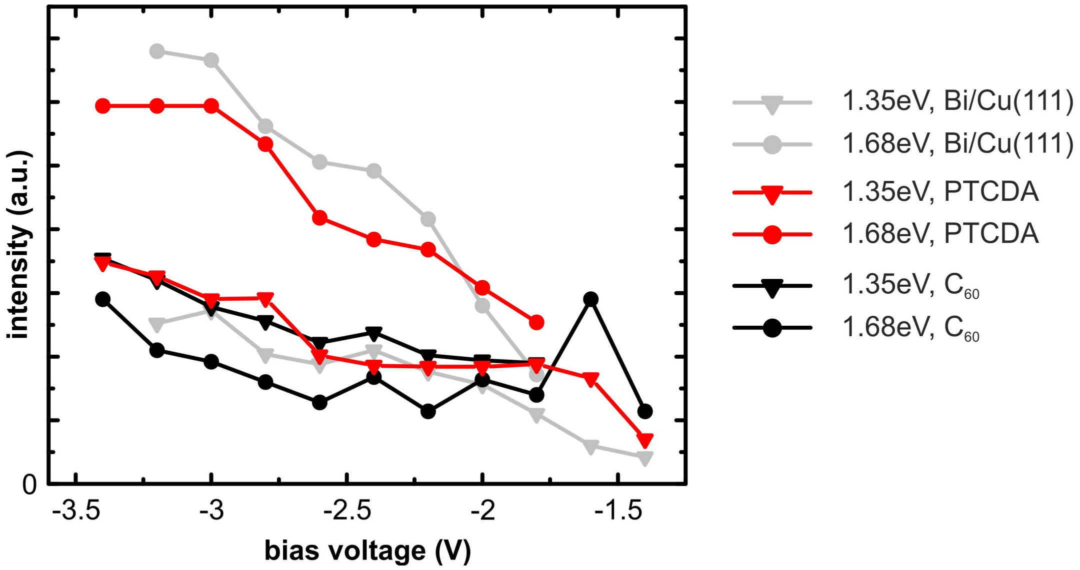

Figure 106: Plot of the emission intensities for photons with energies of 1.35eV and 1.68eV at negative bias voltage. At this bias polarity, the final states for the inelastic transitions are provided by the rather uniform LDOS of the tip. For the 1.35eV-mode, the emission intensities are very similar for all sample species. The emission intensity of the 1.68eV-mode is generally higher for the Bi/Cu(111)-substrate and PTCDA. In contrast, for C_{60}, the emission intensity of this mode is significantly reduced.

Above, we discussed a shift of the initial states for the inelastic transitions away from the Fermi energy from the sample. Indications for this behavior can also be found in the intensity plots for both transition energies for C_{60} and the 1.35eV-curves for PTCDA and the substrate shown in Fig. 106. The 1.35eV-curves are uniformly low down to −2.6V. From −2.8V on, a small increase of the intensity can be observed. This matches the onset of inelastic transitions from the elevated LDOS around −1.3V close to the Fermi energy of the tip (see Fig. 105 c). For the same reason, the intensity of the 1.68eV-mode for C_{60} rises from approximately −3.0V on.

13.6 THE ENHANCEMENT OF PLASMONIC LIGHT EMISSION

The above discussion allowed a deeper understanding of the role of the molecules on the excitation efficiency versus the bias voltage. However, a very peculiar effect that occurs in our data has not yet been addressed in detail: The enhancement of the overall yield induced on the molecules on the initial monolayer of Bi on Cu(111). Such behavior is in contrast to the usually observed reduction of the emission yield for molecules adsorbed on noble metals.

Here, the two factors may play a role. On the one hand, the LDOS provided by the molecules modifies the ratio of inelastic to elastic tunneling channels which may lead to an increased inelastic tunneling probability above the molecules. On the other hand, the interaction with the substrate defines the number of non-radiative energy dissipation channels and affects the lifetime of the inelastically tunneling electrons inside the molecules. This affects the efficiency of the TIP excitation (see chapter 10.1.4). Both effects will be discussed in further detail below.

13.6.1 *Local Density of States*

A representative set of spectroscopic data including dI/dV-spectra, spectra of the overall photon yield, and the corresponding tip retraction curves for all sample species is revisited in Fig. 107.

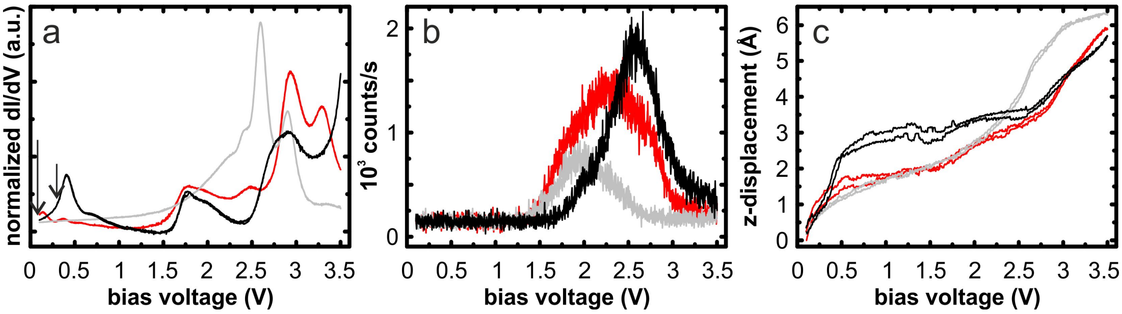

Figure 107: Representative set of spectroscopic data gathered with tip 2. a) Normalized dI/dV-data. b) Spectra of the overall photon yield. c) Relative z-displacement of the tip. Data revisited from Fig. 88.

Here, especially the lowest unoccupied molecular orbitals provide an increased local density of final states as compared to the substrate for both, PTCDA and C_{60}. We observe the strongest enhancement of the emission intensity for the C_{60}-domains. The latter provide a particularly high number of final states for inelastic transitions from the LUMO around 0.4eV. Also the PTCDA domains exhibit a somewhat increased LDOS at these final state energies as compared to the substrate.

At the same time, the dI/dV-spectra for the molecules exhibit a generally lower increase over wide parts of the spectra, i.e. the number of overall tunneling channels increases slower. The slower increase of the overall tunneling channels is also manifested in the corresponding tip-retraction curves. Over a wide range of bias voltages, the slope of the tip retraction curve for the substrate is steeper than the slope of those for the molecular species.

Both, an increased number of inelastic tunneling channels and a decreased number of elastic tunneling channels would be expected to lead to an increased inelastic tunneling probability induced on the molecules as compared to the substrate.

13.6.2 *Decoupling of the Molecules from the Substrate*

For molecules adsorbed directly on noble metal substrates without further decoupling, the light emission is usually reduced [13, 58, 140, 217](see chapter 10.1). A modified sample LDOS provided by the molecules might be an explanation for the reduction. However, it seems odd that for all kinds of molecular species adsorbed directly on noble metal surfaces the LDOS would always act in favor of a decreased emission yield.

Additionally, an enhancement of the plasmonic light emission with respect to the substrate has only been observed if the molecules were somehow decoupled from the surface [16, 31, 198, 219]. This indicates that the coupling of the molecules to the substrate might play a crucial role for the enhancement of the excitation efficiency of the TIP modes also in our case.

To further understand the effect of the decoupling on the excitation efficiency, we may once again apply the picture of the molecules acting as dynamic dipole oscillators discussed in chapter 10.1.4 [59, 220]: Energy dissipation from the molecules to the substrate damps the dipole oscillations of the molecules. Decoupling the molecules from the substrate prolongs the lifetime of the electrons inside the molecular states and reduces the damping. This way the dipole oscillations of the molecules may be driven more efficiently by the inelastic current. The molecules oscillating in phase with the TIP modes may increase the total dipole moment of the emitting antenna and enhance the light emission.

For our case, this picture may also yield an explanation for the stronger emission enhancement by the C_{60}-domains as compared to the PTCDA. Due to the three dimensional geometry of the fullerenes, the C_{60}-molecules may be less coupled due to the extension of the molecules in surface normal direction. Additionally, the C_{60}-molecules may posses a larger dipole moment perpendicular to the surface plane which leads to an enhanced coupling between the TIP-modes and the oscillating dipoles of the molecules.

13.6.2.1 *Coupling-Strength between the Molecules and the Bi/Cu(111)-substrate*

For an even stronger decoupling, i.e. longer lifetimes of the electronic states, a depopulation of the excited molecular states by direct transitions inside the molecules becomes possible. The longer the lifetime of an electron inside the excited molecular state, the higher the probability for a transition inside the molecule. These energetic transitions couple to the TIP modes which significantly enhances these channels as compared to the pure direct radiative decay of the excitations [17]. A further increased lifetime of the excitons further increases the probability of exciton-TIP coupling and therefore enhances the emission yield. Molecular fingerprints are then imprinted to the characteristic emission spectra for the specific tip-sample junction.

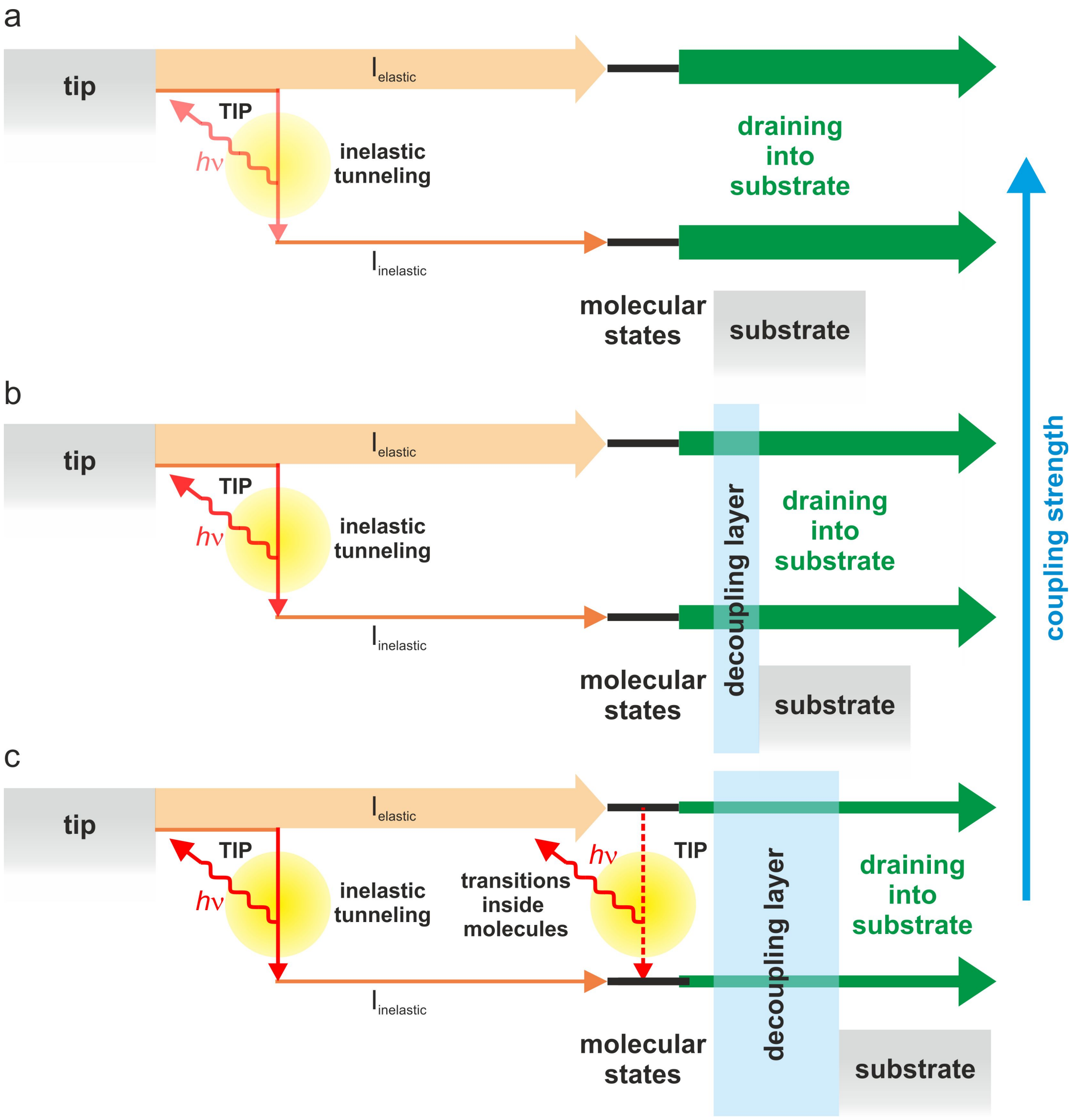

Figure 108: Inelastic tunneling scheme to illustrate the effect of the strength of the coupling between the molecules and the substrate.

Looking at the characteristics of the light emission analyzed in the experiments presented here gives us a further idea of the coupling strength. The enhancement of the induced light emission indicates a weaker coupling of the molecules than to e.g. noble metal substrates, e.g. Ag(111).

A slight enhancement of the light emission induced by inelastically tunneling electrons has been observed for porphrin molecules that exhibited a geometric decoupling from the underlying low-index Cu-surfaces. Here, the core of the molecules is lifted from the substrate, by "standing up" on tilted functional groups [198, 219]. In our case, the increase of the emission yield above the molecules is quite significant. Such enhancements of plasmon-mediated light emission have been observed for pyridine-molecules decoupled from an Ag(111)-substrate by one or two layers of C_{60}-molecules [14, 21] or porphyrin molecules decoupled from a ruthenium surface by a monolayer of graphene [31]. However, in the latter cases, the decoupling through the spacer layers was additionally accompanied by a non-planar-adsorption configuration of the pyridine-molecules.

However, for the system presented here, no emission features that point to radiative transitions inside the molecules are observed (see section 13.1). The depopulation of the molecular states excited by elastic tunneling[3] happens directly into the substrate before electronic transitions may happen inside the molecules. This indicates that the coupling between the molecules and the Bi/Cu(111)-substrate is still stronger than for such systems that support molecular fluorescence. Emission features associated to the direct radiative decay of electronic excitations of the molecules, have e.g. been observed for organic molecules that have been decoupled from the underlying metal substrate by a thin insulating layer of salt or oxide [15, 16, 18, 34]. Similar results including molecular fluorescence have been reported for especially synthesized molecules, that had been chemically engineered to yield a particularly strong geometric decoupling by lifting their chromophore from the surface by functional groups [34].

Fig. 108 visualizes the effect of the coupling strength between the molecules and the substrate on the possible ways and the efficiency of the TIP-excitation. In the case of strong coupling, the TIP-exitation efficiency by inelastic tunneling is significantly reduced (see Fig. 108 a). Further decoupling enhances the TIP excitation efficiency by inelastic tunneling (see Fig. 108 b). Once the coupling becomes weak enough, molecular fluorescence becomes available as a further channel of TIP excitation (see Fig. 108 c).

---

[3] Here, the term "excitation" refers to the population of an otherwise empty molecular electronic state by an elastically tunneling electron.

13.7 SUMMARY

In chapters 12 and 13 we presented and discussed STM-LE data for PTCDA and C_{60} adsorbed on the initial monolayer of Bi on Cu(111). In contrast to the same organic molecules adsorbed on Ag(111) (see chapters 9 and 10), an enhanced overall photon yield as compared to the substrate can be induced on the organic layers at certain bias voltages.

The adsorbed organic species manipulate the LDOS of the surface. In a careful analysis of comprehensive spectroscopic data sets, we could correlate the changes in the overall photon yield to features in the dI/dV-data of the respective sample species. Simulations of the spectra of the overall photon yield from our STS-data further corroborated earlier suggestions that the emission intensity versus the bias voltage is governed by the changing ratio of inelastic to elastic tunneling channels which is manipulated by the LDOS of the sample [192, 211].

The enhancement of the emission yield induced on the molecules as compared to the Bi/Cu(111)-substrate is in contrast to the findings for organic species directly adsorbed on noble metal surfaces. Such enhancement of the light emission is usually only observed if the molecules are somehow decoupled from the surface. From this, we may conclude a weaker interaction between the molecules and the substrate for Bi/Cu(111) than e.g. for Ag(111).

A weaker coupling between the molecules and the substrate reduces the amount of non-radiative energy transfer and allows a more efficient excitation of the tip-sample junction via inelastic tunneling into molecular states. The coupling between the molecules and the Bi/Cu(111)-substrate is still too strong to support molecule specific fluorescence.

Such weak interaction between organic molecules and the underlying substrate and the resulting increased emission intensity is rather unexpected without further geometric decoupling of the molecules. In the following chapter, we will see that an enhancement of the induced light emission can also be observed for molecules on ultrathin Bi-structures. The discussion of the data will shed further light into the origin of the surprisingly low coupling between the molecules and the substrate.

14

HETEROGENEOUS BI-LAYERS ON CU(111)

In chapter 11, we briefly discussed the growth of Bi on Cu(111) in the low coverage regime up to the initial closed monolayer of Bi on Cu(111). In chapters 12 and 13, we presented and discussed data for organic layers adsorbed on the initial closed monolayer.

Our results reveal a peculiarly weak interaction between the adsorbed molecular layers and the Bi/Cu(111) substrate. The coupling between the molecules and the substrate affects the number of non-radiative decay channels and the efficiency of the TIP-excitation. However, the reason for the weak interaction has not been discussed in detail, yet.

To further investigate the properties of thin Bi-films as a substrate for thin organic layers in STM-LE experiments, we studied the light emission induced on slightly larger coverages of Bi on Cu(111). Here, we use a Cu(111)-sample covered with Bi-overlayer-structures of various thickness as a playground to explore the effect of the different Bi-layers on the induced light emission. Further, we study the influence of organic overlayers on further Bi-structures on Cu(111) apart from the initial monolayer.

14.1 TOPOGRAPHIC SURFACE STRUCTURE

Fig. 109 a and b show the topography of a Cu(111) sample with a Bi-coverage of approx. 2.2ML ± 0.5ML [1].

Most structures found on the surface exhibit a roughly rectangular shape. This can be understood considering the growth mode of Bi on Cu(111). Here, we may assume a growth similar to that observed for Bi on Ag(111). In literature, at Bi coverages above 1ML on Ag(111), the growth of thin Bi(110)-nanowires which are elongated along the Bi$[1\bar{1}0]$-axis (the Ag$[1\bar{1}0]$ direction of the substrate) was reported [121]. The preferred growth direction of the wires is associated to a stronger, covalent bonding of the Bi along the axis in which the wires are elongated as opposed to the weaker van der Waals interactions which dominate the bonding along the perpendicular axis [121]. When further increasing the Bi coverage, the nanowires grow wider into flat stripes (e.g. found at 1.75ML Bi-coverage on Ag(111)), merge and transform into 2 d islands [121]. This is in good agreement with the rectangular shapes observed in our topography data which matches the preferred growth of the Bi-structures along favored directions.

At the coverage given in our experiment, we may precisely identify the respective heights of the observed structures with respect to the Cu(111)-substrate by a careful analysis of the occurring step heights. Therefore, a variety of step heights on the sample were measured. Exemplary, line profiles indicated with different colors in Fig. 109 a and b are shown in Fig. 109 c-f.

---

[1] Here, the coverage is given in terms of Bi-layers on the surface. A Bi-coverage of 1ML in this convention means that the Cu(111) surface is fully covered with a single layer of Bi. Sometimes, the coverage is also given in terms of Cu(111) surface atoms. 1ML in the connotation used here corresponds to 0.53ML in terms of Cu(111)-layers, i.e. 0.53 Bi atoms per Cu surface atom.

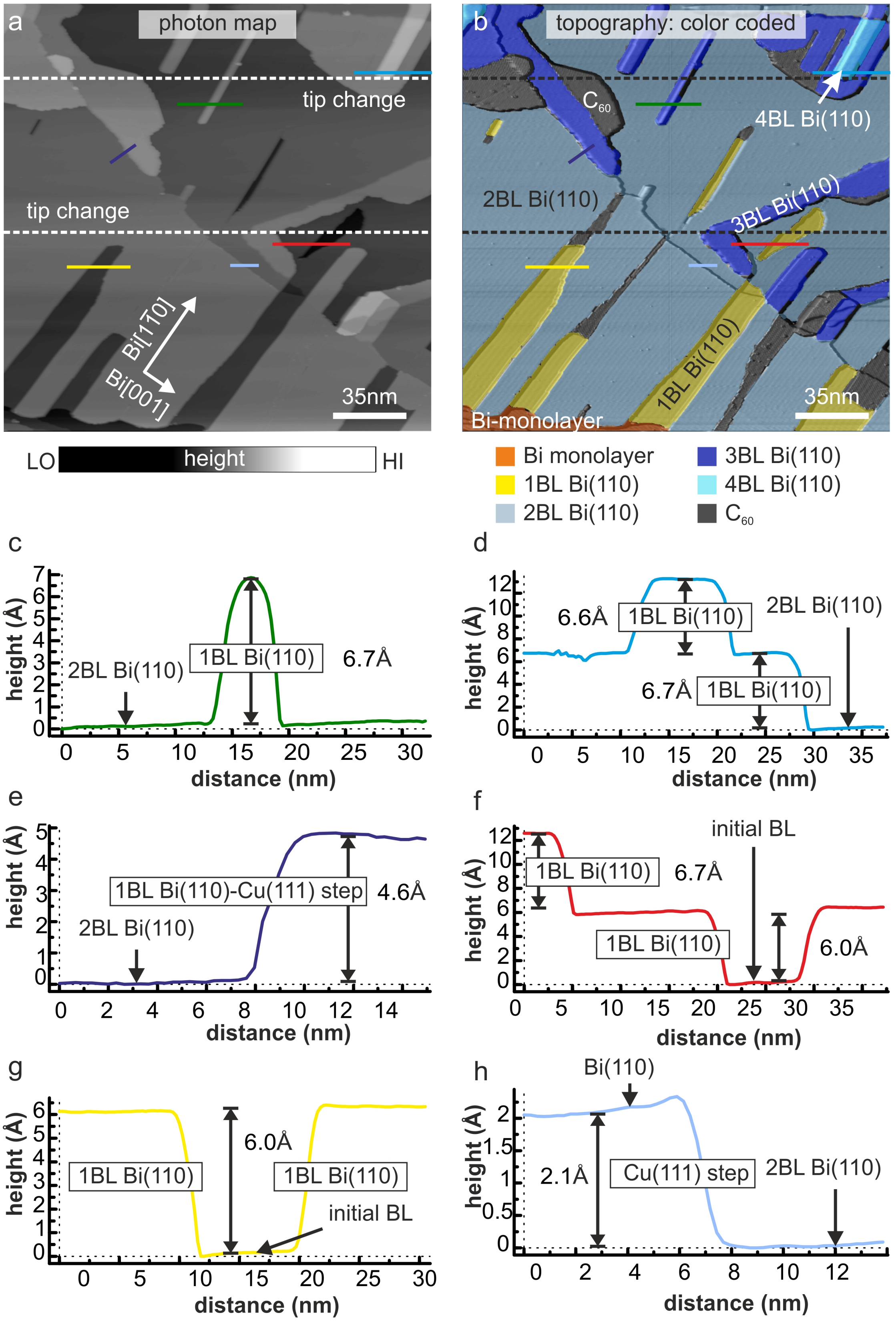

Figure 109: Bi/Cu(111) sample with a Bi coverage of approximately 2.2 ± 0.5ML. a) Standard representation of the topography and b) Shaded top view of the same topography in which the different Bi-structures on the surface were overlaid in different colors. $V = 2$V, $I = 100$pA, $T = 80$K.

The height differences between most Bi-domains are found to measure roughly 6.5 ± 0.5Å. This agrees well to the value of twice the interlayer spacing of bulk Bi(110) which is 6.6Å [243] and proposes a bilayer growth of the Bi on Cu(111) as found e.g. for Bi-nanowires and islands on Ag(111) [121] or the growth of Bi on silicon(111) [244] or highly oriented pyrolitic graphite [245] where the bilayer growth is assigned to the energetically favored pairing of Bi(110)-layers, i.e. a saturation of dangling bonds.

This height difference also occurs paired with additional height differences of roughly 2Å. The latter are associated with steps in the Cu(111)-substrate[2]. A Cu(111) step runs e.g. diagonally from the top left to the bottom right through the area imaged in Fig. 109 a.

The structure in the bottom left corner of the area imaged in Fig. 109 a and b, exhibits wavy striped structure. This is the characteristic structure of the initial monolayer of Bi on Cu(111) as discussed in chapter 11. Taking this structure as a reference point, we may assign the different Bi-structures heights with respect to this "wetting layer". According to the identification of the respective structures, the shaded top view of the topography shown in Fig. 109 a was overlaid with different colors in Fig. 109 b. To allow for an easy identification of the depicted structures, the rest of the topographies in this chapter will be shown in a shaded top view and overlaid with different colors according to the color code introduced here. A schematic model for the proposed growth of Bi on Cu(111) is shown in Fig. 110.

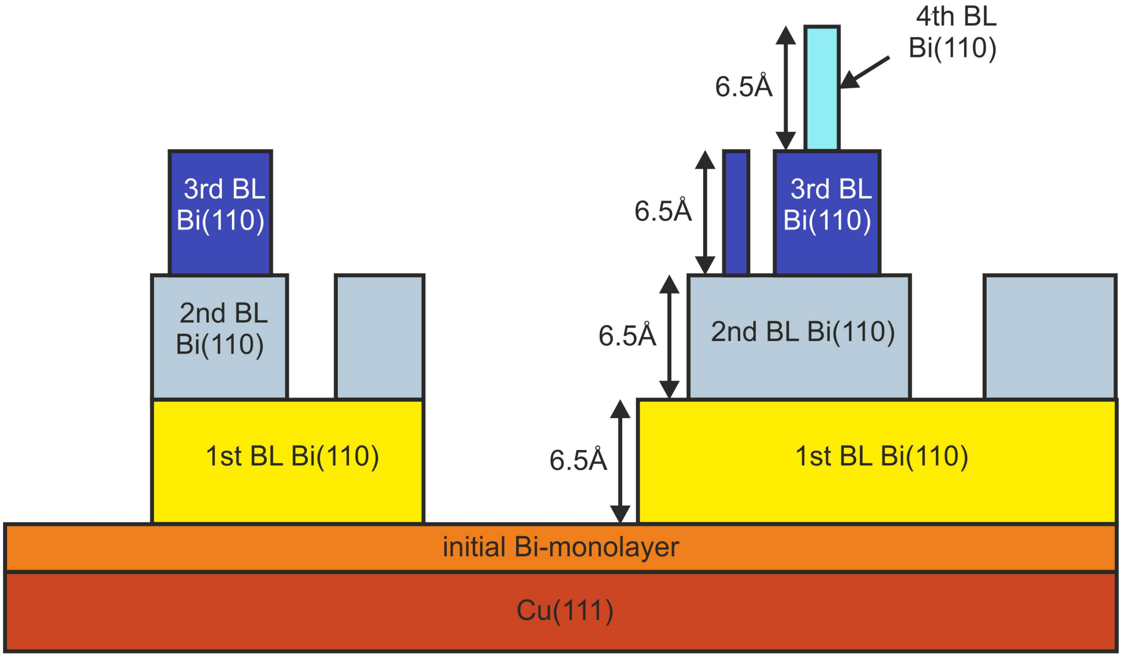

Figure 110: Schematic of the initial growth of Bi on Cu(111) at a coverage of around 2.2ML. After the closing of the initial Bi-monolayer, which acts as a wetting layer in this case, Bi grows in bilayers. Residual parts of the initial dealloyed Bi-monolayer are still found in between the Bi-bilayer domains. The respective step heights between the Bi-structures are indicated.

---

[2] Literature value: 2.1Å [246].

Additionally to the Bi-domains, several C_{60}-islands can be observed in the imaged area. The molecules were evaporated at room temperature subsequently to the deposition of Bi, to a coverage of approx. 1/10ML. Within the molecular islands, the C_{60}-molecules are hexagonally ordered.

14.2 LIGHT EMISSION INDUCED ON PRISTINE BI-STRUCTURES ON CU(111)

Ultrathin metal films, such as the Bi-overlayers discussed above are of interest due to their potential use in technological applications. Their electronic structure is governed by the confinement between the surface and the interface layer and their electronic and structural properties may be easily tuned by the film thickness [247–249]. Here, we want to analyze the light emission induced on such thin Bi-layers of different thickness.

14.2.1 *Contrasts in the Overall Photon Yield Evoked by Overlayers of Different Thickness*

Fig. 111 shows the color coded topography shaded top views of two different surface areas along with the corresponding photon maps. The data were acquired at different bias voltages of 2V and 3V, respectively. Both photon maps reveal different light emission yields induced on the respective Bi-structures.

Bi-structures of the same height with respect to the Cu(111) substrate are found to exhibit the same induced overall photon yield. Two minor tip changes are indicated by horizontal dashed lines in Fig. 111 a, b. The tip changes are accompanied by slight changes in the induced overall photon yield on all structures. The general contrasts between the structures remain unchanged.

For the 1BL-Bi-structures, the lateral distribution of the overall photon yield in the photon map recorded at 2V exhibits a modulation along the direction of the stripes that are found in the topography.

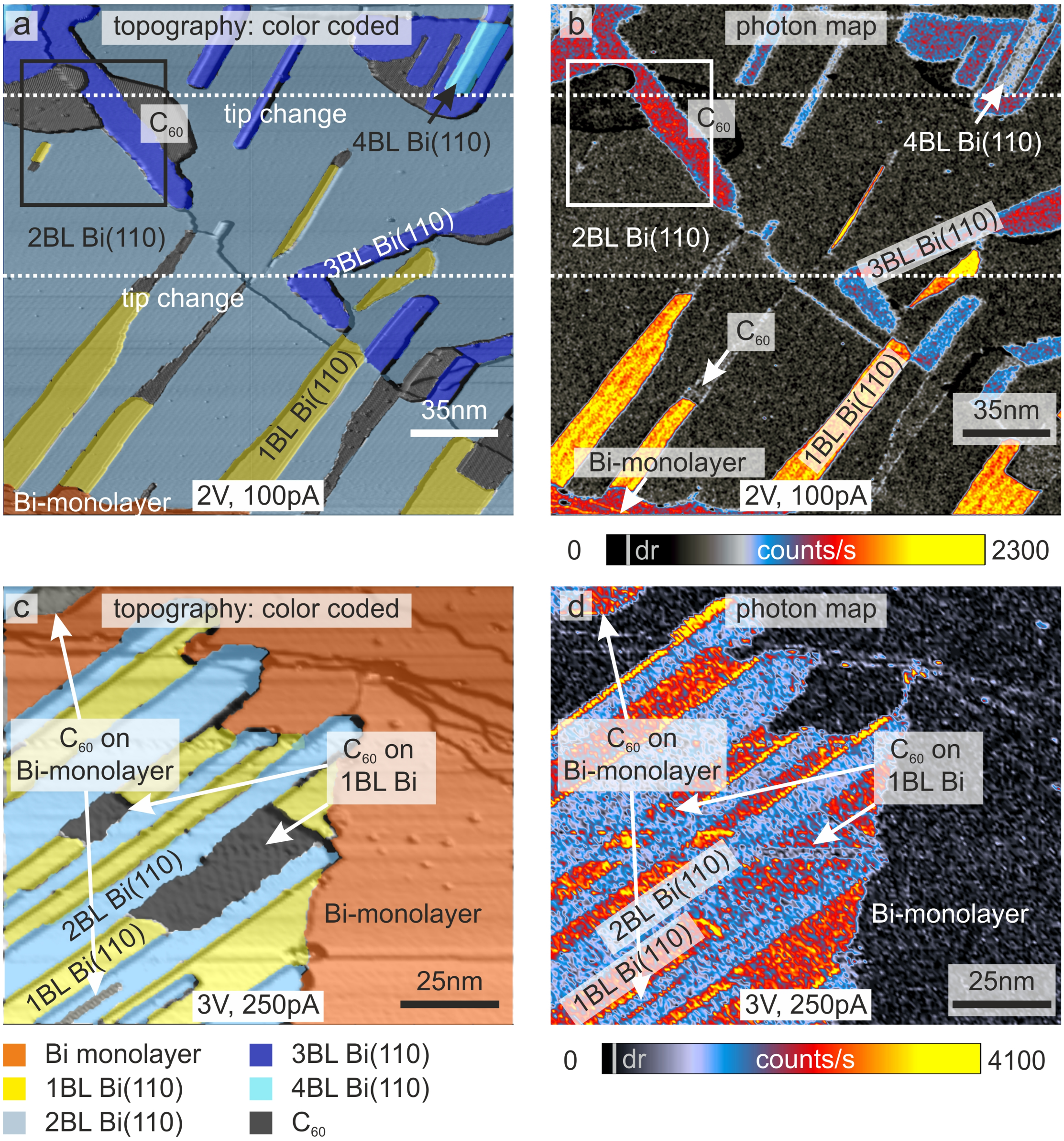

Figure 111: Topographies and corresponding photon maps acquired on the Bi/Cu(111) surface at different bias voltages. a) Color coded shaded top view representation of a topography (as depicted in Fig. 109 b), and b) the corresponding photon map acquired at 2V. c) and d) Color coded shaded top view representation of the topography and the corresponding photon map of a different surface area acquired at 3V. Vertical lines on the intensity scales of the photon maps indicate the dark count rate (dr). a), b) $V_{sample} = 2V$, $I = 100pA$, c), d) $V_{sample} = 3V$, $I = 250pA$, $T = 80K$.

14.3 ELECTRONIC STRUCTURE OF THE BI-STRUCTURES

The photon yield does not scale linearly with the height of the Bi-structures. In Fig. 111 b, the 1BL- and 3BL-structures exhibit significantly higher photon yields than the 2BL and 4BL-structures. This clearly indicates that the role of the Bi-layers for the light emission intensity is more than that of a spacer layer which increases the spacing between the tip-and the Cu(111)-substrate. Rather, the electronic structure of the Bi-films is actively involved in the light emission.

Comparing the photon maps recorded at different tunneling energies in Fig. 111 b and d, the contrast between the respective structures changes. This becomes particularly clear, when e.g. comparing the photon yields for the Bi-monolayer and the 2BL-Bi-domains. While at a bias voltage of 2V, the photon yield for the Bi-monolayer is clearly higher than for the 2BL-Bi-domains, the situation is reversed at 3V. This proposes differences in the overall photon yield versus the tunneling energy.

To gain a deeper insight into the changes of the overall photon yield induced on the respective structures with the bias voltage, spectroscopic measurements were performed in the surface area displayed in Fig. 111 c and d. The experimental conditions at which the spectroscopic data were acquired were rather unstable, so that only a few spectroscopic runs were performed. The dI/dV-spectra and spectra of the overall photon yield shown in Fig. 112 give a taste of the differences in electronic structure and induced photon yield for 1BL and 2BL thick Bi-structures. The differences in the electronic structure for both overlayers also manifests themselves in differences of the overall photon yield versus the bias voltage.

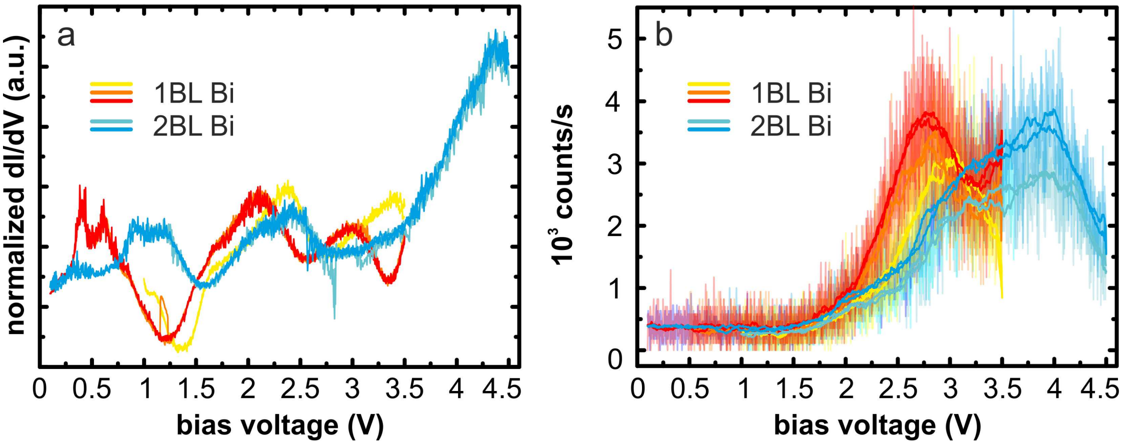

Figure 112: Spectroscopic data acquired on Bi-structures of 1BL and 2BL height with respect to the initial Bi-wetting layer. a) The normalized dI/dV-signal and b) the overall photon yield. Both structures exhibit clear differences in the dI/dV-spectra along with differences in the overall photon yield. I = 250pA, 0.5V/s, 800 points, T = 80K.

14.4 THE EFFECT OF ORGANIC ADLAYERS ON THE INDUCED LIGHT EMISSION

The surface areas depicted in Fig. 111 exhibit several C_{60}-domains. In Fig. 111 a and b, the molecules are found on 1BL-, 2BL-, and 3BL-Bi-structures. The surface area depicted in Fig. 111 c and d additionally exhibits a C_{60}-domain adsorbed on the initial Bi-monolayer.

The photon map shown in Fig. 111 b was acquired at 2V. At this bias voltage, all depicted C_{60}-domains exhibit a photon yield smaller that that of the respective underlying substrate. The photon map shown in Fig. 111 d was recorded at 3V. In agreement to our findings presented in chapter 12, the photon yield induced on C_{60} on the initial Bi-monolayer is clearly higher than on the Bi-monolayer itself. For the C_{60}-domains on the 1BL-Bi-structures, the photon yield on the molecules is similar but slightly smaller than on the substrate.

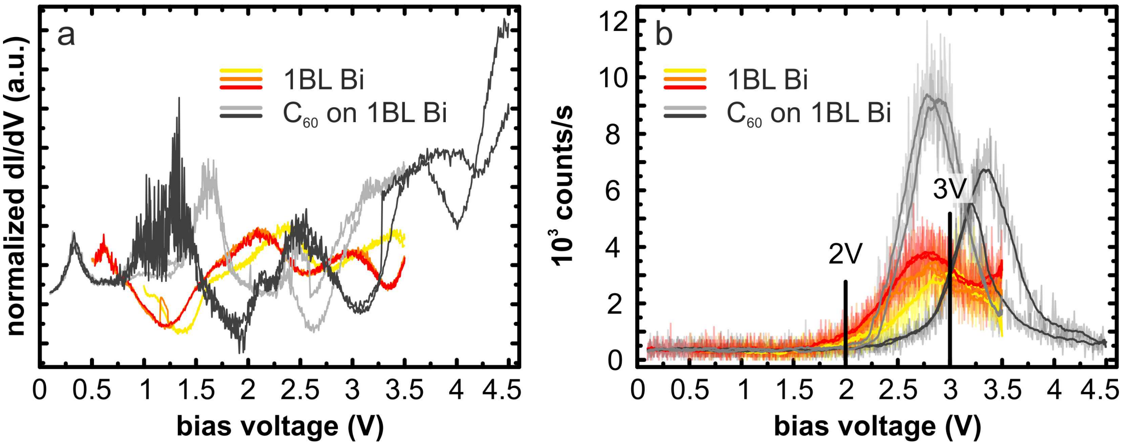

Figure 113: Spectroscopic data acquired on C_{60} adsorbed on 1BL-Bi. a) The normalized dI/dV-signal and b) the overall photon yield. Within the bias voltage range between approx. The spectra acquired on C_{60} exhibit instabilites that may be due to e.g. the attachment or detachment of a C_{60} molecule to or from the tip. Vertical lines indicate the tunneling voltages at which the photon maps shown in Fig. 111 were recorded. $I = 250pA$, 0.5V/s, 800 points, $T = 80K$.

Fig. 113 shows corresponding spectroscopic data for C_{60} on 1BL-Bi and the pristine 1BL-Bi-substrate. Several spectroscopic runs are shown for both, the molecules and the substrate. In particular for the spectroscopic data gathered on the C_{60}-domain, significant deviations between the spectra taken in both spectroscopic runs can be observed. For example, the initial rise and the maxima of the overall photon yield are significantly shifted with respect to each other. This goes along with significant changes in the corresponding dI/dV-data. Also the different spectra acquired on the 1BL-Bi-structure exhibit a slight shift in energy between the different spectroscopic runs. However, these variations between the spectroscopic runs are much smaller than for the case of C_{60}.

The variations between the spectroscopic runs point to instabilities in the tunneling junction such as the attachment or detachment of a C_{60}-molecule to or from the tip. Such a change may e.g. have happened during the recording of the spectrum acquired on the C_{60}-domain shown in dark gray in Fig. 113. Here, a significant difference between the spectrum acquired for rising and falling bias voltage can be observed.

In good agreement to the intensity distribution in the photon map shown in Fig. 111 b, at 2V the spectra of the overall photon yield for the 1BL Bi-substrate exhibit a higher emission yield than the molecular overlayer. At 3V, depending on the spectroscopic run, the overall photon yield is either significantly higher than that induced on the 1BL Bi-layer (light gray spectrum) or almost equal (dark gray spectrum). The latter situation is in agreement to the photon map presented in Fig. 111 d.

Fig. 114 presents a detail of the surface area depicted in the upper right quadrant in Fig. 111 a and b (indicated by a square in the respective figures). The imaged surface area exhibits three C_{60}-domains. The two larger C_{60}-islands are adsorbed on 2BL-Bi, the smallest C_{60} domain, found in the top central part of the imaged area, is adsorbed on 3BL-Bi.

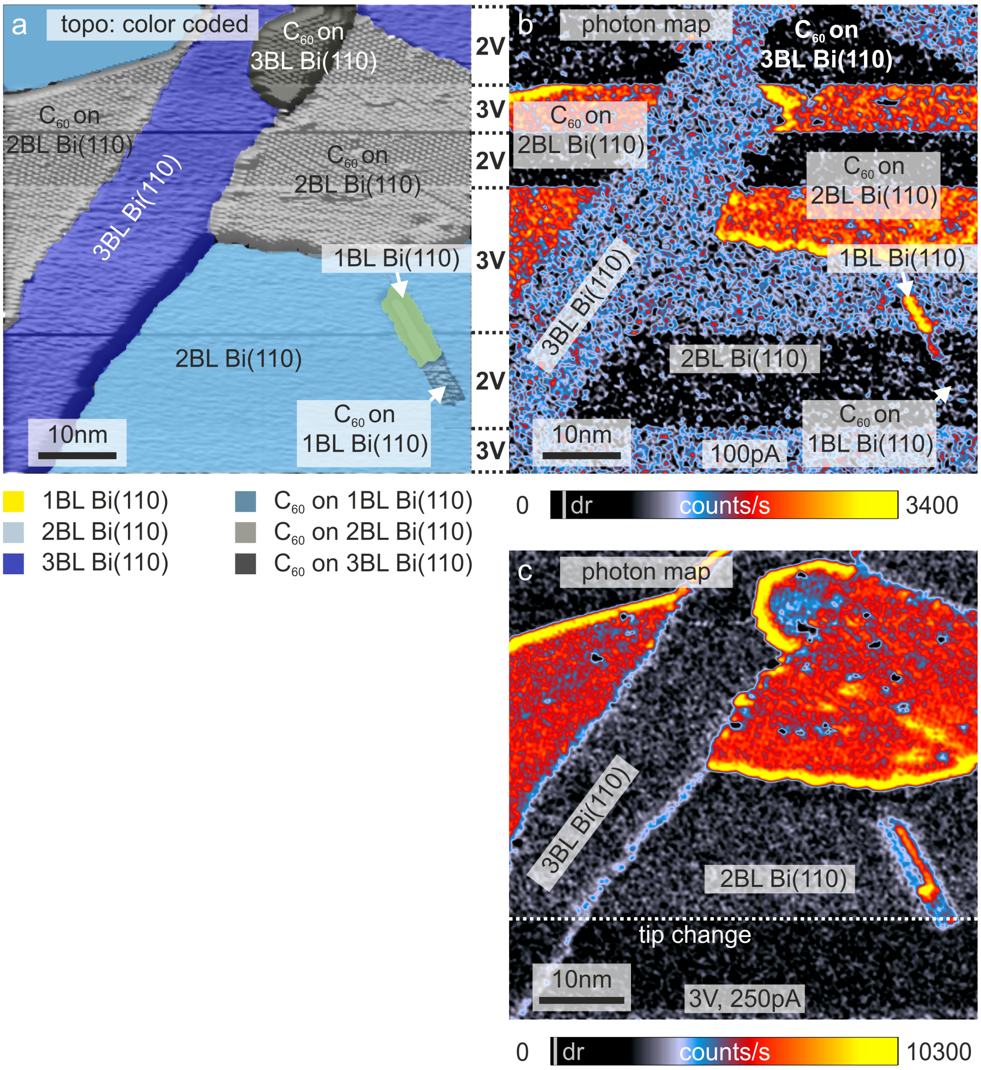

Figure 114: Contrast in the photon maps between the C_{60}-layers and the Bi-substrate. a) Color coded shaded top view representation of the topography and b) the corresponding photon map. During the imaging, the bias voltage was switched back and forth between 2V and 3V. c) Photon map of the same surface area entirely recorded at 3V. Vertical lines on the intensity scales of the photon maps indicate the dark count rate (dr). a) $V_{sample} = 2V/3V$, $I = 100pA$, $T = 80K$, b) $V_{sample} = 3V$, $I = 250pA$, $T = 80K$.

During the imaging presented in Fig. 114 a and b, the bias voltage was switched back and forth between 2V and 3V. The contrast reversibly changes from higher photon emission intensity induced on the 2BL-Bi-structure as compared to the C_{60}-domain adsorbed on this substrate to an enhanced photon emission intensity induced on the molecular layers at 3V. Fig. 114 c presents a photon map of the same surface area that was entirely recorded at 3V. It reveals that also the photon yield induced on the C_{60}-domain on 3BL-Bi is clearly enhanced as compared to the pristine 3BL-Bi-substrate.

14.4.1 *Spectra of the Emitted Light*

Fig. 115 presents spectra of the emitted light recorded on different sample structures. Fig. 115 a depicts spectra acquired on the different Bi-structures, as well as on C_{60}-domains adsorbed on 1BL-Bi. For an easier comparability, only the smoothed spectra are displayed in Fig. 115 a. In Fig. 115 b, the raw data is additionally displayed in lighter colors.

The light emission induced on all sample structures including the molecular domains, exhibits broad energetic distributions over a photon energy range of several tenths of an eV. The emission spectra for the respective sample species recorded at a bias voltage of 2V exhibit different shapes and peak positions. Comparing these spectra to emission spectra acquired at 3V shown in Fig. 115 b, reveals that the characteristic spectral shape for the 2BL and 3BL Bi-structures C_{60} on 1BL-Bi is not fully developed at 2V. Depending on the electronic structure provided by the respective structures, only parts of the characteristic TIP-spectrum are available. At 3V, the shapes of the emission spectra for 2BL and 3BL-Bi and C_{60} on 1BL-Bi are very similar.

The spectra for C_{60} show no indication for molecule specific emission features. Thus, similar to the case of C_{60} on the initial Bi-monolayer, also for these systems, we may assume that the TIPs are purely excited by inelastically tunneling electrons. The excitation channel of elastic tunneling ("hot electron injection") into the molecules followed by subsequent transitions between molecular electronic states is not yet available at the given coupling strength.

The emission spectrum of 1BL-Bi shown in Fig. 115 a exhibits a high energy cutoff around 2eV which roughly corresponds to the quantum cutoff of eV_{Bias}. The high energy cutoff for the emission spectrum of C_{60} on 1BL-Bi is clearly below eV_{Bias}. As discussed in chapter 13 for molecular overlayers on the initial monolayer of Bi on Cu(111), this suggests that the final states for inelastic transitions provided by the molecules lie at higher energies than those provided by the 1BL-Bi-substrate.

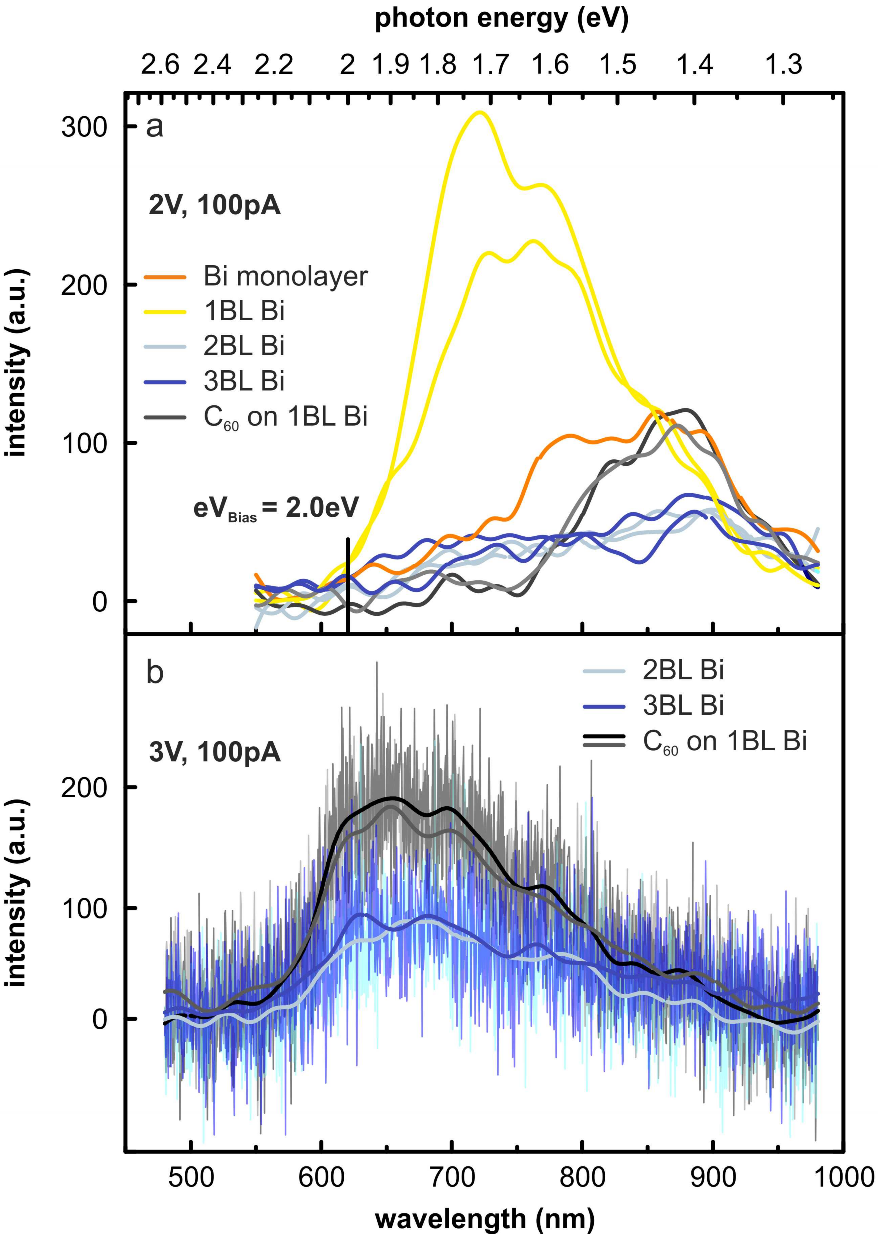

Figure 115: Spectra of the emitted light induced on Bi-structures of different thickness as well as on C_{60} adsorbed on 1BL-Bi. $V_{sample} = 2V/3V$, $I = 100pA$, acquisition time 300s, $T = 80K$.

14.5 SUMMARY AND DISCUSSION

14.5.1 *Light Emission from Pristine Bi-Layers of different Thickness*

In this chapter, we studied the light emission induced on different ultrathin Bi-overlayers on Cu(111) with thicknesses reaching from the initial Bi-monolayer to structures of several BL thickness. The structures coexisted on the sample which allowed for a simultaneous study with the same tunneling tip.

Photon maps acquired at different bias voltages exhibit clear contrasts between the different Bi-domains. The spectra of the overall photon yield further reveal different induced emission intensities versus the bias voltage depending on the film thickness. This goes along with variations in the corresponding electronic structures of the Bi-domains, as e.g. evident from our dI/dV-spectra for 1BL and 2BL-Bi-structures.

The dependence of the electronic structure on the film thickness especially for thin Bi-overlayers is in good agreement to calculations for free standing and hydrogen terminated thin Bi(110)-films [240, 247, 248]. It is further supported by ARPES and STS measurements on Bi(110) [247] on highly oriented pyrolitic graphite (HOPG) and ARPES studies on Bi(110)- and Bi(111)-films on Si(111) [250, 251]. In particular, quantum well states form within the layers due to the vertical confinement of electrons [248, 250].

Our preliminary STM-LE results propose that the different electronic structures significantly influence the light emission induced on the different Bi-overlayers. On the one hand, the electronic structure of the films may provide final states for elastic and inelastic tunneling channels and therefore influence the emission yield. On the other hand, also light emission from electronic transitions between quantum well states might play a role, as has e.g. been observed for thin sodium layers on Cu(111) [252] or copper nitride (Cu_3N) nanocrystals embedded in the surface of a Cu(110) substrate [253]. In particular, for such systems, multiple channels of excitation might be involved simultaneously, which may enhance the induced emission yield [253].

Further work needs to be done to obtain a full spectroscopic picture of the different Bi-structures and resolve the influence of the electronic structure on the light emission induced on ultrathin Bi-films more clearly. The tunability of the electronic structure and consequently the induced light emission as a function of the film thickness bear great potential for technological applications.

14.5.2 *Light Emission Induced on Organic Adlayers on Bi/Cu(111)*

For C_{60} adsorbed on different Bi-overlayers on Cu(111) reaching from the initial Bi-monolayer to Bi-structures up to 3BL thickness, at certain bias voltages, we observed a higher emission yield induced on the molecular domains as compared to the substrate.

Though they exhibit a low density of states near the Fermi level, a few BL thick Bi-films e.g. on HOPG have been proposed to exhibit a metallic character [245]. Usually, the interaction between the molecules and a metallic substrate would be expected to attenuate the light emission intensity. This is obviously not the case here.

The surprisingly low interaction between the molecules and the Bi-films might be further explained by the bonding structure of the Bi-layers within the thin films. In our topographic data, we exclusively observe Bi-structures with a height of multiples of a Bi-bilayer[3]. This is in agreement to literature data for thin Bi(110)-films on different other substrates, where the formation of such bilayers was assigned to the saturation of dangling bonds [121, 182, 245, 247]. Bi has five valance electrons. In bulk Bi, it therefore has a coordination number of 3. At the surface, the symmetry is broken so that the coordination number might be reduced. Calculations for free standing Bi-films of odd layer thickness reveal that the coordination number of the surface atoms is only 2 [247]. By the pairing of p_z-orbitals of two atomic layers, dangling bonds are removed and the coordination number is restored to 3 as in the case of bulk Bi [247]. Therefore, e.g. in their surface reactivity, the surface of Bi(110)-films might be significantly different from the surface of the (110)-oriented surface of Bi-crystals [254]. For example, thin Bi(110)-films on HOPG have been shown to be very inert to oxidization which is in variance to the (110)-surface of bulklike-ordered Bi [254].

The initial Bi-monolayer, i.e. the wetting layer, has been proposed to play a special role due to the direct contact with the substrate [248, 254]. It was suggested that the initial Bi-layer on HOPG efficiently isolates the further Bi-bilayers from the substrate [248]. This would be in good agreement with our experimental results that propose a rather low interaction between organic adlayers and the initial Bi-monolayer on Cu(111) (see chapters 12 and 13). Also in our case, the bonding of Bi-atoms to the substrate might saturate bonds and effectively translocate the charge density of the Bi-film away from the surface. The resulting small overlap between the wave functions of the Bi-film and the organic layers [116] might be an explanation for the surprisingly low interaction between both revealed in our data.

Our preliminary results underline the important role of the particular bonding structure and location of the involved charge densities for the interaction with functional overlayers. They suggest a great potential for the use of ultrathin Bi-films as substrates e.g. for molecular overlayers in organic semiconductor-devices. Further work needs to be done to fully characterize and understand the electroluminescence induced on pristine and molecularly covered Bi-films to make use of it in technological applications.

---

[3] Note that in some of the references cited in this chapter, single atomic layers of Bi are also referred to as "bilayers" since they consist of two sublayers with a small vertical displacement in the order of 0.14Å. In variance to this nomenclature, in this thesis, the term "bilayer" refers to two paired atomic layers of Bi.

Part V

CONCLUSION AND OUTLOOK

15

SUMMARY AND CONCLUSION

In the course of the work conducted for this thesis, a state-of-the-art STM-LE experiment was set up. The initial experiments concentrated on the plasmonic light emission induced by the inelastic tunneling of electrons from initial states in the tip to final states in the sample and vice versa. The analysis of the induced light emission on pristine and molecule covered surfaces allowed an insight into the fundamental physics that govern the lateral and energetic distribution of the emission intensity.

15.1 EMISSION CHARACTERISTICS OF NANOSCALE JUNCTIONS

The emission spectra induced with different tips on the same sample surface may exhibit significant differences. This also applies for microscopic changes of the same macroscopic tip due to the particular influence of the microscopic tip geometry on the spectrum of excitable tip induced plasmon (TIP) modes and consequently the emission spectrum.

When inducing the light emission above molecular domains adsorbed e.g. on noble metal substrates or the initial monolayer of Bi on Cu(111), a similar spectrum of TIP-modes is excited for both, the molecules and the substrate. However, fingerprints of the molecular LDOS are observed in form of e.g. high energy cutoffs and spectral weights in the emission spectra. For the systems studied here, no molecular fluorescence, i.e. molecule specific peaks in the emission spectra were observed.

15.2 CONTRASTS IN PHOTON MAPPING

Local surface defects may evoke variations in the lateral distribution of the induced emission intensity. This is reflected as contrasts in the photon maps.

This thesis presented a tunneling energy resolved study of the contrasts evoked by Ag(111)-step edges which serve as examples for one dimensional atomic scale surface defects. By tuning the bias voltage during a surface scan, its effect on the contrasts evoked by the defects is recorded within a single comprehensive frame. This resolved significant changes of the contrast with the applied bias voltage.

The analysis of the results presented in this thesis supports earlier works that ascribe a crucial role for lateral variations of the emission yield observed at Ag(111)-step edges to local variations in the LDOS of the sample [25]. Also in the analysis of our molecularly resolved photon maps for C_{60} on Ag(111), the influence of the LDOS on the lateral distribution of the emission yield is further corroborated.

In addition, when tunneling above surface defects and molecular layers, changes in the direction of the k-vectors of the inelastically tunneling electrons may lead to variations in the coupling efficiency to the TIP modes. This may lead to an additional lateral modulation of the emission yield. Since this effect depends on the orientation of the dipole moment of the TIPs, it depends on the specific tip used. Such tip-specific orientiation of the dipole moment may also explain the lateral asymmetry of the induced emission yield with respect to the centers of the molecules observed in our data.

Here, the results presented in this thesis contribute to the ongoing discussion about the origin of the molecular resolution in photon maps for various sample systems [14, 58, 140, 217].

15.3 ENHANCEMENT OF PLASMONIC LIGHT EMISSION

This thesis presented photon maps of different archetype organic species adsorbed on Ag(111). The light emission induced on the molecules was found to be reduced as compared to the emission yield induced on the substrate. In contrast, for the same molecules adsorbed on ultrathin Bi-films on Cu(111), the induced photon yield is increased for the molecules as compared to the substrate.

The different behavior of the induced emission yield for the different systems is assigned to different coupling strengths between the molecules and the substrate. The coupling influences the non-radiative energy transfer to the substrate and the lifetime of the molecular electronic states. This influences the efficiency with which the TIP-modes may be excited by inelastic tunneling into molecular states.

Similar enhancements of the overall photon yield are usually associated to a weakened interaction between the molecules and the substrate, e.g. by a thin decoupling layer or the geometry of the adsorbed molecules. In the case of molecules adsorbed on Bi/Cu(111), the enhancement occurs without such additional decoupling.

The findings for the Bi/Cu(111)-systems presented here are in good agreement with our previous ARPES experiments on adsorbed organic layers on $BiAg_2$/Ag(111) performed in collaboration with the group of Prof. Dr. Enrique Ortega [118]. The ARPES data indicates an unexpectedly low interaction between the molecules and the substrate with minimal effects on both, the electronic states of the molecules and the surface state of the $BiAg_2$-surface alloy (see A). The intrinsically weak interaction is ascribed to the bonding structures of the thin Bi-induced structures.

Additionally, the adsorption of organic molecules onto the surface changes the LDOS. This way, the inelastic tunneling probability is manipulated. A resulting increase of the inelastic tunneling probability into the molecules can further play into the observed enhancement of the emission yield.

15.4 SYSTEMATIC TAILORING OF OPTICAL PROPERTIES ON THE NANOSCALE

The detailed STM-LE spectroscopic study of PTCDA and C_{60} on the initial monolayer of Bi on Cu(111) allowed a deeper understanding of role of adsorbed organic layers for the induced light emission efficiency. The analysis presented here could further support earlier works, showing that the induced emission yield versus the bias voltage is governed by the LDOS [211].

Changes in the excitation efficiency versus the applied bias voltage were correlated to changes in the LDOS providing final states for elastic and inelastic tunneling. The ratio of the amounts of elastic and inelastic tunneling channels defines the inelastic tunneling probability and therefore the emission yield at a certain bias voltage. These findings suggest that specific organic overlayers may be used to selectively manipulate the LDOS and thereby control the intensity characteristics of the current induced light emission.

A further decoupling of the molecules from the substrate, e.g. by an insulating layer, may additionally yield molecular fluorescence. The transitions inside the molecules would open an additional excitation channel for the TIP modes and lead to molecule specific features in the emission spectra. This would allow to manipulate not only the intensity of the induced light emission but also the energy of the emitted photons by choosing the appropriate molecular species. Further STM-LE experiments on such systems may help to further characterize the specific electroluminescence channels and efficiently exploit the orbital structure of semiconducting organic molecules.

However, there are further ways to manipulate the electronic structure of a surface beyond applying overlayers. The electronic structure of thin Bi-films crucially depends on the film thickness. The preliminary experiments on differently thick ultrathin layered Bi-structures presented in this thesis show significant differences in the emission yield induced at a certain bias voltage.

Further experiments are needed to explore the light emission induced on these structures in more detail. The vertical confinement of the electrons within the Bi-overlayers leads to the formation of quantum well states [248, 250]. This yields the possibility to targetedly engineer the electronic structure and provide excitation channels specific to the film thickness [252, 253].

On the route of exploring novel properties of materials for future electronic devices, the results presented in this thesis yield a stepping stone to efficiently exploit the promising properties of different materials. The choice of substrate allows to control the possible pathways and the overall efficiency of the tunneling current induced excitations. Further, semiconducting organic overlayers may be used to tune the excitation efficiency versus the bias voltage.

The ultrathin Bi-structures on Cu(111) studied in this thesis are especially interesting candidates for a future use in technological applications. Their peculiarly low interaction with applied functional layers, e.g. organic molecules, bears the possibility to combine the functionalities of different materials while the electronic structures of both, the substrate and the overlayer, may be manipulated individually. This way customized components with the desired properties may be systematically tailored.

16

FUTURE PROSPECTS

16.1 COMPLEMENTARY ARPES EXPERIMENTS ON THE BI/CU(111) SYSTEM

The systems studied in this thesis open possibilities for further experiments and studies. In literature, Bi-induced structures on Cu(111) have been discussed for their electronic states which exhibit large spin orbit splittings and make them interesting candidates for spintronic applications [114, 115, 115, 117, 119].

While this thesis addressed the influence of the interaction between organic layers and ultrathin Bi-structures on Cu(111) on the induced light emission, the effect of the adsorption on the electronic structure of both, the Bi/Cu(111) substrate and the adsorbed molecules remain to be resolved. In this context, ARPES measurements may complement the STM and STM-LE data presented here.

The appendix presents ARPES measurements which reveal that the spin orbit-split surface state of the Bi/Ag(111) surface alloy remains unchanged under different organic overlayers [118]. Also the electronic structure of the molecules is barely affected by the adsorption. In view of the large similarities between Bi-induced structures on Cu(111) and Ag(111), similar results may be expected also for the systems studied here. Such a lack of interaction between a substrate and a functional overlayer bears great potential for technological applications, in which the functionalities of both may be tuned individually. Beyond this, a thorough characterization of the systems by STM-LE and ARPES may help to merge the two fields of plasmonics and spintronics.

16.2 FUTURE SAMPLE SYSTEMS: HETEROGENEOUS ORGANIC LAYERS

The data presented and discussed in this thesis prove that our STM-LE setup is capable of performing comprehensive state of the art measurements. The setup may be used to characterize a variety of systems ranging from self-assembled organic layers to artificially constructed structures.

Though organic layers were involved in the experiments presented here, this thesis concentrated on the plasmonic light emission from the tip-sample junction. Future experiments may concentrate on molecules that exhibit a sufficient decoupling from the substrate in order to analyze molecule specific fluorescence and phosphorescence.

In view of technological applications, molecular acceptor-donor heterostructures may be a system of choice [255]. Oftentimes, these structures are formed by stacking layers of different molecules. Earlier experiments in our group studied the lateral mixing of different organic species in self assembled heterogeneous monolayers [153, 154]. Spectroscopic STM and STM-LE experiments may resolve the electronic structure and luminescent properties with great lateral precision. This bares the potential to further miniaturize donor-acceptor structures in technological applications.

16.3 EXTENSION OF THE STM-LE SETUP: TIME RESOLVED STM-LE EXPERIMENTS

Usually the integration times for imaging and spectroscopy in STM experiments lie in the order of ms which makes the technique rather slow in view of time-resolved experiments. However, there are several approaches to also conduct time-resolved STM-experiments [168, 256, 257]. A current project in our group is to extend the experimental setup to be able to conduct time resolved STM-LE measurements.

To study dynamics at surfaces by STM, such as voltage or field induced switching, voltage pulses may be applied. When fast voltage pulses are sent to the tunneling junction, the wiring of the STM may affect the shape of the pulse. Thus, the particular shape of a voltage pulse that reaches the tunneling junction of an STM is a priory not known.

The plasmonic STM-induced light emission happens on a fs-time scale. Also the detection of single photons by the APD happens on a very fast time scale, i.e. in the ns regime. Thus, the light emitted from the tip-sample junction may be used to probe the shape of fast voltage pulses at the tunneling junction [54]. Preliminary experiments in our group have shown that pulses with rise and fall times in the order of a few ns may reach the tunneling junction. This is the time-regime of the lifetime of electronic excitations of organic molecules that are decoupled from the underlying metal substrate e.g. by a thin layer of salt.

This is the basis for time resolved STM-LE studies on organic molecules and enables potential STM-LE pump-probe experiments may be conducted by applying two voltage pulses with a certain delay within a ns-time range, e.g. to study the dynamics of single molecules with ultimate spatial resolution.

16.4 FUTURE EXPERIMENTAL PROSPECTS: BALLISTIC ELECTRON EMISSION MICROSCOPY

In chapter 10, we compared our data to results obtained with ballistic electron emission microscopy (BEEM). This technique focuses on the analysis of the ballistic fraction of the tunneling current penetrating though molecular and metallic layers [132, 258] and may be regarded as complementary to STM-LE.

Several of the necessary steps to additionally implement BEEM to our experimental setup have already been performed. In BEEM-experiments, Schottky diodes are used as an energy-filter to separate ballistic and non-ballistic electrons. A Schottky diode may be formed by a thin Bi-film on silicon. Such samples have already successfully been prepared in our setup.

BEEM demands for an additional electric contact to the Bi-film to drain the non-ballistic electrons. This additional contact can be provided by a modified tip holder. Prototypes already exist.

Similar to photon maps in STM-LE, BEEM-maps, i.e. maps of the ballistic tunneling current, may be gathered simultaneously to the topography and photon map. BEEM-spectroscopy may be performed simultaneously to constant current STS and STM-LE spectroscopy.

By combining BEEM and STM-LE in our experimental setup, it will be possible to gather an even larger set of complementary information in the same experimental run.

This way, the same conditions and therefore maximum comparability are granted for the entire data set.

On the one hand, BEEM provides information about the ballistic, i.e. dissipationless transport channels. On the other hand STM-LE may reveal which of the non-ballistic channels are connected to excitations which decay radiatively. Such combination of complementary experimental techniques may provide a comprehensive picture of the electronic transport channels for a variety of different sample systems with the high spatial resolution of an STM.

Part VI

APPENDIX

A

ARPES ON MOLECULES ON BI/AG(111)

This thesis addressed the light emission from pristine and molecule covered ultrathin Bi-films on Cu(111). In recent literature, such Bi-films have especially been discussed for their electronic structure. The metallic surface states of Bi(111) and Bi(110) exhibit a considerably large spin-orbit splitting [238], [102], [259]. Also the electronic structures of Bi-induced structures on Cu(111) or Ag(111) are subject to spin orbit splitting. The surface states of the Bi/Cu(111) and Bi/Ag(111) surface alloys [114], [115], [117] as well as quantum well states within the initial monolayer of Bi on Cu(111) have been shown to exhibit exceptionally large Rashba-type splittings, also referred to as giant spin-splittings [115], [119].

The spin-splitting of electronic states may be exploited in prospect technological applications: So called spintronic devices use the spin of electrons as an additional information channel beyond its charge. This increases the possible storage density provided by the electronic structure. Due to the particularly large spin-splitting, Bi-induced structures on Cu(111) and Ag(111) are interesting candidates for spintronic applications.

In future electronic components, it would be desirable to combine these characteristic spintronic properties with supplementary functionalities provided by additional overlayers. Photoemission spectroscopy (PES) experiments may further reveal the effects of the adsorption of organic layers on the electronic structure on both sides of the interface, i.e. on the spin-split electronic bands of the Bi/Cu(Ag)(111) surface and on the electronic states of the molecules. In particular, this information complements the STM and STM-LE data presented in this thesis.

In cooperation with the group of Prof. Dr. Enrique Ortega, we performed angle resolved photoemission spectroscopy (ARPES) experiments to resolve the interaction between the Bi/Ag(111)-surface alloy and different archetype organic overlayers. The results of our mutual work were published in Ref. [118] and shall be briefly revisited in this appendix. A short introduction to Bi/Cu(111) and Bi/Ag(111) surface alloys is given in chapter 11. This chapter is in wide parts closely oriented on Ref. [118].

A.1 EXPERIMENTAL DETAILS

The ARPES measurements presented here were conducted in the group of Prof. Dr. Enrique Ortega in Donostia (San Sebastián), Spain. The technique of ARPES will not explicitly be described here, for further details on the experimental technique e.g. the thesis of Aitor Mugarza is recommended [260]. Sample preparation and experiments were performed under UHV conditions with a base pressure better than $5 \times 10^{-10}\,\mathrm{mbar}$. The sample was held at a temperature of about 150K.

An Ag(111) single crystal was prepared by repeated cycles of Neon^{+}-sputtering and annealing. 1/3ML of Bi[1] was evaporated from a Knudsen cell onto the clean Ag(111)-surface while the sample was kept at room temperature. Subsequent annealing to around 550K ensured the formation a monolayer of the $\sqrt{3} \times \sqrt{3}$- ordered Bi/Ag(111)-surface alloy. The sample quality was checked by LEED. Subsequently molecular overlayers (C_{60}, Cl-FeOEP, and PTCDA) of different thicknesses were evaporated from calibrated Knudsen cells. The ARPES measurements were performed with a SPECS Phoibos 150 analyzer[2] using the Helium I line (21.2eV) provided by a monochromized gas discharge lamp.

The complementary STM experiments were performed in the group of Prof. Dr. Rolf Möller, Duisburg, Germany. The experiments were conducted at a base pressure better than $5 \times 10^{-10} mbar$ while the entire scanning unit including the tip and the sample were held at 80K. 1/3ML of Bi was evaporated onto a slightly preheated clean Ag(111)-single crystal. LEED was used to check the sample quality. About 0.5ML PTCDA were evaporated from a Knudsen cell while the sample was held at room temperature.

A.2 ARPES RESULTS

The ARPES experiments presented here studied the interaction of the giant spin-split metallic surface state of the Bi/Ag(111)-surface alloy and organic overlayers. In the surface alloy, every third Ag(111)-surface atom is replaced by a Bi-atom. Here, we will also refer to the surface alloy by its elemental formula $BiAg_2$. At the given Bi-coverage, the gradual dealloying of the sample had already started for small parts of the sample. This is a sign that the Ag(111)-sample has been fully covered with a "monolayer" of the $BiAg_2$ surface alloy. In the following, the $BiAg_2$/Ag(111)-sample will also be referred to as $BiAg_2$-sample for simplicity.

Three different molecules serve as prototypes of different classes of molecules, C_{60} as a fullerene, iron(III)-octaethylporphyrin chloride (Cl-FeOEP) as an example of the family of porphyrin and the closely related phthalocyanine-molecules, and PTCDA as a perylene-based organic molecule. In the case of Cl-FeOEP, the chlorine (Cl) atom was attached as a ligand to the Fe central atom to stabilize the molecule in the gas phase. For simplicity, in the following we will refer to Cl-FeOEP simply as FeOEP. For each molecular species, the thickness of the overlayers was progressively increased during the experiments.

A.2.1 *C_{60} on $BiAg_2$/Ag(111)*

Fig. 116 shows ARPES data for C_{60} on $BiAg_2$. Fig. 116 a-d shows the variation of the $BiAg_2$-surface state with rising molecular coverage. The red dashed line is a fit to the surface state of the pristine $BiAg_2$-sample serving as a guide to the eye. With rising molecular coverage the intensity of the surface state is slowly attenuated. No alternations or energetic shifts of the $BiAg_2$-surface state bands are observed.

---

[1] Here, the coverage is stated in terms of Ag(111) surface atoms, i.e. every third Ag-atom in the Ag(111)-surface was replaced by a Bi-atom. This corresponds to a coverage of 0.5ML in terms of closed Bi-layers on the Ag(111) surface.

[2] energy resolution ≈ 40meV, momentum resolution ≈ 0.1°

This is quite surprising. Usually, the interaction with an overlayer, even in the case of weak interaction, would be expected to modify the surface state in some way, e.g. by the formation of hybridized bands [261] or at least in a shift of the energetic position of the surface state [262], [261], [263]. The fact that the $BiAg_2$-surface state remains completely unaffected in our data points to an unexpectedly low interaction between the molecules and the substrate.

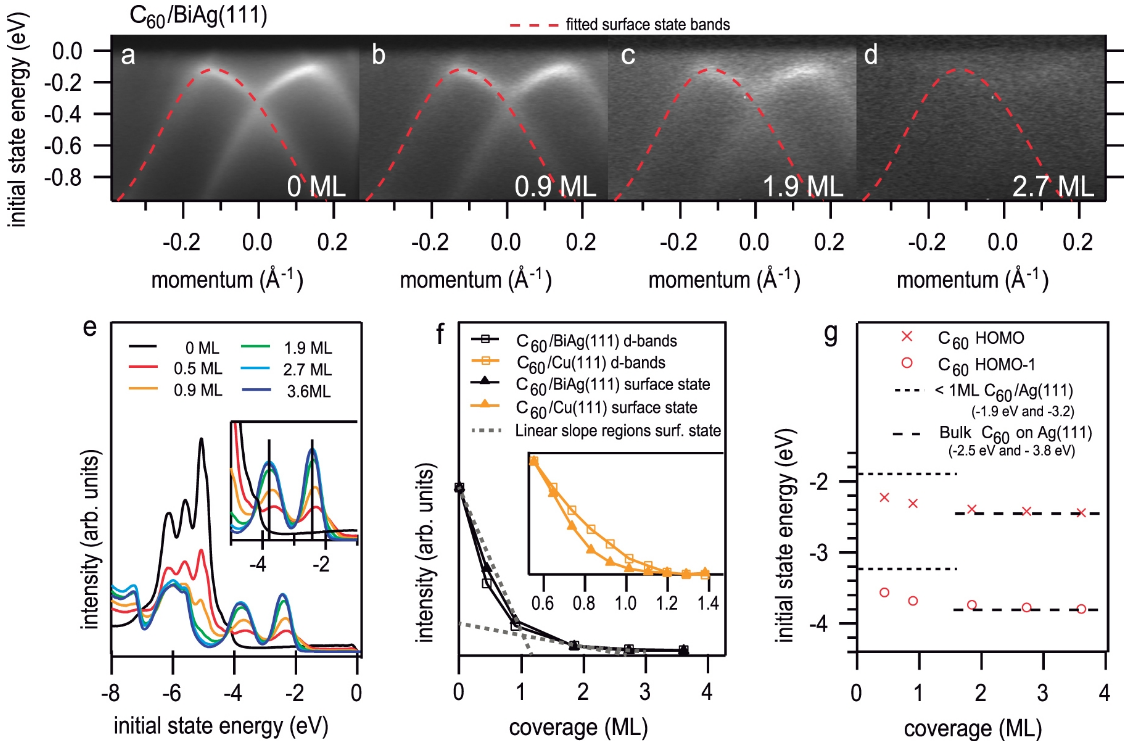

Figure 116: ARPES data for different coverages of C_{60} on $BiAg_2/Ag(111)$. a-d) The variation of the spin split $BiAg_2$ surface state bands with rising C_{60} coverage. The dashed red lines are a fit to the surface state of the clean $BiAg_2$ surface and serve as a guide to the eye. e) Energy distribution curves (zero momentum) for different molecular coverages. The features assigned to the Ag d-bands are found below $-4.5eV$. With rising C_{60} coverage, molecular electronic states arise e.g. around $-2.5eV$ and $-3.9eV$ (see inset). f) The variation of the intensity of the $BiAg_2$ surface state and the Ag d-bands with rising molecular coverage. The gray dotted lines are a guide to the eye to highlight that the attenuation behavior clearly changes when the coverage is increased beyond 1ML. This indicates layer by layer growth. For comparison of the attenuation behavior, the inset shows corresponding data for C_{60} on Cu(111). g) The molecular energy level realignment for the HOMO and HOMO-1 with rising coverage. For comparison, the dotted and dashed lines indicate the energetic positions of the corresponding molecular orbitals for C_{60} on Ag(111) for submonolayer coverage and thick layers (close to bulk value). (Published in [118]).

Fig. 116 e shows normal emission energy distribution curves[3] (EDCs) acquired on differently thick C_{60} films. The substrate d-bands are localized at energies between approximately $-4.5eV$ and $-7eV$. With rising molecular coverage, the intensity of these bands decreases while at the same time new features at e.g. $-2.5eV$ and $-3.9eV$ arise in

---

[3] momentum $= 0$

the spectra (see also the detail shown in the inset in Fig. 116 e). These features may be assigned to molecular states, i.e. the highest occupied molecular orbital (HOMO) and the second highest molecular orbital (HOMO−1) of the adsorbed C_{60}. The data do not exhibit any new, hybridized electronic states (intra-gap stateas) that might result from molecule-substrate interactions, e.g. strong chemisorptive bonding [264].

The intensity variation of the $BiAg_2$-surface state and the substrate d-bands with rising molecular coverage is plotted in Fig. 116 f. For comparison, the inset shows corresponding data for C_{60} on Cu(111) which is considered a rather weakly interacting system[4]. The intensity of both, the surface state and the substrate d-bands, decreases considerably faster for C_{60} on Cu(111) than for C_{60} on $BiAg_2$. This suggests, that the interaction between C_{60} adlayers and $BiAg_2$ is even weaker than for the case of Cu(111). The attenuation behavior exhibits a kink at a coverage of approx. 1ML. As a guide to the eye, the gray dotted lines indicate regions of approximately linear decay up to a coverage of 1ML and between 1ML and 2ML. This points to a layer by layer growth for C_{60} on $BiAg_2$/Ag(111) or at least to a wetting of the $BiAg_2$/Ag(111) surface before the second monolayer starts to form. This excludes different growth modes of C_{60} on Cu(111) and $BiAg_2$ as a possible explanation for the faster attenuation.

So far, we mainly considered the effects of the adsorption of molecular layers on the electronic structure of the substrate. Conversely, we may also look at the electronic states of the molecules in order to classify the strength of the interaction between the molecules and the substrate.

The energetic position of the HOMO and the HOMO−1 versus the molecular coverage is plotted in Fig. 116 g. Up to the closing of the second monolayer, the molecular orbitals shift towards higher binding energies, i.e. away from the Fermi level, with rising coverage. At a coverage of 1.9ML, their energetic positions have almost reached the bulk value and exhibit only minor changes with further increasing coverage.

The size of the molecular energy level realignment, i.e. the energetic shifting of the molecular orbitals with rising molecular coverage, is an indication for the interaction strength. The differences in the measured energy of the molecular orbitals can be explained by an electrostatic screening effect as discussed in Ref. [264]: The kinetic energy of a photoelectron and the associated measured binding energy, are affected by the Coulomb interaction with the associated photohole that is left behind in the photoemission process. The created hole leads to a polarization of its surroundings, i.e. the substrate and the surrounding molecules, which screens the photohole from the corresponding photoelectron. The efficiency of the screening depends on the strength of the molecule-molecule and molecule-substrate interactions. The larger the screening effect, the higher the kinetic energy of the photoelectron and the lower the measured binding energy. With increasing thickness of the molecular layer, the molecule-substrate interaction is decreased and the screening becomes weaker, resulting in an increase of the binding energy.

For comparison to the C_{60} on $BiAg_2$ data, the HOMO and HOMO-1 positions for C_{60} on Ag(111) are exemplary indicated by dashed lines for submonolayer coverage and thick layers (close to bulk value) in Fig. 116 g. The observed molecular energy level realignment in our data is significantly smaller than that observed for C_{60} on adsorbed on Ag(111) and also other (111)- oriented noble metal surfaces [266], [265], [267]. Thus, also the effects on this site of the interface, i.e. the electronic structure of the molecular layer, points to an very weak interaction between the molecules and the substrate.

---

[4] judging from the small molecular level realignment upon adsorption [265] (see discussion)

A.2.2 *FeOEP on BiAg$_2$/Ag(111)*

The weak interaction between the C_{60}-overlayer and the BiAg$_2$-substrate revealed in Fig. 116 is quite surprising for a metallic surface. This rises the question whether also other organic species that would usually exhibit a stronger interactions with metallic substrates than C_{60} would modify the BiAg$_2$ surface state in any way when applied to the surface.

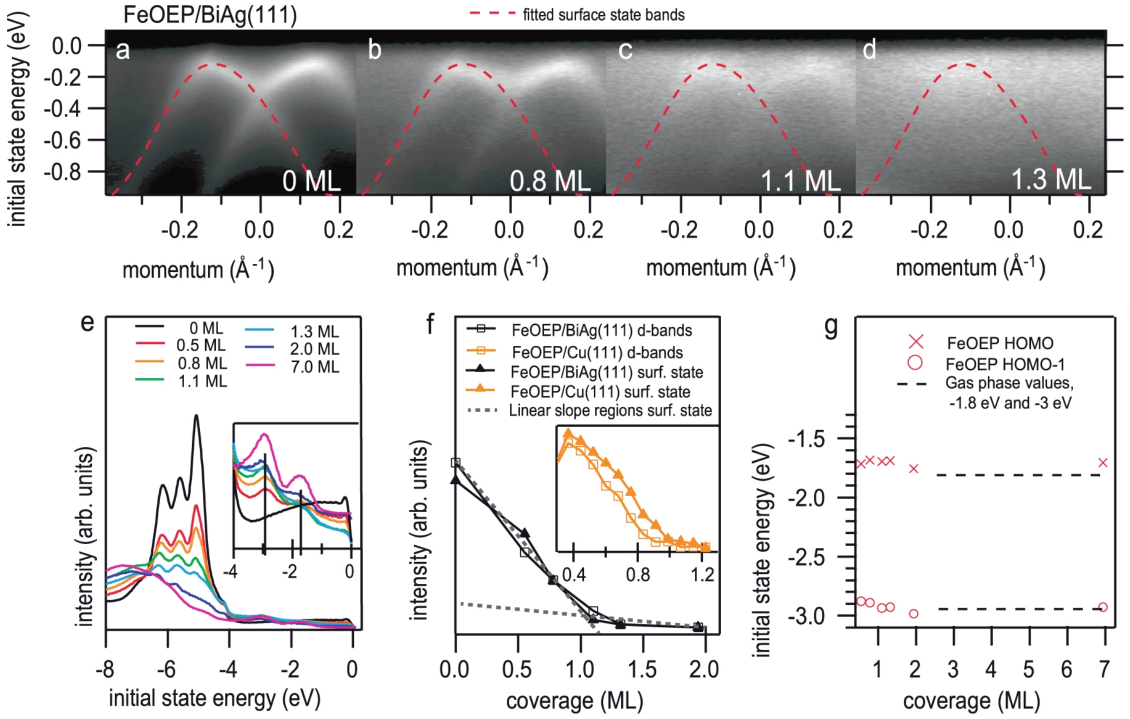

Figure 117: ARPES data for different coverages of FeOEP on BiAg$_2$/Ag(111). a-d) The variation of the spin split BiAg$_2$ surface state bands with rising FeOEP coverage. The dashed red lines are a fit to the surface state of the clean BiAg$_2$ surface and serve as a guide to the eye. e) Energy distribution curves (zero momentum) for different molecular coverages. The features assigned to the Ag d-bands are found below -4.5eV. With rising FeOEP coverage, molecular electronic states arise e.g. around -1.8eV (HOMO) and -3.0eV (HOMO-1) (see inset). f) The variation of the intensity of the BiAg$_2$ surface state and the Ag d-bands with rising molecular coverage. The gray dotted lines are a guide to the eye to highlight that the attenuation behavior clearly changes when the coverage is increased beyond 1ML. This indicates layer by layer growth. For comparison of the attenuation behavior, the inset shows corresponding data for FeOEP on Cu(111). g) The molecular energy level realignment for the HOMO and HOMO-1 with rising coverage. For comparison, the dashed lines indicate gas phase values for the energetic positions of the corresponding molecular orbitals for FeOEP. (Published in [118]).

FeOEP is a porphyrin with a ferromagnetic central atom. For similar molecules, strong interactions with metal substrates have been observed [268], [269]. Recently, our group analyzed FePEP on Cu(111) where we found that the molecules may partially be dechlorinated upon adsorption, i.e. the geometric configuration of the molecules changes [270]. This points to a considerable molecules-substrate interaction. However, the ARPES data for FeOEP on $BiAg_2$ shown in Fig. 117 reveals a similarly weak interaction between the molecules and the substrate as observed for C_{60} on $BiAg_2$.

Once again, the surface state remains unchanged upon the adsorption of the molecules (see Fig. 117 a-d). Like for C_{60} on $BiAg_2$, no hybridized states are found (see Fig. 117 e). As compared to C_{60} on $BiAg_2$, the intensity attenuates much faster for FeOEP deposited on $BiAg_2$. For the latter system, the intensity of the surface state bands is almost completely faded out at a coverage of 1.3ML (see Fig. 117 a-d and f). This faster attenuation of the ARPES signals is may be assigned to a larger atomic density of the FeOEP layers as compared to C_{60} layers.

Here, the variation of the surface state and d-bands with molecular coverage as compared to FeOEP adsorbed on Cu(111) is more similar, however, the attenuation of the electronic bands is still slightly slower for FeOEP on $BiAg_2$ (see Fig. 117 f). Similar to the case of C_{60} on $BiAg_2$, the intensity variation of the $BiAg_2$-surface state and substrate d-bands exhibits a kink at an FeOEP coverage of approx. 1ML. Thus, also for this molecular species, we may assume a complete wetting of the $BiAg_2$-surface before second layer growth sets in.

A very weak interaction between the $BiAg_2$-surface and FeOEP is also supported by the energetic realignment of the molecular levels which is rather small from submonolayer coverage to bulk (see Fig. 117 g).

A.2.3 *PTCDA on $BiAg_2$/Ag(111)*

PTCDA is a molecular species that has been found to interact rather strongly with metallic substrates such as Cu(111) or Ag(111) [266], [264], [271]. The adsorption character of PTCDA on noble metal surfaces varies form strong chemisorption on Cu(111) to weaker interaction on Au(111) (described "soft chemisorption" or even physisorption in literature) [266], [264].

For PTCDA on Ag(111), a hybridized molecule-substrate band has been observed [266], [271]. Even the weak interaction between PTCDA and Au(111) still leads to a small energetic shift of the Au-surface state upon adsorption [262]. Also, the molecular states of this system still exhibit a significant energetic realignment between monolayer and multilayer PTCDA films [266].

Fig. 118 summarizes our ARPES results for PTCDA on $BiAg_2$. Like in the case of the other two molecular species described above, the data again reveal no sign for the formation of hybrid states or any other modification of the $BiAg_2$ surface state by the molecular overlayers. This suggests a very weak interaction also in this case.

In contrast to the molecular level realignment for C_{60} and FeOEP, in the case of PTCDA, with rising coverage, the energy of the PTCDA HOMO rises with increasing coverage up to 2ML. Also, instead of one single HOMO energy, at low coverage, a close inspection of the EDCs yields two features which may be assigned to HOMOs of the adsorbed PTCDA molecules. This will be discussed in futher detail in section A.4.2.

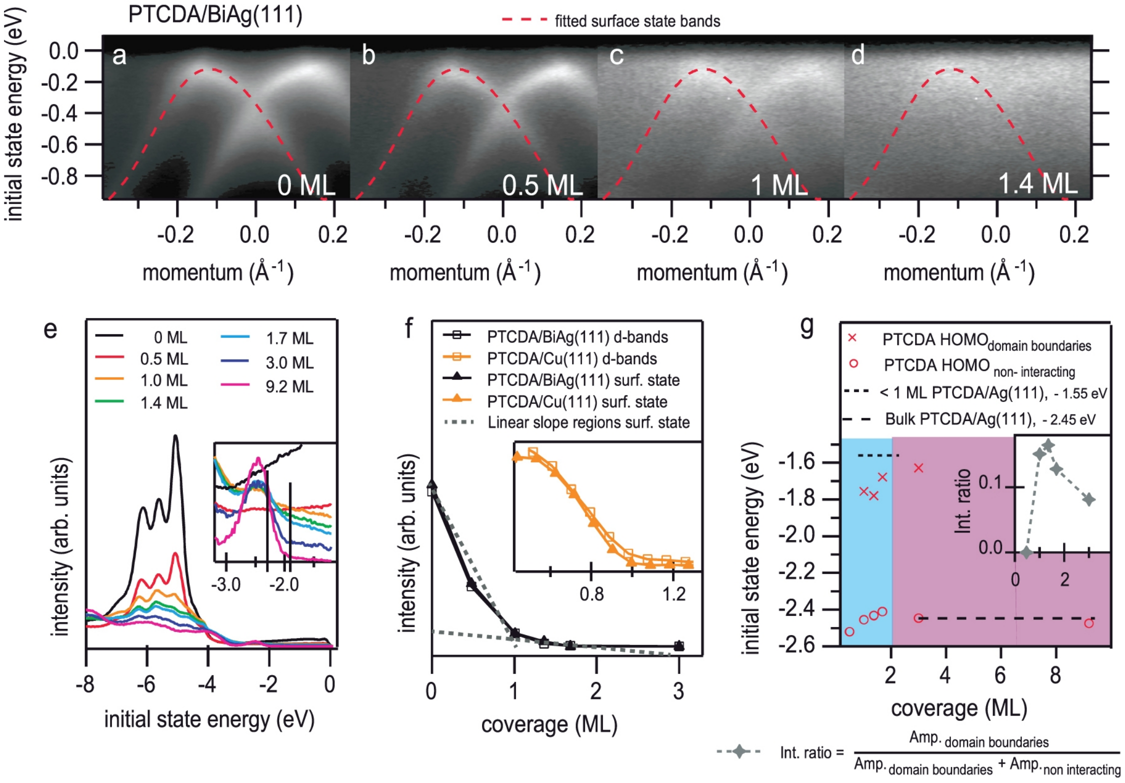

Figure 118: ARPES data for different coverages of PTCDA on $BiAg_2/Ag(111)$. a-d) The variation of the spin split $BiAg_2$ surface state bands with rising PTCDA coverage. The dashed red lines are a fit to the surface state of the clean $BiAg_2$ surface and serve as a guide to the eye. e) Energy distribution curves (zero momentum) for different molecular coverages. The features assigned to the Ag d-bands are found below -4.5eV. With rising PTCDA coverage, molecular electronic states arise e.g. around -2.45eV (see inset). f) The variation of the intensity of the $BiAg_2$ surface state and the Ag d-bands with rising molecular coverage. The gray dotted lines are a guide to the eye to highlight that the attenuation behavior clearly changes when the coverage is increased beyond 1ML. This indicates layer by layer growth. For comparison of the attenuation behavior, the inset shows corresponding data for PTCDA on Cu(111). g) The molecular energy level realignment for the HOMO with rising coverage. For comparison, the dotted and dashed lines indicate the energetic positions of the HOMO for PTCDA on Ag(111) for submonolayer coverage and thick layers (close to bulk value). (Published in [118]).

A.3 STM ON PTCDA ON BIAG$_2$/AG(111)

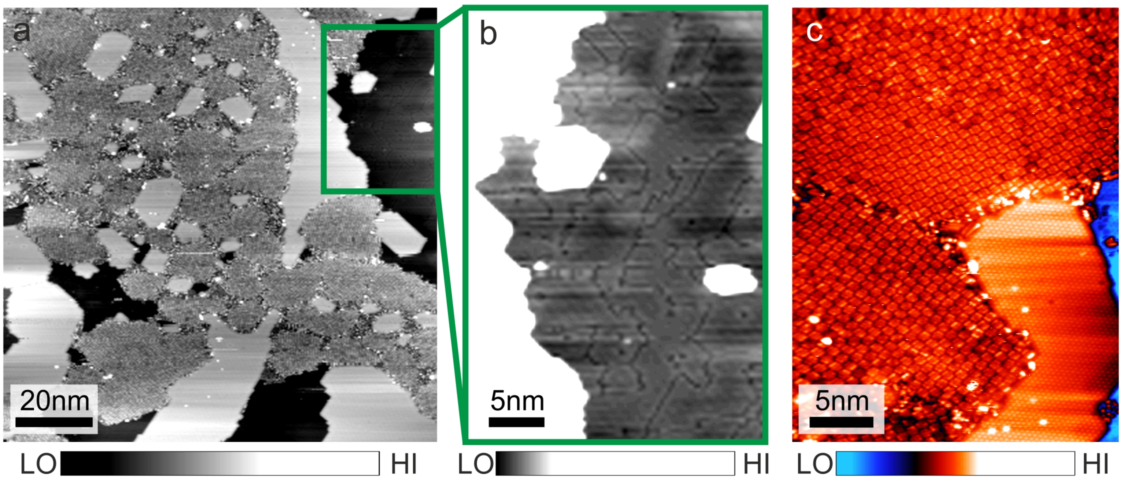

Figure 119: STM topographic images acquired on a BiAg$_2$/Ag(111) sample with a PTCDA coverage of about 0.5ML. a) Overview of a surface area with a size of approx. $120\mathrm{nm} \times 120\mathrm{nm}$. $V_{sample} = 1\mathrm{V}$, $I = 30\mathrm{pA}$, $T = 80\mathrm{K}$. The depicted area exhibits both, highly ordered BiAg$_2$-islands as well as lower BiAg$_2$-domains. The PTCDA-domains are exclusively observed on the lower BiAg$_2$-structure. No second layer growth is observed for the molecules at the given coverage. b) Zoom of the surface area marked by the rectangle in a). The topographically lower BiAg$_2$-areas exhibit a large number of defects and domain boundaries. c) Detailed scan of a PTCDA covered surface area which exhibits different domains separated by domain boundaries. In the lower right quadrant of the image, an atomically resolved highly ordered BiAg$_2$-island is found. (Similarly published in [118]).

Fig. 119 show exemplary STM data acquired on a BiAg$_2$/Ag(111) sample onto which approx. 0.5ML PTCDA were evaporated. Two different kinds of BiAg$_2$-domains that result from the formation procedure of the Bi/Ag(111)-surface alloy can be observed. The BiAg$_2$/Ag(111) sample exhibits topographically higher, highly ordered domains and topographically lower domains exhibiting a significant amount of domain boundaries and local defects. The explanation for these two structures can be found in the formation of the BiAg$_2$ surface alloy [232], [231]: Bi is evaporated onto the Ag(111) surface. The Bi-atoms displace Ag(111)-surface atoms and form a dilute surface alloy. With rising coverage, the Bi-atoms in the dilute surface alloy adopt a $\sqrt{3} \times \sqrt{3}$-configuration, minimizing the surface strain as well as the total energy of the surface [231]. This is the path of formation for the topographically lower BiAg$_2$ areas, which are prone to surface defects and domain boundaries. The displaced Ag-atoms diffuse around the surface until they encounter Bi-atoms which are not yet incorporated into the surface. Both atomic species then assemble into highly ordered islands on top of the remaining pristine Ag(111) surface areas. This way, the almost defect free highly ordered topographically higher BiAg$_2$-areas are formed.

The PTCDA-domains are found to grow exclusively on the lower BiAg$_2$-structures. Although the PTCDA molecules assemble into ordered domains where the molecules roughly assume the well known "herringbone structure" [150], a closer look reveals a certain disorder within the domains. Additionally, the molecular islands exhibit a large amount of domain boundaries.

A.4 DISCUSSION

In this appendix chapter, we have investigated the molecule-substrate interaction for three different archetype molecular species adsorbed on the $BiAg_2$-alloy. Upon adsorption of the molecular layers, no modification of the giant spin orbit split $BiAg_2$-surface state, e.g. in form of energetic shifts or hybridization effects, was observed. Conversely, regarding the other side of the interface, only small shifts were observed in the energetic level realignment of the molecular layers. Both results point to a surprisingly weak interaction for all examined molecular species.

To further verify the absence of hybridization between molecular states and the $BiAg_2$-surface state, detailed ARPES data for coverages of about 1ML for each molecular species are shown in Fig. 120 a-d. While Fig. 116 - 118 showed ARPES data for the binding energy region in between the Fermi level and -1eV, this time, we want to concentrate on higher binding energies where the HOMOs of the adsorbed molecules are located. The energetic extend of the HOMO and HOMO-1 orbitals is indicated by green dashed and red solid lines in Fig. 120. To allow for a detailed inspection of the $BiAg_2$-surface state bands, the HOMO peaks were subtracted in the data show in Fig. 120 e-g. The color scale for this data set was inverted for better visualization. Also in this representation, no signs for hybridization are found as the surface state disperses completely unaffected through the energetic regions of the molecular orbitals.

Previous studies by Moreschini et al. addressed the effect of Xenon(Xe)-overlayers on the $BiAg_2$-surface [261]. As a noble gas, Xe would be expected to be especially weakly interacting with the surface state of the $BiAg_2$-surface alloy. Still, the authors observe hybridization effects as well as a shift of the surface state bands by a few ten meV. Also the surface states of other metallic surfaces, even in the case of weak interaction, usually at least exhibit an energetic shift upon the adsorption of adlayers [261], [262], [263]. This is in contrast to our data where we do not observe such behavior (see Fig. 116 - 118 a-d, Fig. 120). This underlines the unprecedentedly large inertness of the $BiAg_2$-substrate in our case.

Apart from leaving the $BiAg_2$-surface state unaffected, the inertness of the $BiAg_2$-surface also manifested itself in low energy level realignments between the molecular orbitals upon adsorption. The differences in the energetic levels of the corresponding molecular orbitals at coverages $\leqslant 1\text{ML}$ and high coverage measured in our case lie in between approx. 20meV and 130meV. On noble metals, energetic shifts in the order of 200meV up to several hundred meV have been observed [266], [264], [272], [265], [267].

A.4.1 *Origin of the Weak Interaction between the $BiAg_2$-surface and organic overlayers*

A very weak interaction between metallic surface states and overlayers has also been found for other material systems. E.g. graphene layers have been shown to interact weakly with metallic surface states e.g. those of Cu(111) [273], Au(111) [274] or Ir(111) [263]. All surface states persisted under a monolayer of graphene. To explain the inertness of the Ir(111) surface state to the overlayer, Varykhalov et al. proposed topological protection to play a role [263]. Here, the tails of the Ir(111) surface state bands connect to bulk d-bands across a bulk bandgap.

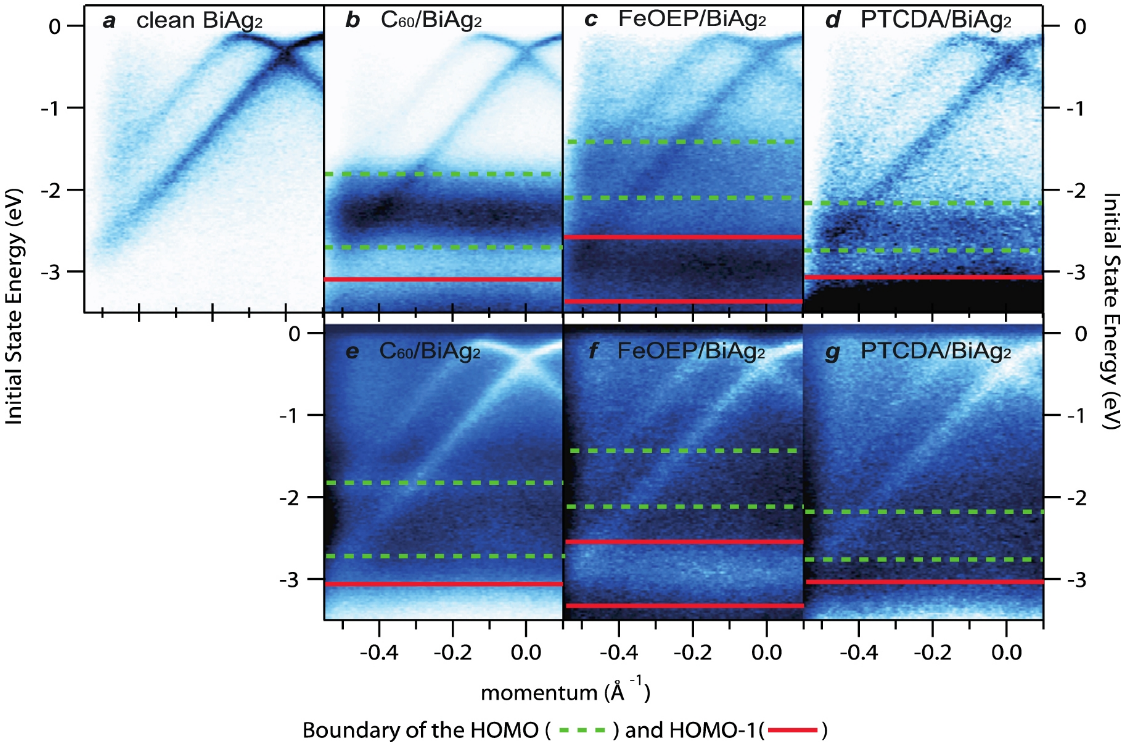

Figure 120: Detailed ARPES data for the $BiAg_2$-surface state. a) Data acquired on the pristine $BiAg_2/Ag(111)$ surface. b-d) Data for a coverage of approximately 1ML of C_{60}, FeOEP, and PTCDA, respectively. The positions of the HOMO and the HOMO−1 are indicated by the green dashed and the red solid lines. e)-g) show the same data, this time with the respective HOMO-peak subtracted, to allow for a detailed view of the surface state within the region of this molecular orbital. The color scale is inverted with respect to a)-d) for improved visualization. (Published in [118]).

In our ARPES data for $BiAg_2/Ag(111)$, the surface state bands have lost almost all intensity in the energy range of the bulk d-bands. Thus, a topological protection for this system is unlikely. Rather, like in the case of the thin Bi-films on Cu(111) discussed in the main part of this thesis (see especially chapter 14), a chemical inertness of the $BiAg_2$-surface resulting from the bonding structure is a plausible explanation for the observed low interaction with organic overlayers.

A surface atom in the (111)-surface of a face centered cubic(fcc)-ordered crystal has a coordination number of 9, whereas the coordination number in bulk would be 12. The surface atoms in fcc(111)-surfaces are not fully coordinated due to a lack of bonding partners. Consequently, the charge density at the surface is increased which may promote an increased reactivity of the surface.

In contrast, the bonding of the Bi-atoms in the $BiCu_2/Cu(111)$ surface leads to fully coordinated atoms and has been shown to effectively locate charge density away from the surface [116]. A similar effect of the bonding structure may also be expected for $BiAg_2/Ag(111)$. The resulting small overlap between the wavefunctions of the molecular overlayers and the $BiAg_2/Ag(111)$ surface leads to a weak interaction between the two [116].

A.4.2 *Effect of the residual interaction between PTCDA and BiAg₂*

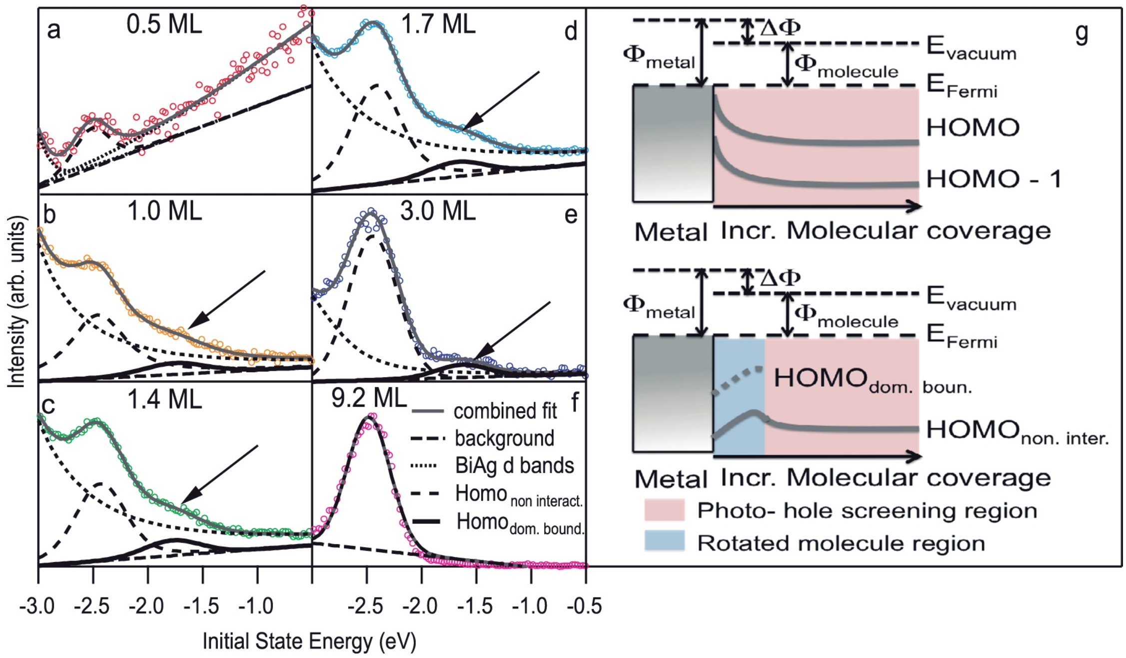

Figure 121: The evolution of molecular orbitals for PTCDA. a)-f) Details of the energy distribution curves along with the results of peak fitting of the data. The open circles represent the PES data. The dotted, dashed and solid lines are fits as indicated by the legend shown in f). The fits reveal not only one but two peaks in the data that are assigned to the HOMO of the adsorbed PTCDA. The small peak around −1.6eV is ascribed to the HOMO of the PTCDA molecules adsorbed on or close to the domain boundaries, also referred to as $\mathrm{HOMO}_{\mathrm{domain\ boundary}}$. For clarity, this feature is highlighted by around in b)-e). The more prominent peak around 2.45eV is ascribed to the HOMO of the PTCDA molecules adsorbed on the highly ordered $BiAg_2$ substrate areas. The interaction between the molecules and the substrate for this molecular orbital is expected to be much weaker than for the PTCDA molecules adsorbed on the domain boundaries. Therefore, the HOMO of the PTCDA molecules adsorbed on the highly ordered substrate areas is also referred to as $\mathrm{HOMO}_{\mathrm{non-interacting}}$. g) Schematic representations of the molecular energy level realignment for the case of C_{60} and FeOEP (top) and PTCDA (bottom). (Published in [118]).

In the attenuation of the ARPES signal with increasing molecular coverage, PTCDA on $BiAg_2$ behaves widely analog to the cases of C_{60} and FeOEP discussed above. However, in the realignment of the molecular levels with increasing PTCDA coverage, significant differences may be observed (see Fig. 118 g). Up to a PTCDA coverage of approximately 2ML, instead of the expected upward shift in energy, the energetic levels of the molecular states first shift towards the Fermi energy. This region is indicated in Fig. 118 g by the blue background.

To further analyze this effect, details of the energy distribution curves for the energetic region below −3eV are shown in Fig. 121 a-f. In fact, when looking closely at the data in the energy region where HOMO of the adsorbed PTCDA layers is expected, not one but two peaks are observed in the data. The more prominent intensity peak is observed around $-2.5eV$, a second peak which is much less pronounced is found around $-1.8eV$. As a guide to the eye this second peak is indicated by arrows in Fig. 121 b-e.

The complementary STM data (see Fig. 119) reveals a certain disorder in the PTCDA-domains. On noble metal substrates, PTCDA usually assembles into large, highly ordered domains. In contrast, here, the molecule covered areas exhibit a large number of domains separated by domain boundaries. Even within the PTCDA-domains, the order of the molecules seems to be disturbed. The shape of the locally ordered areas within the PTCDA-domains resembles the shape of the ordered parts of the topographically lower $BiAg_2$-areas. These observations point to an increased interaction of the molecules with the substrate at the $BiAg_2$-domain boundaries. Such interaction may also influence the energetic positions of the molecular orbitals such as the HOMO.

Considering such local modification of the electronic states of the molecules, the more prominent peak observed in Fig. 121 may be assigned to the HOMO of the PTCDA molecules adsorbed on regularly ordered $BiAg_2$ areas. This peak is also referred to as the non-interacting HOMO. The considerably smaller peak closer to the Fermi energy can accordingly be assigned to the PTCDA adsorbed close to or directly above the domain boundaries. This second peak is also referred to as the interacting HOMO or domain boundary HOMO. This interpretation of the peaks in our EDCs is also supported by the intensity ratio of the domain boundary HOMO-peak and overall intensity of both HOMO peaks versus the molecular coverage as plotted in the inset in 118 g. The relative intensity of the domain boundary HOMO is largest at a coverage of approx. $1ML$.

The energy of molecular orbitals may significantly depend on the adsorption geometry [264]. Kraft et al. showed this in STS experiments on PTCDA on Ag(111) [275]. PTCDA molecules with slightly different adsorption geometries, i.e. different orientations of the molecules above the substrate, exhibited differences in the energies of their molecular electronic states. This was assigned to different interactions with the substrate.

The molecular level realignment for C_{60}, FeOEP and PTCDA is schematically depicted in Fig. 121 g. In the case of C_{60} and FeOEP, the energy of the molecular orbitals is slightly shifted towards the Fermi level upon adsorption as shown in the top schematic in Fig. 121 g. This may be understood in terms of a less effective screening of the photoholes from the escaping photoelectrons with rising molecular coverage [264] (see section A.2.1).

In contrast, for PTCDA, the molecular energy level realignment follows a different behavior as schematically depicted in the bottom part of Fig. 121 g. This might be understood as follows: the residual interaction between the molecules and the substrate induces a certain disorder of the molecular film increasing the overall energy. With rising coverage, the overall order of the molecular film is increased as the molecules start to adsorb on the highly ordered, topographically higher $BiAg_2$ islands that usually do not exhibit domain boundaries. For coverages larger than $1ML$, the first PTCDA layer (wetting layer) additionally decouples the molecules from the substrate and thus further decreases the interaction. Thus, molecule-molecule interactions dominate the ordering in higher layers. The increased ordering leads to a shift of the orbital energies towards the Fermi energy up to a coverage of approx. 2ML. This region is indicated by a blue background in Figs. 118 and 121 g.

The following energetic level realignment with further rising coverage may be understood analog the the molecular level realignment C_{60} and FeOEP as discussed above. This region is indicated by a brown background in Figs. 118 and 121 g.

From the observed molecular level realignment for PTCDA, we may infer that for this molecular species, the residual interaction with the substrate is the strongest.

A.5 SUMMARY AND CONCLUSION

In summary, the ARPES experiments presented in this chapter showed that the $BiAg_2$-surface state as well as its spin character, i.e. the size of the spin splitting, remained preserved underneath different organic layers. Conversely, also the effect of the adsorption on the electronic structure of the molecules is remarkably small. Thus, e.g. the hole injection barrier of the molecular layer, i.e. the energy difference between the Fermi level and the HOMO [264], remains virtually constant upon adsorption. This is a great advantage when envisaging the use of $BiAg_2$ as a substrate to organic adlayers in future organic electronic components.

The ARPES experiments as well as the STM-LE experiments presented in this thesis suggest an exceptionally weak interaction between Bi-induced structures on Cu(111) and organic overlayers. This peculiar behavior may be understood as the result of the bonding of the Bi-atoms in these structures. Thus, also for the Bi induced structures that were characterized by STM-LE in this thesis, a similar chemical inertness of the spin character of the electronic states can be expected. Further ARPES measurements may help to confirm this assumption.

A minimum interaction between different components is a highly desirable property in electronic devices since it allows a manipulation of the functional layers. The results presented here may pave the way to not only exploit the peculiar properties of the system in possible plasmonic applications, as suggested by the STM-LE experiments, but also include prospect uses in spintronic applications and organic electronics. The thorough characterization of molecule covered Bi-structures on Cu(Ag)(111) by STM-LE complemented by other techniques may even enable merging all three fields, i.e. plasmonics, spintronics, and organic electronics for a future use in technological applications.

LIST OF ABBREVIATIONS

1 Å	1 Ångstrøm = 0.1 nm = $1 \cdot 10^{-10}$ m
amu	atomic mass unit
approx.	approximately
ARPES	angle resolved photoemission spectroscopy
Cl-FeOEP	iron(III)-octaethylporphyrin chloride
CuPc	copper-phthalocyanine
dI/dV	the derivative of the tunneling current with respect to the bias voltage
dr	dark count rate
eq.	equation
et al.	et alii (and others)
eV	electron volt
fcc	face centered cubic
Fig.	Figure
HOMO	highest occupied molecular orbital
IVC	current-to-voltage converter
LDOS	local density of states
LEED	low energy electron diffraction
LT	low temperature
LT-STM	low-temperature scanning tunneling microscope/microscopy
LUMO	lowest unoccupied molecular orbital
ML	monolayer
OLED	organic light emitting device
PES	photoelectron spectroscopy
PTCDA	3,4,9,10-perylene-tetracarboxylicacid-dianhydride
Ref.	reference
SEM	scanning electron microscope/microscopy
STM	scanning tunneling microscope/microscopy
STM-LE	STM-induced light emission
STS	scanning tunneling spectroscopy
UHV	ultra high vacuum
vs.	versus

LIST OF PUBLICATIONS

ARTICLES

1. Cottin, M. C.; Bobisch, C. A.; Schaffert, J.; Jnawali, G.; Sonntag, A.; Bihlmayer, G.; Möller, R.: Anisotropic scattering of surface state electrons at a point defect on Bi(111). In: *Applied Physics Letters* **98**, 022108-022108-3 (2011) → [108].
2. Cottin, M.C.; Schaffert, J.; Sonntag, A.; Karacuban, H.; Möller, R.; Bobisch, C.A., Supramolecular architecture of organic molecules: PTCDA and CuPc on a Cu(111) substrate. In: *Applied Surface Science* **258**, 2196 - 2200 (2012) → [154].
3. Bobisch, C.A.; Bernhart, A.M.; Kaspers, M.R.; Cottin, M.C.; Schaffert, J.; Möller, R.: Electronic Transport on the Nanoscale. In: *Atomic Scale Interconnection Machines*, 197-214, Series: Advances in Atom and Single Molecule Machines, Editor: Joachim, Christian; Springer Berlin Heidelberg (2012) → [276].
4. Schaffert, J.; Cottin, M.C.; Sonntag, A.; Karacuban, H.; Bobisch, C.A.; Lorente, N.; Gauyacq, J.-P.; Möller, R.: Imaging the dynamics of individually adsorbed molecules. In: *Nature Materials* **12**, 223-227 (2012) → [168].
5. Schaffert, J.; Cottin, M.C.; Sonntag, A.; Karacuban, H.; Utzat, D.; Bobisch, C.A.; Möller, R.: Scanning noise microscopy. In: *Review of Scientific Instruments* **84**, 043702 (2013) → [184].
6. Cottin, M.C.; Bobisch, C.A.; Schaffert, J.; Jnawali, G.; Bihlmayer, G.; Möller, R.: Interplay between Forward and Backward Scattering of Spin-Orbit Split Surface States of Bi(111). In: *Nano Letters* **13**, 2717-2722 (2013) → [109].
7. Van Vörden, D.; Lange, M.; Schmuck, M.; Schaffert, J.; Cottin, M.C.; Bobisch, C.A.; Möller, R.: Substrate induced dehydrogenation: Transformation of octa-ethyl-porphyrin into tetra-benzo-porphyrin. In: *The Journal of Chemical Physics* **138**, 211102 (2013) → [277].
8. Schaffert, J.; Cottin, M.C.; Sonntag, A.; Bobisch, C.A.; Möller, R.; Gauyacq, J. P.; Lorente, N.: *Tunneling electron induced rotation of a copper phthalocyanine molecule on Cu (111)*. In: *Physical Review B* **88**, 075410 (2013) → [278].
9. Van Vörden, D.; Lange, M.; Schaffert, J.; Cottin, M.C.; Schmuck, M.; Robles, R.; Wende, H.; Bobisch, C.A.; Möller, R.: Surface-induced dechlorination of FeOEP-Cl on Cu(111). In: *ChemPhysChem* **13**, 3472-3475 (2013) → [270].
10. Cottin, M.C.; Lobo-Checa, J.; Schaffert, J.; Bobisch, C.A.; Möller, R.; Ortega, J.E.; Walter, A.L.: A chemically inert Rashba split interface: electronic structure of C_{60}, FeOEP and PTCDA on $BiAg_2$/Ag(111) substrates. In: *New Journal of Physics* **16**, 045002 (2014) → [168].

REFERENCES

[1] Chemical sciences and society summit (CS3). In *Organic Electronics for a Better Tomorrow: Innovation, Accessibility, Sustainability*, 2012. URL http://www.rsc.org/globalassets/04-campaigning-outreach/realising-potential-of-scientists/research-policy/global-challenges/organic-electronics-for-a-better-tomorrow1.pdf. accessed online August 10 2015. (Cited on page 4.)

[2] Tsuyoshi Sekitani, Hiroyoshi Nakajima, Hiroki Maeda, Takanori Fukushima, Takuzo Aida, Kenji Hata, and Takao Someya. Stretchable active-matrix organic light-emitting diode display using printable elastic conductors. *Nat Mater*, 8 (6):494–499, June 2009. ISSN 1476-1122. URL http://dx.doi.org/10.1038/nmat2459. (Cited on page 4.)

[3] John A. Rogers, Takao Someya, and Yonggang Huang. Materials and Mechanics for Stretchable Electronics. *Science*, 327(5973):1603–1607, 2010. doi: 10.1126/science.1182383. URL http://www.sciencemag.org/content/327/5973/1603.abstract. (Cited on page 4.)

[4] Jeff Hecht. PHOTONIC FRONTIERS: OPTICAL ANTENNAS: Optical antennas concentrate light and direct beams, 2013. URL http://www.laserfocusworld.com/articles/print/volume-49/issue-09/features/photonic-frontiers-optical-antennas-optical-antennas-concentrate-light-and-direct-beams.html. (Cited on page 4.)

[5] Javier Alda, José M Rico-García, José M López-Alonso, and G Boreman. Optical antennas for nano-photonic applications. *Nanotechnology*, 16(5):S230, 2005. URL http://stacks.iop.org/0957-4484/16/i=5/a=017.

[6] Palash Bharadwaj and Bradley Deutsch and Lukas Novotny. Optical Antennas. *Adv. Opt. Photon.*, 1(3):438–483, Nov 2009. doi: 10.1364/AOP.1.000438. URL http://aop.osa.org/abstract.cfm?URI=aop-1-3-438. (Cited on page 4.)

[7] Lukas Novotny and Niek van Hulst. Antennas for light. *Nat Photon*, 5(2):83–90, February 2011. ISSN 1749-4885. URL http://dx.doi.org/10.1038/nphoton.2010.237. (Cited on page 4.)

[8] Michael S. Eggleston, Kevin Messer, Liming Zhang, Eli Yablonovitch, and Ming C. Wu. Optical antenna enhanced spontaneous emission. *Proceedings of the National Academy of Sciences*, 112(6):1704–1709, 2015. doi: 10.1073/pnas.1423294112. URL http://www.pnas.org/content/112/6/1704.abstract. (Cited on page 4.)

[9] Wei Bao, M. Melli, N. Caselli, F. Riboli, D. S. Wiersma, M. Staffaroni, H. Choo, D. F. Ogletree, S. Aloni, J. Bokor, S. Cabrini, F. Intonti, M. B. Salmeron, E. Yablonovitch, P. J. Schuck, and A. Weber-Bargioni. Mapping Local Charge

Recombination Heterogeneity by Multidimensional Nanospectroscopic Imaging. *Science*, 338(6112):1317–1321, 2012. doi: 10.1126/science.1227977. URL `http://www.sciencemag.org/content/338/6112/1317.abstract`. (Cited on page 4.)

[10] J.K. Gimzewski, B. Reihl, J.H. Coombs, and R.R. Schlittler. Photon emission with the scanning tunneling microscope. *Zeitschrift für Physik B Condensed Matter*, 72 (4):497–501, 1988. ISSN 0722-3277. doi: 10.1007/BF01314531. URL `http://dx.doi.org/10.1007/BF01314531`. (Cited on pages 4, 9, and 27.)

[11] J. Aizpurua, S. P. Apell, and R. Berndt. Role of tip shape in light emission from the scanning tunneling microscope. *Phys. Rev. B*, 62:2065–2073, Jul 2000. doi: 10.1103/PhysRevB.62.2065. URL `http://link.aps.org/doi/10.1103/PhysRevB.62.2065`. (Cited on pages 5, 30, 40, 78, 104, 109, 110, 111, 112, 113, and 114.)

[12] Chi Chen, C. A. Bobisch, and W. Ho. Visualization of Fermi's Golden Rule Through Imaging of Light Emission from Atomic Silver Chains. *Science*, 325(5943):981–985, 2009. doi: 10.1126/science.1174592. URL `http://www.sciencemag.org/content/325/5943/981.abstract`. (Cited on pages 5, 10, and 40.)

[13] N. L. Schneider, F. Matino, G. Schull, S. Gabutti, M. Mayor, and R. Berndt. Light emission from a double-decker molecule on a metal surface. *Phys. Rev. B*, 84: 153403, Oct 2011. doi: 10.1103/PhysRevB.84.153403. URL `http://link.aps.org/doi/10.1103/PhysRevB.84.153403`. (Cited on pages 5, 31, 40, 118, 146, 148, 193, and 217.)

[14] Theresa Lutz, Christoph Große, Christian Dette, Alexander Kabakchiev, Frank Schramm, Mario Ruben, Rico Gutzler, Klaus Kuhnke, Uta Schlickum, and Klaus Kern. Molecular Orbital Gates for Plasmon Excitation. *Nano Letters*, 13(6):2846–2850, 2013. doi: 10.1021/nl401177b. URL `http://pubs.acs.org/doi/abs/10.1021/nl401177b`. (Cited on pages 5, 24, 31, 40, 46, 131, 146, 148, 150, 151, 152, 154, 193, 214, 218, and 240.)

[15] Elizabeta Cavar, Marie-Christine Blüm, Marina Pivetta, François Patthey, Majed Chergui, and Wolf-Dieter Schneider. Fluorescence and Phosphorescence from Individual C_{60} Molecules Excited by Local Electron Tunneling. *Phys. Rev. Lett.*, 95:196102, Nov 2005. doi: 10.1103/PhysRevLett.95.196102. URL `http://link.aps.org/doi/10.1103/PhysRevLett.95.196102`. (Cited on pages 5, 10, 31, 148, 193, and 219.)

[16] Chi Chen, Ping Chu, C. A. Bobisch, D. L. Mills, and W. Ho. Viewing the Interior of a Single Molecule: Vibronically Resolved Photon Imaging at Submolecular Resolution. *Phys. Rev. Lett.*, 105:217402, Nov 2010. doi: 10.1103/PhysRevLett.105.217402. URL `http://link.aps.org/doi/10.1103/PhysRevLett.105.217402`. (Cited on pages 5, 9, 10, 31, 40, 148, 155, 169, 193, 217, and 219.)

[17] Z. C. Dong, X. L. Zhang, H. Y. Gao, Y. Luo, C. Zhang, L. G. Chen, R. Zhang, X. Tao, Y. Zhang, and J. G. Yang, J. L.and Hou. Generation of molecular hot electroluminescence by resonant nanocavity plasmons. *Nat Photon*, 4(1):50–54,

January 2010. ISSN 1749-4885. URL http://dx.doi.org/10.1038/nphoton.2009.257. (Cited on pages 194, 195, and 217.)

[18] X. H. Qiu, G. V. Nazin, and W. Ho. Vibrationally Resolved Fluorescence Excited with Submolecular Precision. *Science*, 299(5606):542–546, 2003. doi: 10.1126/science.1078675. URL http://www.sciencemag.org/content/299/5606/542.abstract. (Cited on pages 9, 10, 31, 148, and 219.)

[19] Frédéric Rossel, Marina Pivetta, François Patthey, and Wolf-Dieter Schneider. Plasmon enhanced luminescencefrom fullerene molecules excited bylocal electron tunneling. *Opt. Express*, 17(4):2714–2721, Feb 2009. doi: 10.1364/OE.17.002714. URL http://www.opticsexpress.org/abstract.cfm?URI=oe-17-4-2714. (Cited on pages 5, 77, and 148.)

[20] Natalia L. Schneider and Richard Berndt. Plasmonic excitation of light emission and absorption by porphyrine molecules in a scanning tunneling microscope. *Phys. Rev. B*, 86:035445, Jul 2012. doi: 10.1103/PhysRevB.86.035445. URL http://link.aps.org/doi/10.1103/PhysRevB.86.035445. (Cited on page 5.)

[21] Christoph Große, Alexander Kabakchiev, Theresa Lutz, Romain Froidevaux, Frank Schramm, Mario Ruben, Markus Etzkorn, Uta Schlickum, Klaus Kuhnke, and Klaus Kern. Dynamic Control of Plasmon Generation by an Individual Quantum System. *Nano Letters*, 14(10):5693–5697, 2014. doi: 10.1021/nl502413k. URL http://dx.doi.org/10.1021/nl502413k. PMID: 25181332. (Cited on pages 5, 46, and 218.)

[22] G. Binnig, H. Rohrer, Ch. Gerber, and E. Weibel. Surface Studies by Scanning Tunneling Microscopy. *Phys. Rev. Lett.*, 49:57–61, Jul 1982. doi: 10.1103/PhysRevLett.49.57. URL http://link.aps.org/doi/10.1103/PhysRevLett.49.57. (Cited on pages 9 and 14.)

[23] website, accessed online, June 20 2014. URL http://www.nobelprize.org/nobel_prizes/chemistry/laureates/1996/index.html. (Cited on pages 9, 37, and 45.)

[24] R. Berndt, R. Gaisch, W. D. Schneider, J. K. Gimzewski, B. Reihl, R. R. Schlittler, and M. Tschudy. Atomic Resolution in Photon Emission Induced by a Scanning Tunneling Microscope. *Phys. Rev. Lett.*, 74:102–105, Jan 1995. doi: 10.1103/PhysRevLett.74.102. URL http://link.aps.org/doi/10.1103/PhysRevLett.74.102. (Cited on pages 9 and 118.)

[25] Germar Hoffmann, Thomas Maroutian, and Richard Berndt. Color View of Atomic Highs and Lows in Tunneling Induced Light Emission. *Phys. Rev. Lett.*, 93:076102, Aug 2004. doi: 10.1103/PhysRevLett.93.076102. URL http://link.aps.org/doi/10.1103/PhysRevLett.93.076102. (Cited on pages 9, 10, 40, 83, 84, 103, 116, 121, 123, 124, and 239.)

[26] Guillaume Schull, Michael Becker, and Richard Berndt. Imaging Confined Electrons with Plasmonic Light. *Phys. Rev. Lett.*, 101:136801, Sep 2008. doi: 10.1103/PhysRevLett.101.136801. URL http://link.aps.org/doi/10.1103/PhysRevLett.101.136801.

[27] Shawn Divitt, Palash Bharadwaj, and Lukas Novotny. The role of gap plasmons in light emission from tunnel junctions. *Opt. Express*, 21(22):27452–27459, Nov 2013. doi: 10.1364/OE.21.027452. URL `http://www.opticsexpress.org/abstract.cfm?URI=oe-21-22-27452`. (Cited on pages 10 and 103.)

[28] R. Berndt and J. K. Gimzewski. Injection luminescence from CdS($11\bar{2}0$) studied with scanning tunneling microscopy. *Phys. Rev. B*, 45:14095–14099, Jun 1992. doi: 10.1103/PhysRevB.45.14095. URL `http://link.aps.org/doi/10.1103/PhysRevB.45.14095`. (Cited on pages 10, 31, and 32.)

[29] Maria Reinhardt, Guillaume Schull, Philipp Ebert, and Richard Berndt. Atomic resolution in tunneling induced light emission from GaAs(110). *Applied Physics Letters*, 96(15):152107, 2010. doi: http://dx.doi.org/10.1063/1.3360203. URL `http://scitation.aip.org/content/aip/journal/apl/96/15/10.1063/1.3360203`. (Cited on pages 10, 31, and 32.)

[30] Frédéric Rossel, Marina Pivetta, and Wolf-Dieter Schneider. Luminescence experiments on supported molecules with the scanning tunneling microscope. *Surface Science Reports*, 65(5):129 – 144, 2010. ISSN 0167-5729. doi: http://dx.doi.org/10.1016/j.surfrep.2010.06.001. URL `http://www.sciencedirect.com/science/article/pii/S0167572910000385`. (Cited on pages 10, 27, 28, 83, and 148.)

[31] Feng Geng, Yanmin Kuang, Yunjie Yu, Yuan Liao, Yao Zhang, Yang Zhang, and Zhenchao Dong. Tunneling electron induced luminescence from porphyrin molecules on monolayer graphene. *Journal of Luminescence*, 157(0):39 – 45, 2015. ISSN 0022-2313. doi: http://dx.doi.org/10.1016/j.jlumin.2014.08.033. URL `http://www.sciencedirect.com/science/article/pii/S0022231314004694`. (Cited on pages 148, 193, 217, and 219.)

[32] Svenja Mühlenberend, Natalia L. Schneider, Markus Gruyters, and Richard Berndt. Plasmon-induced fluorescence and electroluminescence from porphine molecules on GaAs(110) in a scanning tunneling microscope. *Applied Physics Letters*, 101(20):203107, 2012. doi: http://dx.doi.org/10.1063/1.4767351. URL `http://scitation.aip.org/content/aip/journal/apl/101/20/10.1063/1.4767351`.

[33] Gaël Reecht, Fabrice Scheurer, Virginie Speisser, Yannick J. Dappe, Fabrice Mathevet, and Guillaume Schull. Electroluminescence of a Polythiophene Molecular Wire Suspended between a Metallic Surface and the Tip of a Scanning Tunneling Microscope. *Phys. Rev. Lett.*, 112:047403, Jan 2014. doi: 10.1103/PhysRevLett.112.047403. URL `http://link.aps.org/doi/10.1103/PhysRevLett.112.047403`. (Cited on page 194.)

[34] San-E Zhu, Yan-Min Kuang, Feng Geng, Jia-Zhe Zhu, Cong-Zhou Wang, Yun-Jie Yu, Yang Luo, Yang Xiao, Kai-Qing Liu, Qiu-Shi Meng, Li Zhang, Song Jiang, Yang Zhang, Guan-Wu Wang, Zhen-Chao Dong, and J. G. Hou. Self-Decoupled Porphyrin with a Tripodal Anchor for Molecular-Scale Electroluminescence. *Journal of the American Chemical Society*, 135(42):15794–15800, 2013. doi: 10.1021/ja4048569. URL `http://dx.doi.org/10.1021/ja4048569`. PMID: 24066644. (Cited on pages 10, 31, 169, 194, and 219.)

[35] W. Nolting. *Grundkurs Theoretische Physik 5/1 - Quantenmechanik Grundlagen*. Springer Verlag, 8 th edition, 2007. (Cited on page 10.)

[36] F. Schwabl. *Quantenmechanik*, volume 7. Auflage. Springer Verlag, 2007. (Cited on page 10.)

[37] Stefan Hüfner. *Photoelectron Spectroscopy: Principles and Applications*. Springer, 3rd edition edition, 2003. (Cited on page 11.)

[38] S. Lounis. Theory of Scanning Tunneling Microscopy. *ArXiv e-prints*, arXiv:1404.0961, Apr 2014. URL `http://arxiv.org/abs/1404.0961`. (Cited on pages 11, 18, and 20.)

[39] G. Binnig, H. Rohrer, Ch. Gerber, and E. Weibel. Tunneling through a controllable vacuum gap. *Applied Physics Letters*, 40(2):178–180, 1982. doi: http://dx.doi.org/10.1063/1.92999. URL `http://scitation.aip.org/content/aip/journal/apl/40/2/10.1063/1.92999`. (Cited on page 14.)

[40] Flemming Besenbacher. Scanning tunnelling microscopy studies of metal surfaces. *Reports on Progress in Physics*, 59(12):1737, 1996. URL `http://stacks.iop.org/0034-4885/59/i=12/a=004`. (Cited on pages 18 and 21.)

[41] J. Tersoff and D.R. Hamann. Theory of Application for the scanning tunneling microscope. *Phys. Rev. Lett.*, 50:1998, 1983. (Cited on page 18.)

[42] J. Tersoff and D. R. Hamann. Theory of the scanning tunneling microscope. *Phys. Rev. B*, 31:805–813, Jan 1985. doi: 10.1103/PhysRevB.31.805. URL `http://link.aps.org/doi/10.1103/PhysRevB.31.805`. (Cited on pages 18 and 19.)

[43] J. Bardeen. Tunnelling from a Many-Particle Point of View. *Phys. Rev. Lett.*, 6:57–59, Jan 1961. doi: 10.1103/PhysRevLett.6.57. URL `http://link.aps.org/doi/10.1103/PhysRevLett.6.57`. (Cited on page 18.)

[44] C. Julian Chen. Origin of atomic resolution on metal surfaces in scanning tunneling microscopy. *Phys. Rev. Lett.*, 65:448–451, Jul 1990. doi: 10.1103/PhysRevLett.65.448. URL `http://link.aps.org/doi/10.1103/PhysRevLett.65.448`. (Cited on page 20.)

[45] Ben Wortmann. PhD thesis, University of Duisburg-Essen, to be published. (Cited on page 20.)

[46] R.M. Feenstra, Joseph A. Stroscio, and A.P. Fein. Tunneling spectroscopy of the Si(111)2 x 1 surface. *Surface Science*, 181(1-2):295 – 306, 1987. ISSN 0039-6028. doi: http://dx.doi.org/10.1016/0039-6028(87)90170-1. URL `http://www.sciencedirect.com/science/article/pii/0039602887901701`. (Cited on pages 21, 22, and 205.)

[47] Klaus Kuhnke. private communication. 2015. (Cited on pages 24, 152, and 153.)

[48] R. C. Jaklevic and J. Lambe. Molecular Vibration Spectra by Electron Tunneling. *Phys. Rev. Lett.*, 17:1139–1140, Nov 1966. doi: 10.1103/PhysRevLett.17.1139. URL `http://link.aps.org/doi/10.1103/PhysRevLett.17.1139`. (Cited on page 27.)

[49] W H Weinberg. Inelastic Electron Tunneling Spectroscopy: A Probe of the Vibrational Structure of Surface Species. *Annual Review of Physical Chemistry*, 29(1): 115–139, 1978. doi: 10.1146/annurev.pc.29.100178.000555. URL `http://dx.doi.org/10.1146/annurev.pc.29.100178.000555`. (Cited on page 27.)

[50] B. C. Stipe, M. A. Rezaei, and W. Ho. Single-Molecule Vibrational Spectroscopy and Microscopy. *Science*, 280(5370):1732–1735, 1998. doi: 10.1126/science.280.5370.1732. URL `http://www.sciencemag.org/content/280/5370/1732.abstract`. (Cited on page 27.)

[51] Sebastian Loth, Christopher P Lutz, and Andreas J Heinrich. Spin-polarized spin excitation spectroscopy. *New Journal of Physics*, 12(12):125021, 2010. URL `http://stacks.iop.org/1367-2630/12/i=12/a=125021`. (Cited on page 27.)

[52] Chao Zhang, Liuguo Chen, Rui Zhang, and Zhenchao Dong. Scanning tunneling microscope based nanoscale optical imaging of molecules on surfaces. *Japanese Journal of Applied Physics*, 54(8S2):08LA01, 2015. URL `http://stacks.iop.org/1347-4065/54/i=8S2/a=08LA01`. (Cited on pages 27, 28, 34, and 40.)

[53] D.T. Pierce, A. Davies, J.A. Stroscio, and R.J. Celotta. Polarized light emission from the metal-metal STM junction. *Applied Physics A*, 66(1):S403–S406, 1998. ISSN 0947-8396. doi: 10.1007/s003390051172. URL `http://dx.doi.org/10.1007/s003390051172`. (Cited on page 28.)

[54] Christoph Grosse, Markus Etzkorn, Klaus Kuhnke, Sebastian Loth, and Klaus Kern. Quantitative mapping of fast voltage pulses in tunnel junctions by plasmonic luminescence. *Applied Physics Letters*, 103(18):183108, 2013. doi: http://dx.doi.org/10.1063/1.4827556. URL `http://scitation.aip.org/content/aip/journal/apl/103/18/10.1063/1.4827556`. (Cited on pages 28 and 244.)

[55] Peter Johansson, R. Monreal, and Peter Apell. Theory for light emission from a scanning tunneling microscope. *Phys. Rev. B*, 42:9210–9213, Nov 1990. doi: 10.1103/PhysRevB.42.9210. URL `http://link.aps.org/doi/10.1103/PhysRevB.42.9210`. (Cited on pages 30, 40, 105, 109, and 110.)

[56] Peter Johansson. Light emission from a scanning tunneling microscope: Fully retarded calculation. *Phys. Rev. B*, 58:10823–10834, Oct 1998. doi: 10.1103/PhysRevB.58.10823. URL `http://link.aps.org/doi/10.1103/PhysRevB.58.10823`. (Cited on pages 30, 40, 105, 107, 109, and 110.)

[57] D. L. Mills. Theory of STM-induced enhancement of dynamic dipole moments on crystal surfaces. *Phys. Rev. B*, 65:125419, Mar 2002. doi: 10.1103/PhysRevB.65.125419. URL `http://link.aps.org/doi/10.1103/PhysRevB.65.125419`. (Cited on pages 31, 40, 106, 146, and 194.)

[58] Feng Geng, Yang Zhang, Yunjie Yu, Yanmin Kuang, Yuan Liao, Zhenchao Dong, and Jianguo Hou. Modulation of nanocavity plasmonic emission by local molecular states of C_{60} on Au(111). *Opt. Express*, 20(24):26725–26735, Nov 2012. doi: 10.1364/OE.20.026725. URL `http://www.opticsexpress.org/abstract.cfm?URI=oe-20-24-26725`. (Cited on pages 31, 46, 143, 144, 146, 150, 151, 153, 154, 193, 208, 217, and 240.)

[59] Y. Zhang, F. Geng, H. Y. Gao, Y. Liao, Z. C. Dong, and J. G. Hou. Enhancement and suppression effect of molecules on nanocavity plasmon emissions excited by tunneling electrons. *Applied Physics Letters*, 97(24):243101, 2010. doi: http://dx.doi.org/10.1063/1.3525603. URL `http://scitation.aip.org/content/aip/journal/apl/97/24/10.1063/1.3525603`. (Cited on pages 31, 143, 146, 148, 169, 193, and 217.)

[60] Z.-C. Dong, X.-L. Guo, A. S. Trifonov, P. S. Dorozhkin, K. Miki, K. Kimura, S. Yokoyama, and S. Mashiko. Vibrationally Resolved Fluorescence from Organic Molecules near Metal Surfaces in a Scanning Tunneling Microscope. *Phys. Rev. Lett.*, 92:086801, Feb 2004. doi: 10.1103/PhysRevLett.92.086801. URL `http://link.aps.org/doi/10.1103/PhysRevLett.92.086801`. (Cited on page 31.)

[61] *SPCM-AQR Single Photon Counting Module*. Perkin Elmer, Inc., 2005. URL `http://sites.fas.harvard.edu/~phys191r/Bench_Notes/D4/SPCMAQR.pdf`. (Cited on pages 34, 68, and 81.)

[62] *Avalanche Dioden - Das ist die perfekte Lawine*. Laser Components. URL `http://www.lasercomponents.com/de/fileadmin/user_upload/home/Datasheets/lc/applikationsreport/avalanche-photodioden.pdf`. (Cited on pages 34 and 36.)

[63] *Avalanche Photodiode - A user guide*. Perkin Elmer, Inc., 2010. URL `http://www.perkinelmer.com/CMSResources/Images/44-6538APP_AvalanchePhotodiodesUsersGuide.pdf`. (Cited on page 36.)

[64] S. Cova, M. Ghioni, A. Lacaita, C. Samori, and F. Zappa. Avalanche photodiodes and quenching circuits for single-photon detection. *Appl. Opt.*, 35(12):1956–1976, Apr 1996. doi: 10.1364/AO.35.001956. URL `http://ao.osa.org/abstract.cfm?URI=ao-35-12-1956`. (Cited on page 36.)

[65] *Characteristics and use of Si APD (Avalanche Photodiode)*. Hamamatsu Photonics K.K., 2004. URL `http://neutron.physics.ucsb.edu/docs/Avalanche_photodiodes_info.pdf`. (Cited on page 36.)

[66] S. M. Sze and Kwok K. Ng. *Physics of Semiconductor Devices*, volume 3rd Edition. Wiley-Interscience, 2007. (Cited on pages 36, 37, and 38.)

[67] Marius Grundmann. *The Physics of Semiconductors*. Springer, 2006. (Cited on page 36.)

[68] Inc. Spectral Instruments. What is a CCD? accessed online, June 3 2015, 2001-2013. URL `http://www.specinst.com/What_Is_A_CCD.html`. (Cited on page 37.)

[69] accessed online, June 2 2015, . URL `http://images-of-elements.com/silver.php`. (Cited on page 39.)

[70] accessed online, September 30 2015, . URL `https://upload.wikimedia.org/wikipedia/commons/d/d8/Münze_Siliqua_Vandalenkönig_Geiserich.jpg`. (Cited on page 39.)

[71] Jose Ruben Morones-Ramirez, Jonathan A. Winkler, Catherine S. Spina, and James J. Collins. Silver Enhances Antibiotic Activity Against Gram-Negative Bacteria. *Science Translational Medicine*, 5(190):190ra81, 2013. doi: 10.1126/scitranslmed.3006276. URL `http://stm.sciencemag.org/content/5/190/190ra81.abstract`. (Cited on page 39.)

[72] Charles E. Mortimer and Ulrich Müller. *Chemie*, volume 6. Auflage. Georg Thieme Verlag, 2006. (Cited on page 39.)

[73] Andrea Resta, Thomas Leoni, Clemens Barth, Alain Ranguis, Conrad Becker, Thomas Bruhn, Patrick Vogt, and Guy Le Lay. Atomic Structures of Silicene Layers Grown on Ag(111): Scanning Tunneling Microscopy and Noncontact Atomic Force Microscopy Observations. *Sci. Rep.*, 3:–, August 2013. URL `http://dx.doi.org/10.1038/srep02399`. (Cited on pages 39 and 139.)

[74] T. C. Hsieh, T. Miller, and T. C. Chiang. Probing the Wave Function of a Surface State in Ag(111): A New Approach. *Phys. Rev. Lett.*, 55:2483–2486, Nov 1985. doi: 10.1103/PhysRevLett.55.2483. URL `http://link.aps.org/doi/10.1103/PhysRevLett.55.2483`. (Cited on page 39.)

[75] R. Paniago, R. Matzdorf, G. Meister, and A. Goldmann. Temperature dependence of Shockley-type surface energy bands on Cu(111), Ag(111) and Au(111). *Surface Science*, 336(1–2):113–122, 1995. ISSN 0039-6028. doi: http://dx.doi.org/10.1016/0039-6028(95)00509-9. URL `http://www.sciencedirect.com/science/article/pii/0039602895005099`.

[76] G. Nicolay, F. Reinert, S. Schmidt, D. Ehm, P. Steiner, and S. Hüfner. Natural linewidth of the Ag(111) $\boldsymbol{L}$ -gap surface state as determined by photoemission spectroscopy. *Phys. Rev. B*, 62:1631–1634, Jul 2000. doi: 10.1103/PhysRevB.62.1631. URL `http://link.aps.org/doi/10.1103/PhysRevB.62.1631`. (Cited on page 39.)

[77] G. Nicolay, F. Reinert, S. Hüfner, and P. Blaha. Spin-orbit splitting of the L -gap surface state on Au(111) and Ag(111). *Phys. Rev. B*, 65:033407, Dec 2001. doi: 10.1103/PhysRevB.65.033407. URL `http://link.aps.org/doi/10.1103/PhysRevB.65.033407`.

[78] F. Reinert, G. Nicolay, S. Schmidt, D. Ehm, and S. Hüfner. Direct measurements of the L -gap surface states on the (111) face of noble metals by photoelectron spectroscopy. *Phys. Rev. B*, 63:115415, Mar 2001. doi: 10.1103/PhysRevB.63.115415. URL `http://link.aps.org/doi/10.1103/PhysRevB.63.115415`. (Cited on page 39.)

[79] Jiutao Li, Wolf-Dieter Schneider, and Richard Berndt. Local density of states from spectroscopic scanning-tunneling-microscope images: Ag(111). *Phys. Rev. B*, 56:7656–7659, Sep 1997. doi: 10.1103/PhysRevB.56.7656. URL `http://link.aps.org/doi/10.1103/PhysRevB.56.7656`. (Cited on page 39.)

[80] L. Limot, T. Maroutian, P. Johansson, and R. Berndt. Surface-State Stark Shift in a Scanning Tunneling Microscope. *Phys. Rev. Lett.*, 91:196801, Nov 2003.

doi: 10.1103/PhysRevLett.91.196801. URL `http://link.aps.org/doi/10.1103/PhysRevLett.91.196801`.

[81] Karina Morgenstern, Kai-Felix Braun, and Karl-Heinz Rieder. Surface-State Depopulation on Small Ag(111) Terraces. *Phys. Rev. Lett.*, 89:226801, Nov 2002. doi: 10.1103/PhysRevLett.89.226801. URL `http://link.aps.org/doi/10.1103/PhysRevLett.89.226801`. (Cited on page 39.)

[82] W. Auwärter, A. Weber-Bargioni, A. Riemann, A. Schiffrin, O. Gröning, R. Fasel, and J. V. Barth. Self-assembly and conformation of tetrapyridyl-porphyrin molecules on Ag(111). *The Journal of Chemical Physics*, 124(19):194708, 2006. doi: http://dx.doi.org/10.1063/1.2194541. URL `http://scitation.aip.org/content/aip/journal/jcp/124/19/10.1063/1.2194541`. (Cited on page 40.)

[83] Dirk Kühne, Florian Klappenberger, Régis Decker, Uta Schlickum, Harald Brune, Svetlana Klyatskaya, Mario Ruben, and Johannes V. Barth. Self-Assembly of Nanoporous Chiral Networks with Varying Symmetry from Sexiphenyl-dicarbonitrile on Ag(111). *The Journal of Physical Chemistry C*, 113(41):17851–17859, 2009. doi: 10.1021/jp9041217. URL `http://dx.doi.org/10.1021/jp9041217`.

[84] Yongfeng Wang, Jörg Kröger, Richard Berndt, and Werner Hofer. Structural and Electronic Properties of Ultrathin Tin-Phthalocyanine Films on Ag(111) at the Single-Molecule Level. *Angewandte Chemie International Edition*, 48(7):1261–1265, 2009. ISSN 1521-3773. doi: 10.1002/anie.200803305. URL `http://dx.doi.org/10.1002/anie.200803305`. (Cited on page 40.)

[85] Anna Llanes-Pallas, Manfred Matena, Thomas Jung, Maurizio Prato, Meike Stöhr, and Davide Bonifazi. Trimodular Engineering of Linear Supramolecular Miniatures on Ag(111) Surfaces Controlled by Complementary Triple Hydrogen Bonds. *Angewandte Chemie International Edition*, 47(40):7726–7730, 2008. ISSN 1521-3773. doi: 10.1002/anie.200802325. URL `http://dx.doi.org/10.1002/anie.200802325`.

[86] Donna A. Kunkel, James Hooper, Scott Simpson, Daniel P. Miller, Lucie Routaboul, Pierre Braunstein, Bernard Doudin, Sumit Beniwal, Peter Dowben, Ralph Skomski, Eva Zurek, and Axel Enders. Self-assembly of strongly dipolar molecules on metal surfaces. *The Journal of Chemical Physics*, 142(10):101921, 2015. doi: http://dx.doi.org/10.1063/1.4907943. URL `http://scitation.aip.org/content/aip/journal/jcp/142/10/10.1063/1.4907943`. (Cited on page 40.)

[87] Felix Schwarz, Yongfeng Wang, Werner A. Hofer, R. Berndt, Erich Runge, and Jörg Kröger. Electronic and Vibrational States of Single Tin-Phthalocyanine Molecules in Double Layers on Ag(111). *The Journal of Physical Chemistry C*, 119(27):15716–15722, 2015. doi: 10.1021/acs.jpcc.5b03392. URL `http://dx.doi.org/10.1021/acs.jpcc.5b03392`. (Cited on page 40.)

[88] E. Goiri, M. Matena, A. El-Sayed, J. Lobo-Checa, P. Borghetti, C. Rogero, B. Detlefs, J. Duvernay, J. E. Ortega, and D. G. de Oteyza. Self-Assembly of Bicomponent Molecular Monolayers: Adsorption Height Changes and Their Consequences. *Phys. Rev. Lett.*, 112:117602, Mar 2014. doi: 10.1103/PhysRevLett.

112.117602. URL http://link.aps.org/doi/10.1103/PhysRevLett.112.117602. (Cited on page 40.)

[89] C. Zhang, B. Gao, L. G. Chen, Q. S. Meng, H. Yang, R. Zhang, X. Tao, H. Y. Gao, Y. Liao, and Z. C. Dong. Fabrication of silver tips for scanning tunneling microscope induced luminescence. *Review of Scientific Instruments*, 82(8):083101, 2011. doi: http://dx.doi.org/10.1063/1.3617456. URL http://scitation.aip.org/content/aip/journal/rsi/82/8/10.1063/1.3617456. (Cited on page 40.)

[90] R. Berndt, J. K. Gimzewski, and P. Johansson. Electromagnetic interactions of metallic objects in nanometer proximity. *Phys. Rev. Lett.*, 71:3493–3496, Nov 1993. doi: 10.1103/PhysRevLett.71.3493. URL http://link.aps.org/doi/10.1103/PhysRevLett.71.3493. (Cited on pages 40, 77, and 105.)

[91] Richard Berndt, James K. Gimzewski, and Peter Johansson. Inelastic tunneling excitation of tip-induced plasmon modes on noble-metal surfaces. *Phys. Rev. Lett.*, 67:3796–3799, Dec 1991. doi: 10.1103/PhysRevLett.67.3796. URL http://link.aps.org/doi/10.1103/PhysRevLett.67.3796. (Cited on pages 103 and 116.)

[92] Richard Berndt and James K. Gimzewski. Photon emission in scanning tunneling microscopy: Interpretation of photon maps of metallic systems. *Phys. Rev. B*, 48: 4746–4754, Aug 1993. doi: 10.1103/PhysRevB.48.4746. URL http://link.aps.org/doi/10.1103/PhysRevB.48.4746. (Cited on pages 40, 103, 116, and 121.)

[93] J. Aizpurua, G. Hoffmann, S. P. Apell, and R. Berndt. Electromagnetic Coupling on an Atomic Scale. *Phys. Rev. Lett.*, 89:156803, Sep 2002. doi: 10.1103/PhysRevLett.89.156803. URL http://link.aps.org/doi/10.1103/PhysRevLett.89.156803. (Cited on pages 40, 105, 110, 128, and 129.)

[94] Daisuke Ino, Taro Yamada, and Maki Kawai. Luminescence from 3,4,9,10-perylenetetracarboxylic dianhydride on Ag(111) surface excited by tunneling electrons in scanning tunneling microscopy. *The Journal of Chemical Physics*, 129(1):014701, 2008. doi: http://dx.doi.org/10.1063/1.2949549. URL http://scitation.aip.org/content/aip/journal/jcp/129/1/10.1063/1.2949549. (Cited on pages 40, 48, 143, 146, and 193.)

[95] Pierre de Marcillac, Noel Coron, Gerard Dambier, Jacques Leblanc, and Jean-Pierre Moalic. Experimental detection of α-particles from the radioactive decay of natural bismuth. *Nature*, 422(6934):876–878, April 2003. ISSN 0028-0836. URL http://dx.doi.org/10.1038/nature01541. (Cited on page 41.)

[96] Ph. Hofmann. The surfaces of bismuth: Structural and electronic properties. *Progress in Surface Science*, 81(5):191 – 245, 2006. ISSN 0079-6816. doi: http://dx.doi.org/10.1016/j.progsurf.2006.03.001. URL http://www.sciencedirect.com/science/article/pii/S0079681606000232. (Cited on page 41.)

[97] Y. Hasegawa, Y. Ishikawa, T. Saso, H. Shirai, H. Morita, T. Komine, and H. Nakamura. A method for analysis of carrier density and mobility in polycrystalline bismuth. *Physica B: Condensed Matter*, 382(1-2):140 – 146, 2006. ISSN 0921-4526. doi: http://dx.doi.org/10.1016/j.physb.2006.02.011. URL http://

www.sciencedirect.com/science/article/pii/S0921452606006363. (Cited on page 41.)

[98] Wyatt915. accessed online, June 2 2015, 2008. URL http://commons.wikimedia.org/wiki/File:Bismuth.jpg. (Cited on page 41.)

[99] S Agergaard, Ch Søndergaard, H Li, M B Nielsen, S V Hoffmann, Z Li, and Ph Hofmann. The effect of reduced dimensionality on a semimetal: the electronic structure of the Bi(110) surface. *New Journal of Physics*, 3(1):15, 2001. URL http://stacks.iop.org/1367-2630/3/i=1/a=315. (Cited on pages 41 and 163.)

[100] M. Hengsberger, P. Segovia, M. Garnier, D. Purdie, and Y. Baer. Photoemission study of the carrier bands in Bi(111). *The European Physical Journal B - Condensed Matter and Complex Systems*, 17(4):603–608, 2000. ISSN 1434-6028. doi: 10.1007/s100510070097. URL http://dx.doi.org/10.1007/s100510070097.

[101] Christian R. Ast and Hartmut Höchst. Fermi Surface of Bi(111) Measured by Photoemission Spectroscopy. *Phys. Rev. Lett.*, 87:177602, Oct 2001. doi: 10.1103/PhysRevLett.87.177602. URL http://link.aps.org/doi/10.1103/PhysRevLett.87.177602. (Cited on pages 41 and 163.)

[102] Yu. M. Koroteev, G. Bihlmayer, J. E. Gayone, E. V. Chulkov, S. Blügel, P. M. Echenique, and Ph. Hofmann. Strong Spin-Orbit Splitting on Bi Surfaces. *Phys. Rev. Lett.*, 93:046403, Jul 2004. doi: 10.1103/PhysRevLett.93.046403. URL http://link.aps.org/doi/10.1103/PhysRevLett.93.046403. (Cited on pages 41, 163, 164, and 249.)

[103] D. Lükermann, S. Sologub, H. Pfnür, and C. Tegenkamp. Sensing surface states of Bi films by magnetotransport. *Phys. Rev. B*, 83:245425, Jun 2011. doi: 10.1103/PhysRevB.83.245425. URL http://link.aps.org/doi/10.1103/PhysRevB.83.245425. (Cited on page 41.)

[104] D. Lükermann, S. Sologub, H. Pfnür, C. Klein, M. Horn-von Hoegen, and C. Tegenkamp. Scattering at magnetic and nonmagnetic impurities on surfaces with strong spin-orbit coupling. *Phys. Rev. B*, 86:195432, Nov 2012. doi: 10.1103/PhysRevB.86.195432. URL http://link.aps.org/doi/10.1103/PhysRevB.86.195432. (Cited on page 41.)

[105] G. Jnawali, Th. Wagner, H. Hattab, R. Möller, A. Lorke, and M. Horn von Hoegen. Two-Dimensional Electron Transport and Scattering in Bi(111) Surface States. *e-Journal of Surface Science and Nanotechnology*, 8:27–31, 2010. doi: 10.1380/ejssnt.2010.27. (Cited on page 41.)

[106] G. Jnawali, C. Klein, Th. Wagner, H. Hattab, P. Zahl, D. P. Acharya, P. Sutter, A. Lorke, and M. Horn-von Hoegen. Manipulation of Electronic Transport in the Bi(111) Surface State. *Phys. Rev. Lett.*, 108:266804, Jun 2012. doi: 10.1103/PhysRevLett.108.266804. URL http://link.aps.org/doi/10.1103/PhysRevLett.108.266804. (Cited on page 41.)

[107] J. I. Pascual, G. Bihlmayer, Yu. M. Koroteev, H.-P. Rust, G. Ceballos, M. Hansmann, K. Horn, E. V. Chulkov, S. Blügel, P. M. Echenique, and Ph. Hofmann.

Role of Spin in Quasiparticle Interference. *Phys. Rev. Lett.*, 93:196802, Nov 2004. doi: 10.1103/PhysRevLett.93.196802. URL `http://link.aps.org/doi/10.1103/PhysRevLett.93.196802`. (Cited on page 41.)

[108] M. C. Cottin, C. A. Bobisch, J. Schaffert, G. Jnawali, A. Sonntag, G. Bihlmayer, and R. Möller. Anisotropic scattering of surface state electrons at a point defect on Bi(111). *Applied Physics Letters*, 98(2):022108, 2011. doi: http://dx.doi.org/10.1063/1.3536528. URL `http://scitation.aip.org/content/aip/journal/apl/98/2/10.1063/1.3536528`. (Cited on pages 42, 163, and xvii.)

[109] Maren C. Cottin, Christian A. Bobisch, Johannes Schaffert, Giriraj Jnawali, Gustav Bihlmayer, and Rolf Möller. Interplay between Forward and Backward Scattering of Spin-Orbit Split Surface States of Bi(111). *Nano Letters*, 13(6):2717–2722, 2013. doi: 10.1021/nl400878r. URL `http://dx.doi.org/10.1021/nl400878r`. PMID: 23672457. (Cited on pages 41, 42, 163, and xvii.)

[110] M. Z. Hasan and C. L. Kane. *Colloquium* : Topological insulators. *Rev. Mod. Phys.*, 82:3045–3067, Nov 2010. doi: 10.1103/RevModPhys.82.3045. URL `http://link.aps.org/doi/10.1103/RevModPhys.82.3045`. (Cited on page 42.)

[111] Fang Yang, Lin Miao, Z. F. Wang, Meng-Yu Yao, Fengfeng Zhu, Y. R. Song, Mei-Xiao Wang, Jin-Peng Xu, Alexei V. Fedorov, Z. Sun, G. B. Zhang, Canhua Liu, Feng Liu, Dong Qian, C. L. Gao, and Jin-Feng Jia. Spatial and Energy Distribution of Topological Edge States in Single Bi(111) Bilayer. *Phys. Rev. Lett.*, 109:016801, Jul 2012. doi: 10.1103/PhysRevLett.109.016801. URL `http://link.aps.org/doi/10.1103/PhysRevLett.109.016801`. (Cited on page 42.)

[112] Ilya K. Drozdov, A. Alexandradinata, Sangjun Jeon, Stevan Nadj-Perge, Huiwen Ji, R. J. Cava, B. Andrei Bernevig, and Ali Yazdani. One-dimensional topological edge states of bismuth bilayers. *Nat Phys*, 10(9):664–669, September 2014. ISSN 1745-2473. URL `http://dx.doi.org/10.1038/nphys3048`. (Cited on page 42.)

[113] Christian Alexander Bobisch. Tunneling spectroscopy of elastic and inelastic processes at surfaces. Habilitation, 2015. (Cited on page 42.)

[114] Christian R. Ast, Jürgen Henk, Arthur Ernst, Luca Moreschini, Mihaela C. Falub, Daniela Pacilé, Patrick Bruno, Klaus Kern, and Marco Grioni. Giant Spin Splitting through Surface Alloying. *Phys. Rev. Lett.*, 98:186807, May 2007. doi: 10.1103/PhysRevLett.98.186807. URL `http://link.aps.org/doi/10.1103/PhysRevLett.98.186807`. (Cited on pages 42, 43, 159, 164, 165, 243, and 249.)

[115] H. Bentmann, F. Forster, G. Bihlmayer, E. V. Chulkov, L. Moreschini, M. Grioni, and F. Reinert. Origin and manipulation of the Rashba splitting in surface alloys. *EPL (Europhysics Letters)*, 87(3):37003, 2009. URL `http://stacks.iop.org/0295-5075/87/i=3/a=37003`. (Cited on pages 243 and 249.)

[116] Hendrik Bentmann, Takuya Kuzumaki, Gustav Bihlmayer, Stefan Blügel, Eugene V. Chulkov, Friedrich Reinert, and Kazuyuki Sakamoto. Spin orientation and sign of the Rashba splitting in Bi/Cu(111). *Phys. Rev. B*, 84:115426, Sep 2011. doi: 10.1103/PhysRevB.84.115426. URL `http://link.aps.org/doi/10.1103/PhysRevB.84.115426`. (Cited on pages 42, 159, 164, 235, and 258.)

[117] L. Moreschini, A. Bendounan, H. Bentmann, M. Assig, K. Kern, F. Reinert, J. Henk, C. R. Ast, and M. Grioni. Influence of the substrate on the spin-orbit splitting in surface alloys on (111) noble-metal surfaces. *Phys. Rev. B*, 80:035438, Jul 2009. doi: 10.1103/PhysRevB.80.035438. URL `http://link.aps.org/doi/10.1103/PhysRevB.80.035438`. (Cited on pages 43, 159, 164, 243, and 249.)

[118] Maren C Cottin, Jorge Lobo-Checa, Johannes Schaffert, Christian A Bobisch, Rolf Möller, J Enrique Ortega, and Andrew L Walter. A chemically inert Rashba split interface electronic structure of C_{60} ,FeOEP and PTCDA on$BiAg_2$/Ag(111) substrates. *New Journal of Physics*, 16(4):045002, 2014. URL `http://stacks.iop.org/1367-2630/16/i=4/a=045002`. (Cited on pages 43, 169, 240, 243, 249, 251, 253, 255, 256, 258, and 259.)

[119] S. Mathias, A. Ruffing, F. Deicke, M. Wiesenmayer, I. Sakar, G. Bihlmayer, E. V. Chulkov, Yu. M. Koroteev, P. M. Echenique, M. Bauer, and M. Aeschlimann. Quantum-Well-Induced Giant Spin-Orbit Splitting. *Phys. Rev. Lett.*, 104:066802, Feb 2010. doi: 10.1103/PhysRevLett.104.066802. URL `http://link.aps.org/doi/10.1103/PhysRevLett.104.066802`. (Cited on pages 44, 159, 163, 164, 165, 243, and 249.)

[120] S. Jakobs, A. Ruffing, D. Jungkenn, M. Cinchetti, S. Mathias, and M. Aeschlimann. Spin structure of Rashba-split electronic states of Bi overlayers on Cu(111). *Journal of Electron Spectroscopy and Related Phenomena*, in press:–, 2014. ISSN 0368-2048. doi: http://dx.doi.org/10.1016/j.elspec.2014.09.003. URL `http://www.sciencedirect.com/science/article/pii/S036820481400187X`. (Cited on pages 44, 163, and 164.)

[121] Hong Liang Zhang, Wei Chen, Xue Sen Wang, Junji Yuhara, and Andrew Thye Shen Wee. Growth of well-aligned Bi nanowire on Ag(111) . *Applied Surface Science*, 256(2):460 – 464, 2009. ISSN 0169-4332. doi: http://dx.doi.org/10.1016/j.apsusc.2009.07.016. URL `http://www.sciencedirect.com/science/article/pii/S0169433209010101`. Physics at Surfaces and Interface (Proceedings of 2nd International Conference on Physics at Surfaces and Interfaces, PSI2009, February 23 - 27, 2009, Puri, India). (Cited on pages 44, 221, 223, and 235.)

[122] Amin Bannani. *Ladungstransport in dünnen metallischen Filmen*. PhD thesis, University of Duisburg-Essen, 2007. (Cited on page 45.)

[123] Andrei V. Yeremenko Eric C. Faulques, Dale L. Perry, editor. *Spectroscopy of Emerging Materials*. Springer Science, 2005. (Cited on page 45.)

[124] W. Kratschmer, Lowell D. Lamb, K. Fostiropoulos, and Donald R. Huffman. Solid C_{60}: a new form of carbon. *Nature*, 347(6291):354–358, September 1990. URL `http://dx.doi.org/10.1038/347354a0`. (Cited on page 45.)

[125] Han Huang, Wei Chen, Shi Chen, Dong Chen Qi, Xing Yu Gao, and Andrew Thye Shen Wee. Molecular orientation of CuPc thin films on C_{60}/Ag(111). *Applied Physics Letters*, 94(16):163304, 2009. doi: http://dx.doi.org/10.1063/1.3122940. URL `http://scitation.aip.org/content/aip/journal/apl/94/16/10.1063/1.3122940`. (Cited on pages 45, 46, and 139.)

[126] Takeo Oku, Nariaki Kakuta, Atsushi Kawashima, Katsunori Nomura, Ryosuke Motoyoshi, Atsushi Suzuki, Kenji Kikuchi, and Gentaro Kinoshita. Formation and Characterization of Bulk Hetero-Junction Solar Cells Using C_{60} and Perylene. *MATERIALS TRANSACTIONS*, 49(11):2457–2460, 2008. doi: 10.2320/matertrans.MB200807. (Cited on pages 45 and 49.)

[127] Jun Yeob Lee and Jang Hyuk Kwon. The effect of C_{60} doping on the device performance of organic light-emitting diodes. *Applied Physics Letters*, 86(6):063514, 2005. doi: http://dx.doi.org/10.1063/1.1861962. URL `http://scitation.aip.org/content/aip/journal/apl/86/6/10.1063/1.1861962`. (Cited on page 45.)

[128] J. K. Gimzewski, S. Modesti, T. David, and R. R. Schlittler. Scanning tunneling microscopy of ordered C_{60} and C_{70} layers on Au(111), Cu(111), Ag(110), and Au(110) surfaces. *Journal of Vacuum Science & Technology B*, 12(3):1942–1946, 1994. doi: http://dx.doi.org/10.1116/1.587676. URL `http://scitation.aip.org/content/avs/journal/jvstb/12/3/10.1116/1.587676`. (Cited on page 45.)

[129] Eric I. Altman and Richard J. Colton. The interaction of C_{60} with noble metal surfaces. *Surface Science*, 295:13 – 33, 1993. ISSN 0039-6028. doi: http://dx.doi.org/10.1016/0039-6028(93)90181-I. URL `http://www.sciencedirect.com/science/article/pii/003960289390181I`. (Cited on pages 45, 49, and 142.)

[130] C. Silien, N. A. Pradhan, W. Ho, and P. A. Thiry. Influence of adsorbate-substrate interaction on the local electronic structure of C_{60} studied by low-temperature STM. *Phys. Rev. B*, 69:115434, Mar 2004. doi: 10.1103/PhysRevB.69.115434. URL `http://link.aps.org/doi/10.1103/PhysRevB.69.115434`.

[131] Tomihiro Hashizume, K. Motai, X. D. Wang, H. Shinohara, Y. Saito, Y. Maruyama, K. Ohno, Y. Kawazoe, Y. Nishina, H. W. Pickering, Y. Kuk, and T. Sakurai. Intramolecular structures of C_{60} molecules adsorbed on the Cu(111)-(1×1) surface. *Phys. Rev. Lett.*, 71:2959–2962, Nov 1993. doi: 10.1103/PhysRevLett.71.2959. URL `http://link.aps.org/doi/10.1103/PhysRevLett.71.2959`.

[132] Amin Bannani, Christian Bobisch, and Rolf Möller. Ballistic Electron Microscopy of Individual Molecules. *Science*, 315(5820):1824–1828, 2007. doi: 10.1126/science.1138668. URL `http://www.sciencemag.org/content/315/5820/1824.abstract`. (Cited on pages 47, 146, 156, 157, and 244.)

[133] G Schull, N Néel, M Becker, J Kröger, and R Berndt. Spatially resolved conductance of oriented C_{60}. *New Journal of Physics*, 10(6):065012, 2008. URL `http://stacks.iop.org/1367-2630/10/i=6/a=065012`. (Cited on pages 45, 153, and 154.)

[134] M. T. Cuberes, R. R. Schlittler, and J. K. Gimzewski. Roomtemperature repositioning of individual C_{60} molecules at Cu steps: Operation of a molecular counting device. *Applied Physics Letters*, 69(20):3016–3018, 1996. doi: http://dx.doi.org/10.1063/1.116824. URL `http://scitation.aip.org/content/aip/journal/apl/69/20/10.1063/1.116824`. (Cited on page 45.)

[135] Gary B. Adams, Michael O'Keeffe, and Rodney S. Ruoff. Van Der Waals Surface Areas and Volumes of Fullerenes. *The Journal of Physical Chemistry*, 98(38): 9465–9469, 1994. doi: 10.1021/j100089a018. URL `http://dx.doi.org/10.1021/j100089a018`. (Cited on page 45.)

[136] A. F. Hebard, M. J. Rosseinsky, R. C. Haddon, D. W. Murphy, S. H. Glarum, T. T. M. Palstra, A. P. Ramirez, and A. R. Kortan. Superconductivity at 18 K in potassium-doped C_{60}. *Nature*, 350(6319):600–601, April 1991. URL `http://dx.doi.org/10.1038/350600a0`. (Cited on page 45.)

[137] M. Stöhr, T. Wagner, M. Gabriel, B. Weyers, and R. Möller. Binary Molecular Layers of C_{60} and Copper Phthalocyanine on Au(111): Self-Organized Nanostructuring. *Advanced Functional Materials*, 11(3):175–178, 2001. ISSN 1616-3028. doi: 10.1002/1616-3028(200106)11:3<175::AID-ADFM175>3.0.CO;2-L. URL `http://dx.doi.org/10.1002/1616-3028(200106)11:3<175::AID-ADFM175>3.0.CO;2-L`. (Cited on pages 46 and 138.)

[138] Meike Stöhr, Thorsten Wagner, Markus Gabriel, Bastian Weyers, and Rolf Möller. Binary Molecular Layers of C_{60} and Copper Phthalocyanine on Au (111): Self-Organized Nanostructuring. *Advanced Functional Materials*, 11(3):175–178, 2001. (Cited on page 46.)

[139] M. Stöhr, Th. Wagner, M. Gabriel, B. Weyers, and R. Möller. Direct observation of hindered eccentric rotation of an individual molecule: Cu-phthalocyanine on C60. *Phys. Rev. B*, 65:033404, Dec 2001. doi: 10.1103/PhysRevB.65.033404. URL `http://link.aps.org/doi/10.1103/PhysRevB.65.033404`. (Cited on page 46.)

[140] R. Berndt, R. Gaisch, J. K. Gimzewski, B. Reihl, R. R. Schlittler, W. D. Schneider, and M. Tschudy. Photon Emission at Molecular Resolution Induced by a Scanning Tunneling Microscope. *Science*, 262(5138):1425–1427, 1993. doi: 10.1126/science.262.5138.1425. URL `http://www.sciencemag.org/content/262/5138/1425.abstract`. (Cited on pages 46, 143, 144, 146, 150, 193, 217, and 240.)

[141] N. L. Schneider, J. T. Lü, M. Brandbyge, and R. Berndt. Light Emission Probing Quantum Shot Noise and Charge Fluctuations at a Biased Molecular Junction. *Phys. Rev. Lett.*, 109:186601, Oct 2012. doi: 10.1103/PhysRevLett.109.186601. URL `http://link.aps.org/doi/10.1103/PhysRevLett.109.186601`. (Cited on page 46.)

[142] O. D. Gordan, S. Hermann, M. Friedrich, and D. R. T. Zahn. Optical Properties of 3,4,9,10-perylenetetracarboxylic dianhydride/copper phthalocyanine superlattices. *Journal of Applied Physics*, 97(6):063518, 2005. doi: http://dx.doi.org/10.1063/1.1861967. URL `http://scitation.aip.org/content/aip/journal/jap/97/6/10.1063/1.1861967`. (Cited on page 47.)

[143] Chengliang Wang, Huanli Dong, Wenping Hu, Yunqi Liu, and Daoben Zhu. Semiconducting π-Conjugated Systems in Field-Effect Transistors: A Material Odyssey of Organic Electronics. *Chemical Reviews*, 112(4):2208–2267, 2012. doi: 10.1021/cr100380z. URL `http://dx.doi.org/10.1021/cr100380z`. PMID: 22111507. (Cited on pages 47 and 49.)

[144] L. Chkoda, C. Heske, M. Sokolowski, and E. Umbach. Improved band alignment for hole injection by an interfacial layer in organic light emitting devices. *Applied Physics Letters*, 77(8):1093–1095, 2000. doi: http://dx.doi.org/10.1063/1.1289804. URL http://scitation.aip.org/content/aip/journal/apl/77/8/10.1063/1.1289804. (Cited on page 47.)

[145] Peter Peumans, Aharon Yakimov, and Stephen R. Forrest. Small molecular weight organic thin-film photodetectors and solar cells. *Journal of Applied Physics*, 93(7):3693–3723, 2003. doi: http://dx.doi.org/10.1063/1.1534621. URL http://scitation.aip.org/content/aip/journal/jap/93/7/10.1063/1.1534621. (Cited on pages 47 and 49.)

[146] Th Wagner, A Bannani, C Bobisch, H Karacuban, and R Möller. The initial growth of PTCDA on Cu(111) studied by STM. *Journal of Physics: Condensed Matter*, 19(5):056009, 2007. URL http://stacks.iop.org/0953-8984/19/i=5/a=056009. (Cited on page 47.)

[147] H Karacuban, S Koch, M Fendrich, Th Wagner, and R Möller. PTCDA on Cu(111) partially covered with NaCl. *Nanotechnology*, 22(29):295305, 2011. URL http://stacks.iop.org/0957-4484/22/i=29/a=295305.

[148] S. Mannsfeld, M. Toerker, T. Schmitz-Hübsch, F. Sellam, T. Fritz, and K. Leo. Combined {LEED} and {STM} study of {PTCDA} growth on reconstructed Au(111) and Au(100) single crystals. *Organic Electronics*, 2(3-4):121 – 134, 2001. ISSN 1566-1199. doi: http://dx.doi.org/10.1016/S1566-1199(01)00018-0. URL http://www.sciencedirect.com/science/article/pii/S1566119901000180. (Cited on page 47.)

[149] S R Forrest. Organic - inorganic semiconductor devices and 3, 4, 9, 10 perylenetetracarboxylic dianhydride: an early history of organic electronics. *Journal of Physics: Condensed Matter*, 15(38):S2599, 2003. URL http://stacks.iop.org/0953-8984/15/i=38/a=001. (Cited on page 47.)

[150] F.S. Tautz. Structure and bonding of large aromatic molecules on noble metal surfaces: The example of PTCDA. *Progress in Surface Science*, 82(9-12):479–520, 2007. URL http://www.sciencedirect.com/science/article/B6TJF-4R6C61V-1/2/ffc7a73734cf1f43fd348d62d946c7fc. (Cited on pages 47, 135, 171, and 256.)

[151] L. Kilian, A. Hauschild, R. Temirov, S. Soubatch, A. Schöll, A. Bendounan, F. Reinert, T.-L. Lee, F. S. Tautz, M. Sokolowski, and E. Umbach. Role of Intermolecular Interactions on the Electronic and Geometric Structure of a Large π-Conjugated Molecule Adsorbed on a Metal Surface. *Phys. Rev. Lett.*, 100:136103, Apr 2008. doi: 10.1103/PhysRevLett.100.136103. URL http://link.aps.org/doi/10.1103/PhysRevLett.100.136103. (Cited on page 47.)

[152] R. Schlaf, B. A. Parkinson, P. A. Lee, K. W. Nebesny, and N. R. Armstrong. HOMO/LUMO Alignment at PTCDA/ZnPc and PTCDA/ClInPc Heterointerfaces Determined by Combined UPS and XPS Measurements. *The Journal of Physical Chemistry B*, 103(15):2984–2992, 1999. doi: 10.1021/jp982834y. URL http://pubs.acs.org/doi/abs/10.1021/jp982834y. (Cited on page 47.)

[153] C. Bobisch, Th. Wagner, A. Bannani, and R. Möller. Ordered binary monolayer composed of two organic molecules: Copper-phthalocyanine and 3,4,9,10-perylene-tetra-carboxylic-dianhydride on Cu(111). *The Journal of Chemical Physics*, 119(18):9804–9808, 2003. doi: http://dx.doi.org/10.1063/1.1615492. URL `http://scitation.aip.org/content/aip/journal/jcp/119/18/10.1063/1.1615492`. (Cited on pages 47, 49, and 243.)

[154] M.C. Cottin, J. Schaffert, A. Sonntag, H. Karacuban, R. Möller, and C.A. Bobisch. Supramolecular architecture of organic molecules: PTCDA and CuPc on a Cu(111) substrate. *Applied Surface Science*, 258(6):2196 – 2200, 2012. ISSN 0169-4332. doi: http://dx.doi.org/10.1016/j.apsusc.2011.02.038. URL `http://www.sciencedirect.com/science/article/pii/S0169433211002297`. International Vacuum Congress (IVC-18). (Cited on pages 47, 243, and xvii.)

[155] Benjamin Stadtmüller, Tomoki Sueyoshi, Georgy Kichin, Ingo Kröger, Sergey Soubatch, Ruslan Temirov, F. Stefan Tautz, and Christian Kumpf. Commensurate Registry and Chemisorption at a Hetero-organic Interface. *Phys. Rev. Lett.*, 108:106103, Mar 2012. doi: 10.1103/PhysRevLett.108.106103. URL `http://link.aps.org/doi/10.1103/PhysRevLett.108.106103`. (Cited on pages 47 and 49.)

[156] Thorsten Wagner. *Organische Heteroschichten - Untersuchung der Wechselwirkung organischer Moleküle auf Metalloberflächen*. PhD thesis, University of Duisburg-Essen, 2006. (Cited on pages 48 and 49.)

[157] Hatice Karacuban. *Grenzflächeneigenschaften organischer Moleküle auf Metalloberflächen*. PhD thesis, University of Duisburg-Essen, 2009. (Cited on pages 48 and 49.)

[158] Christian Bobisch. Untersuchung heterogener Molekülschichten. Master's thesis, University of Duisburg-Essen, 2003. (Cited on page 48.)

[159] Izabela I. Rzeznicka, Taro Yamada, and Maki Kawai. Light emission from {PTCDA} bilayer on Au(111) induced in scanning tunneling microscopy. *Surface Science*, 605(23-24):2032 – 2037, 2011. ISSN 0039-6028. doi: http://dx.doi.org/10.1016/j.susc.2011.07.024. URL `http://www.sciencedirect.com/science/article/pii/S0039602811003244`. (Cited on pages 48 and 193.)

[160] Gopala Krishna V. V. Thalluri, Donato Spoltore, Fortunato Piersimoni, John N. Clifford, Emilio Palomares, and Jean V. Manca. Study of interface properties in CuPc based hybrid inorganic-organic solar cells. *Dalton Trans.*, 41:11419–11423, 2012. doi: 10.1039/C2DT31402A. URL `http://dx.doi.org/10.1039/C2DT31402A`. (Cited on page 49.)

[161] Linsen Li, Min Guan, Guohua Cao, Yiyang Li, and Yiping Zeng. Low operating-voltage and high power-efficiency OLED employing MoO3-doped CuPc as hole injection layer. *Displays*, 33(1):17 – 20, 2012. ISSN 0141-9382. doi: http://dx.doi.org/10.1016/j.displa.2011.10.002. URL `http://www.sciencedirect.com/science/article/pii/S0141938211000898`. (Cited on page 49.)

[162] K. Narayan, S. Varadharajaperumal, G. Mohan Rao, M. Manoj Varma, and T. Srinivas. Effect of thickness variation of hole injection and hole blocking layers on the performance of fluorescent green organic light emitting diodes. *Current Applied Physics*, 13(1):18 – 25, 2013. ISSN 1567-1739. doi: http://dx.doi.org/10.1016/j.cap.2012.06.004. URL `http://www.sciencedirect.com/science/article/pii/S1567173912002477`. (Cited on page 49.)

[163] Benjamin Stadtmüller, Daniel Lüftner, Martin Willenbockel, Eva M. Reinisch, Tomoki Sueyoshi, Georg Koller, Serguei Soubatch, Michael G. Ramsey, Peter Puschnig, F. Stefan Tautz, and Christian Kumpf. Unexpected interplay of bonding height and energy level alignment at heteromolecular hybrid interfaces. *Nat Commun*, 5:–, 2014. URL `http://dx.doi.org/10.1038/ncomms4685`. (Cited on page 49.)

[164] H. Karacuban, M. Lange, J. Schaffert, O. Weingart, Th. Wagner, and R. Möller. Substrate-induced symmetry reduction of CuPc on Cu(111): An LT-STM study. *Surface Science*, 603(5):L39 – L43, 2009. ISSN 0039-6028. doi: http://dx.doi.org/10.1016/j.susc.2009.01.029. URL `http://www.sciencedirect.com/science/article/pii/S0039602809001241`. (Cited on pages 49 and 135.)

[165] Ingo Kröger, Benjamin Stadtmüller, Christoph Stadler, Johannes Ziroff, Mario Kochler, Andreas Stahl, Florian Pollinger, Tien-Lin Lee, Jörg Zegenhagen, Friedrich Reinert, and Christian Kumpf. Submonolayer growth of copper-phthalocyanine on Ag(111). *New Journal of Physics*, 12(8):083038, 2010. URL `http://stacks.iop.org/1367-2630/12/i=8/a=083038`. (Cited on pages 49 and 139.)

[166] Christoph Stadler, Soren Hansen, Ingo Kroger, Christian Kumpf, and Eberhard Umbach. Tuning intermolecular interaction in long-range-ordered submonolayer organic films. *Nat Phys*, 5(2):153–158, February 2009. ISSN 1745-2473. URL `http://dx.doi.org/10.1038/nphys1176`. (Cited on pages 49 and 135.)

[167] Ingo Kröger. *Adsorption von Phthalocyaninen auf Edelmetalloberflächen*. PhD thesis, 2011. (Cited on pages 49 and 139.)

[168] Johannes Schaffert, Maren C. Cottin, Andreas Sonntag, Hatice Karacuban, Christian A. Bobisch, Nicolás Lorente, Jean-Pierre Gauyacq, and Rolf Möller. Imaging the dynamics of individually adsorbed molecules. *Nat Mater*, 12(3):223–227, March 2013. ISSN 1476-1122. URL `http://dx.doi.org/10.1038/nmat3527`. (Cited on pages 50, 75, 244, and xvii.)

[169] N. Wintjes, M. Lange, D. van Vörden, H. Karacuban, D. Utzat, and R. Möller. Very compact design for a low-temperature tuning fork atomic force microscope. *Journal of Vacuum Science & Technology B*, 28(3):C4E21–C4E23, 2010. doi: http://dx.doi.org/10.1116/1.3374720. URL `http://scitation.aip.org/content/avs/journal/jvstb/28/3/10.1116/1.3374720`. (Cited on page 54.)

[170] Manfred Lange. *Elementare Dissipationsprozesse in der Rastertunnel- und Rasterkraftmikroskopie*. PhD thesis, University of Duisburg-Essen, 2014. (Cited on pages 55, 57, 58, and 63.)

[171] Manfred Lange. Frequenzmodulierte Rasterkraftmikroskopie: Aufbau eines Tieftemperatur-Geräts. Master's thesis, University of Duisburg-Essen, 2008. (Cited on pages 57 and 58.)

[172] Maren Cottin. Rastertunnelmikoskopie und -spektroskopie an organischen und anorganischen dünnen Schichten bei tiefen Temperaturen. Master's thesis, University of Duisburg-Essen, 2010. (Cited on page 58.)

[173] *Models LT-3-110 and LT-3B Heli-tran open cycle cryogenic refrigeration system*. Advanced Research Systems, Inc., 905 Harrison St., Allentown, Pennsylvania 18103. (Cited on page 63.)

[174] Georgy Kichin, Christian Weiss, Christian Wagner, F. Stefan Tautz, and Ruslan Temirov. Single Molecule and Single Atom Sensors for Atomic Resolution Imaging of Chemically Complex Surfaces. *Journal of the American Chemical Society*, 133(42):16847–16851, 2011. doi: 10.1021/ja204624g. URL `http://dx.doi.org/10.1021/ja204624g`. PMID: 21962083. (Cited on page 64.)

[175] Prokop Hapala, Ruslan Temirov, F. Stefan Tautz, and Pavel Jelínek. Origin of High-Resolution IETS-STM Images of Organic Molecules with Functionalized Tips. *Phys. Rev. Lett.*, 113:226101, Nov 2014. doi: 10.1103/PhysRevLett.113.226101. URL `http://link.aps.org/doi/10.1103/PhysRevLett.113.226101`. (Cited on page 64.)

[176] L. Bartels, G. Meyer, K.-H. Rieder, D. Velic, E. Knoesel, A. Hotzel, M. Wolf, and G. Ertl. Dynamics of Electron-Induced Manipulation of Individual CO Molecules on Cu(111). *Phys. Rev. Lett.*, 80:2004–2007, Mar 1998. doi: 10.1103/PhysRevLett.80.2004. URL `http://link.aps.org/doi/10.1103/PhysRevLett.80.2004`. (Cited on page 64.)

[177] Leo Gross, Fabian Mohn, Nikolaj Moll, Peter Liljeroth, and Gerhard Meyer. The Chemical Structure of a Molecule Resolved by Atomic Force Microscopy. *Science*, 325(5944):1110–1114, 2009. doi: 10.1126/science.1176210. URL `http://www.sciencemag.org/content/325/5944/1110.abstract`. (Cited on page 64.)

[178] Ben Wortmann et al. in preparation. (Cited on page 64.)

[179] Merlin Schmuck. Präparation von PTCDA Schichten. Bachelorthesis, 2010. (Cited on page 64.)

[180] Dennis van Vörden. Dynamische Tieftemperatur Rasterkraftmikroskopie: Untersuchung von Energiedissipation auf Oberflächen. Master's thesis, University of Duisburg-Essen, 2010. (Cited on page 64.)

[181] *Acton Series Monochromators and Spectrographs*. Princeton Instruments Spectroscopy Group. (Cited on pages 68 and 70.)

[182] T. Nagao, J. T. Sadowski, M. Saito, S. Yaginuma, Y. Fujikawa, T. Kogure, T. Ohno, Y. Hasegawa, S. Hasegawa, and T. Sakurai. Nanofilm Allotrope and Phase Transformation of Ultrathin Bi Film on Si(111)-7×7. *Phys. Rev. Lett.*, 93:105501, Aug 2004. doi: 10.1103/PhysRevLett.93.105501. URL `http://link.aps.org/doi/10.1103/PhysRevLett.93.105501`. (Cited on pages 73 and 235.)

[183] C Bobisch, A Bannani, M Matena, and R Möller. Ultrathin Bi films on Si(100). *Nanotechnology*, 18(5):055606, 2007. URL `http://stacks.iop.org/0957-4484/18/i=5/a=055606`. (Cited on page 73.)

[184] J. Schaffert, M. C. Cottin, A. Sonntag, H. Karacuban, D. Utzat, C. A. Bobisch, and R. Möller. Scanning noise microscopy. *Review of Scientific Instruments*, 84(4):043702, 2013. doi: http://dx.doi.org/10.1063/1.4801458. URL `http://scitation.aip.org/content/aip/journal/rsi/84/4/10.1063/1.4801458`. (Cited on pages 75 and xvii.)

[185] P. Zahl, M. Bierkandt, S. Schröder, and A. Klust. The flexible and modern open source scanning probe microscopy software package GXSM. *Rev. Sci. Instr.*, 74(3):1222, 2003. (Cited on page 75.)

[186] *WinSpec Spectroscopy Software*. Princeton Instruments, 3660 Quakerbridge Rd, Trenton, NJ 08619, version 2.6b edition, December 2012. (Cited on pages 75 and 82.)

[187] I. Horcas, R. Fernandez, J. M. Gomez-Rodriguez, J. Colchero, J. Gomez-Herrero, and A. M. Baro. WSXM: A software for scanning probe microscopy and a tool for nanotechnology. *Review of Scientific Instruments*, 78(1):013705, 2007. doi: 10.1063/1.2432410. URL `http://link.aip.org/link/?RSI/78/013705/1`. (Cited on page 75.)

[188] URL `http://www.originlab.com/`. (Cited on page 75.)

[189] URL `www.coreldraw.com`. (Cited on page 75.)

[190] André Miede, 2010. URL `https://www.ctan.org/pkg/classicthesis`. (Cited on page 75.)

[191] Johannes Schaffert. Rastertunnelmikoskopie an organischen Molekülen bei tiefen Temperaturen. Master's thesis, University of Duisburg-Essen, 2009. (Cited on page 77.)

[192] Richard Berndt and James K. Gimzewski. Isochromat spectroscopy of photons emitted from metal surfaces in an STM. *Annalen der Physik*, 505(2):133–140, 1993. ISSN 1521-3889. doi: 10.1002/andp.19935050205. URL `http://dx.doi.org/10.1002/andp.19935050205`. (Cited on pages 83, 118, 121, 130, 131, 200, and 220.)

[193] Ebru Özen. Lichtemission von reinen und adsorbatbedeckten Metalloberflächen induziert durch tunnelnde Elektronen. Master's thesis, University of Duisburg-Essen, 2013. (Cited on page 83.)

[194] Ludwig Bartels, S. W. Hla, A. Kühnle, G. Meyer, K.-H. Rieder, and J. R. Manson. STM observations of a one-dimensional electronic edge state at steps on Cu(111). *Phys. Rev. B*, 67:205416, May 2003. doi: 10.1103/PhysRevB.67.205416. URL `http://link.aps.org/doi/10.1103/PhysRevB.67.205416`. (Cited on pages 84 and 121.)

[195] Sarah Heidorn and Karina Morgenstern. Spatial variation of the surface state onset close to three types of surface steps on Ag(111) studied by scanning tunnelling spectroscopy. *New Journal of Physics*, 13(3):033034, 2011. URL `http://stacks.iop.org/1367-2630/13/i=3/a=033034`. (Cited on page 86.)

[196] Xuefeng Cui, Cong Wang, Adam Argondizzo, Sean Garrett-Roe, Branko Gumhalter, and Hrvoje Petek. Transient excitons at metal surfaces. *Nat Phys*, 10(7):505–509, July 2014. ISSN 1745-2473. URL `http://dx.doi.org/10.1038/nphys2981`. (Cited on page 86.)

[197] J Mitra, Lei Feng, Michael G Boyle, and P Dawson. Electromagnetic interaction between a metallic nanoparticle and surface in tunnelling proximity - modelling and experiment. *Journal of Physics D: Applied Physics*, 42(21):215101, 2009. URL `http://stacks.iop.org/0022-3727/42/i=21/a=215101`. (Cited on pages 104, 109, 110, and 114.)

[198] Germar Hoffmann, Laurent Libioulle, and Richard Berndt. Tunneling-induced luminescence from adsorbed organic molecules with submolecular lateral resolution. *Phys. Rev. B*, 65:212107, Jun 2002. doi: 10.1103/PhysRevB.65.212107. URL `http://link.aps.org/doi/10.1103/PhysRevB.65.212107`. (Cited on pages 105, 128, 129, 145, 146, 148, 169, 193, 217, and 218.)

[199] Germar Hoffmann, Richard Berndt, and Peter Johansson. Two-Electron Photon Emission from Metallic Quantum Wells. *Phys. Rev. Lett.*, 90:046803, Jan 2003. doi: 10.1103/PhysRevLett.90.046803. URL `http://link.aps.org/doi/10.1103/PhysRevLett.90.046803`. (Cited on page 106.)

[200] Christian Bobisch. private communication. 2015.

[201] Chi Chen, Christian Alexander Bobisch, and Wilson Ho. unpublished. (Cited on page 106.)

[202] P Dawson and Michael G Boyle. Light emission from scanning tunnelling microscope on polycrystalline Au films - what is happening at the single-grain level? *Journal of Optics A: Pure and Applied Optics*, 8(4):S219, 2006. URL `http://stacks.iop.org/1464-4258/8/i=4/a=S23`. (Cited on pages 107, 109, and 116.)

[203] C. Maurel, R. Coratger, F. Ajustron, G. Seine, R. Péchou, and J. Beauvillain. Effect of multiple tips on light emission induced by {STM} from gold nanostructures. *Surface Science*, 529(3):359 – 364, 2003. ISSN 0039-6028. doi: http://dx.doi.org/10.1016/S0039-6028(03)00270-X. URL `http://www.sciencedirect.com/science/article/pii/S003960280300270X`. (Cited on page 109.)

[204] G. Hoffmann, J. Aizpurua, P. Apell, and R. Berndt. Influence of tip geometry in light emission from the scanning tunnelling microscope. *Surface Science*, 482-485, Part 2(0):1159 – 1162, 2001. ISSN 0039-6028. doi: http://dx.doi.org/10.1016/S0039-6028(00)01079-7. URL `http://www.sciencedirect.com/science/article/pii/S0039602800010797`. (Cited on page 109.)

[205] R. W. Rendell and D. J. Scalapino. Surface plasmons confined by microstructures on tunnel junctions. *Phys. Rev. B*, 24:3276–3294, Sep 1981. doi: 10.1103/PhysRevB.

24.3276. URL `http://link.aps.org/doi/10.1103/PhysRevB.24.3276`. (Cited on pages 110 and 114.)

[206] R. W. Rendell, D. J. Scalapino, and B. Mühlschlegel. Role of Local Plasmon Modes in Light Emission from Small-particle Tunnel Junctions. *Phys. Rev. Lett.*, 41:1746–1750, Dec 1978. doi: 10.1103/PhysRevLett.41.1746. URL `http://link.aps.org/doi/10.1103/PhysRevLett.41.1746`. (Cited on page 110.)

[207] A. W. McKinnon, M. E. Welland, T. M. H. Wong, and J. K. Gimzewski. Photon-emission scanning tunneling microscopy of silver films in ultrahigh vacuum: A spectroscopic method. *Phys. Rev. B*, 48:15250–15255, Nov 1993. doi: 10.1103/PhysRevB.48.15250. URL `http://link.aps.org/doi/10.1103/PhysRevB.48.15250`. (Cited on page 116.)

[208] Y. Uehara, T. Fujita, and S. Ushioda. Scanning Tunneling Microscope Light Emission Spectra of $\mathrm{Au}(110)-(2\times 1)$ with Atomic Spatial Resolution. *Phys. Rev. Lett.*, 83:2445–2448, Sep 1999. doi: 10.1103/PhysRevLett.83.2445. URL `http://link.aps.org/doi/10.1103/PhysRevLett.83.2445`. (Cited on pages 116 and 120.)

[209] C. A. Bobisch, A. Bannani, Yu. M. Koroteev, G. Bihlmayer, E. V. Chulkov, and R. Möller. Conservation of the Lateral Electron Momentum at a Metal-Semiconductor Interface Studied by Ballistic Electron Emission Microscopy. *Phys. Rev. Lett.*, 102:136807, Apr 2009. doi: 10.1103/PhysRevLett.102.136807. URL `http://link.aps.org/doi/10.1103/PhysRevLett.102.136807`. (Cited on page 116.)

[210] F Mugele, A Rettenberger, J Boneberg, and P Leiderer. The influence of tip-sample interaction on step fluctuations on Ag(111). *Surface Science*, 400 (1 - 3):80 – 86, 1998. ISSN 0039-6028. doi: http://dx.doi.org/10.1016/S0039-6028(97)00843-1. URL `http://www.sciencedirect.com/science/article/pii/S0039602897008431`. (Cited on page 118.)

[211] Peng Chen, Weihua Wang, Nian Lin, and Shengwang Du. Manipulating photon emission efficiency with local electronic states in a tunneling gap. *Opt. Express*, 22(7):8234–8242, Apr 2014. doi: 10.1364/OE.22.008234. URL `http://www.opticsexpress.org/abstract.cfm?URI=oe-22-7-8234`. (Cited on pages 130, 205, 220, and 240.)

[212] Ebru Ekici et al. unpublished. (Cited on page 131.)

[213] K. Manandhar, T. Ellis, K.T. Park, T. Cai, Z. Song, and J. Hrbek. A scanning tunneling microscopy study on the effect of post-deposition annealing of copper phthalocyanine thin films. *Surface Science*, 601(17):3623 – 3631, 2007. ISSN 0039-6028. doi: http://dx.doi.org/10.1016/j.susc.2007.07.007. URL `http://www.sciencedirect.com/science/article/pii/S0039602807007601`. (Cited on page 139.)

[214] I. Chizhov, G. Scoles, and A. Kahn. The Influence of Steps on the Orientation of Copper Phthalocyanine Monolayers on Au(111). *Langmuir*, 16(9):4358–4361, 2000. doi: 10.1021/la9916225. URL `http://dx.doi.org/10.1021/la9916225`. (Cited on page 139.)

[215] T.J.Z. Stock and J. Nogami. Copper phthalocyanine thin films on Cu(111): Submonolayer to multi-layer. *Surface Science*, 637 - 638(0):132 – 139, 2015. ISSN 0039-6028. doi: http://dx.doi.org/10.1016/j.susc.2015.03.028. URL `http://www.sciencedirect.com/science/article/pii/S0039602815000886`. (Cited on page 139.)

[216] Han Huang, Swee Liang Wong, Wei Chen, and Andrew Thye Shen Wee. LT-STM studies on substrate-dependent self-assembly of small organic molecules. *Journal of Physics D: Applied Physics*, 44(46):464005, 2011. URL `http://stacks.iop.org/0022-3727/44/i=46/a=464005`. (Cited on page 139.)

[217] R. Berndt, R. Gaisch, W.D. Schneider, J.K. Gimzewski, B. Reihl, R.R. Schlittler, and M. Tschudy. Photon emission from adsorbed C_{60} molecules with subnanometer lateral resolution. *Applied Physics A*, 57(6):513–516, 1993. ISSN 0947-8396. doi: 10.1007/BF00331750. URL `http://dx.doi.org/10.1007/BF00331750`. (Cited on pages 143, 146, 148, 150, 217, and 240.)

[218] X. Tao, Z. C. Dong, J. L. Yang, Y. Luo, J. G. Hou, and J. Aizpurua. Influence of a dielectric layer on photon emission induced by a scanning tunneling microscope. *The Journal of Chemical Physics*, 130(8):084706, 2009. doi: http://dx.doi.org/10.1063/1.3080766. URL `http://scitation.aip.org/content/aip/journal/jcp/130/8/10.1063/1.3080766`. (Cited on pages 144 and 146.)

[219] Z.-C. Dong, A. Kar, P. Dorozhkin, K. Amemiya, T. Uchihashi, S. Yokoyama, T. Kamikado, S. Mashiko, and T. Okamoto. Tunneling electron induced luminescence from monolayered Cu-TBP porphyrin molecules adsorbed on Cu(100). *Thin Solid Films*, 438-439(0):262 – 267, 2003. ISSN 0040-6090. doi: http://dx.doi.org/10.1016/S0040-6090(03)00797-1. URL `http://www.sciencedirect.com/science/article/pii/S0040609003007971`. The 5th International Conference on Nano-Molecular Electronics. (Cited on pages 145, 146, 169, 193, 217, and 218.)

[220] Y. Zhang, X. Tao, H. Y. Gao, Z. C. Dong, J. G. Hou, and T. Okamoto. Modulation of local plasmon mediated emission through molecular manipulation. *Phys. Rev. B*, 79:075406, Feb 2009. doi: 10.1103/PhysRevB.79.075406. URL `http://link.aps.org/doi/10.1103/PhysRevB.79.075406`. (Cited on pages 146, 147, and 217.)

[221] K. Sakamoto, K. Meguro, R. Arafune, M. Satoh, Y. Uehara, and S. Ushioda. Light emission spectra of the monolayer-island of C_{60} molecules on Au(111) induced by scanning tunneling microscope. *Surface Science*, 502 - 503 (0):149 – 155, 2002. ISSN 0039-6028. doi: http://dx.doi.org/10.1016/S0039-6028(01)01924-0. URL `http://www.sciencedirect.com/science/article/pii/S0039602801019240`. (Cited on page 148.)

[222] W. L. Barnes. Fluorescence near interfaces: The role of photonic mode density. *Journal of Modern Optics*, 45(4):661–699, 1998. doi: 10.1080/09500349808230614. URL `http://dx.doi.org/10.1080/09500349808230614`. (Cited on page 148.)

[223] Alexander Kabakchiev, Klaus Kuhnke, Theresa Lutz, and Klaus Kern. Electroluminescence from Individual Pentacene Nanocrystals. *ChemPhysChem*, 11

(16):3412–3416, 2010. ISSN 1439-7641. doi: 10.1002/cphc.201000531. URL http://dx.doi.org/10.1002/cphc.201000531. (Cited on page 148.)

[224] URL http://creativecommons.org/licenses/by-nc-sa/3.0/. (Cited on page 153.)

[225] G. Schull and R. Berndt. Orientationally Ordered (7 × 7) Superstructure of C_{60} on Au(111). *Phys. Rev. Lett.*, 99:226105, Nov 2007. doi: 10.1103/PhysRevLett.99.226105. URL http://link.aps.org/doi/10.1103/PhysRevLett.99.226105. (Cited on page 154.)

[226] Christian Alexander Bobisch. *Mikroskopie mit ballistischen Elektronen*. PhD thesis, University of Duisburg-Essen, 2007. (Cited on page 157.)

[227] G. Bian, X. Wang, T. Miller, and T.-C.m Chiang. Origin of giant Rashba spin splitting in Bi/Ag surface alloys. *Phys. Rev. B*, 88:085427, Aug 2013. doi: 10.1103/PhysRevB.88.085427. URL http://link.aps.org/doi/10.1103/PhysRevB.88.085427. (Cited on page 159.)

[228] Guang Bian, T. Miller, and T.-C. Chiang. Rashba splitting and dichroism of surface states in Bi/Ag surface alloy. *Journal of Electron Spectroscopy and Related Phenomena*, 201(0):36 – 41, 2014. ISSN 0368-2048. doi: http://dx.doi.org/10.1016/j.elspec.2014.10.003. URL http://www.sciencedirect.com/science/article/pii/S0368204814002230.

[229] G. Bihlmayer, S. Blügel, and E. V. Chulkov. Enhanced Rashba spin-orbit splitting in Bi/Ag(111) and Pb/Ag(111) surface alloys from first principles. *Phys. Rev. B*, 75:195414, May 2007. doi: 10.1103/PhysRevB.75.195414. URL http://link.aps.org/doi/10.1103/PhysRevB.75.195414. (Cited on page 159.)

[230] Y. Girard, C. Chacon, G. de Abreu, J. Lagoute, V. Repain, and S. Rousset. Growth of Bi on Cu(111): Alloying and dealloying transitions. *Surface Science*, 617(0):118 – 123, 2013. ISSN 0039-6028. doi: http://dx.doi.org/10.1016/j.susc.2013.06.015. URL http://www.sciencedirect.com/science/article/pii/S0039602813001878. (Cited on pages 159, 160, and 162.)

[231] K. H. L. Zhang, I. M. McLeod, Y. H. Lu, V. R. Dhanak, A. Matilainen, M. Lahti, K. Pussi, R. G. Egdell, X.-S. Wang, A. T. S. Wee, and W. Chen. Observation of a surface alloying-to-dealloying transition during growth of Bi on Ag(111). *Phys. Rev. B*, 83(23):235418–, June 2011. URL http://link.aps.org/doi/10.1103/PhysRevB.83.235418. (Cited on pages 159, 160, 161, and 256.)

[232] Chiaki Kato, Yuki Aoki, and Hiroyuki Hirayama. Scanning tunneling microscopy of Bi-induced Ag(111) surface structures. *Phys. Rev. B*, 82:165407, Oct 2010. doi: 10.1103/PhysRevB.82.165407. URL http://link.aps.org/doi/10.1103/PhysRevB.82.165407. (Cited on pages 159, 160, 161, and 256.)

[233] D. Kaminski, P. Poodt, E. Aret, N. Radenovic, and E. Vlieg. Surface alloys, overlayer and incommensurate structures of Bi on Cu(111). *Surface Science*, 575(3):233 – 246, 2005. ISSN 0039-6028. doi: http://dx.doi.org/10.1016/

j.susc.2004.11.001. URL http://www.sciencedirect.com/science/article/pii/S0039602804014335. (Cited on pages 159, 160, 161, and 162.)

[234] K H L Zhang, I M McLeod, M Lahti, K Pussi, and V R Dhanak. The evolution of the electronic structure at the Bi/Ag(111) interface studied using photoemission spectroscopy. *Journal of Physics: Condensed Matter*, 24(43):435502, 2012. URL http://stacks.iop.org/0953-8984/24/i=43/a=435502. (Cited on page 160.)

[235] Chun Hsien Chen, Keith D. Kepler, Andrew A. Gewirth, B. M. Ocko, and Jia Wang. Electrodeposited bismuth monolayers on gold (111) electrodes: comparison of surface x-ray scattering, scanning tunneling microscopy, and atomic force microscopy lattice structures. *The Journal of Physical Chemistry*, 97(28):7290–7294, 1993. doi: 10.1021/j100130a028. URL http://dx.doi.org/10.1021/j100130a028. (Cited on page 160.)

[236] F. Delamare and G.E. Rhead. First stages of the deposition of bismuth on copper examined by LEED: Ii. the (111) substrate. *Surface Science*, 35(0):185 – 193, 1973. ISSN 0039-6028. doi: http://dx.doi.org/10.1016/0039-6028(73)90213-6. URL http://www.sciencedirect.com/science/article/pii/0039602873902136. (Cited on page 161.)

[237] Takeshi Tono, Toru Hirahara, and Shuji Hasegawa. In situ transport measurements on ultrathin Bi(111) films using a magnetic tip: possible detection of current-induced spin polarization in the surface states. *New Journal of Physics*, 15 (10):105018, 2013. URL http://stacks.iop.org/1367-2630/15/i=10/a=105018. (Cited on page 163.)

[238] T. Hirahara, K. Miyamoto, I. Matsuda, T. Kadono, A. Kimura, T. Nagao, G. Bihlmayer, E. V. Chulkov, S. Qiao, K. Shimada, H. Namatame, M. Taniguchi, and S. Hasegawa. Direct observation of spin splitting in bismuth surface states. *Phys. Rev. B*, 76:153305, Oct 2007. doi: 10.1103/PhysRevB.76.153305. URL http://link.aps.org/doi/10.1103/PhysRevB.76.153305. (Cited on pages 164 and 249.)

[239] Hendrik Bentmann and Friedrich Reinert. Enhancing and reducing the Rashba-splitting at surfaces by adsorbates: Na and Xe on Bi/Cu(111). *New Journal of Physics*, 15(11):115011, 2013. URL http://stacks.iop.org/1367-2630/15/i=11/a=115011. (Cited on pages 164 and 165.)

[240] Yu. M. Koroteev, G. Bihlmayer, E. V. Chulkov, and S. Blügel. First-principles investigation of structural and electronic properties of ultrathin Bi films. *Phys. Rev. B*, 77:045428, Jan 2008. doi: 10.1103/PhysRevB.77.045428. URL http://link.aps.org/doi/10.1103/PhysRevB.77.045428. (Cited on pages 164 and 234.)

[241] Guillaume Schull, Nicolas Néel, Peter Johansson, and Richard Berndt. Electron-Plasmon and Electron-Electron Interactions at a Single Atom Contact. *Phys. Rev. Lett.*, 102:057401, Feb 2009. doi: 10.1103/PhysRevLett.102.057401. URL http://link.aps.org/doi/10.1103/PhysRevLett.102.057401. (Cited on page 182.)

[242] S. W. Wu, G. V. Nazin, and W. Ho. Intramolecular photon emission from a single molecule in a scanning tunneling microscope. *Phys. Rev. B*, 77:205430, May 2008. doi: 10.1103/PhysRevB.77.205430. URL `http://link.aps.org/doi/10.1103/PhysRevB.77.205430`. (Cited on page 193.)

[243] J. Sun, A. Mikkelsen, M. Fuglsang Jensen, Y. M. Koroteev, G. Bihlmayer, E. V. Chulkov, D. L. Adams, Ph. Hofmann, and K. Pohl. Structural determination of the Bi(110) semimetal surface by LEED analysis and *ab initio* calculations. *Phys. Rev. B*, 74:245406, Dec 2006. doi: 10.1103/PhysRevB.74.245406. URL `http://link.aps.org/doi/10.1103/PhysRevB.74.245406`. (Cited on page 223.)

[244] J. T. Sadowski, T. Nagao, S. Yaginuma, Y. Fujikawa, T. Sakurai, A. Oreshkin, M. Saito, and T. Ohno. Stability of the quasicubic phase in the initial stage of the growth of bismuth films on Si(111)-7x7. *Journal of Applied Physics*, 99(1):014904, 2006. doi: http://dx.doi.org/10.1063/1.2150598. URL `http://scitation.aip.org/content/aip/journal/jap/99/1/10.1063/1.2150598`. (Cited on page 223.)

[245] P.J. Kowalczyk, O. Mahapatra, D.N. McCarthy, W. Kozlowski, Z. Klusek, and S.A. Brown. STM and XPS investigations of bismuth islands on HOPG. *Surface Science*, 605(7 - 8):659 – 667, 2011. ISSN 0039-6028. doi: http://dx.doi.org/10.1016/j.susc.2010.12.032. URL `http://www.sciencedirect.com/science/article/pii/S0039602810005212`. (Cited on pages 223, 234, and 235.)

[246] A. Samsavar, E. S. Hirschorn, T. Miller, F. M. Leibsle, J. A. Eades, and T. C. Chiang. High-resolution imaging of a dislocation on Cu(111). *Phys. Rev. Lett.*, 65:1607–1610, Sep 1990. doi: 10.1103/PhysRevLett.65.1607. URL `http://link.aps.org/doi/10.1103/PhysRevLett.65.1607`. (Cited on page 223.)

[247] G. Bian, X. Wang, T. Miller, T.-C. Chiang, P. J. Kowalczyk, O. Mahapatra, and S. A. Brown. First-principles and spectroscopic studies of Bi(110) films: Thickness-dependent Dirac modes and property oscillations. *Phys. Rev. B*, 90:195409, Nov 2014. doi: 10.1103/PhysRevB.90.195409. URL `http://link.aps.org/doi/10.1103/PhysRevB.90.195409`. (Cited on pages 226, 234, and 235.)

[248] P. J. Kowalczyk, O. Mahapatra, S. A. Brown, G. Bian, X. Wang, and T.-C. Chiang. Electronic Size Effects in Three-Dimensional Nanostructures. *Nano Letters*, 13(1):43–47, 2013. doi: 10.1021/nl3033119. URL `http://dx.doi.org/10.1021/nl3033119`. PMID: 23198917. (Cited on pages 234, 235, and 241.)

[249] Tadaaki Nagao, Takumi Doi, Takeharu Sekiguchi, and Shuji Hasegawa. Epitaxial Growth of Single-Crystal Ultrathin Films of Bismuth on Si(111). *Japanese Journal of Applied Physics*, 39(7S):4567, 2000. URL `http://stacks.iop.org/1347-4065/39/i=7S/a=4567`. (Cited on page 226.)

[250] G. Bian, T. Miller, and T.-C. Chiang. Electronic structure and surface-mediated metastability of Bi films on Si(111)-7 $\times$ 7 studied by angle-resolved photoemission spectroscopy. *Phys. Rev. B*, 80:245407, Dec 2009. doi: 10.1103/PhysRevB.80.245407. URL `http://link.aps.org/doi/10.1103/PhysRevB.80.245407`. (Cited on pages 234 and 241.)

[251] T. Hirahara, T. Nagao, I. Matsuda, G. Bihlmayer, E. V. Chulkov, Yu. M. Koroteev, P. M. Echenique, M. Saito, and S. Hasegawa. Role of Spin-Orbit Coupling and Hybridization Effects in the Electronic Structure of Ultrathin Bi Films. *Phys. Rev. Lett.*, 97:146803, Oct 2006. doi: 10.1103/PhysRevLett.97.146803. URL `http://link.aps.org/doi/10.1103/PhysRevLett.97.146803`. (Cited on page 234.)

[252] Germar Hoffmann, Jörg Kliewer, and Richard Berndt. Luminescence from Metallic Quantum Wells in a Scanning Tunneling Microscope. *Phys. Rev. Lett.*, 87:176803, Oct 2001. doi: 10.1103/PhysRevLett.87.176803. URL `http://link.aps.org/doi/10.1103/PhysRevLett.87.176803`. (Cited on pages 234 and 241.)

[253] Anna Strózecka, Jingcheng Li, Robin Schürmann, Gunnar Schulze, Martina Corso, Fabian Schulz, Christian Lotze, Sascha Sadewasser, Katharina J. Franke, and Jose Ignacio Pascual. Electroluminescence of copper-nitride nanocrystals. *Phys. Rev. B*, 90:195420, Nov 2014. doi: 10.1103/PhysRevB.90.195420. URL `http://link.aps.org/doi/10.1103/PhysRevB.90.195420`. (Cited on pages 234 and 241.)

[254] P. J. Kowalczyk, D. Belic, O. Mahapatra, S. A. Brown, E. S. Kadantsev, T. K. Woo, B. Ingham, and W. Kozlowski. Anisotropic oxidation of bismuth nanostructures: Evidence for a thin film allotrope of bismuth. *Applied Physics Letters*, 100(15):151904, 2012. doi: http://dx.doi.org/10.1063/1.3701166. URL `http://scitation.aip.org/content/aip/journal/apl/100/15/10.1063/1.3701166`. (Cited on page 235.)

[255] Haibo Wang and Donghang Yan. Organic heterostructures in organic field-effect transistors. *NPG Asia Mater*, 2:69–78, April 2010. ISSN 1884-4049. URL `http://dx.doi.org/10.1038/asiamat.2010.44`. (Cited on page 243.)

[256] Arie van Houselt and Harold J. W. Zandvliet. *Colloquium* : Time-resolved scanning tunneling microscopy. *Rev. Mod. Phys.*, 82:1593–1605, May 2010. doi: 10.1103/RevModPhys.82.1593. URL `http://link.aps.org/doi/10.1103/RevModPhys.82.1593`. (Cited on page 244.)

[257] P A Sloan. Time-resolved scanning tunnelling microscopy for molecular science. *Journal of Physics: Condensed Matter*, 22(26):264001, 2010. URL `http://stacks.iop.org/0953-8984/22/i=26/a=264001`. (Cited on page 244.)

[258] Mario Prietsch. Ballistic-electron emission microscopy (BEEM): studies of metal/semiconductor interfaces with nanometer resolution. *Physics Reports*, 253 (4):163 – 233, 1995. ISSN 0370-1573. doi: http://dx.doi.org/10.1016/0370-1573(94)00082-E. URL `http://www.sciencedirect.com/science/article/pii/037015739400082E`. (Cited on page 244.)

[259] Y. Ohtsubo, J. Mauchain, J. Faure, E. Papalazarou, M. Marsi, P. Le Fèvre, F. Bertran, A. Taleb-Ibrahimi, and L. Perfetti. Giant Anisotropy of Spin-Orbit Splitting at the Bismuth Surface. *Phys. Rev. Lett.*, 109:226404, Nov 2012. doi: 10.1103/PhysRevLett.109.226404. URL `http://link.aps.org/doi/10.1103/PhysRevLett.109.226404`. (Cited on page 249.)

[260] Aitor Mugarza Ezpeleta. *Electronic Structure of Low-Dimensional Systems Analyzed by Angle Resolved Photoemission Spectroscopy*. PhD thesis, University of the Basque Country, 2002. URL `http://www.sc.ehu.es/waporcoj/aitor_tesis/tesis.PDF`. (Cited on page 249.)

[261] L. Moreschini, A. Bendounan, C. R. Ast, F. Reinert, M. Falub, and M. Grioni. Effect of rare-gas adsorption on the spin-orbit split bands of a surface alloy: Xe on Ag(111)-($\sqrt{3} \times \sqrt{3}$)R30°-Bi. *Phys. Rev. B*, 77:115407, Mar 2008. doi: 10.1103/PhysRevB.77.115407. URL `http://link.aps.org/doi/10.1103/PhysRevB.77.115407`. (Cited on pages 251 and 257.)

[262] Nicoleta Nicoara, Elisa Román, José M. Gómez-Rodríguez, José A. Martín-Gago, and Javier Méndez. Scanning tunneling and photoemission spectroscopies at the PTCDA/Au(1 1 1) interface. *Organic Electronics*, 7(5):287 – 294, 2006. ISSN 1566-1199. doi: http://dx.doi.org/10.1016/j.orgel.2006.03.010. URL `http://www.sciencedirect.com/science/article/pii/S1566119906000553`. (Cited on pages 251, 254, and 257.)

[263] A. Varykhalov, D. Marchenko, M. R. Scholz, E. D. L. Rienks, T. K. Kim, G. Bihlmayer, J. Sánchez-Barriga, and O. Rader. Ir(111) Surface State with Giant Rashba Splitting Persists under Graphene in Air. *Phys. Rev. Lett.*, 108:066804, Feb 2012. doi: 10.1103/PhysRevLett.108.066804. URL `http://link.aps.org/doi/10.1103/PhysRevLett.108.066804`. (Cited on pages 251 and 257.)

[264] Norbert Koch. Energy levels at interfaces between metals and conjugated organic molecules. *Journal of Physics: Condensed Matter*, 20(18):184008, 2008. URL `http://stacks.iop.org/0953-8984/20/i=18/a=184008`. (Cited on pages 252, 254, 257, 260, and 262.)

[265] Ku-Ding Tsuei, Jih-Young Yuh, Chyuan-Tsyr Tzeng, Ren-Yu Chu, Shih-Chun Chung, and King-Lung Tsang. Photoemission and photoabsorption study of C_{60} adsorption on Cu(111) surfaces. *Phys. Rev. B*, 56:15412–15420, Dec 1997. doi: 10.1103/PhysRevB.56.15412. URL `http://link.aps.org/doi/10.1103/PhysRevB.56.15412`. (Cited on pages 252 and 257.)

[266] S. Duhm, A. Gerlach, I. Salzmann, B. BrÃ¶ker, R.L. Johnson, F. Schreiber, and N. Koch. PTCDA on Au(1 1 1), Ag(1 1 1) and Cu(1 1 1): Correlation of interface charge transfer to bonding distance. *Organic Electronics*, 9(1):111 – 118, 2008. ISSN 1566-1199. doi: http://dx.doi.org/10.1016/j.orgel.2007.10.004. URL `http://www.sciencedirect.com/science/article/pii/S1566119907001437`. (Cited on pages 252, 254, and 257.)

[267] C.-T. Tzeng, W.-S. Lo, J.-Y. Yuh, R.-Y. Chu, and K.-D. Tsuei. Photoemission, near-edge x-ray-absorption spectroscopy, and low-energy electron-diffraction study of C_{60} on Au(111) surfaces. *Phys. Rev. B*, 61:2263–2272, Jan 2000. doi: 10.1103/PhysRevB.61.2263. URL `http://link.aps.org/doi/10.1103/PhysRevB.61.2263`. (Cited on pages 252 and 257.)

[268] Yun Bai, Florian Buchner, Ina Kellner, Martin Schmid, Florian Vollnhals, Hans-Peter SteinrÃ¼ck, Hubertus Marbach, and J Michael Gottfried. Adsorption of

cobalt (II) octaethylporphyrin and 2H-octaethylporphyrin on Ag(111): new insight into the surface coordinative bond. *New Journal of Physics*, 11(12):125004, 2009. URL `http://stacks.iop.org/1367-2630/11/i=12/a=125004`. (Cited on page 253.)

[269] Mattia Fanetti, Arrigo Calzolari, Paolo Vilmercati, Carla Castellarin-Cudia, Patrizia Borghetti, Giovanni Di Santo, Luca Floreano, Alberto Verdini, Albano Cossaro, Ivana Vobornik, Emilia Annese, Federica Bondino, Stefano Fabris, and Andrea Goldoni. Structure and Molecule - Substrate Interaction in a Co-octaethyl Porphyrin Monolayer on the Ag(110) Surface. *The Journal of Physical Chemistry C*, 115(23):11560–11568, 2011. doi: 10.1021/jp2011233. URL `http://dx.doi.org/10.1021/jp2011233`. (Cited on page 253.)

[270] Dennis van Vörden, Manfred Lange, Johannes Schaffert, Maren C. Cottin, Merlin Schmuck, Roberto Robles, Heiko Wende, Christian A. Bobisch, and Rolf Möller. Surface-Induced Dechlorination of FeOEP-Cl on Cu(111). *ChemPhysChem*, 14(15): 3472–3475, 2013. ISSN 1439-7641. doi: 10.1002/cphc.201300497. URL `http://dx.doi.org/10.1002/cphc.201300497`. (Cited on pages 253 and xvii.)

[271] Y. Zou, L. Kilian, A. Schöll, Th. Schmidt, R. Fink, and E. Umbach. Chemical bonding of PTCDA on Ag surfaces and the formation of interface states. *Surface Science*, 600(6):1240 – 1251, 2006. ISSN 0039-6028. doi: http://dx.doi.org/10.1016/j.susc.2005.12.050. URL `http://www.sciencedirect.com/science/article/pii/S0039602806000458`. (Cited on page 254.)

[272] G. K. Wertheim and D. N. E. Buchanan. Interfacial reaction of C_{60} with silver. *Phys. Rev. B*, 50:11070–11073, Oct 1994. doi: 10.1103/PhysRevB.50.11070. URL `http://link.aps.org/doi/10.1103/PhysRevB.50.11070`. (Cited on page 257.)

[273] Andrew L. Walter, Shu Nie, Aaron Bostwick, Keun Su Kim, Luca Moreschini, Young Jun Chang, Davide Innocenti, Karsten Horn, Kevin F. McCarty, and Eli Rotenberg. Electronic structure of graphene on single-crystal copper substrates. *Phys. Rev. B*, 84:195443, Nov 2011. doi: 10.1103/PhysRevB.84.195443. URL `http://link.aps.org/doi/10.1103/PhysRevB.84.195443`. (Cited on page 257.)

[274] Joseph M Wofford, Elena Starodub, Andrew L Walter, Shu Nie, Aaron Bostwick, Norman C Bartelt, Konrad Thürmer, Eli Rotenberg, Kevin F McCarty, and Oscar D Dubon. Extraordinary epitaxial alignment of graphene islands on Au(111). *New Journal of Physics*, 14(5):053008, 2012. URL `http://stacks.iop.org/1367-2630/14/i=5/a=053008`. (Cited on page 257.)

[275] A. Kraft, R. Temirov, S. K. M. Henze, S. Soubatch, M. Rohlfing, and F. S. Tautz. Lateral adsorption geometry and site-specific electronic structure of a large organic chemisorbate on a metal surface. *Phys. Rev. B*, 74:041402, Jul 2006. doi: 10.1103/PhysRevB.74.041402. URL `http://link.aps.org/doi/10.1103/PhysRevB.74.041402`. (Cited on page 260.)

[276] C.A. Bobisch, A.M. Bernhart, M.R. Kaspers, M.C. Cottin, J. Schaffert, and R. Möller. Electronic Transport on the Nanoscale. In Christian Joachim, editor,

Atomic Scale Interconnection Machines, Advances in Atom and Single Molecule Machines, pages 197–214. Springer Berlin Heidelberg, 2012. ISBN 978-3-642-28171-6. URL `http://dx.doi.org/10.1007/978-3-642-28172-3_15`. (Cited on page xvii.)

[277] D. van Vörden, M. Lange, M. Schmuck, J. Schaffert, M. C. Cottin, C. A. Bobisch, and R. Möller. Communication: Substrate induced dehydrogenation: Transformation of octa-ethyl-porphyrin into tetra-benzo-porphyrin. *The Journal of Chemical Physics*, 138(21):211102, 2013. doi: http://dx.doi.org/10.1063/1.4810879. URL `http://scitation.aip.org/content/aip/journal/jcp/138/21/10.1063/1.4810879`. (Cited on page xvii.)

[278] J. Schaffert, M. C. Cottin, A. Sonntag, C. A. Bobisch, R. Möller, J.-P. Gauyacq, and N. Lorente. Tunneling electron induced rotation of a copper phthalocyanine molecule on Cu(111). *Phys. Rev. B*, 88:075410, Aug 2013. doi: 10.1103/PhysRevB.88.075410. URL `http://link.aps.org/doi/10.1103/PhysRevB.88.075410`. (Cited on page xvii.)

ACKNOWLEDGMENTS

Here, I would like to thank the people that contributed to this thesis and the success of the STM-LE project.

First, I would like to thank Prof. Dr. Rolf Möller for giving me the opportunity to conduct the work for my thesis in his group. Further, I thank him for helpful discussions and support in setting up the STM and the light detection system.

Great thanks also go to Dr. Christian Bobisch for guidance and help in all projects I worked at during the past years. As a project leader within the SFB 616, he initiated the STM-LE experiments in Duisburg-Essen. He went out of his way supervising the STM-LE project and sharing all of his scientific expertise.

Discussions with Prof. Dr. Hermann Nienhaus were always a great way to get new inputs and to further understand the data (or be more confused about it).

During the main part of the work on the STM-LE project, I worked in the lab with Ebru Ekici. Together, we built the most recent scanning unit that is in use in the STM-LE experiment right now (and another earlier version). We spent countless hours in the dark, optimizing the light detection setup and conducting experiments. We fixed a sheer endless number of broken components of the experimental setup, some of which we did not even know they existed before. We (almost) never gave up in believing there was light at the end of the tunnel(ing) and finally succeeded in conducting the first experiments presented on the newly established setup which are presented in this thesis. Without her, it would not have been possible to lead the STM-LE-project to a success.

Johannes Schaffert worked with me during the first few years of my PhD studies. I thank him for the fruitful joined research and fun times in the lab.

Special thanks go to Detlef Utzat, Tobias Roos, Doris Steeger, and Willy Platz. With their invaluable expertise, they spared no effort to grant technical support wherever needed. They were a great help in setting up the STM-LE experiment and always a source of moral support.

Additionally, over the past years I profited a lot from the shared expertise of several further present and former members of the Möller group: Ben Wortmann, Manfred Lange, Dennis van Vörden, Mark Kaspers, Alexander Bernhart, Andreas Sonntag, Hatice Karacuban, David Krix, Ulrich Hagemann, Kornelia Huba, Sebastian Bauer, Paul Graf, Philip Kapitza, Nico Schmidt, Merlin Schmuck, Matthias Müller and many others. I thank these people for fruitful discussions, collaborations and especially for the constructive and fun working atmosphere in the group. Many of my colleges also became friends over the years.

Apart from my work at the University of Duisburg-Essen, I had the opportunity to work in the group of Prof. Dr. Enrique Ortega in Donostia, Spain, for three months. I want to thank the entire group for the warm welcome and broadening my horizon. I especially thank Dr. Jorge Lobo-Checa and Dr. Andrew Walter who I performed, analyzed and discussed the ARPES data on the $BiAg_2$-system with.

Further, I profited from collaborations with Dr. Nicolás Lorente and Dr. Gustav Bihlmayer.

I thank the Studienstiftung des deutschen Volkes for support during my diploma studies and the first years of my PhD studies. Also, I profited from being part of the collaborative research center "Sonderforschungsbereich (SFB) 616". I especially want to emphasize Maria Dunke who went out of her way to especially support the PhD students in the SFB. I thank her for helping me overcome bureaucratic barriers, the opportunity to actively contribute to the organization of internal workshops, for moral support and always believing in me and the success of my scientific projects.

Dagmar and Ingo Thiele managed the administrative matters in the Möller group.

With special regard to this thesis, I thank Christian Bobisch, Ebru Ekici, Sebastian Bauer, Ben Wortmann, and Kornelia Huba for proofreading. Birte Cöster supported the analysis of the spectroscopic data by importing data sets into Origin Pro. Dr. Christian Notthoff performed SEM-measurements with me to provide us with images of our STM-LE tips. Further, I thank Dr. Detlef Diesing for helpful discussions.

Apart from the scientific contributions to this work, I want to thank my friends and family for love and support, providing distraction and listening to all my stories about work.

ERKLÄRUNG

Hiermit versichere ich, dass ich die vorliegende Arbeit selbstständig, ohne unzulässige Hilfe Dritter und ohne Benutzung anderer als der angegebenen Hilfsmittel angefertigt habe. Die aus fremden Quellen direkt oder indirekt übernommenen Gedanken sind als solche kenntlich gemacht. Die Arbeit wurde bisher weder im Inland noch im Ausland in gleicher oder ähnlicher Form einer anderen Prüfungsbehörde vorgelegt.

Die Arbeit wurde unter wissenschaftlicher Betreuung durch Herrn Prof. Dr. Rolf Möller an der Fakultät für Physik der Universität Duisburg-Essen angefertigt.

Duisburg, 1. Oktober 2015

Maren Cottin